

The Effect of Knockdown and Mutation of the Ganglioside-Induced
Differentiation-Associated Protein 1 (GDAP1) on Mitochondrial Shape
and Cell Metabolism

Dissertation
zur Erlangung des Grades
"Doktor der Naturwissenschaften"
am Fachbereich Biologie
der Johannes Gutenberg-Universität
in Mainz

Christina Wolf

Geboren am 24.04.1990 in Grevenbroich

Mainz, 2020

First supervisor: [REDACTED]

Second supervisor: [REDACTED]

Date of oral examination: 02.11.2020

This work was accomplished in the laboratory and under the supervision of [REDACTED], Institute for Molecular Medicine, University Medical Center Mainz of the Johannes Gutenberg-University Mainz. Partial experiments were performed in the laboratory [REDACTED], Dept of Biomedical Sciences, University of Padova, Padova, Italy (October/November 2018) and [REDACTED], Luxembourg Centre for Systems Biomedicine (LCSB), University of Luxembourg, Belvaux, Luxembourg (December 2019).

Declaration

I hereby declare that I conducted this thesis by myself and without any inappropriate help. I have indicated all sources used in the work. I have not or had not submitted the work now presented as a PhD thesis for a higher degree or any other scientific examination at another university or faculty.

Mainz, 07.08.2020

(Christina Wolf)

Table of Content

1.	Abstract.....	1
2.	Zusammenfassung.....	2
3.	Introduction	3
3.1.	Mitochondria	3
3.1.1.	The mitochondrial structure	3
3.1.2.	Glycolysis, TCA cycle and ATP generation.....	4
3.1.3.	Mitochondrial Calcium homeostasis.....	7
3.1.4.	Mitochondria and oxidative stress.....	8
3.1.5.	Mitochondrial dynamics	11
3.1.6.	Mitofusins	13
3.2.	Charcot-Marie Tooth disease and the role of GDAP1 and MFN2	15
3.2.1.	Charcot-Marie Tooth Disease	15
3.2.1.	GDAP1	16
3.3.	Aim of this work.....	25
4.	Materials	26
4.1.	Chemicals	26
4.2.	Consumables	28
4.3.	Antibodies	29
4.1.	Dyes for live cell imaging.....	30
4.2.	Buffer Compositions	31
4.3.	Kits.....	33
4.4.	Plasmid DNA.....	33
4.5.	Primers for PCR and qPCR.....	33
4.6.	Cell culture Media	34
4.1.	Cell lines and mice	35
4.1.1.	Cell lines	35
4.1.2.	BirA mice	36
4.2.	Equipment.....	36
4.3.	Softwares	37
5.	Methods	38

5.1.	Cell Biology	38
5.1.1.	Culturing and passaging	38
5.1.2.	Cryopreservation of cell lines	38
5.1.3.	Thawing of cells	38
5.1.4.	Transient transfection	39
5.1.5.	Patient-derived iPSC generation and differentiation to NPCs.....	39
5.1.6.	NPC and motoneuron differentiation of patient-derived iPSCs with small molecules.....	40
5.1.7.	Isolation and cultivation of murine cortical neurons	40
5.2.	Molecular biology	41
5.2.1.	Protein isolation from cells	41
5.2.2.	BCA protein assay	41
5.2.3.	SDS-PAGE	42
5.2.4.	Blue Native Page	42
5.2.5.	Virus production in HEK cells.....	43
5.2.6.	Real-time quantitative qPCR for titer determination of the viruses	44
5.2.7.	Genotyping of Rosa26-BirA mice.....	44
5.2.8.	Virus transduction of primary cortical neurons	45
5.2.9.	Pulldown of GDAP1 in primary neurons.....	45
5.2.10.	Isolation of Mitochondria	46
5.2.11.	MAM and ER isolation of cultured cells.....	46
5.2.12.	BioGEE assay (Thermo Scientific and VCP BIO).....	47
5.2.13.	GSH-PrSSG Assay.....	47
5.2.14.	PEG alkylation gel shift.....	48
5.2.15.	Biotin Switch Assay	48
5.2.16.	Phos-tag™ Blots.....	49
5.2.17.	Aequorine Measurement	49
5.2.18.	Glucose uptake.....	50
5.2.19.	BTeam.....	50
5.3.	Mass Spectrometry	51
5.3.1.	Protein digestion and LC-MS analysis	51
5.3.2.	Data processing and Label-free Quantification	51
5.4.	Microscopy	52
5.4.1.	Transmission electron microscopy.....	52
5.4.2.	Immunocytochemistry	52

5.4.3.	High Content Microscopy.....	53
5.4.4.	FEMP sensor.....	53
5.4.5.	Confocal microscopy and Imaris image analysis.....	54
5.4.6.	Statistics.....	54
6.	Results.....	56
6.1.	Impaired mitochondrial dynamics and metabolism upon GDAP1 depletion	56
6.1.1.	The effect of GDAP1 KD on mitochondrial fission and fusion proteins	56
6.1.2.	Reduced MERCS correlate with reduced GDAP1 expression.....	57
6.1.3.	Altered MCU expression in KD cells	60
6.1.4.	Increased calcineurin expression does not cause the mitochondrial shape phenotype in KD cells	61
6.1.5.	Proteomic analysis of isolated mitochondria and MAMs	63
6.1.6.	Increased glutaminolysis but reduced fatty acid synthesis upon GDAP1 KD ..	65
6.1.7.	GDAP1 silencing leads to reduced pyruvate conversion by an inactive PDH..	70
6.1.8.	Mitochondrial shape in patient-derived neuronal progenitor cells shift towards increased fusion activity.....	73
6.1.9.	Transmission electron microscopy reveals increased number of MERCS in patient-derived NPCs.....	75
6.1.10.	Patient-derived small molecule neuronal progenitor cells (smNPCs) reveal diminished intracellular glutamine concentrations	76
6.1.11.	CMT patient-derived motoneurons share similarities with the KD cells in MCU and DRP1 expression levels	78
6.1.12.	CMT-derived motoneurons exhibit increased glutaminolysis and reduced fatty acids	79
6.2.	The influence of GDAP1 expression on the intracellular redox state and on redox modification of proteins	82
6.2.1.	Mitochondrial phenotype can be reproduced with cells overexpressing WT and mutant GDAP1	82
6.2.2.	Neither inhibition of CaN nor AMPK signaling can reverse the mitochondrial shape in overexpressing cell lines.....	84
6.2.3.	Glutathione levels in SH-SY5Y cell lines.....	87
6.2.4.	GAPDH glutathionylation is not affected upon reduced GDAP1 expression....	89
6.2.5.	Posttranslational modification of Mitofusin 2 is dependent on GDAP1 expression	91

6.3.	Proteomic analysis of GDAP1 interaction partners in dependence of the redox state.....	94
7.	Discussion.....	100
7.1.	More elongated mitochondria in GDAP1 KD cells	100
7.2.	Impaired Ca ²⁺ signaling and reduced MERCs in GDAP1 KD cells	101
7.3.	Impaired IP3-mediated Ca ²⁺ release from the ER.....	105
7.4.	Metabolic defects upon aberrant GDAP1 expression	107
7.5.	Altered protein glutathionylation in GDAP1 KD cells.....	109
7.6.	Metabolic alterations are reproducible in CMT4A patient-derived motoneurons ...	112
8.	Literature.....	114
9.	Appendix.....	142
	Abbreviations	142
	Acknowledgements	147
	Curriculum vitae	149

List of Figures

Figure 1 Mitochondrial structure.....	3
Figure 2 Schematic illustration of the glycolysis and the TCA cycle	6
Figure 3 Elimination of intracellular ROS.....	9
Figure 4 Outer mitochondrial membrane fusion and fission regulating proteins.....	12
Figure 5 Schematic illustration of GDAP1 protein structure and its functional domains	17
Figure 6 The amphipathic pattern of the HD domain in the GDAP1 protein.....	21
Figure 7 Scheme of MAM, ER and mitochondrial isolation.....	47
Figure 8 Effect of GDAP1 KD on mitochondrial fission and fusion proteins	57
Figure 9 Reduced MERCS correlate with reduced GDAP1 expression	59
Figure 10 Altered MCU expression in GDAP1 KD cells.....	61
Figure 11 Increased CaN expression does not cause the mitochondrial shape phenotype in GDAP1 KD cells	62
Figure 12 Expression pattern of proteins involved in mitochondrial dynamics	64
Figure 13 Expression levels of metabolic proteins implicated in TCA cycle, glycolysis and glutaminolysis are altered in GDAP1 KD cells.....	65
Figure 14 Increased glutaminolysis upon GDAP1 KD	67
Figure 15 Reduced fatty acid synthesis upon GDAP1 KD	69
Figure 16 Inhibition of the AMPK signaling pathway does not reverse GDAP1-induced mitochondrial modifications.....	71
Figure 17 Abundance and activity of the Pyruvate dehydrogenase	72
Figure 18 Schematic illustration of the TCA cycle and dysregulations upon reduction of GDAP1 expression	73
Figure 19 More elongated mitochondria in patient-derived neuronal progenitor cells	74
Figure 20 TEM reveals reduced mitochondrial size in patient-derived NPCs	75
Figure 21 TEM reveals an increased number of MERCS in patient-derived NPCs but reduced integrity	76
Figure 22 Patient-derived small molecule NPCs (smNPCs) reveal diminished intracellular glutamine concentrations.....	77
Figure 23 CMT patient-derived motoneurons share similarities with the KD cells in MCU and DRP1 expression.....	79
Figure 24 CMT-derived motoneurons reveal increased glutaminolysis and reduced fatty acid synthesis	80
Figure 25 Abundance and activity of the PDH in CMT-derived motoneurons	81
Figure 26 The mitochondrial shape is changed in cells overexpressing WT and mutant GDAP1	83

Figure 27 Altered expression levels of mitochondrial fission proteins in cells overexpressing WT and mutant cells	84
Figure 28 Inhibition of CaN does not reverse the mitochondrial shape in GDAP1 overexpressing cells	85
Figure 29 Inhibition of the AMPK signaling pathway in GDAP1 overexpressing cell lines does not show any alteration of mitochondrial shape.....	86
Figure 30 Glutathione levels in SH-SY5Y cell lines	88
Figure 31 Altered GAPDH migration in GDAP1 KD cells.....	91
Figure 32 Posttranslational modification is dependent on GDAP1 expression	93
Figure 33 Proteomic screen for GDAP1 interaction partner.....	95
Figure 34 GDAP1 interaction partners in dependence of the redox state	96
Figure 35 No alteration in cofilin1 protein levels but reduced cofilin1-mitochondria contacts in GDAP1 KD cells.....	98
Figure 36 Regulation of mitochondrial dynamics via cofilin1 and DRP1 recruitment to the OMM and alterations in metabolism of GDAP1 KD cells.....	99
Figure 37 Hypothesized mechanism of GDAP1 and cofilin interaction on mitochondrial shape	104

List of Tables

Table 1 Chemicals	26
Table 2 Consumables	28
Table 3 Antibodies	29
Table 4 Dyes for live cell imaging	30
Table 5 Buffer Compositions	31
Table 6 Kits.....	33
Table 7 Plasmids	33
Table 8 Primers for PCR and qPCR.....	33
Table 9 Cell culture media and supplements	34
Table 10 Cell culture media compositions.....	34
Table 11 Cell lines	35
Table 12 Equipment.....	36
Table 13 Softwares.....	37
Table 14 qPCR for Virus DNA titration	44
Table 15 Rosa26-BirA Genotyping.....	45

1. Abstract

Mutations in the gene encoding for the ganglioside-induced differentiation-associated protein 1 (GDAP1) cause the hereditary polyneuropathy Charcot-Marie-Tooth disease (CMT). Structurally, the GDAP1 protein possesses a transmembrane domain anchored in the outer mitochondrial membrane (OMM) and two domains, sharing similarities to glutathione-transferases (GST) – enzymes catalyzing the conjugation of the antioxidant glutathione to electrophilic residues. GDAP1 is highly involved in mitochondrial dynamics, ongoing processes of fusion and fission. Changes in GDAP1 expression levels can disturb this balance and shift the mitochondrial shape to either fragmented mitochondria when overexpressed or fused mitochondria when silenced.

This work not only confirmed that perturbed GDAP1 expression leads to more mitochondrial elongation in GDAP1 knockdown (KD) cell lines but also in neuronal cells derived from autosomal-recessive CMT4A patients caused by a GDAP1 mutation. A potential interaction with the cytosolic actin-binding factor cofilin1 was also identified. Cofilin1 regulates the depolymerization of actin filaments, the abundance of the intracellular signaling hubs mitochondria-ER contact sites (MERCs) and mitochondrial fragmentation mediated by the mitochondrial fission factor dynamin-related protein 1 (DRP1). This may be a leading cause for the morphological and metabolic impairments observed in this work. Hence, translocation of DRP1 to the OMM was reduced, and MERCs had an increased width in GDAP1 KD cells, resulting in an impaired Ca^{2+} transfer upon stimulation of the inositol-1,4,5-tris-phosphate receptor (IP3R).

We also observed an inefficient pyruvate conversion to acetyl-CoA, a crucial Ca^{2+} -dependent process controlling citrate production and entry into the TCA cycle. Additionally, we observed that GDAP1 KD cells and patient-derived motoneurons revealed a significant reduction in cytosolic fatty acids and that both *in vitro* models shifted their mitochondrial metabolism towards increased glutaminolysis – most likely, a compensatory effect, though GDAP1 KD cells were still less efficient for mitochondrial ATP production.

Hence, this work shed light on metabolic alterations in GDAP1 KD but also in CMT4A patient-derived cells and contributed to further explanation of potential GDAP1 targets.

2. Zusammenfassung

Die erblich bedingte Polyneuropathie Charcot-Marie-Tooth-Krankheit (CMT) kann durch Mutationen im Gen für das *ganglioside-induced differentiation-associated protein 1 (GDAP1)* verursacht werden. Das GDAP1-Protein besitzt eine in der äußeren Mitochondrienmembran verankerte Transmembrandomäne und zwei Domänen, die Ähnlichkeiten mit Glutathion-Transferasen (GST) aufweisen – Enzyme, die die Konjugation des Antioxidans Glutathion an elektrophile Reste katalysieren.

GDAP1 ist in hohem Maße an der Dynamik von Fusion und Fission der Mitochondrien beteiligt. Diese zwei gegenläufigen und ausbalancierten Prozesse ermöglichen es den Mitochondrien, auf diverse Signale zu reagieren, um den Energiebedarf der Zellen zu decken. Änderungen im Expressionslevel von GDAP1 können dieses Gleichgewicht stören und die mitochondriale Morphologie erscheint entweder fragmentiert oder fusioniert, wenn die GDAP1-Expression entsprechend erhöht oder verringert ist.

Die vorliegende Arbeit bestätigte nicht nur, dass ein Mangel an GDAP1 zu einer stärkeren mitochondrialen Elongation in GDAP1-Knockdown-Zelllinien (KD) führt. Diesen Effekt konnten wir auch in neuronalen Zellen nachweisen, die von autosomal-rezessiven CMT4A-Patienten mit Mutationen in GDAP1 stammen. Darüber hinaus habe ich eine mögliche Interaktion mit dem zytosolischen Aktin-bindenden Protein Cofilin1 identifiziert. Cofilin1 reguliert die Depolymerisierung der Aktinfilamente, das Vorkommen und die Eigenschaften der intrazellulären Signalknoten Mitochondrien-ER-Kontaktstellen (MERCs) und dadurch ebenfalls die mitochondriale Fragmentierung durch das Fissionsprotein, *dynamin-related protein 1 (DRP1)*. Diese Interaktion könnte eine Hauptursache für die in dieser Arbeit beobachteten morphologischen und metabolischen Beeinträchtigungen sein. Die Translokation von DRP1 an die OMM war ebenfalls reduziert, und der Zwischenraum der MERCs deutlich erhöht in den GDAP1-KD-Zellen, was zu einem gestörten Ca^{2+} -Transfer bei Stimulation des Inositol-1,4,5-Tris-Phosphat-Rezeptors (IP3R) führte.

Wir beobachteten auch eine ineffizientere Umwandlung von Pyruvat in Acetyl-CoA, ein entscheidender Ca^{2+} -abhängiger Prozess, der die Zitratproduktion und den TCA-Zyklus beeinflusst. Darüber hinaus beobachteten wir, dass GDAP1-KD-Zellen und Motoneuronen von CMT4A-Patienten eine signifikante Reduktion der zytosolischen Fettsäuren aufzeigten und dass beide *in vitro*-Modelle ihren mitochondrialen Metabolismus in Richtung einer erhöhten Glutaminolyse verlagerten - höchstwahrscheinlich ein kompensatorischer Effekt, wenngleich GDAP1-KD-Zellen dennoch eine weniger effiziente mitochondriale ATP-Produktion aufwiesen. Durch die Identifikation von GDAP1-Interaktionspartnern und der metabolischen Veränderungen in GDAP1 KD und CMT-Patientenzellen trug diese Arbeit zu einem besseren Verständnis der Vorgänge der CMT-Erkrankung bei.

3. Introduction

3.1. Mitochondria

3.1.1. The mitochondrial structure

Mitochondria are semi-autonomous cellular organelles, derived from bacterial symbionts (Capps et al., 2003; Wallace, 2005). They were first discovered in the 1840s, and initially referred to as “bioblasts” and “elementary organisms” (Altmann, 1894; Cowdry, 1953; Ernster and Schatz, 1981). They contain their own circular DNA (mitochondrial DNA, mtDNA), of around 16 kilo base pairs (kbp), containing 37 genes. Out of these, 13 genes encode for subunits of the complexes of the respiratory chain, which generates around 90 % of cellular ATP via oxidative phosphorylation (OXPHOS) (Chan, 2006; Salin et al., 2015). Mitochondria are the most abundant cellular organelles (Lewis et al., 2018). The mitochondrial structure is composed of an outer membrane (outer mitochondrial membrane, OMM) and an inner membrane (inner mitochondrial membrane, IMM), which encloses the mitochondrial matrix and where the complexes of the electron transport system (ETS) are localized (Figure 1).

The outer mitochondrial membrane reveals a high permeability for uncharged molecules and

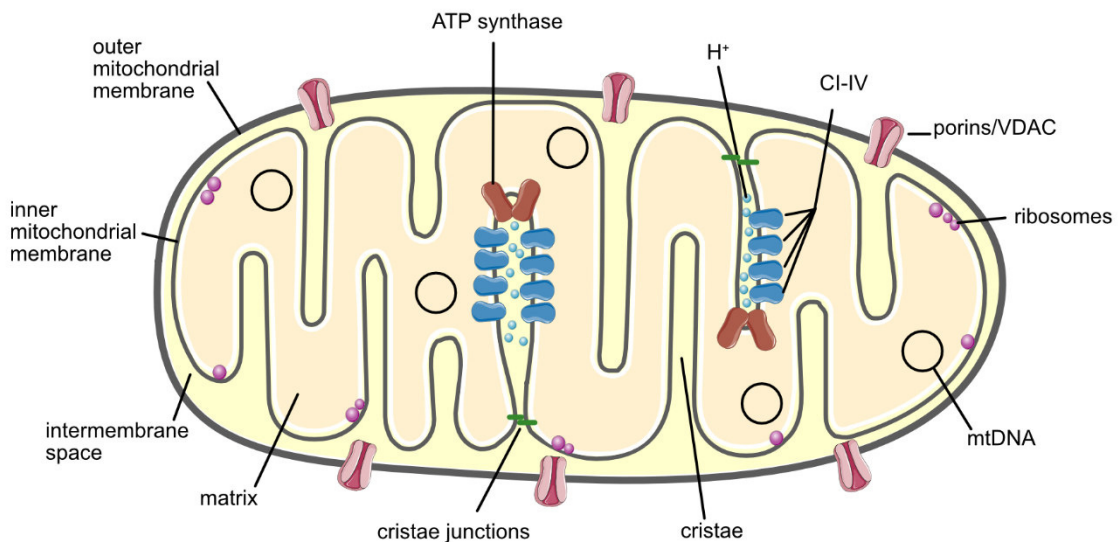


Figure 1 Mitochondrial structure

Schematic illustration of the mitochondrial structure composed of an outer and inner mitochondrial membrane, which forms invaginations, termed cristae, the location of complex I-IV and ATP synthase. ATP generation is fuelled by the proton (ΔpH) and electrochemical gradient ($\Delta\psi\text{m}$). The permeability of the OMM is achieved by porins/voltage-dependent anion channels (VDAC). The mitochondrial matrix contains the mitochondrial DNA (mtDNA) and ribosomes for protein biosynthesis.

ions up to 5 kilo Dalton (kDa) in size and mainly consist of so-called porins, such as the voltage-dependent anion channels (VDAC), facilitating the transport into the intermembrane space or vice versa (Bender & Martinou, 2016; Kühlbrandt, 2015; Rizzuto, De Stefani, Raffaello, &

Mammucari, 2012). The diffusion of any ions and larger molecules through the IMM into the matrix in contrast is highly regulated by specific transport proteins to maintain the mitochondrial membrane potential generated by the respiratory system for ATP generation (Kühlbrandt, 2015). Furthermore, the matrix has a high density of proteins, all implicated in either DNA replication, biosynthesis or TCA cycle, to mention but a few (Kühlbrandt, 2015). Electron microscopy images reveal small invaginations of the inner mitochondrial membrane into the matrix, called the cristae (Palade, 1953). They serve to increase the IMM surface and are the position of the ETS for mitochondrial ATP production. Hence, the cristae lumen is separated from the intermembrane space by so-called cristae junctions and enriched with protons and the electron transporter protein cytochrome *c*, while the cristae membrane is mainly the site of ATP generation by the electron transport system. Davies et al. showed that the complexes of the respiratory chain are not randomly distributed along the IMM in the cristae rather the ATP synthase is forming dimers along the edges of the cristae with an angle of 70°, hence supposedly generating the overall cristae formation and appearance (Figure 1) (Davies et al., 2011).

3.1.2. Glycolysis, TCA cycle and ATP generation

The cellular energy production and metabolism can be divided into three parts – glycolysis, tricarboxylic acid cycle (TCA or Krebs cycle) and the electron transport system. Glycolysis consists of the conversion of glucose to NADPH and two pyruvate molecules. Pyruvate is either converted to lactate by lactate dehydrogenase (LDHA) or predominantly transported into the mitochondrial matrix to fuel the TCA cycle as citrate after I) decarboxylation and oxidation into acetyl-CoA by the Ca²⁺-dependent pyruvate dehydrogenase complex (PDC) and II) conversion of acetyl-CoA and oxaloacetate (OAA) to citrate by citrate synthase (CISY) (Figure 2). During glycolysis, the net energy profit is 2 ATP per glucose molecule. Oxidative phosphorylation (OXPHOS) by the ETS yields more than 30 ATP molecules per glucose molecule, which highlights the importance of a well-functioning pyruvate entry into the mitochondria (Bender and Martinou, 2016). While the OMM is permeable for pyruvate, its transport into the mitochondrial matrix is regulated by the mitochondrial pyruvate carrier (MPC) located in the inner mitochondrial membrane (Papa et al., 1971). The MPC is composed of two subunits, which are termed MPC1 and MPC2, though yeast express a third subtype, the Mpc3 (Bricker et al., 2012; Herzig et al., 2012). Active MPC complex formation involves a heteromeric complex of both MPC1 and MPC2 subunits (Bricker et al., 2012; Compan et al., 2015). The pyruvate transport by the MPC is supported and fueled by the proton gradient of the IMM, which is maintained by the complexes of the ETS. Matrix pyruvate can either enter the TCA

Introduction

after conversion by the multi-enzyme PDC or converted to oxaloacetic acid (OAA) by pyruvate carboxylase (PC) in an ATP-consuming manner. The pyruvate carboxylase is part of gluconeogenesis and mainly driven by high mitochondrial pyruvate concentrations to accelerate the glucose production via malate, lactate or pyruvate synthesis (Bender and Martinou, 2016). The PDC in contrast is composed of three subunits, the pyruvate dehydrogenase (PDH, E1), dihydrolipoyl transacetylase (DLAT, E2), and dihydrolipoyl dehydrogenase (DLD, E3). Its activity is regulated by two opposing enzymes – the PDH kinase (PDK) and the PDH phosphatase subunit 1 (PDP1) (reviewed by Tovar-Mendez, Miernyk, & Randall, 2003). The PDK catalyzes the phosphorylation of three serine residues of the PDH α subunit, inhibiting its activity, while the PDP1 in contrast activates the PDC by dephosphorylation in a Ca^{2+} -dependent manner (Roche et al., 2001).

The conversion of acetyl-CoA to citrate is the critical stage, which determines the effectivity of the TCA and later ATP generation. Consequently, breakdown of acetyl-CoA favors the generation of NADH and FADH_2 , which serve as electron donors to fuel the respiratory chain to generate the main cellular ATP (Fornie et al., 2004; Mailloux et al., 2007), since the activity of various enzymes of the TCA cycle, such as malic enzyme 1 (ME1), isocitrate dehydrogenase (IDH) or glucose-6-phosphate dehydrogenase (G6PD) are NADP-dependent and result in the reduction to NADPH or NADH (Figure 2). Aconitase catalyzes the transformation of citrate to isocitrate, which is further processed by isocitrate dehydrogenase (IDH) to produce α -ketoglutarate with NADH and H^+ as by-product. Once α -ketoglutarate is produced, it is further processed to succinyl-CoA, succinate, fumarate and malate via activity of the α -ketoglutarate dehydrogenase, succinyl-CoA synthetase, succinate dehydrogenase and fumarate, respectively. In case of an inefficient pyruvate import or conversion, cytosolic α -ketoglutarate can also be imported into the mitochondrial matrix to enter the TCA cycle. Additionally, α -ketoglutarate can be produced by the glutamate-dehydrogenase after glutamine conversion to glutamate (Vacanti et al., 2014). Hence, several metabolic pathways have evolved to compensate a defect in the glycolysis and pyruvate metabolism. The activity of IDH not only favors the reaction of α -ketoglutarate with H_2O_2 that results in the production of succinate, CO_2 and H_2O as a nonenzymatic decarboxylation process. IDH also favors the production of the antioxidant glutathione via NADPH generation, making α -ketoglutarate an important scavenger of reactive oxygen species (ROS) (Liu et al., 2018; Mailloux et al., 2007).

The citrate shuttle on the other hand involves the transport of citrate into the cytoplasm where it can be converted back to Acetyl-CoA, which in turn serves as a building block for fatty acid synthesis (Menendez and Lupu, 2007).

Introduction

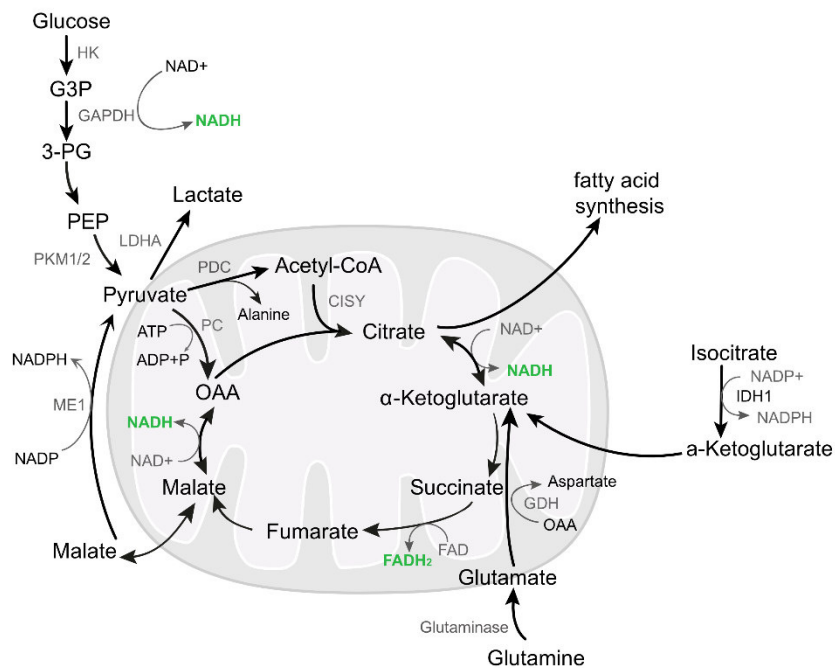


Figure 2 Schematic illustration of the glycolysis and the TCA cycle

Glycolysis produces pyruvate, which can be either converted to lactate catalyzed by the lactate dehydrogenase (LDHA) or transported into the mitochondrion to enter the TCA cycle after decarboxylation and oxidation into acetyl-CoA. This reaction is catalyzed by the pyruvate dehydrogenase complex (PDC). Pyruvate carboxylase (PC) is activated by an excess of intramitochondrial pyruvate, producing oxaloacetate (OAA) in an ATP-consuming manner, which in turn can be further transformed to malate, transferred to the cytosol and finally reconverted to pyruvate via malic enzyme 1 (ME1). The citrate synthase (CISY) catalyzes the production of citrate, which either enters the TCA or is shuttled out of the mitochondrion to fuel fatty acid synthesis. Isocitrate dehydrogenase (IDH1) generates α -ketoglutarate and NADPH out of Isocitrate and NADP⁺. α -ketoglutarate is also generated by the conversion of glutamate via glutamate dehydrogenase (GDH).

The respiratory system is composed of five complexes, namely the NADH dehydrogenase (complex I, CI), succinate dehydrogenase (complex II, CII), cytochrome bc1 (complex III, CIII), cytochrome oxidase (complex IV, CIV) and ATP synthase (complex V, CV). Complex I, III, IV and V are partially encoded and produced in the mitochondrial matrix – complex II is also part of the TCA cycle and fully encoded by nuclear DNA and transported after transcription and translation into the mitochondria (Rutter et al., 2010). The activity of CI, CIII and CIV generates a proton gradient (ΔpH) along the inner mitochondrial membrane via transport of H⁺ protons from the matrix into the intermembrane space, which also generates an electrochemical gradient ($\Delta\psi_m$) (Saraste, 1999). The protons are generated by electron transfer from NADH at CI and succinate and FADH₂ at CII and are further transferred to the coenzyme Q and complex III, followed by the cofactor cytochrome c (Saraste, 1999). Electron transfer to the active center of CIV induces the reduction of O₂ to H₂O and enhancement of the proton gradient (Saraste, 1999). CV, also named the ATP synthase, uses the electrochemical gradient to phosphorylate ADP to ATP (Capaldi et al., 1994; Jonckheere et al., 2012). The proton gradient

generates a mechanical rotational energy of the F_0 subunit of the complex V, which is used to drive the synthesis of ADP to ATP (Jonckheere et al., 2012).

3.1.3. Mitochondrial Calcium homeostasis

Calcium (Ca^{2+}) is an important intracellular first and second messenger for countless biological processes, having its main storage in the endoplasmic reticulum (ER) (Koch, 1990; Lam and Galione, 2013). There is a diverse range of signaling functions, varying from cell differentiation to neuronal neurotransmitter release to apoptosis induction (Bouschet and Henley, 2005; Mekahli et al., 2011). Ca^{2+} is an indispensable intracellular messenger, but prolonged Ca^{2+} extrusion and a dysregulated Ca^{2+} homeostasis can lead to cell death (Bouschet and Henley, 2005). Its cytosolic concentrations at steady-state are around 100 nM while the ER[Ca^{2+}] levels range from 0.1-1 mM (Bygrave and Benedetti, 1996; Putney and Tomita, 2012).

The binding of Ca^{2+} to various proteins, such as phospholipase C (PLC) or Calcineurin (CaN) has an important effect on cellular signaling pathways. As such, the interaction of PLC stimulates the generation of inositol 1,4,5-trisphosphate (IP3), the ligand for the ER-bound IP3 receptor (IP3R), which in turn leads to Ca^{2+} release from the ER into the cytosol (Putney and Tomita, 2012). In response to this Ca^{2+} release and in order to refill the store, the mechanism of the store-operated calcium entry (SOCE) plays a vital role. It is composed of the proteins stromal interacting molecule 1 (STIM1) and Orai1 that are located at the ER and plasma membrane, respectively (Putney and Tomita, 2012). Stimulated by ER[Ca^{2+}] depletion, STIM1 translocates close to the plasma membrane, where it activates the Orai1 channels to induce Ca^{2+} entry from extracellular space to the cytosol (Putney and Tomita, 2012). The sarco/endoplasmic reticulum Ca^{2+} -ATPase (SERCA) located in the ER membrane is then activated and pumps Ca^{2+} into the ER lumen, where it is bound by Ca^{2+} -binding proteins, such as Calreticulin, calnexin or the glucose-regulated protein 78 (GRP78/BiP) for Ca^{2+} buffering and storage (Bouschet and Henley, 2005; Mekahli et al., 2011; Papp et al., 2003).

Besides the ER, mitochondria are indispensable intracellular Ca^{2+} stores and interact with subplasmalemmal STIM1 after ER[Ca^{2+}] depletion and SOCE activation (Frieden et al., 2005). Recent studies exhibited that mitochondrial Ca^{2+} uptake is a crucial factor for SOCE activation, whilst this effect is diminished after uncoupling and loss of mitochondrial membrane potential (Naghdi et al., 2010). Mitochondria are here vital cellular organelles which take up Ca^{2+} entering the cytosol through the plasma membrane to eventually relay the Ca^{2+} to the ER (Frieden et al., 2005). Hence, a loss of subplasmalemmal mitochondria also can largely affect the ER[Ca^{2+}] levels (Frieden et al., 2005). Specialized contact sites between the ER and

mitochondria, termed mitochondria-ER contact sites (MERCs), facilitate a rapid mitochondrial Ca^{2+} uptake, primarily via VDAC at the OMM (Szabadkai et al., 2006). After IP_3 -derived intracellular Ca^{2+} release, MERCs exhibit increased Ca^{2+} levels with up to 50 μM (Schlesinger et al., 1997). Two terms that are often used as synonyms to describe these contact sites are MERCs and MAMs, mitochondria-associated membranes. While MERCs describe the “architecture and ultrastructural organization”, MAMs rather refer to the “biophysical enrichment” defining the composition of lipids and proteins (Giacomello and Pellegrini, 2016). Henceforth, I will distinguish these terms by this definition.

Several matrix proteins are Ca^{2+} -dependent, such as the PDP1, and it has been shown that Ca^{2+} influx significantly induces mitochondrial ATP production. Ca^{2+} transport along the IMM is mainly driven by the mitochondrial calcium uniporter (MCU) which forms a complex with several other scaffolding proteins (Tomar et al., 2016). The main driving force for Ca^{2+} influx across the IMM is the mitochondrial membrane potential (Rizzuto et al., 2012). Ca^{2+} extrusion in contrast is regulated by the $\text{Na}^+/\text{Ca}^{2+}$ exchanger NCLX, the mitochondrial analog for the plasma membrane resident NCX channel (Kim et al., 2012; Rizzuto et al., 2012). Notably, less is known about the outward channels in the mitochondria, especially regarding Na^+ - independent Ca^{2+} channels. However, to prevent Ca^{2+} overload in the mitochondria, which can be caused – besides others – by increased ROS levels, the mitochondrial permeability transition pore (mPTP) has been identified and is activated and opened either transiently or persistently in response to high Ca^{2+} levels in the mitochondrial matrix (Rizzuto et al., 2012). The mPTP holds a high conductance and its permanent opening leads to a disruption of the membrane potential, inactivity of the ETS and hence, to mitophagy or even cell death mediated by the extrusion of apoptotic proteins – cytochrome *c* and various caspases that usually reside in the mitochondrial cristae (Halestrap, 2009; Rizzuto et al., 2012).

3.1.4. Mitochondria and oxidative stress

Oxidative stress can be understood as an imbalance between the production of free radicals, in particular, reactive oxygen species (ROS) and the antioxidant processes for inactivation and scavenging (Robert et al., 2014; Uttara et al., 2009; Wüllner et al., 1999).

One of the main ROS producers is the ER protein oxidoreductin α (Ero1 α), whose catalytic function on building disulfide bridges during protein folding generates H_2O_2 and an increase in oxidized glutathione (GSSG) levels (Appenzeller-Herzog, 2011; Cuozzo and Kaiser, 1999). Other radicals, such as superoxide anion (O_2^-) or hydroxyl radicals (HO^\bullet) are unstable and very reactive (Finkel and Holbrook, 2000).

Introduction

Mitochondria are the main ROS producers of the cell in the process of energy production via oxidative phosphorylation (Murphy, 2009; Turrens, 2003). Here, complex I and III of the respiratory chain are the main sources of mitochondrial ROS (Turrens, 1997). To cope with oxidative stress, the elements of the “redox triangle” (Yoboue et al., 2018) – ER, mitochondria and peroxisomes – are in close proximity within the cell. Peroxisomes are single membrane-bound organelles, whose main functions include the beta-oxidation of fatty acids, detoxification of glyoxylates and the metabolism of ROS (Wanders and Waterham, 2006). However, mitochondria also provide various mechanisms to scavenge ROS and to avoid oxidative stress-induced mitophagy. Various enzymes are specialized to eliminate cellular H_2O_2 , such as catalases or glutathione peroxidase (GPX) 1 and 4 whose main function is to reduce H_2O_2 to H_2O while reduced glutathione (GSH, γ -L-glutamyl-L-cysteinylglycine) is oxidized to a glutathione dimer GSSG, which is produced as side-product (Figure 3) (Lubos et al., 2011). GSH is a tripeptide composed of glutamate, cysteine and glycine that is intracellularly produced in two ATP-dependent steps (Lewerenz et al., 2013). GSH as such is a nucleophilic molecule,

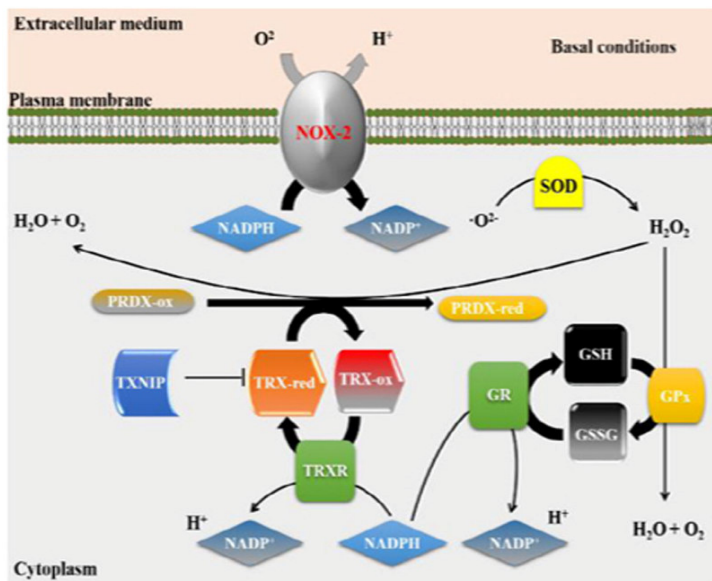


Figure 3 Elimination of intracellular ROS

O_2^- can be converted to O_2 and H_2O_2 by superoxide dismutases (SOD), which in turn can be eliminated by either the activity of glutathione peroxidase (GPX) via oxidation of GSH to GSSG or by peroxidexins. Oxidized PRDX can be reduced by Thioredoxins, which are converted into their active state by thioredoxin reductase. In these reactions, NADPH serves as the necessary electron source. NOX-2 is the membrane bound NADPH oxidase, which oxidizes molecular oxygen to superoxide anion; GR – glutathione reductase, TRX – thioredoxin, TRXR - thioredoxin reductase, ox – oxidized, red – reduced (adapted from Madrigal-Matute et al., 2015).

which can easily react with endogenous electrophiles (Ketterer et al., 1983). The reaction of GSH and GSSG can either result in the reduction of disulfides or the modification of thiols, catalyzed by glutathione redoxins (GRX) (Deponce, 2013). This glutathione conjugation to thiol groups occurs as an antioxidant reaction as described, but also has the advantage of protecting thiols against presumable toxic oxidation to sulfinic or sulfonic acid, an irreversible oxidation leading to protein unfolding, toxic aggregation and eventually to cell death (Fucci et al., 1983; Kruyer et al., 2019; Wolf et al., 2020). Glutathione transferases (GST) catalyze the conjugation of GSH to electrophilic residues, but also protect proteins and DNA from oxidative stress (Allocati et al., 2018; Lin et al., 2009). GSTs are specific enzymes that are distinguished by their location – cytosolic, mitochondrial, or microsomal GSTs. Microsomal GSTs are often

referred to as MAPEG, membrane-associated proteins involved in eicosanoid and glutathione metabolism, and are integral membrane-bound proteins (Allocati et al., 2018), while cytosolic and mitochondrial GSTs are usually soluble proteins (Deponce, 2013). Cytosolic GSTs are classified into alpha, zeta, theta, mu, pi, sigma and omega GSTs (Allocati et al., 2018). Structurally, the active-side domain of GSTs determines the GSH-binding ability and is commonly termed as the G-side and a substrate binding site, the H-site (Googins et al., 2020). While the majority of GSTs have a tyrosine residue in their active side chain, mitochondrial kappa-class, as well as cytosolic theta-class GSTs reveal a serine residue (Allocati et al., 2018).

In vitro depletion of GSH levels can be achieved by either the inhibition of GSH production, for example via buthionine-sulfoximine (BSO) or by GST inhibition via ethacrynic acid (EA) (Awasthi et al., 1993; Drew and Miners, 1984). EA reacts with GSTs, resulting in a conjugate of EA with GST (Awasthi et al., 1993; Wüllner et al., 1999). Glutathione reductase in turn can revert GSSG to GSH in an NADPH-dependent manner, producing NADP⁺. Furthermore, peroxiredoxin (PRDX) 3 and in particular PRDX5, which is also present in peroxisomes, are specified to reduce H₂O₂ in mitochondria. PRDXs are the main drivers of H₂O₂ detoxification – almost 90 % of mitochondrial H₂O₂ is reduced by PRDXs (Cox et al., 2010). Superoxide dismutases (SOD1 and SOD2) are ROS scavengers highly present in the mitochondrial matrix and intermembrane space, respectively, and convert O₂⁻ to H₂O₂ and molecular oxygen (O₂) (Docampo and Moreno, 2017; Yoboue et al., 2018).

In order to scavenge potentially toxic ROS or RNS, protein thiols (SH, sulfhydryl groups) can be oxidized and modified. Such posttranslational modifications (PTM) of proteins can have a strong impact on the protein's function itself and on the cellular mechanisms. In particular, thiols in cysteine residues are susceptible to posttranslational modification due to their physiological accessibility and their pKa. PTMs such as nitrosylation, oxidation, glutathionylation or sulfydration of sulfhydryl groups can change the overall charge of the protein residues and lead to conformational changes and hence to activation or inhibition of a protein's function (Bak and Weerapana, 2015). In addition to this, modification of proteins not only leads to an inability of complex formation but also primarily to conformational changes of residues, shifting the potential along the structure and eventually affecting the protein's function. For instance, in the case of VDAC1 the ability to transport metabolites and maintaining the cellular signaling pathways between mitochondria and the cytosol can be affected. VDAC activation and opening seems to be highly regulated by nitrosylation in terms of an increase in reactive nitrogen species (RNS) (Sultana et al., 2006). This nitrosylation of VDAC1 affects the channel opening and conductance (Yang et al., 2012). VDAC1 controls the transition of various metabolites such as Ca²⁺ and ATP and is involved in pro-apoptotic

processes, for example the transport of the apoptogenic factors cytochrome *c* or caspases. Interaction of VDAC1 with Bcl-XI has been confirmed to enhance this release, but protein nitrosylation of VDAC1 may have an inhibitory effect on this mechanism (Sultana et al., 2006). Once ROS are leaking out of the mitochondria into the cytosol via VDAC1 (Han et al., 2003), they can interact with extramitochondrial cytosolic proteins. For instance, the glycolytic enzyme glyceraldehyde-3-phosphate dehydrogenase (GAPDH) is glutathionylated in the presence of both H₂O₂ and GSH, which can furthermore induce an intramolecular disulfide, structural alteration and finally inhibition of its enzymatic function (Barinova et al., 2017; De Simoni et al., 2013). Hence, ROS and RNS are not only toxic molecules but are also vital intracellular signaling molecules regulating processes such as ATP production, Ca²⁺ signaling, mitophagy or even mitochondrial dynamics (D'Autréaux and Toledano, 2007; Shutt et al., 2012; Turkan, 2018). Accordingly, the redox regulation of transcription factors such as nuclear factor κB (NFκB) or nuclear factor erythroid 2-related factor (Nrf2), in particular via glutathionylation, is also a pro-survival response (Deponte, 2013; Groeger et al., 2009; Sies et al., 2017). Such ROS-induced signaling processes are termed as oxidative eustress rather than oxidative stress (Sies et al., 2017).

Especially neurons are susceptible to cell damage upon oxidative stress since they highly depend on OXPHOS due to their high energy demand (Liu et al., 2017). Considering this, the levels of antioxidants are rather low in the mitochondria. Consequently, neurodegenerative diseases often reveal a defect in mitochondrial respiration, increased generation of ROS, accumulation of mtDNA mutations, impairment of mitochondrial Ca²⁺ signaling or increased immune responses, which eventually enhance ROS levels and oxidative stress (reviewed in Liu et al., 2017; Mangialasche et al., 2009).

3.1.5. Mitochondrial dynamics

Mitochondria are highly dynamic organelles that undergo continuous processes of fusion and fission to maintain their function (Chan, 2012). For what is known so far, these two mechanisms are independent of each other (Malka et al., 2005), but are vital for cell survival by rapid reactions to external stresses and hence, to meet the cell's energy demand (Cho et al., 2009a; Meeusen et al., 2004). Several environmental conditions regulate the mitochondrial network as such – cellular stress level, oxidative or nitrosative stress, DNA damage or autophagy induction. Per se, fusion of the inner mitochondrial membrane (IMM) requires mitochondrial membrane potential and electrical gradient (Meeusen et al., 2004) but both OMM and IMM fusion is dependent on guanosine triphosphate (GTP) hydrolysis (Malka et al., 2005; Meeusen et al., 2004). Mitochondrial fission events regulate and enable mitochondrial transport

throughout the cells and especially along the neurons' axons (Berthet et al., 2014; Fukumitsu et al., 2016), whereas the fusion process can also spare mitochondria from mitophagy by allowing an exchange of biolipids and mtDNA (Ono et al., 2001; Toyama et al., 2016; Twig and Shirihai, 2011). Mitochondrial morphology in neurons appears to depend on their distinct localization. Hence, in most neuronal cell types, mitochondria in the dendrites are rather long, whereas axonal mitochondria show a more fragmented shape (Lewis et al., 2018).

In response to cellular and in particular oxidative stress, several mechanisms lead to a change of mitochondrial morphology to cope with the challenges and to avoid mitophagy or even autophagy and cell death.

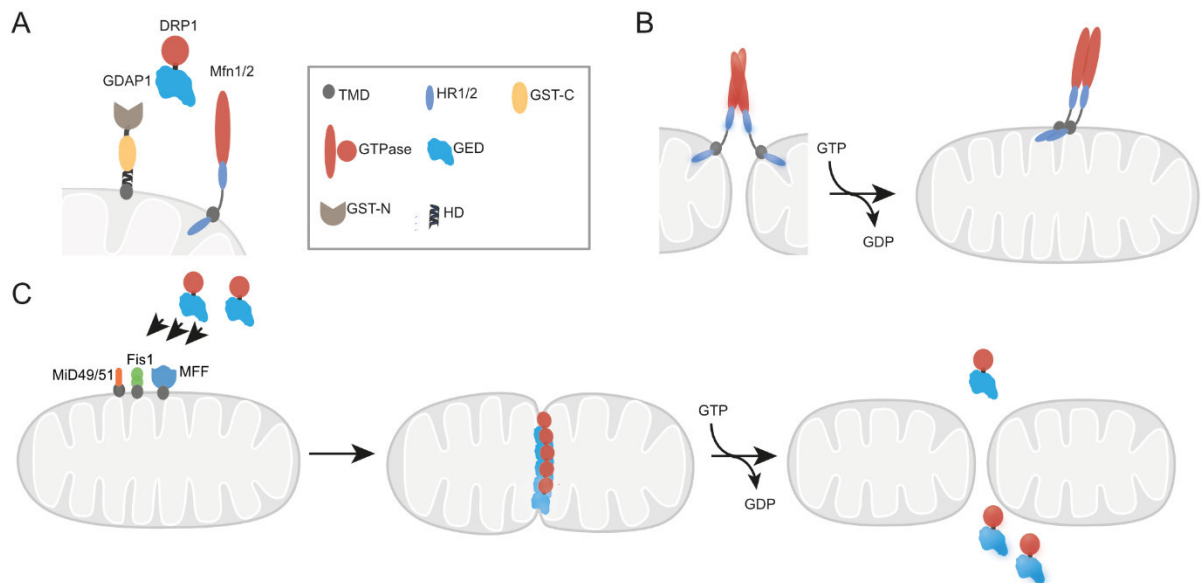


Figure 4 Outer mitochondrial membrane fusion and fission regulating proteins

A) GDAP1, DRP1 and MFN2 as fission and fusion proteins of the outer mitochondrial membrane (OMM) with their respective protein domains. TMD – transmembrane domain; HR1/2 – heptad region 1/2; GST-C – C-terminal glutathione transferase; GST-N – N-terminal glutathione transferase; GTPase – Guanidine-triphosphatase; GED – GTPase effector domain; HD – hydrophobic domain; B) MFN1 and MFN2 proteins can form homo- or heterodimers on two adjacent mitochondria to induce outer mitochondrial fusion via GTP-hydrolysis. C) Fission process induced by DRP1 translocation to the mitochondria, binding to its receptors MFF, Fis1 or MiD49/51 at the OMM. DRP1 oligomerizes and encircles and constricts the mitochondrion, resulting in fission via GTP-hydrolysis.

Fusion of adjacent mitochondria can be induced by homo- or heterodimers of the GTPases Mitofusin 1 and 2 (MFN1/MFN2) (Figure 4B). Both proteins are located at the outer mitochondrial membrane. Fusion of the inner mitochondrial membrane is mediated by the GTPase optical atrophy 1 (OPA1). OPA1 activation goes along with its proteolytic cleavage; this process may be linked to loss of membrane potential (Mishra et al., 2014). In steady-state, the long and shorter isoforms are both present in the mitochondria (Ishihara et al., 2006; Song et al., 2007). Recent studies show that the cleavage relies to a high extent on OXPHOS activity – the enzymatic cleavage is achieved by the ATP-dependent metalloprotease Yme1L and is increased under high OXPHOS conditions (Mishra et al., 2014).

Fragmentation of mitochondria can be primarily mediated by the cytosolic GTPase dynamin-related protein 1 (DRP1), which translocates to the outer mitochondrial membrane after activation, forms oligomers and encircles the mitochondrion, thereby inducing fragmentation (Figure 4C) (Smirnova et al., 2001; Yoon et al., 2001). DRP1 is composed of four domains: an N-terminal GTPase domain, a dynamin-like domain, an insert B domain, and a C-terminal GTPase effector domain, the GED (Cho et al., 2009a). Regulated by altered Ca^{2+} levels, this mechanism is controlled by opposing phosphorylation and dephosphorylation events. The activity is highly dependent on the phosphorylation state of two serine residues Ser616 and Ser637, which exert opposite effects on the mitochondrial morphology – Ser616 phosphorylation activates its translocation (Kashatus et al., 2015) while Ser637 phosphorylation inhibits its activation (Chang and Blackstone, 2007). Phosphorylation of Ser616 is promoted by Cyclin-dependent kinase (CDK), Cyclin B or CDK5, while in contrast protein kinase A (PKA) causes phosphorylation of Ser637 respectively. Activated by cytosolic Ca^{2+} and calmodulin binding, the phosphatase calcineurin (CaN) dephosphorylates the DRP1 Ser637 (Cereghetti et al., 2008). Nitrosative stress may also influence mitochondrial respiration, biogenesis and dynamics (Clementi et al., 1998; Nisoli et al., 2003). Specifically, Cho et al. proposed that S-nitrosylation of C644 of DRP1 induces mitochondrial fission (Cho et al., 2009b). Indispensable for its mitochondrial binding are further OMM proteins including the fission 1 protein (Fis1), MiD49/51 and the mitochondrial fission factor (MFF) (Otera et al., 2010; Yoon et al., 2003). Depending on the stimuli inducing mitochondrial fission by DRP1/MFF, MFF phosphorylation of Ser155 and Ser172 is required (Lewis et al., 2018; Toyama et al., 2016).

3.1.6. Mitofusins

Mitofusin 1 and Mitofusin 2 are mitochondrial proteins residing at the outer mitochondrial membrane mediating mitochondrial fusion by forming homo- or heterotypic dimers. They are proteins consisting of 741 and 757 amino acids (aa) respectively and share similarities in function and in 82 % of structure (Chen et al., 2003). Both proteins consist of an N-terminal GTP-domain followed by a coiled-coil heptad-repeat domain (HR1) and two transmembrane domains (TMD) separated by one amino acid. Between the TMD and the HR1 domains only MFN2 harbors one proline-rich domain, which is most probably involved in protein-protein interactions (Schrepfer, Scorrano, 2016). The C-terminus consists of a second HR2 domain. The cytosolic location of the C-terminal domain of the mitofusins has recently been challenged – presumably, the C-terminus resides in the intermembrane space (IMS) of mitochondria (Mattie et al., 2018). With these findings, the assumption of the fusion process involving the

dimerization of the HR2 domains of two MFNs *in trans* to induce the tethering of mitochondria was questioned again (Koshiba et al., 2004).

Several studies show that there is a link between redox homeostasis and mitochondrial morphology and function. The process of mitochondrial hyperfusion represents a cellular mechanism to cope with oxidative stress, protecting the mitochondria and the cell from mitophagy and autophagy, respectively (Shutt et al, 2012). The work from Shutt et al. shows a GSSG-induced oligomerization of MFN2 with subsequent mitochondrial hyperfusion mediated by its cysteine 684 (C684). Along these lines, the observations that were made on mitochondrial hyperfusion induced by the oxidative stress indicator GSSG have now been expanded. Not only mutation of the C684 of MFN2, but also truncation of the C-terminus with its HR2 domain ablates the mitochondrial fusion activity in a redox-activated manner (Shutt et al., 2012; Mattie et al., 2018). The C684 is suggested to be the fusion-regulating and -inducing amino acid (Shutt et al., 2012). MFN2 has 14 cysteines, out of which two reside in the C-terminus which is presumed to be lying in the intermembrane space. C684 is one out of five conserved cysteines of MFN2, and affects redox-mediated mitochondrial respiration and fusion activity in response to H₂O₂, while the residual four cysteines are spread along the N-terminus of the protein (Thaher et al., 2017; Wolf et al., 2020). Hence, the induction of disulfide bindings via C-terminal cysteines occurs most probably in the IMS and is highly redox-driven.

The functional differences of the MFNs probably implicate the organelle tethering *in trans* between mitochondria or between mitochondria and the ER via MFN2, whereas MFN1 rather mediates the fusion process together with OPA1 at the inner membrane (Li et al., 2019; Pyakurel et al., 2015). While after GTP hydrolyzation MFN1 loosens the affinity to its counterpart but has a greater GTP turnover, MFN2 proteins remain as dimers – this strong binding makes MFN2 more effective as a tethering molecule (Li et al., 2019). Besides its mitochondrial localization, MFN2 is also found at the ER and especially enriched at MAMs (de Brito and Scorrano, 2009). These intracellular signaling hubs are important for the organellar exchange of various molecules and biolipids, but especially specialized for ATP and Ca²⁺ supply, hence making them a central regulator of mitochondrial metabolism and autophagy (de Brito and Scorrano, 2009). Though it is still under debate which role MFN2 plays in the regulation of MAMs, it has long been proposed that MFN2 is a crucial protein for the tethering of these two organelles by forming homo- or heterotypic dimers (de Brito and Scorrano, 2009). However, in the past years, this model was challenged by studies showing that MFN2 depletion rather leads to an increase than decrease of these contact sites (Cosson et al., 2012; Filadi et al., 2015). The increased proximity led to elevated Ca²⁺ transfer to the mitochondria, leading to an excess in Ca²⁺ levels and hence, to increased cell death. Consequently, MFN2-derived tethering in MERCS supposedly occupies a protective role, keeping the organelles in non-toxic

proximity (Filadi et al., 2015). MFN2 was also observed to be phosphorylated by PINK1, which subsequently makes it a target of the E3 ubiquitin ligase parkin to translocate to the mitochondria to initiate mitophagy, a process of mitochondrial degradation (Chen and Dorn, 2013). MFN1 on the other side is also closely related to apoptotic processes. The extracellular-signal-regulated kinase (ERK) phosphorylates MFN1 in its HR1 region, which induces mitochondrial fragmentation and oligomerization of the proapoptotic protein BCL-2-antagonist/killer (BAK), making the cell more susceptible to apoptotic stimuli (Brooks et al., 2007). To date, several mutations in the MFN2 sequence have been detected that lead to the Charcot-Marie-Tooth disease type 2A (CMT2A) and exhibit abnormalities in the mitochondrial shape, transport and distribution along the axons in both fibroblasts from CMT2A patients and MFN-R94Q expressing transgenic mice (Amiott et al., 2008; Guillet et al., 2011; Verhoeven et al., 2006).

3.2. Charcot-Marie Tooth disease and the role of GDAP1 and MFN2

3.2.1. Charcot-Marie Tooth Disease

Due to the central role of mitochondria in energy production and stress-responses, it is crucial that all the regulatory processes that control mitochondrial well-being and functions are finely tuned. It is therefore not surprising that mutations of various mitochondrial proteins are known to date that can easily cause mitochondria-associated diseases. Concomitantly, defects in the mitochondrial dynamic machinery, oxidative or nitrosative stress has been described in various neurological diseases, including Alzheimer's or Huntington's disease (reviewed in Liu et al., 2017; Mangialasche et al., 2009). OPA1 mutation is related to autosomal dominant optic atrophy (ADOA) (Eiberg et al., 1994; Owens et al., 2007). Mutations in the *MFN2* gene or in the gene encoding the ganglioside-induced differentiation-associated protein 1 (*GDAP1*) can cause the peripheral neuropathy Charcot-Marie-Tooth disease (CMT).

CMT is the most common inherited peripheral neuropathy with a prevalence of 1 in 2500 people (Skre, 1974). The disease was initially described in 1886 by Jean-Martin Charcot, and Pierre Marie and Henry Tooth as "peroneal muscular atrophy" (Kazamel and Boes, 2015). To date, more than 80 genes are known that can lead to this disease once mutated, out of which many encode mitochondrial proteins (Cassereau et al., 2020). The molecular functions of affected proteins range from vesicular transport, composition of the myelin sheath, protein folding or degradation processes (Niemann et al., 2006). The disease affects peripheral motor and sensory neurons, but can also lead to abnormalities in the cerebral white matter (Lee et al., 2017; Ouvrier et al., 1981). Clinically, CMT can be classified into different types, regarding

the mode of inheritance, electrophysiological characteristics and the age of disease onset (Timmerman et al., 2013). Consequently, a distinction between axonal or demyelinating forms and autosomal recessive or dominantly inherited protein mutations can be made. Demyelinating disease types (CMT1 and CMT4) are characterized by a slower nerve conduction velocity due to an impairment of the myelin sheaths along the axons, while the axonal disease types (CMT2) rather result in affected muscle action potentials with largely unaffected nerve conduction velocity (Arnold et al., 2015; Banchs et al., 2009). Progressive muscle weakness in feet and lower leg muscles can occur as first symptoms, leading to characteristic foot deformations (*pes cavus*) (Arnold et al., 2015).

Besides the axonal and demyelinating disease groups, a third classification has been defined, termed as the intermediate type of CMT disease, where the patients show overlapping symptoms. Only a few mutations are known yet, but examples are mutations in the dynamin 2, gap junction protein 1 and pyruvate dehydrogenase kinase (Nicholson and Myers, 2006; Perez-Siles et al., 2016).

Among all disease types, CMT1A is the most common one, and CMT2A is the most frequent axonal form with an onset in early childhood and slowly progressing muscle weakness, distal muscle atrophy and length-dependent sensory loss (Amiott et al., 2008; Feely et al., 2011; Züchner et al., 2004). Roughly 20 % of the cases are caused by a mutation in the mitochondrial protein MFN2. Among these, most of the mutations affect the GTPase domain of MFN2 (Feely et al., 2011).

To date, up to 40 mutations in the GDAP1 protein are registered, leading to either autosomal dominant or recessive CMT2 or CMT4A, of which CMT4A is the most frequent one (Martin et al., 2015). The incidence of dominant inheritance of GDAP1 mutations is less frequent with a less severe disease progression and a later onset of disease symptoms in contrast to recessively inherited mutations with an early disease onset and more severe progression of muscle weakness, vocal cord and diaphragmatic paresis (Cassereau et al., 2011a). Among the known disease-related GDAP1 mutations, those patients suffering from truncated GDAP1 protein expression were wheelchair-bound latest at the age of 40 (Cassereau et al., 2011a).

3.2.1. GDAP1

3.2.1.1. GDAP1 structure and its effect on mitochondrial dynamics and function

GDAP1 is a tail-anchored protein at the outer mitochondrial and peroxisomal membrane and is mainly expressed in CNS neurons, DRG motor- and sensory neurons, but not in glial and Schwann cells (Cuesta et al., 2002; Niemann et al., 2005; Pedrola et al., 2008; Wagner et al., 2009). It was initially detected as one of 10 cDNAs (GDAP 1-10) being upregulated during

neuronal differentiation upon ganglioside-induced cholinergic differentiation of the murine neuroblastoma cell line Neuro2A (Liu et al., 1999; Niemann et al., 2005). Its gene is located on chromosome 8 and encodes a protein of a size of 358 aa and 39 kDa. Due to observations regarding the mitochondrial morphology corresponding to GDAP1 expression levels, GDAP1 is regarded as a fission-related protein (Niemann et al., 2005). However, the exact mechanism of GDAP1-induced fragmentation still needs to be clarified. GDAP1 harbors one C-terminal mitochondria-targeted tail-anchor transmembrane domain (TMD), a C-terminal hydrophobic domain (HD) and a C- and N-terminal domain, respectively, that are facing the cytosol and share similarities to theta, zeta or omega class glutathione-transferases (GSTs) (Figure 5) (Huber et al., 2016; Marco et al., 2004; Shield et al., 2006). Two additional alpha helices are located between the N- and C-terminal GST (GST-N, GST-C) domains ranging from amino acids 152 to 195, termed the α 4- α 5 loop (Cassereau et al., 2011a; Marco et al., 2004). The GDAP1 sequence has four cysteines that are conserved among vertebrates, three of which are located in the GST domain – two in the N-terminal and one in the C-terminal GST (Wolf et al., 2020). Genomic screening of 39 autosomal dominant CMT2 (ADCMT2) patients identified 27 % patients carrying a mutation in the GDAP1 gene (Crimella et al., 2010). Crimella et al. reported until such time unknown dominant mutations in GDAP1 in the GST region of the protein which presumably have an impact on the protein structure and function (Crimella et al., 2010). In particular, the described mutation R226S, located in the α 5 helix of the GST and the S34C mutation, which is the highly conserved GST core region, leads to early onset of disease symptoms in patients (Crimella et al., 2010).

Mitochondrial targeting of the TMD has been observed to be reliant on positively charged

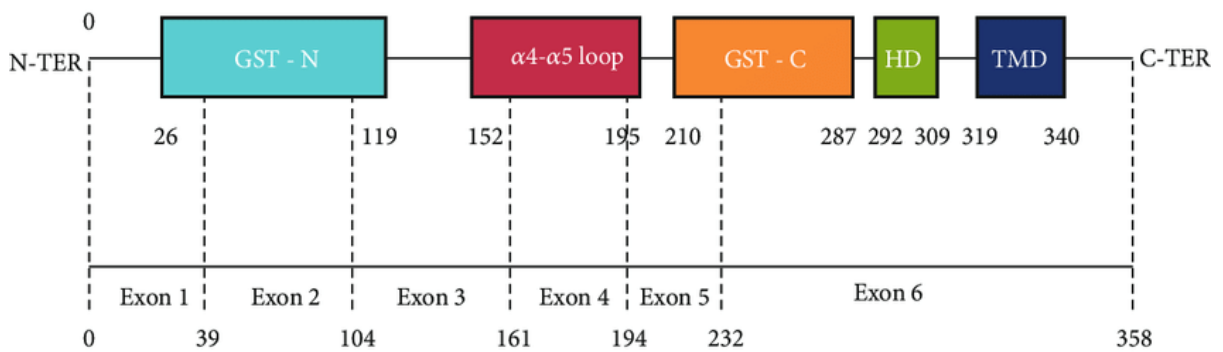


Figure 5 Schematic illustration of GDAP1 protein structure and its functional domains

The GDAP1 protein consists of an N-terminal and a C-terminal GST domain (GST-N and GST-C), framing the α 4- α 5 loop. The HD domain is also located in the cytosol, followed by the C-terminal TMD. Exon and amino acid localizations are indicated. GST – glutathione transferase; HD – hydrophobic domain; TMD – transmembrane domain (adapted from Mai et al., 2019)

amino acids adjacent to the TMD sequence and the TMD alone does not induce mitochondrial fission (Pedrola et al., 2008; Wagner et al., 2009). While the HD domain does not affect the TMD targeting, it does impair mitochondrial fission activity and even both mitochondrial and

Introduction

peroxisomal fission activity are under the control of GDAP1 expression, but highly dependent on the HD domain (Huber et al., 2013, 2016; Niemann et al., 2009). Hence, impaired mitochondrial fragmentation and increased tubular morphologies of mitochondria and peroxisomes are described by silencing of GDAP1 or expression of a truncated GDAP1 protein lacking the HD domain (Googins et al., 2020; Huber et al., 2013, 2016; Niemann et al., 2009). The expression of GDAP1 with either deletion or scrambling of this domain in COS7 cells diminishes the mitochondrial fission function and mutation of the amino acid R310 flanking the HD domain also leads to elongated mitochondria and is a CMT-related mutation (Azzedine et al., 2003; Wagner et al., 2009).

Presumably, the C-terminal HD domain of GDAP1 resides in the cytosol (Huber et al., 2016). As already observed in previous studies, dominantly and recessively inherited mutations of GDAP1 (dmGDAP1 and rmGDAP1) reveal opposite effects on the mitochondrial shape – while recessive disease mutations lead to reduced fission activity and elongated mitochondria, dominant disease mutations in GDAP1 lead to a pronounced fission activity (Niemann et al., 2005, 2009). Besides an impaired fusion activity, cells expressing dmGDAP1 also have a reduced mitochondrial membrane potential (Niemann et al., 2009). Interestingly, Niemann et al. observed that the induction of GDAP1 expression on mitochondrial fission can be counteracted by MFN2 expression and ruled out a fusion-inhibiting function of GDAP1 (Niemann et al., 2005). Cells co-expressing dmGDAP1 with MFN2, in contrast contained fragmented mitochondria and were not able to fuse (Niemann et al., 2009). Hence, the observed phenotypes also largely depend on the mode of inheritance of GDAP1 mutations in CMT patients.

Importantly, GDAP1 is not able to induce mitochondrial fission when it is overexpressed together with a dominant-negative DRP1 (K38A) (Niemann et al., 2009). There is no GDAP1-mediated fragmentation of both mitochondria and peroxisomes after GDAP1 overexpression in DRP1 or MFF depleted cells, suggesting that fission activity of GDAP1 is dependent on MFF and DRP1 in both cell organelles, as peroxisomal fragmentation is controlled by DRP1 and MFF as well (Camões et al., 2009; Gandre-Babbe and Van Der Blik, 2008; Huber et al., 2013; Otera et al., 2010).

A comparison of dmGDAP1 or rmGDAP1 for their impact on ROS levels or susceptibility for apoptosis upon actinomycin D and staurosporine was determined via cytochrome *c* release. The treatment leads to an increase of both when cells were expressing dmGDAP1 R120W and T157P rather than the recessive disease mutations R120Q and R310Q, compared to GDAP1 wildtype (WT) and vector controls (Niemann et al., 2009). In contrast to either Fis1 or DRP1 knockdown (KD), GDAP1 KD does not alter the susceptibility of the cells to apoptosis (Niemann et al., 2009).

Introduction

Estela et al. connected both Fis1 and GDAP1 to an impairment of mitochondrial transport and microtubule interaction in yeast models. Loss of Fis1 expression leads to an impairment of spindle formation and a delay in the cell cycle at G2/M phase (Estela et al., 2011). Though, the authors did not observe a fission-inducing activity of GDAP1 expression in WT and Fis1 Δ yeast, Estela et al. observed a rescuing effect of GDAP1 for the defective spindle formation and the cell cycle delay. Neither dominant or recessive missense GDAP1 mutations, nor truncated GDAP1 protein lacking the HD and TMD could rescue these effects. As a possible mechanistic link between these two proteins, they identified an interaction of GDAP1 and Fis1 with β -tubulins (TUBB). Disease mutations located in the α 4- α 5 loop of GDAP1 even revealed an enhanced interaction and hence, a presumable gain-of function. These findings are highlighting the importance of an effective interaction between microtubules and mitochondria – both, in respect to mitotic spindle formation, as well as for mitochondrial transport along neurons' axons. And possibly, GDAP1 holds a vital role in these processes.

CMT2K patients with the heterozygous missense dominant C240Y mutation in GDAP1, a conserved cysteine located in the C-terminal GST domain, were studied in detail for their mitochondrial respiratory capacity (Cassereau et al., 2009). Fibroblasts from these patients reveal a 50% reduction in CI activity with a concomitant diminished CI-driven ATP synthesis (Cassereau et al., 2009). These fibroblasts also have an enhanced citrate synthase activity and an increased mitochondrial mass. The mitochondrial shape is also affected, tending towards increased fission compared to fibroblasts from non-carrier relatives (Cassereau et al., 2009).

Given the fact that mutations in both mitochondrial fusion and fission proteins MFN2 and GDAP1 can lead to CMT, it is even more valuable to note that a combination of both mutated proteins can lead to a more severe disease progression. Several patients have been identified so far who harbor mutations in both, the *GDAP1* and *MFN2* gene (Angheliescu et al., 2017; Cassereau et al., 2011b; Kostera-Pruszczyk et al., 2014). Recently, a patient with an early disease onset at 5 years of age was diagnosed with CMT with severe disease presentations. Sequencing of these genes unveiled an inherited dominant mutation in the GST-C domain (E222K), which had been described previously in two families, and a de-novo missense mutation in the MFN2 gene (P201L) (Angheliescu et al., 2017; Kabzińska et al., 2014). The GDAP1 mutation alone, which affected his father and grandmother, presented only a mild disease progression. Molecular investigations were performed by Cassereau et al., who studied a patient's fibroblasts with a homozygous mutation in GDAP1 (Q163X) paired with heterozygous MFN2 mutation (R468H). The results exhibited both a complex I inactivity and defective mitochondrial uncoupling, which had separately been shown previously for GDAP1 and MFN2 mutations, respectively (Cassereau et al., 2011b). Cells expressing MFN2 mutation

alone only present the defect in mitochondrial uncoupling, while a second control only expressing a dominant GDAP1 mutation illustrates a CI defect. The combination of GDAP1 and MFN2 mutations lead to a significant decline in ATP production, most probably because the CI cannot compensate for the mitochondrial uncoupling in these patients and the mitochondrial OXPHOS is less efficient (Cassereau et al., 2011b). Hence, the severity of CMT is not only determined by the location of the mutation but also by the combination of several mutations.

The ubiquitously expressed zinc finger transcription factor ying yang 1 (YY1) regulates neural development as well as nuclear gene transcription of several mitochondrial proteins such as the cytochrome *c* oxidase and presumably, it is also involved in the regulation of GDAP1 protein transcription (He and Casaccia-Bonofil, 2008; Lescuyer et al., 2002; Ratajewski and Pulaski, 2009). As such, Ratajewski et al. identified a YY1 binding site in the highly conserved human GDAP1 promotor region by chromatin immunoprecipitation (ChIP) (Ratajewski and Pulaski, 2009). In line with this, there is a YY1-induced GDAP1 promotor activation (Ratajewski and Pulaski, 2009). Elevation of YY1 also leads to an increase in GDAP1 mRNA levels and equally, YY1 silencing reduced GDAP1 mRNA copies, though it is not yet clear if it has the same effect at protein levels (Ratajewski and Pulaski, 2009).

3.2.1.2. The sequence similarity of GDAP1 to GSTs and its effect on GSH levels and ROS

GDAP1 belongs to a novel subfamily of GSTs due to the sequence similarities of its two GST domains, according to structural and phylogenetic analyses (Cuesta et al., 2002; Marco et al., 2004). Still, its structure is different enough to be distinct from known classes – particularly due to its TMD, since all known and identified GSTs are soluble and not membrane-bound, except MAPEGs (Cuesta et al., 2002; Marco et al., 2004). Other major structural differences are the additional two α helices in the α 4- α 5 loop, which are not present in most of the GSTs (Marco et al., 2004; Pedrola et al., 2005; Shield et al., 2006). Cuesta et al. identified the GSH binding site of the N-terminal thioredoxin-like domain of typical GSTs, as well as an α -helical structure in the GST-C domain that may play a role in xenobiotic structure recognition (Cuesta et al., 2002).

Huber et al. confirmed for the first time that the N-terminal GST domain does have a theta-class-like GST activity and is efficient in GSH conjugation (Huber et al., 2016). Dimerization of the protein, which is a hallmark of canonical GSTs upon oxidation, is verified for GDAP1 WT, and also for rmGDAP1, such as R120Q and R310Q as well as for dmGDAP1 proteins – including R120W and Q218E mutations (Huber et al., 2016; Shield et al., 2006). GDAP1

lacking the TMD or HD domains can also efficiently form homodimers (Huber et al., 2016). As the affinity of known theta-class GSTs is high for GST substrates ethacrynic acid, *p*-nitrobenzylchloride and 1,2-epoxy-3-(4-nitrophenoxy)propane but low for GSH-agarose which also accounts for GDAP1, the GST function of GDAP1 could be comparable to theta-class GSTs (Huber et al., 2016; Sheehan et al., 2001). Importantly, the authors observed that the HD domain of GDAP1 is crucial for the GST function of GDAP1 and proposed a model showing that the HD domain possesses an amphipathic pattern where it is able to regulate the GST activity of the protein, eventually affecting the mitochondrial shape (Figure 6) (Huber et al., 2016). In its inactive state, the HD domain blocks the GST while once active, it can induce mitochondrial membrane curvature leading to fission. This model would also contribute to dominant and recessive GDAP1 CMT-causing disease mutations and completes previous observations of altered mitochondrial shape dependent on the mode of inheritance of the GDAP1 CMT disease mutation. Hence, dmGDAP1 would rather lead to a hyperactive GST function and fragmented mitochondria, whereas rmGDAP1 in contrast shifts the protein into an inactive GST and hyperfused mitochondrial network (Huber et al., 2016).

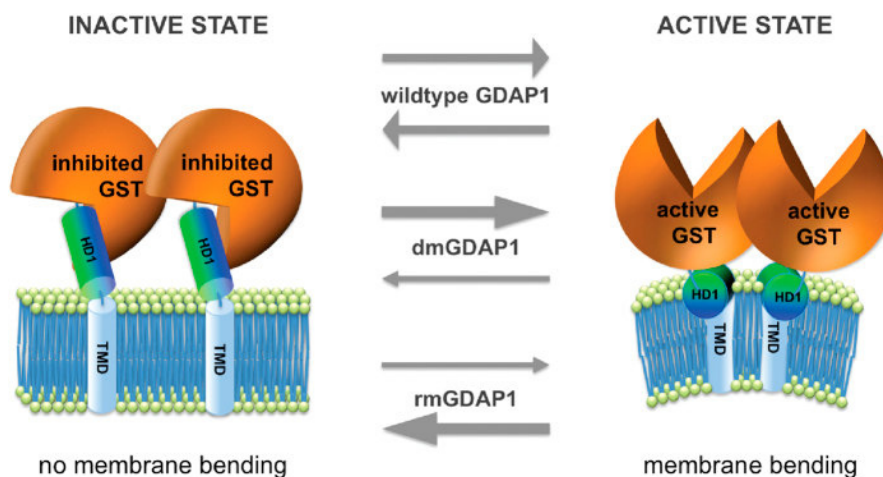


Figure 6 The amphipathic pattern of the HD domain in the GDAP1 protein

Schematic illustration of the GDAP1 protein targeted to the outer mitochondrial membrane (OMM) explains the molecular function of the HD domain to regulate the protein activity as a glutathione transferase (GST). GDAP1 WT shifts between the active and inactive conformation upon specific stimuli, while CMT-disease mutants are presumably arrested in the active or inactive conformation. Hence, dominant inherited mutations (dmGDAP1) lead to an overreactive GST function, leading to an increased mitochondrial fission activity, while the HD domain in recessive mutations (rmGDAP1) rather inhibits the GST function and the mitochondria are in a hyperfused state (adapted from Huber et al., 2016).

Googins et al. recently challenged the conclusions of an active GST-function with stability assays via scanning fluorimetry under different temperatures (Googins et al., 2020). They noted that the HD domain not only bears an autoinhibitory and -activating function, but also highly contributes to the stability of the protein since GDAP1 proteins lacking the HD domain exhibit a significantly decreased temperature-dependent stability (Googins et al., 2020).

Differential scanning fluorimetry was also performed in the presence of GSH to examine the GSH-binding ability of GDAP1. However, in contrast to a GST Mu subtype, GDAP1 was not able to bind GSH (Googins et al., 2020). Importantly, GDAP1 has a confirmed substrate binding affinity of the $\alpha 4$ - $\alpha 5$ loop subjected to the GST substrate EA. By crystallizing GDAP1 and comparing its structure to Mu GST, the authors mentioned several structural differences in the protein folding, leading to an altered folding of the presumed GSH-binding G-site of GDAP1 (Googins et al., 2020). Additionally, given the close localization of the HD and the $\alpha 4$ - $\alpha 5$ loop, it may indicate an interaction of the domains, which affects the protein stability, substrate binding or OMM targeting (Googins et al., 2020).

Furthermore, Noack et al. observed an increase of GSH levels in response to overexpression of GDAP1 but not of GDAP1 bearing the recessive disease mutation R310Q (Noack et al., 2012). GDAP1 even protects from oxidative glutamate toxicity in HT22 cells, which is also attenuated in the mutants (Noack et al., 2012). Along with this, Noack et al. observed reduced glutathione as well as reduced membrane potential in fibroblasts from autosomal recessive CMT4A patients indicating that GDAP1 expression affects the oxidative potential intracellularly by regulating GSH levels also in patient-derived cells (Noack et al., 2012). However, no difference was observed in mitochondrial shape (Noack et al., 2012). Very recently, it has been shown that CMT2K patient fibroblasts reveal a defect in complex I activity. Concomitant higher ROS levels and decreased protein thiols were shown in a patient with a disease mutation in the C-terminal GST domain (C240Y) (Cassereau et al., 2009, 2020). Altogether, this provides evidence that altered GDAP1 expression or disease-causing mutations - especially in its GST-domains - have a severe impact on oxidative stress and thus on mitochondrial morphology, biogenesis and energy supply. The fact that described phenotypes as well as clinical observations are more prominent in CMT patients suffering from mutations in one of the GST domains points towards its importance in antioxidant effects and its probable effect as GST on other mitochondrial or cytoplasmic proteins (Cassereau et al., 2011a; Crimella et al., 2010; Huber et al., 2016).

3.2.1.3. Effect of GDAP1 on the cellular calcium homeostasis

GDAP1 is located at MAMs interacting with the vesicle trafficking regulating protein RAB6B and caytaxin via its $\alpha 4$ - $\alpha 5$ loop, which plays a role in the “anterograde movement of the mitochondria” (Pla-Martín et al., 2013). GDAP1-silencing in SH-SY5Y cells reduces the transport of mitochondria, diminishes the ability of mitochondria to distribute throughout the cell upon Ca^{2+} demand, and leads to an impairment of Ca^{2+} homeostasis (Pla-Martín et al., 2013). Pla-Martín et al. observed a reduced SOCE activity after GDAP1 depletion, which also

involves the Ca^{2+} influx dynamics of mitochondria (Pla-Martín et al., 2013). Reduced GDAP1 expression also results in fewer MERCS in SH-SY5Y cell lines. In contrast, overexpression of GDAP1 in HeLa cells leads to increased contacts of the organelles, and this effect fails to appear with transfection of recessive GDAP1 mutations (Pla-Martín et al., 2013). Steady-state $\text{cyt}[\text{Ca}^{2+}]$ levels are increased in GDAP1-silenced cells, while alterations in ER or mitochondrial Ca^{2+} levels or dynamics were ruled out. On the contrary, SOCE-driven mitochondrial Ca^{2+} uptake is largely affected in these cells (Pla-Martín et al., 2013). An ensuing study of González-Sánchez et al. proposes that silencing of GDAP1 in SH-SY5Y cell lines leads to an abolished SOCE-driven mitochondrial respiratory activity (González-Sánchez et al., 2017). Comparing the mitochondrial distribution upon SOCE activation in cells with recessive and dominant CMT disease-associated GDAP1 mutations, they observed an impaired mitochondrial subplasmalemmal migration only in cells expressing recessive mutations located in the $\alpha 4$ - $\alpha 5$ loop of GDAP1 (González-Sánchez et al., 2017). In contrast to this, the expression of dominant GDAP1 disease mutations rather leads to a hyperactive SOCE and hence, increased SOCE amplitudes upon activation (González-Sánchez et al., 2017).

Junctophilin-1 (JPH1) may be a protein of interest in this relation. Junctophilins are crucial for the formation of so-called junctional membrane structures between the ER in excitable cells or SR in muscle cells and the plasma membrane to sustain the interaction of the plasma membrane with intracellular ion channels (Pla-Martín et al., 2015; Takeshima et al., 2000). JPH1 is an ER-resident protein and also found in MAMs but in particular provides the activity of the SOCE-driven Ca^{2+} uptake by mediating the interaction of STIM1 and Orai1 (Landstrom et al., 2014; Li et al., 2010). Pla-Martín et al. observed a GDAP1-dependent colocalization with STIM1 upon Ca^{2+} release from the ER (Pla-Martín et al., 2015). A CMT2K patient was also identified with a mutation (R213P) in JPH1 in addition to a R120W mutation in the *GDAP1* gene (Pla-Martín et al., 2015). Interestingly, this patient also presented a more severe clinical outcome; furthermore, defects in the SOCE activity in GDAP1-silenced cell models were rescued by overexpression of WT, but not the patient-related JPH1 mutant (Pla-Martín et al., 2015).

3.2.1.1. Animal models with depletion or overexpression of GDAP1

Several animal models have been generated so far for examining the role of GDAP1 in CMT disease. Studies with *Drosophila melanogaster* with a KD of the fly *GDAP1* orthologue or GDAP1 overexpression (OE) show a retinal neurodegeneration and decline of synapses, as well as muscle degeneration (Del Amo et al., 2015). Furthermore, impairments in mitochondrial distribution and morphology emerged. Importantly, the observed phenotype in KD flies can be

rescued by overexpression of the human GDAP1 protein, emphasizing its phylogenetically conserved function (Del Amo et al., 2015). Both overexpression (OE) and knockdown (KD) of GDAP1 lead to an increase in GSH levels and higher GSH to GSSG ratios in fly thoraces (Del Amo et al., 2015). Accordingly, ROS levels decrease in the GDAP1 OE model, together with less glutathionylation and nitrosylation PTMs but increase significantly in KD flies (Del Amo et al., 2015). An ensuing study of these flies concentrates on the metabolic phenotype and surprisingly, OE and KD of GDAP1 in flies lead to an equal metabolic pattern. Both fly models show an early defect in insulin signaling, most likely leading to an accumulation of carbohydrates together with increased levels of pyruvate, PDK and mitochondrial ATP levels (López del Amo et al., 2017).

Niemann et al. generated a mouse model that expresses a truncated GDAP1 protein caused by a deletion in exon 5 and hence lacking its TMD (Niemann et al., 2014). Phenotypically, the mice develop a mild hypomyelinating peripheral neuropathy and expose a disturbed GSH to GSSG ratio towards increased GSSG levels. Interestingly, the researchers observed that the cytosolic paralogue GDAP1L1 migrates to the mitochondria in response to increased GSSG levels, which is apparently occurring in a compensatory manner to the dysfunctional GDAP1 protein and explains the mild disease phenotype in these mice (Niemann et al., 2014). GDAP1L1 shares around 70 % of sequence similarity with GDAP1, including the GST domains (Shield et al., 2006).

A second GDAP1 mouse model was generated and described by Barneo-Muñoz et al. (Barneo-Muñoz et al., 2015). GDAP1 knockout (KO) was achieved by the deletion of exon 1; first motor deficits can be observed in mice at the age of three months (Barneo-Muñoz et al., 2015). The GDAP1 KO mice have reduced motor nerve conduction velocities and compound muscle action potentials at 5 months of age but no impairment of axon myelination. These findings, together with a significant loss of motoneurons (MN) at 5 months of age, very much resemble the clinical features of the autosomal recessive CMT2K disease type (Barneo-Muñoz et al., 2015). Mitochondria from embryonic MN analyzed by transmission electron microscopy reveal an increased aspect ratio paired with reduced circularity in GDAP1 KO neurons, indicating increased mitochondrial fusion activity in these cells compared to WT mice (Barneo-Muñoz et al., 2015). Evaluation of Ca^{2+} dynamics in embryonic MN from WT and GDAP1 KO mice also reveal a strong defect in SOCE in the KO mice (Barneo-Muñoz et al., 2015). In an ensuing study with these mice, the authors observed increased neuroinflammation in the spinal cord and sciatic nerve but not in the brain or cerebellum (Fernandez-Lizarbe et al., 2019). The authors also found an overactivity of the innate immune system, which could largely contribute to the observed loss of synapses and hence highlights the importance of the immune system in the pathophysiology of CMT patients (Fernandez-Lizarbe et al., 2019). Quantification of

ROS in primary cultures of MN indicate increased ROS and superoxide levels (Fernandez-Lizarbe et al., 2019).

Eijkenboom et al. found that GDAP1 KD in zebrafish leads to a morphological defect in the development of embryos and to a loss of sensory neurons in tail sections, which results in a loss of temperature sensitivity (Eijkenboom et al., 2019). Evaluation of mitochondria in these embryos in dermal cells did not reveal any morphological differences, but more detailed and tissue-specific analyses are pending (Eijkenboom et al., 2019).

3.3. Aim of this work

Mitochondrial energy production is an indispensable process and tightly regulated, while the mitochondrial protein GDAP1 is known to influence numerous mitochondrial processes, amongst others the mitochondrial dynamics – especially in Charcot-Marie-Tooth disease-associated mutations. I sought to determine in different *in vitro* models how besides the mitochondrial shape, the mitochondrial ER-contact sites are affected, including the Ca^{2+} signaling between the organelles, since SOCE-impairments have been studied so far. I further analyzed the consequences of reduced expression or CMT-disease related mutations of GDAP1 on mitochondrial ATP generation and metabolic patterns.

Especially of interest was to identify a possible interaction partner and to clarify how GDAP1 as a presumable GST can alter mitochondrial dynamics.

Several cell culture models were included in this work, including stable SH-SY5Y cell lines with a silenced GDAP1 expression and its non-targeted control, which have been described in Pla-Martín et al., 2013. Furthermore, this work is based on experiments with cell lines overexpressing an empty vector, GDAP1 WT, the R310Q disease-related point mutation, and S34A, a loss of function mutation of the active center serine in the N-terminal GST domain.

Moreover, neuronal progenitor cells and motoneurons from patient-derived fibroblasts were studied for their mitochondrial shape and metabolic phenotype. Patient #1 has two heterozygous point-mutations L239F and R273G in the C-terminal GST domain, while patient #2 possesses a homozygous mutation in the donor site of the intron 4, which leads to exon 4 skipping and eventually to a truncated protein lacking the C-terminal GST and transmembrane domain of GDAP1 (Noack et al., 2012).

4. Materials

4.1. Chemicals

Table 1 Chemicals

Chemical	Supplier
1.4-Dithiothreitol (DTT)	Carl Roth, Karlsruhe, Germany
10.000 Units/ml Penicillin 10 mg/ml Streptomycin	Sigma-Aldrich, Steinheim, Germany
10x Tris/glycine/SDS Running Buffer	Bio-Rad Laboratories GmbH, München, Germany
2-Deoxy-D-glucose	Sigma-Aldrich, Steinheim, Germany
2-Mercaptoethanol, 50 mM	Life Technologies, Carlsbad, USA
4 % Roti®-Histofix	Carl Roth, Karlsruhe, Germany
5,5'-dithiobis-(2-nitro-benzoic acid) (DTNB)	Sigma-Aldrich, Steinheim, Germany
Adenosine-5'-triphosphate (ATP)	Sigma-Aldrich, Steinheim, Germany
Agarose Basic	AppliChem GmbH, Darmstadt, Germany
Ascorbic Acid	Sigma-Aldrich, Steinheim, Germany
Bromocresol green	Carl Roth, Karlsruhe, Germany
Bromophenol blue	Sigma-Aldrich, Steinheim, Germany
Carbachol	Sigma-Aldrich, Steinheim, Germany
Chameleon® Duo Pre-stained Protein Ladder	Li-Cor Biosciences, Lincoln, USA
Coelenterazine-N-AM	Santa Cruz Biotechnology, Dallas, USA
Complete Mini Protease Inhibitor Cocktail	Roche, Basel, Switzerland
Dako Fluorescence Mounting Medium	Dako, Glostrup, Denmark
dbcAMP	Sigma-Aldrich, Steinheim, Germany
Digitonin, 5%	Invitrogen, Carlsbad, USA
Dimethyl sulfoxide (DMSO)	Sigma-Aldrich, Steinheim, Germany
Dorsmorphin 99021	Axon Medchem
Dulbeccos Phosphate buffered Saline	Sigma-Aldrich, Steinheim, Germany
EDTA	Sigma-Aldrich, Steinheim, Germany
EGTA	Sigma-Aldrich, Steinheim, Germany
Ethacrynic acid (EA)	Santa Cruz Biotechnology, Heidelberg, Germany
Ethanol Rotipuran 99,8%	Carl Roth, Karlsruhe, Germany

Materials

FK-506 calcineurin inhibitor	Invivogen, San Diego, USA
GenJet™ In Vitro DNA Transfection Reagent	Signagen® Laboratories, Frederick, USA
Glutathion-Ethylester, Biotin-Amid (BioGEE)	Invitrogen, Carlsbad, USA
Glutathione Reductase from baker's yeast	Sigma-Aldrich, Steinheim, Germany
Glycerol	Sigma-Aldrich, Steinheim, Germany
GoTaq Polymerase G2 DNA	Promega, Madison, USA
Guanosine-triphosphate	Sigma-Aldrich, Steinheim, Germany
HEPES	Sigma-Adrich, Steinheim, Germany
Knockout DMEM	Invitrogen, Carlsbad, USA
L-Glutathione, oxidized (GSSG)	Sigma-Aldrich, Steinheim, Germany
L-Glutathione, reduced (GSH)	Sigma-Aldrich, Steinheim, Germany
Magnesium acetate (MgAc2)	Carl Roth, Karlsruhe, Germany
Mannitol	Sigma-Aldrich, Steinheim, Germany
Matrigel	BD Biosciences
MG Midori Green Advance	Biozym Scientific GmbH, Hessisch Oldendorf, Germany
MM(PEG)24 Methyl-PEG-Maleimide Reagent	Thermo Scientific, Waltham, USA
Monopotassium phosphate (K2PO4)	Carl Roth, Karlsruhe, Germany
N-(Biotinoyl)-N-(Iodoacetyl) Ethylenediamide (BIAM)	Invitrogen, Carlsbad, USA
N2 Supplement	Invitrogen, Carlsbad, USA
Native Page cathode buffer (20x)	Invitrogen, Carlsbad, USA
Native Page running buffer (20x)	Invitrogen, Carlsbad, USA
Native Page sample buffer (4x)	Invitrog Invitrogen, Carlsbad, USA en
Natriumchloride	Carl Roth, Karlsruhe, Germany
N-Ethylmaleimide	Sigma-Aldrich, Steinheim, Germany
NP-40	AppliChem GmbH, Darmstadt, Germany
Nuclease-free Water	Life Technologies
Oligomycine	Sigma-Aldrich, Steinheim, Germany
Percoll®	Sigma-Aldrich, Steinheim, Germany
Pierce RIPA-Buffer	Thermo Scientific, Waltham, USA
Ponceau S solution	Sigma-Aldrich, Steinheim, Germany
Potassium chloride	Carl Roth, Karlsruhe, Germany
Powdered Milk	Carl Roth, Karlsruhe, Germany

Materials

Rapamycine	Sigma-Aldrich, Steinheim, Germany
Retinoic Acid	Sigma-Aldrich, Steinheim, Germany
Roti®-ImmunoBlock (10x)	Carl Roth, Karlsruhe, Germany
S.O.C. Medium	Invitrogen, Carlsbad, USA
SB-431542	Ascent Scientific, Abcam, Cambridge, UK
Sodium Bisulfide	Sigma-Aldrich, Steinheim, Germany
sodium succinate	Sigma-Aldrich, Steinheim, Germany
STO-609 acetate	Tocris, Bristol, UK
Sucrose	Sigma-Aldrich, Steinheim, Germany
TCEP	Sigma-Aldrich, Steinheim, Germany
Tris	Carl Roth, Karlsruhe, Germany
TRIS (Tris(hydroxymethyl)-aminomethan)	Carl Roth, Karlsruhe, Germany
Triton X-100	Carl Roth, Karlsruhe, Germany
Trypan Blue stain, 0.4%	Invitrogen, Carlsbad, USA
TurboFectin 8.0	Origene, Rockville, USA
Zinc chloride	Sigma-Aldrich, Steinheim, Germany
β-Nicotinamide adenine dinucleotide 2'-phosphate reduced tetrasodium salt hydrate (NADPH)	Sigma-Aldrich, Steinheim, Germany

4.2. Consumables

Table 2 Consumables

Consumable	Supplier
10 cm Petridishes	Greiner Bio-One, Kremsmünster, Austria
24-well plate	Greiner Bio-One, Kremsmünster, Austria
500cm ² Square TC-treated Culture Dish	Corning, Corning, USA
6-well plate	Greiner Bio-One, Kremsmünster, Austria
96-well plate transparent	Greiner Bio-One, Kremsmünster, Austria
96-well plate white	Greiner Bio-One, Kremsmünster, Austria
Cell scraper	Sarstedt, Nümbrecht, Germany
CoolCell® cell freezing container	Biocision, San Rafael, USA
Cryotubes, 2 ml	Biochrom, Cambridge, UK
Falcons, 50 ml and 15 ml	Sarstedt, Nümbrecht, Germany
Glassware	Schott, Mainz, Germany
Mini-Protean TGX Stain-Free Precast Gels,	Bio-Rad, Hercules, USA

Materials

4-15 %	
Neubauer Counting chamber	HBG, Gießen, Germany
Screenstar microplate 96 well plate	Greiner Bio-One, Kremsmünster, Austria
SuperSep™ Phos-tag™ Precast Gels	Fujifilm Wako Chemicals, Minato, Japan
Trans-Blot Turbo Mini/Midi PVDF Transfer Pack	Bio-Rad, Hercules, USA
Tubes 0.2 ml, 0.5 ml, 1.5 ml, 2 ml, 5 ml	Starlab, Hamburg, Germany

4.3. Antibodies

Table 3 Antibodies

Antibody	Supplier	Host species	Dilution
Actin Clone C4	Merck Chemicals, Darmstadt, Germany	Mouse	IB: 1:4000
BNIP3 Clone D7U1T	Cell Signaling, Danvers, USA	Rabbit	IB: 1:1000
Calcineurin Clone G182-1847	BD Biosciences, San José, USA	Mouse	IB: 1:1000
Calnexin Clone C5C9	Cell Signaling, Danvers, USA	Rabbit	IB: 1:1000
Cofilin1 Clone D3F9	Cell Signaling, Danvers, USA	Rabbit	IB: 1:1000 ICC: 1:100
CoxI Clone 1D6E1A8	Abcam, Cambridge, UK	Mouse	IB: 1:1000
CoxIV Clone 3E11	Cell Signaling, Danvers, USA	Rabbit	IB: 1:1000
DRP1, Clone 4E11B11	Cell Signaling, Danvers, USA	Mouse	IB: 1:1000
G6PD Clone D5D2	Cell Signaling, Danvers, USA	Rabbit	IB: 1:1000
GAPDH Clone 14C10	Cell Signaling, Danvers, USA	Rabbit	IB: 1:2000
GDAP1, polyclonal	Prestige Antibodies® Merck, Darmstadt, Germany	Rabbit	IB: 1:750
Glutamate dehydrogenase (GDH) Clone D9F7P	Cell Signaling, Danvers, USA	Rabbit	IB: 1:1000
GRP75/Mortalin N52A/42	UC Davis/NIH NeuroMab Facility, Davis, USA	Mouse	ICC: 1:20
IRDye® 680RD Streptavidin	Li-Cor, Lincoln, USA		IB: 1:3000
LAMP1 Clone D2D11	Cell Signaling, Danvers, USA	Rabbit	IB: 1:1000
Map2	Synaptic Systems, Göttingen, Germany	Guinea pig	ICC: 1:1000

Materials

Map2 Clone HM-2	Prestige Antibodies® Merck, Darmstadt, Germany	Mouse	ICC: 1:100
MFF, polyclonal	Proteintech, Rosemont, USA	Rabbit	IB: 1:1000
Mitofusin 2 Clone 4H8	Abnova, Taipeh, Taiwan	Mouse	IB: 1:500
Phospho-Cofilin (S3) 77G2	Cell Signaling, Danvers, USA	Rabbit	1:1000
Phospho-pyruvate dehydrogenase α 1 (S293)	Cell Signaling, Danvers, USA	Rabbit	1:1000
Pyruvate dehydrogenase (PDH) E1, clone C54G1	Cell Signaling, Danvers, USA	Rabbit	1:1000
Pyruvate dehydrogenase (PDH), subunit E2/E3; clone 13G2AE2BH5	Abcam, Cambridge, UK	Mouse	IB: 1:1000
Sec62	Kind gift from [REDACTED] [REDACTED] [REDACTED]	Rabbit	IB: 1:1000
Smi32	Biologend, San Diego, USA	Mouse	ICC: 1:1000
β III tubulin	Synaptic Systems, Göttingen, Germany	Rabbit	ICC: 1:5000
β III Tubulin Clone TuJ-1	R&D Systems, MAB1195	Mouse	IB: 1:1000
Stim1/GOK, Clone 5A2	Abnova, Taipeh, Taiwan	Mouse	IB: 1:1000
TOM20 polyclonal	Prestige Antibodies® Merck, Darmstadt, Germany	Rabbit	IB: 1:1000
VDAC1 Clone 20B12AF2	Abcam, Cambridge, UK	Mouse	IB: 1:1000

4.1. Dyes for live cell imaging

Table 4 Dyes for live cell imaging

Dye	Supplier
BODIPY™ 558/568 C12	Invitrogen, Carlsbad, USA
Draq5	Abcam, Cambridge, UK
Hoechst	Sigma-Aldrich, Steinheim, Germany
MitoTracker™ Green FM	Invitrogen, Carlsbad, USA
Molecular Probes™ 2-NBDG	Invitrogen, Carlsbad, USA
Tetramethylrhodamine methyl ester	Sigma-Aldrich, Steinheim, Germany

4.2. Buffer Compositions

Table 5 Buffer Compositions

Buffer	Supplements
Aequorine basic saline solution	135 mM NaCl 5 mM KCl 0.4 mM KH ₂ PO ₄ 1 mM MgSO ₄ x 7 H ₂ O 20 mM HEPES 0.1 % (w/v) glucose 0.2 pH 7.4 adjustment at 37°C with NaOH 10 N
KPE Buffer	16 ml 0,1 M KH ₂ PO ₄ 84 ml 0,1 M K ₂ HPO ₄ 5 mM EDTA
MAM isolation buffer 1 (IB1 buffer)	225 mM Mannitol 75 mM Sucrose 0.1 mM EGTA 30 mM Tris-HCl pH 7.4
MAM isolation buffer 2 (IB2 buffer)	225 mM Mannitol 75 mM Sucrose 30 mM Tris-HCl pH 7.4
Mitochondria isolation buffer I	0.32 M Sucrose 10 mM Tris-HCl pH 7.4 10 µM EDTA
Mitochondria isolation buffer II	0.5 M Sucrose 10 mM Tris-HCl pH 7.4 10 µM EDTA
MRB buffer	250 mM Mannitol 5 mM HEPES 0.5 mM EGTA, pH 7.4
Native Page Anode buffer (1l)	950 ml MilliQ H ₂ O 50 ml Native Page running buffer (20x)
Native Page dark blue cathode buffer (500ml)	25 ml Native Page running buffer (20x) 25 ml Native Page cathode buffer (20x) 450 ml MilliQ H ₂ O
Native Page light blue cathode buffer (500 ml)	25 ml Native Page running buffer (20x) 2.5 ml Native Page cathode buffer (20x)

Materials

	472.5 ml MilliQ H ₂ O
NuPage transfer buffer (20x)	25 mM Bicine 25 mM Bis-Tris 1 mM EDTA
PEG assay buffer	80 mM Tris pH 7.4 10 % (v/v) glycerol 2 % (w/v) SDS 0.05 % (w/v) bromcresol green
Percoll medium	225 mM Mannitol 25 mM HEPES 1 mM EGTA, 30 % (v/v) Percoll®
PhosTag™ Running Buffer	0.5 mol/l Tris 0.5 mol/l MOPS 0.5 % (w/v) SDS 0.5 mol/l sodium bisulfite
PhosTag™ 10x Transfer buffer	25 mM Tris 192 mM glycine 20 % (v/v) methanol 10 mM EDTA
SSA/HCl Buffer	1,3 % (w/v) sulfosalicylic acid 8 mM HCl
TBS	150 mM NaCl 50 mM Tris-HCl, pH 7.5
TBS-T	150 mM NaCl 50 mM Tris-HCl, pH 7.5 0.1 % (v/v) Tween®20
Tyrode's Buffer	145 mM NaCl, 20 mM HEPES, 5 mM NaHCO ₃ , 5 mM KCl, 1,5 mM CaCl ₂ , 1 mM MgCl ₂ , 0,4 mM KH ₂ PO ₄

4.6. Cell culture Media

Table 9 Cell culture media and supplements

Cell culture medium/supplement	Supplier
Puromycin (10 mg/ml)	InvivoGen, San Diego, USA
0.05 % Trypsin-EDTA	Life-Technologies, Carlsbad, USA
10,000 U/ml Penicillin- 10 mg/ml Streptomycin	Sigma-Aldrich, Steinheim, Germany
B27 supplement	Invitrogen, Carlsbad, USA
DMEM-F12	Thermo Scientific, Waltham, USA
Dulbecco's PBS (D-PBS) without calcium and magnesium	Sigma-Aldrich, Steinheim, Germany
HyClone fetal bovine serum	Thermo Scientific, Waltham, USA
L-Glutamine	Life Technologies, Carlsbad, USA
MEM NEAA (100x) Non-Essential Amino Acids	Life Technologies, Carlsbad, USA
Neurobasal medium	Thermo Scientific, Waltham, USA
Opti-MEM™	Thermo Scientific, Waltham, USA

Table 10 Cell culture media compositions

Cell culture media	Recipes
Neurobasal medium for primary neurons	Neurobasalmedium 2% B-27 Supplement 1% (v/v) L-Glutamine 100 U/ml penicillin and 100 µg/ml streptomycin
SH-SY5Y medium	DMEM/F-12 10% (v/v) FBS 100 U/ml penicillin and 100 µg/ml streptomycin 1% (v/v) L-Glutamine 1% (v/v) NEAA

4.1. Cell lines and mice

4.1.1. Cell lines

Table 11 Cell lines

Cell line	Characteristics	Reference
SH-SY5Y-EV	Stably transfected SH-SY5Y with empty vector (EV) pPB-CAG-HA-DEST-IRES-Venus	Generated in the lab
SH-SY5Y-GDAP1-WT	Stably transfected SH-SY5Y with pPB-CAG-HA-GDAP1-DEST-IRES-Venus inducing a stable overexpression of GDAP1-wt	Generated in the lab
SH-SY5Y-GDAP1(R310Q)	Stably transfected SH-SY5Y with pPB-CAG-HA-GDAP1-DEST-IRES-Venus inducing a stable overexpression of the GDAP1-R310Q mutation	Generated in the lab
SH-SY5Y-GDAP1(S34A)	Stably transfected SH-SY5Y with pPB-CAG-HA-GDAP1-DEST-IRES-Venus inducing a stable overexpression of the GDAP1-S34A mutation	Generated in the lab
SH-SY5Y-pLKO-NT (Ctrl)	Stably transfected SH-SY5Y with the pLKO.1 vector with non-targeted shRNA	Kind gift of ██████████ ██████████ (Pla-Martín et al., 2013)
SH-SY5Y-G4 (GDAP1 KD)	Stably transfected SH-SY5Y with the pLKO.1 vector with targeted shRNA against GDAP1-WT	Kind gift of ██████████ ██████████ (Pla-Martín et al., 2013)
Human iPSCs from healthy donor	Reprogrammed from healthy donor-derived fibroblasts (Noack et al., 2012)	iPSC generation was performed in cooperating laboratory of the Life and Brain Center Bonn
Human iPSCs from CMT4A patient #1	Reprogrammed from CMT4A patient-derived fibroblasts with heterozygous mutations L239F	iPSC generation was performed in cooperating laboratory of the Life and Brain Center Bonn

Materials

	and R273G in the GDAP1 protein sequence (Noack et al., 2012)	
Human iPSCs from CMT CMT4A patient #2	Reprogrammed from CMT4A patient-derived fibroblasts with a homozygous mutation of the intron 4 splice donor site (Noack et al., 2012)	iPSC generation was performed in cooperating laboratory of the Life and Brain Center Bonn

4.1.2. BirA mice

The transgenic mouse line Gt(ROSA)26Sortm1(birA)Mejr (ROSA26-BirA) of a C57BL/6N background was used in this work. The biotin ligase BirA was inserted into the gene locus of the ROSA26 promotor and has been described by Driegen et al. in 2005.

4.2. Equipment

Table 12 Equipment

Equipment	Supplier
Water bath	Memmert, Schwabach, Germany
6-Tube Magnetic Separation Rack	Cell Signaling, Danvers, USA
Beckman Coulter Optima L-80 XP Ultracentrifuge	Beckman Coulter, Brea, USA
Fresco 21 Centrifuge Heraeus	Thermo Scientific, Waltham, USA
Heratherm Incubator	Thermo Scientific, Waltham, USA
Infinite 2000 Pro microplate reader	Tecan, Männedorf, Switzerland
Luna™ Automated Cell Counter	Logos Biosystems, South Korea
Milli-Q-Plus machine	Milipore, Burlington, USA
Mini-PROTEAN® Tetra Cell electrophoresis system	Bio-Rad, Hercules, USA
MSC-Advantage sterile bench	Thermo Scientific, Waltham, USA
Nanodrop 2000c	Peqlab, Peqlab, Germany
Nitrogen cavitation chamber	Parr Instrument Company, Moline, USA
Novex™ NativePAGE™ 4-16 % Bis-Tris Protein-Gel	Invitrogen, Carlsbad, USA

Materials

Odyssey SA Infrared Imaging System	Li-Cor, Bad Homburg, Germany
Opera Phenix™ spinning disc high content screening microscope	Perkin Elmer, Waltham, USA
pH-Meter CG 810	Schott, Mainz, Germany
Pipettes	Eppendorf, Hamburg, Germany
PowerPac Basic Power Supply	Bio-Rad, Hercules, USA
special accuracy weighing machine CPA 10035	Sartorius, Göttingen, Germany
SpectraMax I3 microplate reader	Molecular Devices LLC, San José, USA
Thermomixer F 1.5	Eppendorf, Hamburg, Germany
Trans-Blot Turbo Transfer System	Bio-Rad, Hercules, USA
Vacunsafe suction pump	Integra Biosciences, Zizers, Switzerland
Vortex-Genie 2	Scientific Industries, Portland, USA
XCell SureLock Mini-Cell Electrophoresis System	Thermo Scientific, Waltham, USA
Yokogawa CV8000 high content microscope	Yokogawa, Musashino, Japan
Zeba™ Spin Desalting Columns	Thermo Scientific, Waltham, USA

4.3. Softwares

Table 13 Softwares

Software	Supplier
Adobe Illustrator	Adobe, San José, USA
Adobe Photoshop	Adobe, San José, USA
Affinity Designer	Serif, Nottingham, UK
Columbus 2.8.0	Perkin Elmer, Waltham, USA
Fiji ImageJ	National Institutes of Health, Bethesda, USA
GraphPad Prism 7/8	Graphpad Software, Inc, San Diego, USA
Imaris 9.5.1	Bitplane, Zürich, Switzerland
Microsoft Office Programs	Microsoft, Redmond, USA
Odyssey SA, Image Studio	Li-Cor, Lincoln, USA
Perkin Elmer Harmony High Content Imaging and Analysis Software	Perkin Elmer, Waltham, USA

5. Methods

5.1. Cell Biology

5.1.1. Culturing and passaging

SH-SY5Y cells are human neuroblastoma cells derived from the SK-N-SH cell line, which was subcloned three times – to SH-SY, SH-SY5 and then to SH-SY5Y cells (Biedler et al., 1978). Cell lines were cultured in supplemented DMEM-F12 medium. The cells were passaged twice a week at a confluency of 80-90 % under sterile conditions in a laminar flow hood and cultured in a humidified incubator at 37 °C and 5% CO₂ supply. After washing the cells with phosphate buffered saline (PBS), 0.05 % Trypsin-EDTA was added to detach the cells. By adding fresh growth medium, the trypsin was inactivated, the cells were centrifuged at 1300 rpm for 3 minutes and the cell pellet taken up in fresh medium to passage into new cell culture dishes. GDAP1 knockdown (KD) cell line and its respective control had been stably transfected with the vector pLKO.1 either containing shRNA against GDAP1 (G4) or a non-targeted control shRNA (pLKO.NT) (Pla-Martín et al., 2013). They were cultured in growth medium as described above with supplementary with 2 µg/ml puromycin. GDAP1 overexpressing cell lines had been generated by colleagues in our laboratory with the pPB-CAG-HA-IRES-Venus empty vector, and encoding either mouse GDAP1 wildtype, GDAP1-R310Q or GDAP1-S34A mutations, respectively.

5.1.2. Cryopreservation of cell lines

Cells were harvested from the cell culture dish as previously described above once a confluency of 80-90 % was reached. After centrifugation, the cells were resuspended and washed with PBS and pelleted again by centrifugation. The cell pellet was taken up in freezing medium (90 % (v/v) FCS and 10 % (v/v) dimethyl-sulfoxide (DMSO)) and immediately aliquoted into cryotubes with 1 ml cell suspension each. The cryotubes were put into a CoolCell™ freezing container and into a -80 °C freezer. For long term storage, cells were transferred into a liquid nitrogen tank.

5.1.3. Thawing of cells

Cryotubes containing frozen cells were thawed by addition of prewarmed growth medium in order to keep the toxic effect of the containing DMSO as low as possible. The cells were

centrifuged at 1300 rpm for 3 min, taken up in fresh growth medium and transferred to a cell culture dish to begin cultivation.

5.1.4. Transient transfection

To transiently introduce plasmids into SH-SY5Y cells, the cells were transfected with the turbofectin 8.0™ transfection reagent (Origene) or GenJet™ in vitro transfection reagent (Signagen), both according to manufacturers' instructions. In brief, on day 1 of the experiment, 2×10^5 cells per well were seeded in a 6-well plate. After 24 h the transfection mix was prepared, containing 100 μ l of Opti-MEM medium and supplemented with 2.5 μ g plasmid DNA and 7.5 μ l Turbofectin transfection reagent. The mixture was briefly vortexed and incubated at RT for 15 min for complex formation before dropwise addition to the cells. For the transfection of the Aequorine plasmid (cytAEQ and mtAEQ), GenJet transfection reagent was used. On the day of transfection, 250 μ l of DMEM-F12 medium was supplemented with 2 μ g of plasmid DNA and 7 μ l of GenJet transfection reagent. The tube was slowly inverted twice and incubated for 15 min at RT before dropwise addition to the cells – 10 μ l and 50 μ l were added per well to a 96 well plate and to a 24-well plate respectively.

5.1.5. Patient-derived iPSC generation and differentiation to NPCs

The generation of iPSCs was achieved in cooperation with the Life and Brain Center Bonn under the headship of [REDACTED] Fibroblasts from two CMT4A patients and one healthy donor were transduced with Sendai viruses (CytoTune, DNAVEC Corporation), which encoded for POU5F1, SOX2, KLF4 and MYC (Marx et al., 2013). The iPSCs were cultured in mTeSR medium in Matrigel-coated plates. For the induction of neuronal differentiation and embryonic body formation, the cells were cultured for four days in DMEM/F12 medium with 10 % (v/v) knockout serum, 1 % (v/v) N2 supplement, 0.05 % (v/v) B-27 supplement, 10 ng/ml fibroblast growth factor (FGF) and 20 ng/ml epidermal growth factor (EGF). For rosette formation, cells were transferred to polyornithine/laminin coated plates for additional 6 days. Supplementing the culture medium with 3 μ M retinoic acid induced the differentiation to neuronal precursor cells (NPCs), which were cultured in the described medium in Matrigel-coated plates.

Methods

5.1.6. NPC and motoneuron differentiation of patient-derived iPSCs with small molecules

In contrast to the differentiation protocol in 5.1.5, iPSCs differentiation was now performed by the addition of small molecules – a less expensive protocol yielding a higher number and reproducibility of differentiated motoneurons (MN). Basically, the protocol described by Reinhardt et al. was followed (Reinhardt et al., 2013). Briefly, for neuronal induction, iPSCs were resuspended in hESC medium supplemented with the small molecules 10 μ M SB-431542 (SB), 1 μ M dorsomorphin (DM), 3 μ M CHIR 99021 and 0.5 μ M PMA for two days. The medium was then substituted by N2B27 medium consisting of DMEM-F12 medium with 1:200 N2 supplement, 1:100 B27 supplement without vitamin A and 1% penicillin, streptomycin, and L-glutamine respectively and with the same composition of small molecules. After two further days in culture, SB and DM small molecules were replaced by 150 μ M Ascorbic Acid (AA), leading to embryonic bodies (EBs) formation on day 6. EBs were plated on 12-well plates, which were coated with Matrigel (1:100 in Knockout DMEM) overnight. After around five passages the smNPC cells were free of non-smNPCs and further kept in culture on Matrigel coated plates and N2B27 medium supplemented with CHIR, PMS and AA. Detaching of the cells for passaging was performed with Accutase®.

Starting from smNPC passage 13, differentiation to MN could be initiated. N2B27 medium with 1 μ M PMA was added 3 days after passaging. After two more days, 1 μ M retinoic acid (RA) and 1 μ M PMA were supplemented to the medium for the following 8 days, until culturing in maturation medium began, consisting of N2B27 medium with BDNF, GDNF and dbcAMP, for two more weeks.

5.1.7. Isolation and cultivation of murine cortical neurons

Prior to the isolation of cortical neurons, coverslips were sterilized and coated with 0.05 mg/ml Poly-D-Lysine (PDL) over night at 37 °C. In order to avoid a toxic effect of soluble PDL, the coverslips were washed three times with MilliQ-H₂O and air-dried afterwards under a vertical laminar flow sterile hood. All media and reagents were prewarmed to 37 °C in a water bath.

To begin with, the pregnant mouse at stage E16 was sacrificed by cervical dislocation. After disinfection of the abdomen, the uterus of the mouse containing the embryos was taken out and put into a petri dish containing HBSS⁺. The brain of one embryo was taken out carefully and transferred into another petri dish containing HBSS⁺ with a spatula. The following steps were performed using a Leica 56D binocular microscope and liquids were kept on ice. Using scalpel and forceps the hemispheres were separated and the meninges of both hemispheres removed carefully. Following, the hippocampus, the olfactory bulb and the thalamus were

Methods

precisely removed. The remaining cortices of the embryos were then each transferred to a 15 ml falcon containing 5 ml HBSS⁺.

The following steps were performed in a vertical laminar flow sterile hood. The cortices were washed three times with HBSS⁻ to avoid inefficient digestion of the subsequently added trypsin due to inhibitory ions. Following, 500 µl trypsin (2.5 % (v/v)) was added to 3.5 ml medium containing the cortices and was incubated at 37°C for 10-15 minutes; at the same time, the tubes were inverted three times until the tissue got swollen. To terminate trypsin activity, 2 ml of heat-inactivated FCS was added, and the tubes inverted. Now, the cortices were washed three times with neurobasal medium (NBM). At the last washing step 2 ml NBM were left in the tube for the following titration. For this, a 1 ml pipette was used to carefully pipette the solution up and down for a maximum of six times in order to disrupt the tissue and to detach single neurons. The falcon tube was filled up to 10 ml with NBM and centrifuged at 300 rpm for 5 min to pellet the residual tissue. The supernatant containing the single cell suspension was transferred to a new falcon, then, cells were counted and seeded onto the coated plates. For 6-well plates, 3-5*10⁵ cells per well were plated; for 24-well plates, around 1*10⁵ cells per well. After 24 hours in culture, half of the medium was removed and replaced by fresh and prewarmed NBM to remove any dead cells. Later medium change was done on day4 and day11 after preparation.

5.2. Molecular biology

5.2.1. Protein isolation from cells

The cells were mostly washed with PBS before addition of radioimmunoprecipitation assay-buffer (RIPA buffer) for lysis, supplemented with protease inhibitors to lyse the cells. Lysed cells were transferred into a 1.5 ml tube and incubated for 15 minutes on ice before centrifugation at 21000 g and 4 °C for 30 minutes. Afterwards, the supernatant was transferred into a new 1.5 tube and used for immunoblotting experiments or frozen at -80 °C for long-term storage.

5.2.2. BCA protein assay

To determine the protein content of the previously enriched samples, the bicinchoninic acid protein assay was performed using the BC Assay protein Quantification Kit provided by Interchim. This assay is based on the reduction of Cu²⁺ in the solution to Cu⁺, which occurs proportionally to the amount of protein. BCA then forms a purple-blue complex with Cu⁺, which

Methods

can be detected photometrically at an absorbance maximum of 562 nm. For preparation of this assay, 15 µl of BSA standards of known concentrations (6.25, 12.5, 25, 50, 100, 200 µg/ml) were pipetted in triplicates onto a 96-well plate. The protein lysates were diluted appropriately (1:25 – 1:100) in PCR grade water and added to the plate as triplicates. 200 µl of the BCA-Reagent was added per well and the plate was incubated at 37 °C for 30 minutes. The photometrical analysis was performed using the Tecan-Reader, the subsequent analysis and determination of protein concentration was done using Microsoft Excel.

5.2.3. SDS-PAGE

Sodium Dodecyl Sulfate Polyacrylamide Gel Electrophoresis (SDS-Page) is used to separate proteins by size. By using SDS, the proteins' intrinsic charge is covered and allows a separation by size, independently from its charge. Denaturing of the proteins is ensured by heating the samples up to 95 °C and dithiothreitol (DTT) reduces inter- and intramolecular disulfide bonds. Samples were diluted to the desired protein concentration and 1x sample buffer was added. The samples were boiled at 95 °C for 5 minutes before they were loaded onto 4-15 % Mini PROTEAN Membrane Stain Free precast gels. Proteins were transferred onto nitrocellulose membranes using the semi-dry Trans-Blot® Turbo™ Transfer System (Bio-Rad). Membranes were blocked with 3 % (w/v) milk powder in TBS-T (1x TBS, 0.05 % (v/v) Tween 20) for 1 hour at room temperature (RT). Chameleon Duo Pre-stained Protein Ladder (Li-Cor Biosciences) was used as molecular weight standard. For visualization, membranes were incubated with an infrared fluorescence IRDye 800-conjugated anti-mouse, 800-conjugated anti-rabbit, or 680-conjugated anti-mouse IgG secondary antibody (1:10.000; Licor), for 1 h at room temperature and detected and analyzed with the Odyssey Infrared Imaging System (Li-Cor Biosciences).

5.2.4. Blue Native Page

Blue Native Page was performed to separate mitochondrial protein complexes in their native conformation by size and hydrophobicity and all steps were performed at 4°C with precooled media and equipment. Mitochondria were initially isolated from indicated cell lines as described in 5.2.10. Ideally, 5-10 µg of mitochondrial proteins were prepared per well. The protocol is modified from the Invitrogen native page Novex bis-tris gel system. Running buffers such as the 1x anode buffer (Invitrogen, BN2001) and the cathode buffers (dark blue and light blue cathode buffer) were prepared on the previous day and pre-cooled. 5 µg of mitochondria were mixed with 1 % (w/v) digitonin and 1x native page sample buffer, and the volume was adjusted

Methods

with H₂O to 10 µl and incubated for 15 minutes on ice before centrifugation at 20000 g for 30 min at 4 °C. The supernatant was transferred to new tubes. 0.5 µl of 5 % G-250 Coomassie was added and the sample was loaded onto native page Novex bis-tris 4-16 % gradient gels (Invitrogen, BN1002). The inner chamber was filled with dark blue cathode buffer, the surrounding chamber with the anode buffer. Mitochondrial proteins slowly migrated into the gel by applying 40 V for 60 minutes, followed by an increase to 100 V for 30 minutes until the dye front migration reached 1/3 of the gel. Dark blue cathode buffer was exchanged with light blue cathode buffer and the run was continued with 100 V for 30 minutes. Voltages were then increased to 150 V until the dye front reached to bottom of the gel. Proteins were transferred to PVDF membranes by wet transfer with precooled NuPage transfer buffer without methanol. The transfer was run for 1 h at 100 V. After the transfer, the membrane was incubated for 15 minutes in 8 % (v/v) acetic acid for fixation and was then destained with 50 % (v/v) methanol and 25 % (v/v) acetic acid. After thorough washing (3-5 times) with TBST, the membrane was incubated with 3 % milk in TBST for blocking and could then be incubated with the desired primary antibody.

5.2.5. Virus production in HEK cells

The production of adeno-associated viruses (AAVs) carrying the genes of interest (GOI) under the control of a WPRE promotor was carried out by a cooperating working group [REDACTED]. Briefly, HEK cells were expanded and transfected via CaPO₄ transfection. 60-65 hours after transfection, cells were harvested and resuspended in 150 mM NaCl, 20 mM Tris pH 8.0 and 0.5 % sodium deoxycholate. Benzonase endonuclease (DNAse/RNAse) was added and incubated at 37 °C for 60 minutes. After centrifugation at 4000 rpm for 10 minutes, the supernatant was transferred into a new falcon and frozen at -20 °C. The solution containing the released viruses was thawed at RT and subjected to heparin-columns for virus purification. The columns were washed with washing buffers with increasing NaCl concentrations – I) 100 mM II) 200 mM and III) 300 mM NaCl in 20 mM Tris pH 8.0 and elution was performed with I) 400 nM II) 450 mM and III) 500 mM NaCl in 20 mM Tris pH 8.0 in a small Amicon concentrator. After centrifugation at 3300 rpm for 2 minutes and a further washing step with PBS, the supernatant of around 250 µl was transferred to new tubes and frozen at -80°C for further quality tests and titration via qPCR.

Methods

5.2.6. Real-time quantitative qPCR for titer determination of the viruses

Viral DNA was extracted to examine the titer of the viruses. 2 µl of each virus (in duplicates each) was diluted in 86 µl sterile water and 10 µl ABI buffer (10x, 500 mM KCl, 100 mM Tris pH 8.0, 50 mM MgCl₂). 1 µl DNase I was added and incubated at 37 °C for 30 minutes. The DNase was inactivated at 70°C for 10 min and 1 µl Proteinase K was added for 1 h at 50 °C to digest the capsid of the virus and to release the viral DNA. After Proteinase K inactivation at 95 °C for 20 min, the DNA was either stored at 4 °C or directly taken for quantitative PCR (qPCR). Viral DNA was diluted 1:50 in PCR grade water. WPRE forward and reverse primers were used. For one reaction, 0.2 µl (100 nM) of both primers was added, as well as 10 µl 2x SYBR green mix, 5 µl DNA Template and 4.6 µl PCR grade water. For the standard curve, a WPRE encoding plasmid was diluted to 10⁷ copies/µl and further diluted to 10⁶, 10⁵ and 10⁴ copies/µl. A 96-well plate was sealed with a sticky foil after standard and templates were added together with the reaction mixture and the PCR was carried out with a BioRad CFX Connect Real-Time Detection System with the following settings:

Table 14 qPCR for Virus DNA titration

	Temperature	Time [m:s]
Cycle 1 (1x)	95 °C	3:00
Cycle 2 (40x)	95 °C	00:10
	64°C	00:45
Generation of the melting curve:		
Cycle 3 (1x)	95 °C	01:00
Cycle 4 (1x)	55 °C	01:00
Cycle 5 (80x)	55 °C	00:10
Setpoint temperature after cycle 2 was increased 0.5 °C for collection of melting curve values.		

Data was analyzed with the $\Delta\Delta Ct$ method.

5.2.7. Genotyping of Rosa26-BirA mice

Mouse biopsies were lysed overnight at 55°C with 200 µl of the DirectPCR Lysis Reagent with freshly added 0.2 mg/ml Proteinase K according to the manufacturer's instructions. The proteinase K was inactivated at 85°C for one hour. The PCR mixture for each sample consisted of 14 µl H₂O, 5 µl of GoTaq buffer, 2 µl dNTPs, 1 µl primer mixture (1:1:1) and 0.125 µl GoTaq Polymerase. Finally, 3 µl of the DNA was added and the program was started (Table 15).

Methods

Table 15 Rosa26-BirA Genotyping

	Temperature	Time [m:s]
Initial Denaturation	94°C	05:00
Cycle initiation (35x)		
Denaturation	94°C	00:30
Annealing	60°C	00:30
Elongation	72°C	00:30
Terminal Elongation	72°C	05:00

The PCR products were loaded onto agarose electrophoresis gels to separate and differentiate the DNAs by size. WT bands appeared at 365 bp, and the Rosa26-BirA insertion leads to a larger DNA band at 455 bp.

5.2.8. Virus transduction of primary cortical neurons

Viruses were produced and the titer was determined as previously described. To transduce primary murine cortical neurons (isolated from C57Bl6 (WT) or Rosa26-BirA mice), viruses were added in a volume that equaled approximately 6×10^7 - 8×10^7 copies/ μ l to one plate of a 6 well plate containing 4 ml of NBM and neurons on day 4 after preparation. To ensure virus uptake and protein production, the neurons were cultured for further 7 days after transduction and processed depending on the experimental purpose. For western blotting, the cells were directly lysed in RIPA buffer supplemented with protease inhibitors. For immunocytochemistry, 4% paraformaldehyde (PFA) was added to the cells for fixation and antibody staining.

5.2.9. Pulldown of GDAP1 in primary neurons

For pulldown of transduced neurons as described in 5.2.8, neurons were washed briefly with PBS and lysed in RIPA buffer supplemented with protease inhibitors. The samples were centrifuged at 21000 g for 30 minutes at 4°C, the protein concentration was measured as described previously and 20 μ g protein lysate was removed as input-control. Protein lysates were either directly incubated with Dynabeads™ MyOne™ Streptavidin T1 according to the manufacturer's protocol or taken for the fusion reaction. The reaction was carried out with these final concentrations of the following reagents: 10 mM HEPES pH 7.4, 35 mM sucrose, 40 mM KCl, 0.25 mM EGTA, 2 mM Mg(CH₃COO)₂, 0.5 mM GTP, 1 mM ATP (K⁺), 5 mM Na succinate, 0.08 mM ADP, 2 mM K₂HPO₄. The mixture was incubated with either GSH or GSSG

Methods

addition at 37 °C for 30 minutes and the reaction was stopped by adding Dynabeads™ MyOne™ Streptavidin T1 for 45 minutes at RT on a shaker. The beads were washed three times with RIPA buffer before adding 1x SDS sample buffer with DTT in PCR grade water. The beads were washed once with PBS and stored at -80 °C until further processing for mass spectrometry.

5.2.10. Isolation of Mitochondria

For enrichment of mitochondria from cell lines, $20-14 \times 10^6$ cells were harvested, resuspended in Mitochondria isolation buffer I and transferred into a nitrogen cavitation chamber (Parr Instrument Company, 4639). After applying a pressure of 80 bar, the chamber was chilled on ice for 10 minutes, and the gas released, which led to rupturing of the cells. To remove unbroken cells and membranes, the suspension was centrifuged for 10 minutes at 2000 g. The supernatant was transferred to a new vial and mitochondria were pelleted by centrifugation at 10.000 g for 10 minutes at 4°C. The mitochondrial pellet was washed with Mitochondria isolation buffer II with a cut-off end pipette tip. After further centrifugation, the crude mitochondrial fraction was now taken up in the appropriate buffer for following experiments.

5.2.11. MAM and ER isolation of cultured cells

Cells were plated into five 500 cm² square plates and grown to confluency. On the day of experiment, the medium was removed, cells were washed once with PBS and subsequently detached with cell scrapers and collected in 50 ml tubes. All steps were performed on ice and at 4 °C. After centrifugation, the cells were washed with PBS and again pelleted before they were resuspended in isolation buffer 1 (IB1). Homogenization was carried out with Teflon glass homogenizers in intervals of 30 s homogenization and 30 s on ice for 10-20 min in order to preserve the integrity of mitochondria and MAMs composition. Centrifugation of the suspension at 700 g for 5 min at 4°C was performed to obtain a pellet composed of nuclei and unbroken cells. The supernatant containing mitochondria, ER and cytosolic fraction was transferred into 2 ml tubes to perform further centrifugation and fractionation. Mitochondria were pelleted by centrifugation at 7000 g for 10 min at 4°C. As mitochondria are highly sensitive to mechanical damage, cut-end tips were used for pipetting for all following steps and mitochondria were carefully detached from the tube well with a soft brush. The supernatant containing the cytosol and ER was transferred to new tubes and mitochondria were washed twice with isolation buffer 2 (IB2) and finally taken up in MRB medium. 1 ml of mitochondria was layered carefully on top of Percoll® medium pre-packaged in ultracentrifugation tubes.

Methods

Ultracentrifugation was performed at 23100 rpm for 30 min at 4°C using the SW40 Ti rotor without brake. Both the upper and lower band, identified as MAMs and pure mitochondria respectively, were divided into 2 tubes and centrifuged at 7000 g for 10 minutes. Pelleted mitochondria were finally taken up in 200 µl MRB medium, whereas the supernatant of the MAM-band contained the pure MAM fraction – the pellet contained residually bound mitochondria.

Further ultracentrifugation at 23700 rpm finally pelleted the cloudy MAMs. The cytosolic fraction containing ER and microsomes was further centrifuged at 20000 g to separate microsomes from cytosol and ER fraction, whereas the ER was further purified when needed by ultracentrifugation at 100000 g for 30 min at 4°C. Western Blotting of the purified fractions confirmed the quality of organelle fractionation.

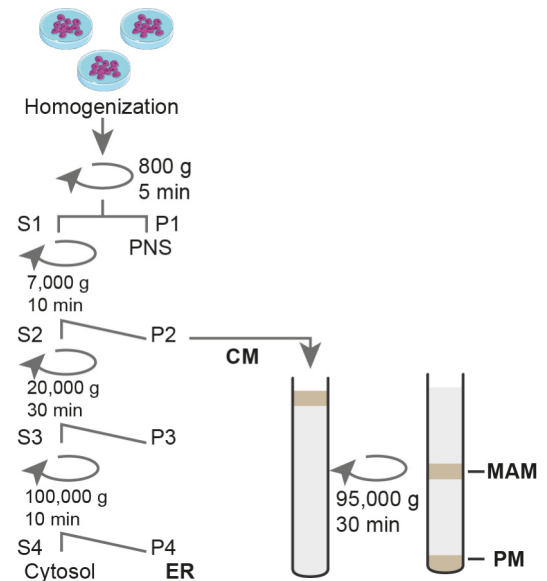


Figure 7 Scheme of MAM, ER and mitochondrial isolation

After homogenization and cell rupture, mitochondria were isolated and further processed by differential centrifugation and Percoll® gradient to purify MAMs. CM – crude mitochondria; MAMs – mitochondria associated membranes; PM – pure mitochondria; S – supernatant; P - pellet

5.2.12. BioGEE assay (Thermo Scientific and VCP BIO)

Mitochondria were obtained from SH-SY5Y cell lines as previously described and after protein quantification 40 µg mitochondria were transferred to new vials and treated with 250 µM biotinylated glutathione (BioGEE). Basically, this molecule is a glutathione (γ-L-Glutamyl-L-cysteinyglycine) which is modified with an ethyl ester at the carboxyl-group of the glycine residue to yield a membrane-permeable molecule. Additionally, a biotin was coupled to the amino group of the γ-L-Glutamyl residue. Ethanol was used as vehicle control and H₂O₂ was added as indicated. After 30 min at 37°C the reaction was quenched with an equal amount of RIPA buffer which also solubilizes the mitochondrial proteins. Streptavidin dynabeads were added and incubated at RT for further 45 minutes on an end-over-end tumbler.

5.2.13. GSH-PrSSG Assay

Cells were plated in a 6-well plate at a density of 200,00 cells/well. On the day of experiment, the cells were treated with ethacrynic acid in a final concentration of 30 µg/ml or

Methods

ethanol as vehicle control for 45 minutes. Cells were washed twice with ice-cold PBS and resuspended in 200 μ L SSA/HCl buffer containing 1.3 % (w/v) sulfosalicylic acid and 8 mM HCl in KPE buffer. For KPE buffer, 0.1 M solutions of KH_2PO_4 and K_2HPO_4 were prepared; 16 mL and 84 mL of these solutions were mixed respectively with 5 mM EDTA in order to obtain 100 mL of a 0.1 M phosphate buffer with a pH of 7.5. Samples were vortexed, incubated on ice for 10 min and centrifuged at 14000 rpm for 10 min. The supernatant was transferred into new microcentrifuge tubes containing 12 μ L of triethanolamine/ H_2O 1:1 for GSH quantification. GSH was then measured by monitoring NADPH consumption by GSH reductase in KPE assay buffer, containing 2.8 mM DTNB (5,5'-dithiobis-(2-nitro-benzoic acid)) and 1.3 mM NADPH, at 390 nm using the Infinite 2000 Pro microplate reader and the SpectraMax I3 microplate reader. The final GSH concentrations were normalized to the total protein amount. For quantification of protein glutathionylation (PrSSG), the pellet obtained after protein precipitation with sulfosalicylic acid was treated with 1 % (v/v) NaBH_4 to remove the bound GSH. The reaction was neutralized with 30 % (w/v) metaphosphoric acid centrifuged at 1000 g for further 15 minutes. The supernatant was used to determine the released GSH in the samples, whereas the pellet was resuspended in 0.2 N NaOH and incubated at 37 °C overnight, followed by protein quantitation (BC Assay, Interchim). All chemicals were obtained from Sigma-Aldrich (St. Louis, USA).

5.2.14. PEG alkylation gel shift

For the PEGylation of free protein thiols of mitochondria, MM(PEG)₂₄ Methyl-PEG-Maleimide reagent (PEG₂₄) was diluted in DMSO to have a stock solution of 250 mM. Binding of one PEG molecule to sulfhydryl groups of cysteines results in a protein shift of 1.2 kDa in SDS PAGE (Kozlowski and Milton Harris, 2001). Isolated mitochondria were incubated in PEG assay buffer and 15 mM PEG₂₄ for 1 h at room temperature in the dark. As a positive control, mitochondrial proteins were reduced with 10 mM TCEP and incubated for 20 min at 95 °C prior to PEG₂₄ addition. DMSO was taken as vehicle control. After boiling the samples at 95 °C, the samples were loaded on SDS-PAGE, followed by blotting to a nitrocellulose membrane for antibody incubation.

5.2.15. Biotin Switch Assay

Prepared cells (ca. 8×10^6 cells) were lysed in RIPA buffer supplemented with protease inhibitors and 25 mM N-Ethylmaleimide (NEM), incubated for 45 minutes at RT, and

Methods

centrifuged at 21000 g for 30 minutes at 4°C. Meanwhile, ZEBRA columns were washed twice with RIPA buffer. The centrifugation settings for washing the ZEBRA columns three times with water and once with Tris HCl pH 7.4 in between the treatments was 1.500 g for 2 min at RT. The supernatant containing the proteins was transferred to the ZEBRA column in order to remove unbound NEM. The flow-through was incubated with either 5 mM DTT or 27 µg/ml recombinant human Grx1 together with 1 mM NADPH, 4 U/ml recombinant glutathione reductase (GR), 1 mM GSH for 30 min at RT or 25 °C respectively (Kehr et al., 2011). The protein suspension was again cleared through the column before adding 0.5 mM N-(biotinoyl)-N-(iodoacetyl) ethylenediamide (BIAM) for 1 h at RT in the dark. After cleaning the sample again from unbound reagents, magnetic streptavidin beads were added to the sample as described above (5.2.9). Beads were washed three times with RIPA buffer and subsequently boiled after addition of 1 x SDS Sample buffer with DTT at 95 °C for 5 min. Removing the bound proteins from the beads was carried out with magnets and the proteins were loaded to SDS-PAGE to perform Western blot analyses of modified or glutathionylated proteins.

5.2.16. Phos-tag™ Blots

For quantification of protein phosphorylation, precast Phos-tag™ gels were used. In this approach, proteins are first exposed to Phos-tag™ acrylamide molecules, which bind phosphorylated proteins, resulting in a slower migration of the specific protein in SDS-PAGE (Kinoshita et al., 2006). Cells were lysed and protein concentration was determined as described previously. Special care had to be taken to add phosphatase inhibitors to the RIPA buffer. The running buffer (5x) was composed of 0.5 mol/l Tris, 0.5 mol/l MOPS, 0.5 % (w/v) SDS and 0.5 mol/l sodium bisulfite. Before loading, 1 mM ZnCl₂ was added to the samples to improve resolution and avoid any disturbances of EDTA. Before protein transfer, the gel was incubated in 1x transfer buffer with 10 mM EDTA twice for 10 min each, followed by one washing step in transfer buffer without EDTA. Semi-dry blotting to PVDF membranes and antibody incubation was performed as described previously.

5.2.17. Aequorine Measurement

For Ca²⁺ measurements, the biosensor aequorine (AEQ) was used, which is a 22 kDa photoprotein isolated from jellyfish *Aequorea Victoria* (Bonora et al., 2013). Upon Ca²⁺ binding, blue light is emitted and can be photometrically measured with a luminometer (Ottolini et al., 2014; Whitaker, 2004). SH-SY5Y cells were grown on 12 mm glass coverslips to a confluency of 40-50 % and transfected with cytosolic or mitochondria-targeted AEQ (cytAEQ/mtAEQ)

Methods

using the GenJet transfection reagent according to the manufacturer's instructions. On the day of experiment, the cells were treated with 5 μM coelenterazine-N-AM in basic saline solution (BS) containing 1 mM CaCl_2 for 2 h at 37°C and 5% CO_2 . Coelenterazine serves as a substrate for the Aequorine enzyme. Coverslips were then placed in the luminometer with constant buffer perfusion with BS supplemented with I) 1 mM Ca^{2+} (30 s) II) 200 μM EGTA (30 s) III) 200 μM Carbachol (CCH) + 200 μM EGTA (120 s) IV) 100 μM Digitonin + 5 mM CaCl_2 (220 s).

5.2.18. Glucose uptake

To monitor glucose uptake of cells in vitro, 2-(N-(7-Nitrobenz-2-oxa-1,3-diazol-4-yl)Amino)-2-Deoxyglucose (2-NBDG) was used, which served as a fluorescent glucose analogue (Zou et al., 2005). Cells were plated into a black 96-well plate with 10000 cells/per well. 24 hours later, the cells were washed twice with PBS or starved of nutrients for 30 minutes before loading with 100 μM 2-NBDG for 30 minutes at 37°C. Subsequently, the cells were washed twice with PBS. PBS also served as negative control to determine any background signal. Fluorescent signal was measured at ex/em 465/540 nm using a plate reader (Tecan Infinite 200 Pro). To normalize the fluorescence signal to the cell number, cells were lysed in 75 μl RIPA buffer after the measurement and protein content was determined via the BC assay.

5.2.19. BTeam

A BRET-based ATP biosensor was used for measurement of relative ATP levels in cells. It integrates an ATP binding unit, a yellow fluorescent protein (YFP), as well as an ATP-independent luciferase (nLuc) (Yoshida, Kakizuka, & Imamura, 2016). Upon ATP binding and in presence of nLuc substrate, bioluminescence resonance energy transfer (BRET) takes place, which leads to a change in emission spectra for nLuc and YFP. The biosensor carries either no targeting sequence or a mitochondrial targeting sequence for quantifying cytoplasmic or intramitochondrial ATP quantities, respectively. The plasmids were transfected into cells that were seeded the prior day onto white 96-well plates with turbofectin transfection reagent as previously described. 48 hours after transfection, medium was exchanged for phenol red-free DMEM-F12 medium with 30 μM nLuc inhibitor and incubated for 30 min to avoid background signal from dead cells. Following, the cells were incubated with the nLuc substrate for 20 min and luminescence and YFP signals were measured using a plate reader at 520/560 nm (ex/em) and 430/470 nm (ex/em) respectively with temperature control at 37°C. After baseline measurement, 25 μM 2-Deoxy-D-Glucose (2DG) was added to the cells to inhibit glycolysis. Resulting changes in fluorescence were measured for another 10 min. To erase

any possible differences in transfection efficiency, the data were expressed as BRET ratio, YFP/nLuc luminescence ratio.

5.3. Mass Spectrometry

Sample preparation, measurement and analysis were performed in cooperation with the Mass Spectrometry Core Facility in [REDACTED] group at the University Medical Center Mainz.

5.3.1. Protein digestion and LC-MS analysis

Samples were prepared for LC-MS using the SP3 protocol as described in Sielaff et al., 2017.

For LC-MS analyses a NanoAQUITY UPLC system (Waters Corporation, Milford, MA) was connected online to a Synapt G2-S high definition mass spectrometer (Waters Corporation) through a NanoLockSpray dual electrospray ion source (Waters Corporation). Samples of 200 ng, which were tryptically digested, were loaded onto a at 55 °C heated HSS-T3 C18 1.8 μm , 75 μm \times 250 mm reversed-phase analytical column (Waters Corporation). Mobile phase A consisted of 0.1 % (v/v) FA and 3 % (v/v) DMSO in water and mobile phase B of 0.1 % (v/v) FA and 3 % (v/v) DMSO in ACN. To separate peptides a 90 min running gradient from 5 to 40 % (v/v) mobile phase B was used at a flow rate of 300 nL/min. Eluting peptides were analyzed by MS using ion-mobility separation (IMS) enhanced data-independent acquisition (DIA) in UDMSE mode as described before (Distler et al., 2014, 2016). In short, precursor ion information was gathered in low-energy MS mode at constant collision energy of 4 eV, while fragment ion information was collected in the elevated energy scan applying drift-time specific collision energies. With 0.6 s for the spectral acquisition time in each mode and 0.05 s interscan delay the overall cycle time was 1.3 s for the acquisition of one cycle of low and elevated energy data. As lock mass [Glu1]-fibrinopeptide was used at 250 fmol/ μL , with a flow rate of 1.5 $\mu\text{L}/\text{min}$ and analyzed every 30 s. The lock mass entered the MS via the reference sprayer of the NanoLockSpray source.

5.3.2. Data processing and Label-free Quantification

Symphony (Waters ver. 1.0.0.191) pipeline was used for raw data processing and database search of LC-MS data. The database was custom made from murine proteome derived from UniProt (UniProtKB release September 2018, 16991 entries), common contaminants and

reverse database. Search parameters included at least 2 fragment ions that had to be detected for peptide identification. For a protein to be reported, a minimum of 5 fragments summed over all assigned peptides had to be monitored. Furthermore, missed cleavages were set to 2, protease to Trypsin, fixed modifiers to carbamidomethylation at cysteine and variable modifiers to oxidation at methionine.

The target-decoy strategy was applied to determine the false discovery rate (FDR) for peptide and protein identification and was set to 0.01. The data of the experimental replicates of each condition were post-processed using the software ISOQuant ver. 1.8 including retention time alignments, exact mass retention time (EMRT) and IMS clustering, normalization and protein homology filtering. Details have been described in Distler et al., 2014 and Distler, Kuharev, Navarro, & Tenzer, 2016. Additionally, the following settings were used: minimum peptide length of 6 amino acids, minimum 2 peptides per protein, minimum max score per cluster 6, FDR 0.01, no missed cleavage and no variable modifications, e.g. methionine oxidation. Absolute sample amounts were calculated for each protein using TOP3. Further analysis was performed with the String and Panther databases.

5.4. Microscopy

5.4.1. Transmission electron microscopy

Ultrastructural analyses of stable SH-SY5Y cell lines and CMT4A patient-derived NPCs were done via electron microscopy in cooperation with the neuropathology group of [REDACTED]. The Ultrathin sections were prepared by this group. For the preparation of the sections, cell pellets were fixed overnight in 3 % glutaraldehyde and subsequently dehydrated for embedding in epoxy resin. Incubation with 1 % osmium tetroxide for 2 hours served for fixation and blackening of the cells. Afterwards, the cells were embedded in epoxy resin, which was hardened overnight at 60 °C. The ultrathin sections of cells with a thickness of 50 nm were achieved using the Ultracut UCT provided by Leica. For the evaluation with the electron microscope and as a differential staining, the sections of epoxy-embedded cells were stained Richardson. Images were acquired with a Zeiss EM-910 transmission electron microscope (Carl Zeiss, Germany) and analysis was performed with Fiji ImageJ Software.

5.4.2. Immunocytochemistry

Cells were plated on sterilized glass coverslips two days prior to the experiment. The cell confluency on the day of experiment should be around 70-80 % in order to distinguish single

Methods

cells. First, the cells were washed once with PBS and then fixed with 4 % PFA for 15 min at RT. After washing three times with PBS, the cells were permeabilized with 0.25 % (v/v) Triton X-100 in PBS for 10 min at RT to improve the intracellular accessibility for the antibodies. The cells were again washed three times with PBS and incubated with 1X ROTI-Block for 30-60 min to avoid unspecific antibody binding. Primary antibodies were added in given dilutions in 1X ROTI block in PBS with 0.1 % (v/v) Triton X-100 and incubated over night at 4°C. After washing with PBS to remove unbound antibodies, fluorophore-conjugated secondary antibodies were incubated for 1 h at RT in the dark. If needed, nuclei were counterstained with 300 nM DAPI for 3-5 min at RT in the dark. Lastly, the coverslips were mounted onto microscope slides with DAKO mounting medium. After chilling at 4°C overnight in the dark, the mounting medium was dried, and microscopic images were taken with Leica SP8 confocal microscope.

5.4.3. High Content Microscopy

High Content Microscopy was performed with an Opera Phenix spinning disc high content screening microscope (Perkin Elmer, USA) and images were acquired with 40x, 1.2 NA water immersion objective and two sCMOS cameras. Dyes used were 300 nM Höchst, 100 nM MitoTracker™ Green FM and 25 nM TMRM and were measured at 405/435, 488/500-550 and 561/570-630 nm (ex/em), respectively. Nuclei staining and mitochondria staining was done by incubating the cells in serum-free medium with 300 nM Höchst and 100 nM MitoTracker™ Green FM for 15 minutes at 37 °C, followed by further 15 min in fresh growth medium after removing the staining solution from the cells. The TMRM was added to Tyrode's buffer in a final concentration of 25 nM. Analyses were done with the analysis packages Harmony (version 4.5) and Columbus (version 2.8.0) containing the PhenoLOGIC™ machine learning plugin (Perkin Elmer). Oligomycin was added at a final concentration of 2 µg/µl; the concentration of FCCP was 1 µM. BODIPY™ 558/568 C₁₂ was added to the cells in parallel to MitoTracker in a final concentration of 1 µM for 15 minutes and cells were subsequently incubated with normal growth medium to incorporate the dyes. Patient-derived motoneurons and smNPCs were imaged with a Yokogawa CV8000 high content microscope.

5.4.4. FEMP sensor

ER-mitochondria contacts were quantified with a FRET-based sensor indicating the proximity between the ER and mitochondria. The plasmid encodes for a YFP-linked outer mitochondrial membrane protein Akap1 and a CFP-conjugated ER-protein Sac1, as well as a fused FK506 binding protein (FKBP) and FKBP-rapamycin binding domain (FRB) domain, respectively.

Methods

These domains can form heterodimers upon rapamycin treatment. The specific localization of these proteins is ensured by the introduction of a self-cleavable Tav2A sequence (Csordás et al., 2010; Naon et al., 2016). The FEMP plasmid (FRET-based ER-mitochondria probe) was transfected with GeneJet transfection reagent as described above. After 48 hours, images were taken with the Perkin Elmer Operetta High-Content Imaging System acquiring the CFP- (410-430/460-500 ex/em), YFP- (490-510/520-560 ex/em) and YFP_{FRET}-emission (410-430/520-560 ex/em), with a 40x water objective for determination of the basal distances between the organelles under temperature and CO₂ control (37°C, 5 % CO₂). Subsequently, the cells were treated with 100 nM rapamycin for 15 minutes for FKBP-FRB dimerization induction and a maximum of YFP_{FRET} signal. Cells were fixed for another 20 minutes with 1 % PFA and imaging was performed again with equal microscopy settings. For the analysis, the Harmony software was used. First, the cells were identified using the YFP channel. Within each cell and region of interest (ROI), the intensities of the three acquired channels were calculated, including background subtraction. The FRET ratio was calculated as following: $(\text{FRET}-\text{FRET}_{\text{background}})/(\text{CFP}-\text{CFP}_{\text{background}})$

5.4.5. Confocal microscopy and Imaris image analysis

SH-SY5Y cells stained against GRP75 and cofilin1 via immunocytochemistry were imaged with a Leica TCS SP8 inverse confocal fluorescence microscope with a 63x/1.4 NA oil immersion objective in z-stacks. Images were analyzed in Imaris 9.5.1 (Bitplane). To improve the signal-to-noise ratio, iterative deconvolution was performed. The software was then used to create 3D surfaces of mitochondria and cofilin1 spots to measure the surface area and to determine the shortest distance of cofilin1 surface to the mitochondrial surface. Colocalizing cofilin1 with a distance $\leq 0 \mu\text{m}$ was duplicated to a new surface, which was taken for the Imaris surface surface contact XTension to quantify the contact area, defined as the percentage of mitochondrial surface in contact with cofilin1.

5.4.6. Statistics

Statistical analyses were performed with GraphPad Prism 7 and data are presented as mean \pm SEM (standard error of the mean), XY graph or Tukey's box and whiskers plot. The ROUT method was applied to determine outliers. Statistical significance was considered when p-value was below 0.05 ($p^* < 0.05$) and was determined with the GraphPad Prism Software applying either the nonparametric Mann-Whitney t-test or the parametric two-tailed t-test when comparing two independent groups. Bonferroni-correction was included in the proteomic

Methods

analyses. One-way ANOVA and two-way ANOVA were applied with Dunn's, Tukey's or Sidak's multiple comparisons test for determining the statistical significance between three or more groups. The D'Agostino-Pearson omnibus normality test was performed to test for a Gaussian distribution.

6. Results

6.1. Impaired mitochondrial dynamics and metabolism upon GDAP1 depletion

6.1.1. The effect of GDAP1 KD on mitochondrial fission and fusion proteins

It has been reported before that GDAP1 impairs the mitochondrial shape and leads to increased mitochondrial fission when overexpressed (Niemann et al., 2005). The following experiments served to study the mitochondrial shape, involving fusion and fission dynamics in GDAP1 knockdown (KD) cells. Stably transfected SH-SY5Y cell lines were used expressing either shRNA against GDAP1 (GDAP1 KD) or non-targeted shRNA as control (Ctrl) (Pla-Martín et al., 2013). The reduction of GDAP1 expression in the KD cells in comparison to the control cells was confirmed via immunoblots (IB) of the total cell lysates with antibodies against GDAP1 and actin as loading control (Figure 8A).

The evaluation of the mitochondrial shape via live cell imaging was performed with MitoTracker™ Green FM stained cells using high content microscopy. The PhenoLOGIC™ machine learning plugin (Harmony) allowed an automated classification of mitochondrial shape in a large number of cells into fragmented, intermediate or tubular mitochondria (Figure 8B). A significant increase in the percentage of cells with tubular mitochondria was seen in the GDAP1 KD cells, with a concomitant decrease of fragmented mitochondria. This led us to further quantify the expression of fission proteins in these cells. MFF serves as a mitochondrial receptor protein for DRP1-binding to the outer mitochondrial membrane (OMM) and is strongly implicated in the process of mitochondrial fragmentation (Otera et al., 2010). There was a significant reduction in MFF protein levels in GDAP1 KD cells compared to the control (Figure 8C). Furthermore, I tested for DRP1 expression levels. DRP1 lacks a transmembrane domain and is mainly located in the cytosol (Lewis et al., 2018; Yoon et al., 2001, 2003). Upon activation by dephosphorylation of Ser637 (by calcineurin) or phosphorylation of Ser616, DRP1 translocates to the mitochondria, where it can bind MFF, and subsequently oligomerizes and induces mitochondrial fragmentation (Lewis et al., 2018; Otera et al., 2010; Toyama et al., 2016; Yoon et al., 2003). Consequently, we measured not only protein expression but also its migration to the mitochondrial surface (Figure 8C, D). In total cell lysates, DRP1 was significantly downregulated in the KD cells compared to the Ctrl (Figure 8C). To quantify mitochondrial translocation, we isolated mitochondria via differential centrifugation after cell rupture with a nitrogen cavitation chamber. Upon immunoblotting of the different fractions (cytosol and mitochondria), I calculated the ratio between mitochondrial and cytosolic DRP1. This approach showed significantly less DRP1 in the mitochondrial fractions (Figure 8D). The reduced expression of both fission factors MFF and DRP1, as well as reduced DRP1

Results

translocation to the mitochondria also matches the observation of decreased fission activity and increased mitochondrial elongation upon reduction of GDAP1 expression.

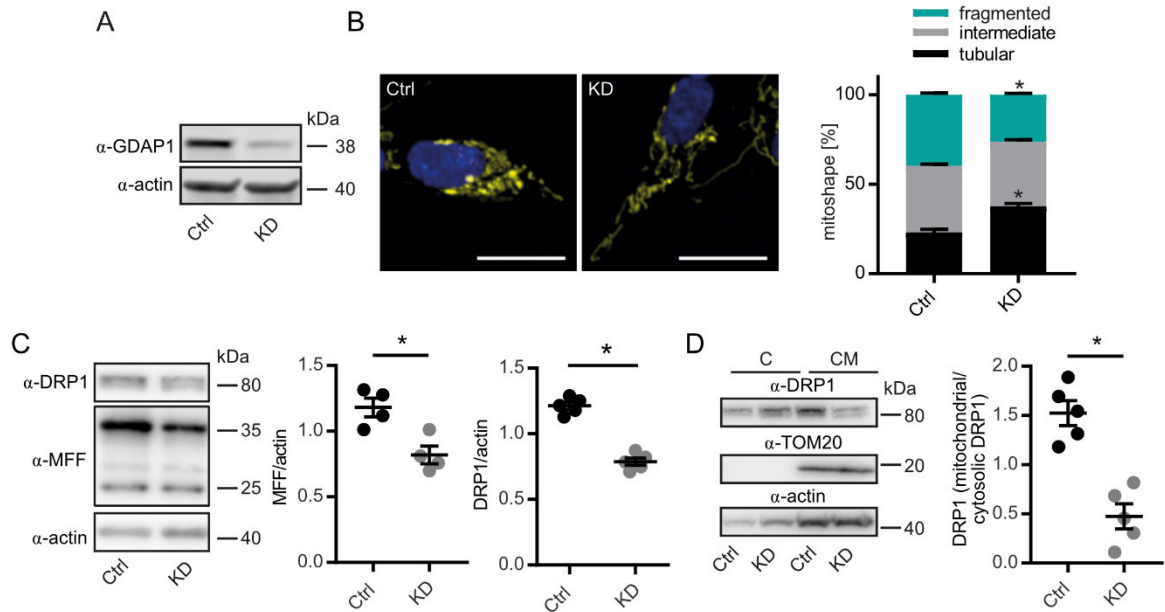


Figure 8 Effect of GDAP1 KD on mitochondrial fission and fusion proteins

Ctrl and GDAP1 KD cells were analyzed for their fusion and fission activity. A) Verification of cell lines: IB of whole-cell lysates stained against GDAP1 and actin as loading control, size is indicated. B) Live cell imaging of both cell lines was performed via high content microscopy after mitochondrial staining with MitoTracker™ Green FM; nuclei were counterstained with Höchst. Scale bar equals 20 μ m. Automated mitochondrial shape analysis and classification were performed with Perkin Elmer Harmony software; the experiment was performed in triplicates; $n > 20,000$ cells per cell line. C) IB of total cell lysates stained against DRP1, MFF and actin. Band intensities were measured, and signals were normalized to actin. D) IB of cytosol (C) and the crude mitochondrial fraction (CM) to calculate the total DRP1 levels and translocation to the mitochondria. Data are displayed as bar graphs with SEM (A) or scatter dot plots with SEM (C-D) and statistical significance was calculated using the two-way ANOVA test with Sidak's multiple comparisons test (B) or nonparametric Mann-Whitney test (C-D), $*p < 0.05$.

6.1.2. Reduced MERCS correlate with reduced GDAP1 expression

Based on previous reports that not only mitochondrial shape but also the abundance of mitochondria-ER contact sites (MERCS) are affected by an altered GDAP1 expression, we sought to determine the MERCS appearance and the Ca^{2+} -signaling from the ER to the mitochondria (Pla-Martín et al., 2013). While MERCS describe the structural appearance, the term mitochondria-associated membranes (MAMs) rather describes the composition of lipids and proteins (Giacomello and Pellegrini, 2016) and I will henceforth follow these definitions. Pla-Martín et al. reported GDAP1 localization in the MAMs and observed reduced ER-mitochondrial colocalization in GDAP1 KD cells (Pla-Martín et al., 2013). At sites of proximity, the abundance of these contact sites can also affect the mitochondrial shape by encircling and constricting the mitochondria even prior to DRP1 recruitment to the OMM (Friedman et al.,

Results

2011). To explain the mitochondrial shape and evaluate the Ca^{2+} signaling between these organelles in GDAP1 KD cells, I analyzed mitochondria-ER contact sites using electron microscopy images in both cell lines. Previous analyses of these images revealed that the contact sites reduce in number upon GDAP1 silencing. Further evaluations of these electron microscopic images additionally demonstrated that though the MERCS' length was not affected, the width was increased upon reduction of GDAP1 expression (Figure 9B). Accordingly, the FEMP probe was used to confirm the observed alterations of the contact sites in living cells (Csordás et al., 2010; Naon et al., 2016). The plasmid encodes a YFP-linked OMM protein Akap1 and a CFP-conjugated ER-resident protein Sac1, as well as a fused FK506 binding protein (FKBP) and FKBP-*rapamycin* binding domain (FRB) domain respectively. ER- and mitochondrially targeted proteins are joined by a T2A site (Thosea asigna virus 2A peptide;) with a self-cleavage activity to ensure an expression of both organelle-bound proteins in equivalent amounts (Naon et al., 2016; Szymczak and Vignali, 2005). Upon close proximity of these proteins, a FRET signal can be measured (Figure 9C) (Csordás et al., 2010; Naon et al., 2016). The FRB and FKBP domains can form heterodimers upon *rapamycin* (*rapa*) treatment (Csordás et al., 2010; Naon et al., 2016). In steady-state, there was no difference between Ctrl and KD cells. After treatment with *rapamycin* to induce dimerization there was a clear increase in the FRET ratio in both cells. However, the KD cells showed a significantly lower signal here compared to the control, supporting the previous finding of an increased distance between the two organelles in KD cells (Figure 9C). Because GDAP1 as a GST was confirmed to bind the GST-binding substrate *ethacrynic acid* (Googins et al., 2020), we also raised the question if GDAP1 may also affect the MERCS' occurrence in dependence of its EA binding ability and GST activity. However, both under basal conditions and upon *rapamycin* treatment, there was no effect of this substrate on MAM abundance in the two cell lines, indicating that the MERCS' width in GDAP1 KD cells is not caused by a GST-linked function of GDAP1. To elucidate if this phenotype impairs the Ca^{2+} transport from the ER to the mitochondria, we did further investigations. Firstly, the Ca^{2+} signaling was measured with *aequorin* luminescence upon stimulation of Ca^{2+} transfer in MERCS by *carbachol* (CCH). Upon Ca^{2+} binding of the *aequorin* photoprotein, blue light is emitted which can be photometrically measured with a luminometer (Ottolini et al., 2014; Whitaker, 2004). CCH stimulates IP3 production, leading to IP3R activation and in turn to subsequent Ca^{2+} release into the MERCS, which is rapidly taken up by mitochondria (Van Acker et al., 2002; White and McGeown, 2002). *Digitonin* was added to provide calibration of luminescent signal into Ca^{2+} through an established equation (Figure 9D) (Brini et al., 1995). Surprisingly, there was a trend towards elevated basal $\text{cyt}[\text{Ca}^{2+}]$ concentration in KD cells. The incline of $\text{cyt}[\text{Ca}^{2+}]$ upon CCH addition was lower in KD cells as well as the AEQ peak, which

Results

was significantly reduced compared to Ctrl, implying that less cytosolic Ca^{2+} was bound by the AEQ (Figure 9E-F). This could be due to either more Ca^{2+} taken up by the mitochondria or less Ca^{2+} being released by the ER. To determine the amount of Ca^{2+} taken up by mitochondria upon CCH addition, equal experiments with mitochondrial aequorine (mtAEQ) were performed, which is targeted to the inner mitochondrial membrane. This approach showed that mitochondrial Ca^{2+} levels were not largely affected in these cells upon CCH addition (Figure 9G).

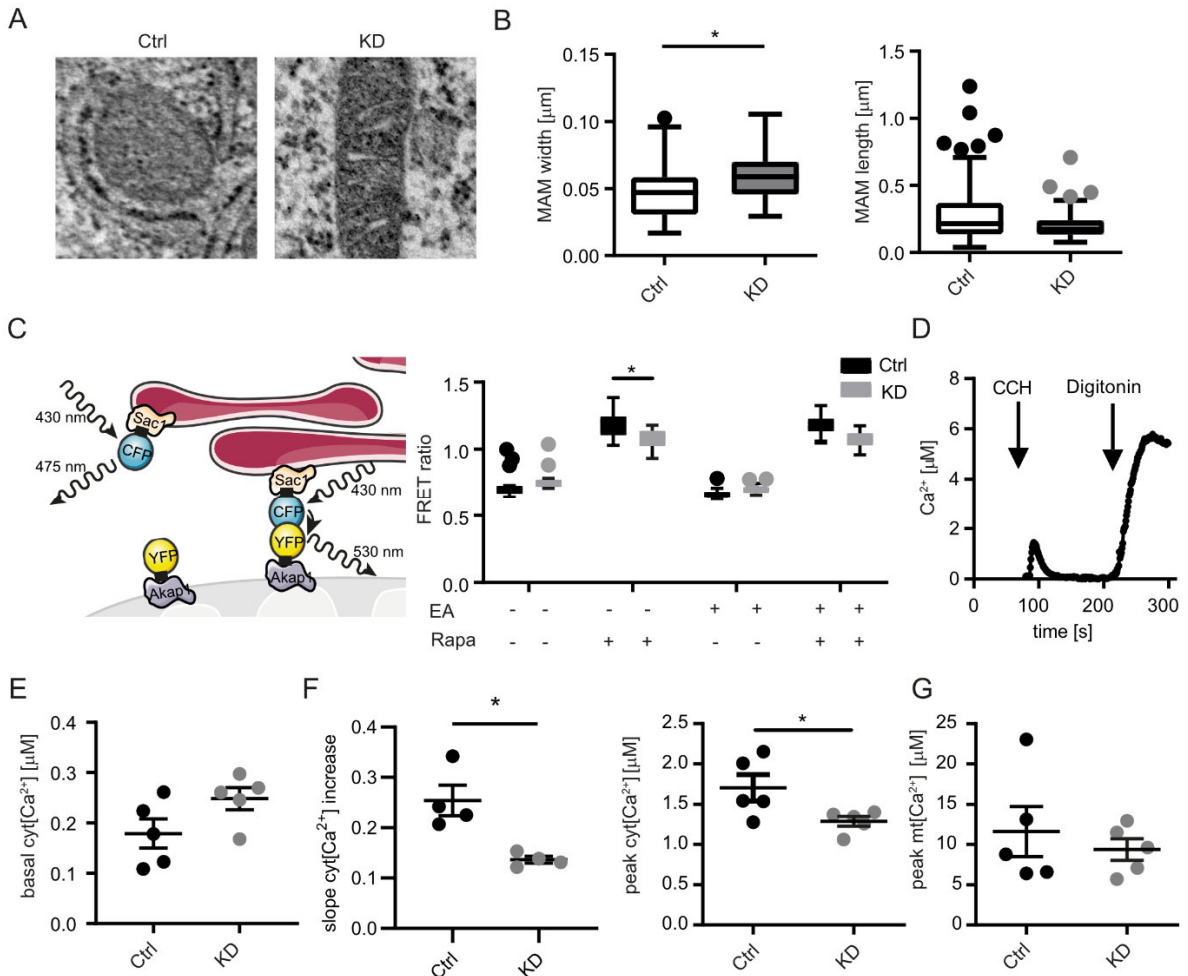


Figure 9 Reduced MERCS correlate with reduced GDAP1 expression

Analysis of the mitochondria-ER contact sites A) Magnification of representative TEM images of Ctrl and GDAP1 KD cells showing a mitochondrion in proximity to the ER n=123 (Ctrl) n=60 (KD) B) Analysis of contact sites in length and width between the organelles n=122 (Ctrl) n=59 (KD) C) Scheme of the FRET-FEMP sensor; the plasmid encodes for CFP- and YFP labeled ER- and mitochondria targeting proteins, Sac1 and Akap1, respectively. Only a close proximity of both organelles leads to the high intensity of YFP_{FRET} -emission (410-430/520-560 ex/em). Rapamycin (rapa) and ethacrynic acid (EA) were added in a final concentration of 100 nM and 30 $\mu\text{g}/\text{ml}$ respectively and results were calculated as $\text{YFP}/\text{CFP}_{\text{FRET}}$ intensity (in quintuplicates each). D) Representative curve for the Ca^{2+} measurement, which was acquired with a luminometer. CCH was added in a final concentration of 200 μM , Digitonin 100 μM E) Quantification of basal $\text{cyt}[\text{Ca}^{2+}]$ levels showed a slight increase of levels in KD cells, n=5 (in triplicates each) F) Slope of cytosolic Ca^{2+} increase upon CCH addition. $\text{Cyt}[\text{Ca}^{2+}]$ was significantly reduced in GDAP1 KD cells upon CCH addition and Ca^{2+} release from the ER, n=5 (in triplicates each) G) Mt $[\text{Ca}^{2+}]$ uptake upon CCH addition did not change remarkably in either cell line, n=5 (in triplicates each). Data are displayed as Tukey's box and whiskers plots (B-D) or scatter dot plots with SEM (E-G); statistical significance was calculated using nonparametric Mann-Whitney test (B; E-G) or Sidak's multiple comparisons test, * $p < 0.05$.

Results

Here, a cytosolic Ca^{2+} phenotype was identified in the KD cells as well as impaired mitochondria-ER contacts and a probably less active IP3R, judging from the slower Ca^{2+} release from the ER. However, we did not detect significant differences in the mitochondrial Ca^{2+} uptake upon CCH stimuli. The aequorin assay cannot be used to quantify steady-state mitochondrial Ca^{2+} levels and we thus addressed ER- and mitochondrial Ca^{2+} channels enriched in MAMs to evaluate if the main proteins routing the Ca^{2+} from the ER to the mitochondria are differently expressed in GDAP1 KD cells.

6.1.3. Altered MCU expression in KD cells

Since mitochondrial morphology, DRP1 activity, and mitochondrial Ca^{2+} uptake are tightly connected mechanisms, I continued with further investigation on Ca^{2+} signaling proteins of the two main intracellular Ca^{2+} stores, the ER and mitochondria (Kowaltowski et al., 2019; Rizzuto et al., 2012). Mitochondria are not only indispensable Ca^{2+} stores in the cell, but Ca^{2+} ions also regulate several processes inside the mitochondrial matrix (Rizzuto et al., 2012). I continued to investigate Ca^{2+} transport proteins of mitochondria, since a change of mitochondrial morphology can impair Ca^{2+} uptake and intracellular Ca^{2+} regulation (Kowaltowski et al., 2019). Kowaltowski et al. observed an increased Ca^{2+} uptake capacity in mitochondria both after pharmacologically inducing mitochondrial fusion and after the expression of a dominant-negative DRP1 protein (Kowaltowski et al., 2019). Fused mitochondria, in contrast, revealed lower steady-state mitochondrial Ca^{2+} levels (Kowaltowski et al., 2019). Furthermore, MERCS appearance and abundance is a crucial factor for mitochondrial Ca^{2+} levels and we observed a clear difference in the distance of mitochondria and ER, as well as altered cytosolic Ca^{2+} kinetics upon CCH addition. Hence, I quantified expression levels of proteins implicated in the Ca^{2+} signaling machinery in total cell lysates. Interestingly, we found a significant upregulation of the mitochondrial calcium uniporter (MCU), a Ca^{2+} channel located in the inner mitochondrial membrane regulating the Ca^{2+} influx into the matrix (Figure 10A) (Mishra et al., 2017). The MCU is assumed to collaborate with the outer mitochondrial membrane protein VDAC1, the voltage-dependent anion channel 1, to maintain mitochondrial Ca^{2+} homeostasis (Xu et al., 2018). However, the KD cells did not show any variation of VDAC1 expression level compared to Ctrl (Figure 10B). Both VDAC1 and MCU are known to regulate the Ca^{2+} transport into the mitochondria, with VDAC1 being enriched in mitochondria-ER contact sites (MERCS) and interacting with the ER-bound IP3R and the glucose-regulated protein (Grp75), the stabilizing protein of this complex (Szabadkai et al., 2006). The MCU upregulation could be compensating the altered proximity of the MERCS yielding a more effective Ca^{2+} import into the mitochondria. However, protein levels of the IP3R and Grp75 did not vary in these cells (Figure 10C-D). As

Results

reported recently, SH-SY5Y cells with a GDAP1 KD as well as motoneurons of GDAP1 KO mice show reduced SOCE-driven Ca^{2+} entry and altered steady-state cytosolic Ca^{2+} levels (Barneo-Muñoz et al., 2015; Pla-Martín et al., 2013).

The increase of MCU expression together with the morphological implications of mitochondria and MERCS in particular pointed towards alterations in Ca^{2+} signaling. However, the similar $\text{mt}[\text{Ca}^{2+}]$ increase between Ctrl and KD can thus be explained by the elevated MCU levels, trying to provide an efficient Ca^{2+} import into the mitochondrial matrix.

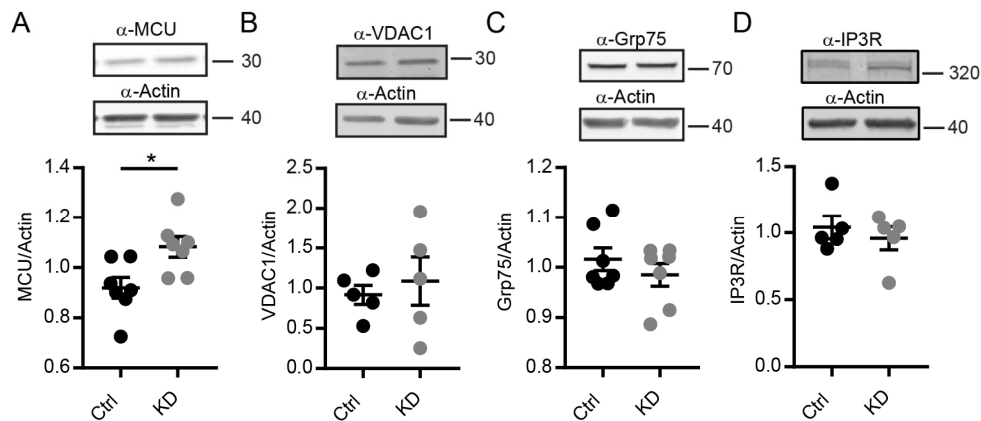


Figure 10 Altered MCU expression in GDAP1 KD cells

IB quantification of whole-cell lysates of Ctrl and GDAP1 KD cells for A) MCU B) VDAC1 C) Grp75 D) IP3R; actin was used as housekeeping gene for normalization, data are displayed as scatter dot plot with SEM and statistical significance was calculated using nonparametric Mann-Whitney test, * $p < 0.05$.

6.1.4. Increased calcineurin expression does not cause the mitochondrial shape phenotype in KD cells

We suspected that the elevated cytosolic Ca^{2+} levels could also be a leading cause of the altered mitochondrial shape in GDAP1 KD cells. As DRP1-induced fission was reduced upon GDAP1 KD, we analyzed the upstream phosphatase Calcineurin, whose activation is strongly Ca^{2+} -dependent (Cereghetti et al., 2008; Gurda et al., 2018). The cytosolic calcium/calmodulin-activated serine/threonine protein phosphatase calcineurin (CaN) dephosphorylates the GTPase DRP1 at Ser637 to induce the migration to the mitochondria and their fragmentation, making it a central regulator of the fusion and fission machinery (Cereghetti et al., 2008; Gurda et al., 2018).

Evaluating the levels of CaN normalized to actin revealed a significant increase of expression in the KD cells compared to the Ctrl (Figure 11A). Another target of CaN is the transcription factor NFAT (Feske et al., 2007; Molkentin, 2004). Once NFAT is dephosphorylated and activated, it translocates to the nucleus and initiates the transcription of various genes

Results

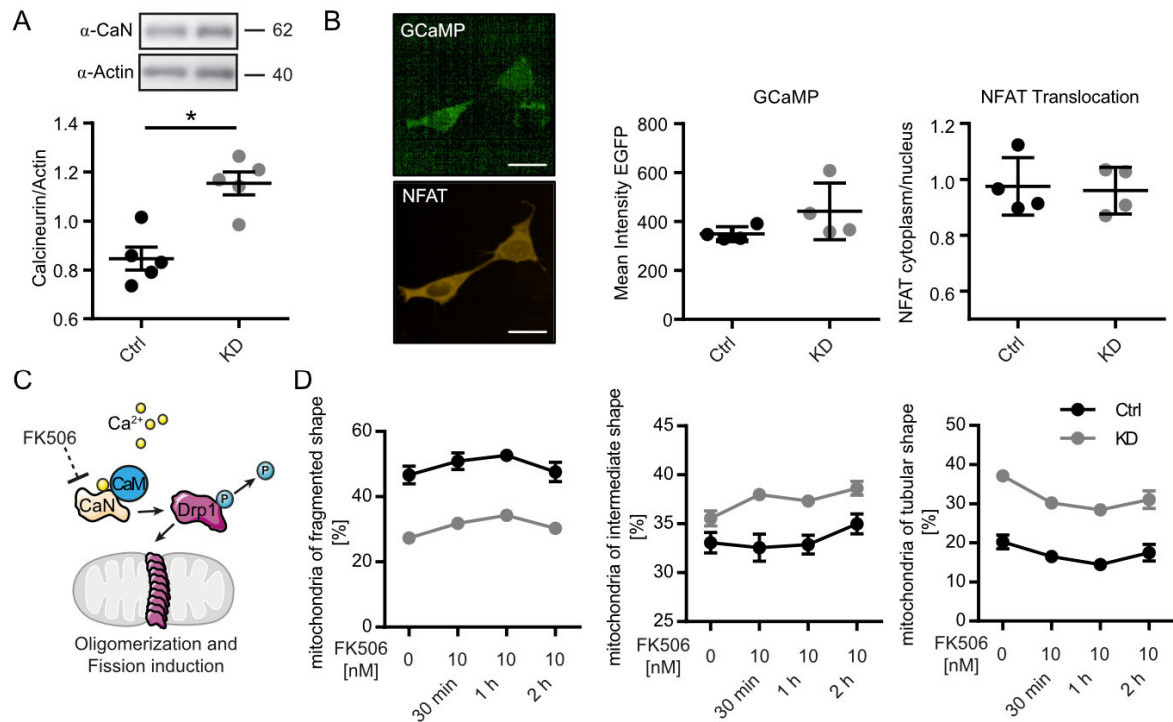


Figure 11 Increased CaN expression does not cause the mitochondrial shape phenotype in GDAP1 KD cells

A) IB of whole-cell lysates against CaN and actin for normalization, n=5 B) Live cell imaging of transfected cells with NFAT-GCaMP plasmid to quantify NFAT translocation to the nucleus and $\text{cyt}[\text{Ca}^{2+}]$ in the Ctrl vs KD cells. The analysis was performed with the Columbus analysis software. Nuclei were counterstained with Draq5; n>200 cells in 4 independent experiments C) Schematic illustration of CaN inhibition; CaM and Ca^{2+} -induced activation of CaN leads to dephosphorylation of DRP1 S637 and binding of DRP1 to its specific outer mitochondrial membrane receptors, where it forms oligomers, allowing fission of this mitochondrion. FK506 binds its intracellular immunophilin receptor FK506-binding protein of 12 kDa (FKB12), interacts with CaN, which is in turn unable to bind its substrates. CaN – calcineurin, CaM – calmodulin D) High content microscopy of live cells yielding mitochondrial classification of SH-SY5Y by staining with MitoTracker™ Green FM; nuclei were counterstained with H \ddot{o} chst; experiments were performed in triplicates, n>13,000 cells per condition in 3 independent experiments; data are displayed as scatter dot plot with SEM or as an XY graph with SEM and statistical significance was calculated using nonparametric Mann-Whitney test, *p<0.05.

encoding for immune response and protection from oxidative stress (Molkentin, 2004). Thus, we also addressed the NFAT translocation together with the cytosolic Ca^{2+} levels by transiently transfecting the GCaMP-NFAT sensor, encoding for a Ca^{2+} -binding cytosolic GCaMP protein conjugated with an EGFP sequence and a fluorescently labeled NFAT protein. Microscopic images were acquired via high-content microscopy and analyzed for the Ca^{2+} -GCaMP intensity in the cytosol and the NFAT translocation to the nucleus (Figure 11B). We neither saw a difference in NFAT translocation, nor in the cytosolic Ca^{2+} levels, which is in contrast to the previous findings using the AEQ sensor. However, the poor transfection efficiencies and the lower sensitivity of the detection compared to the luminometer should be considered here. The increased CaN levels could also be a compensatory effect of the DRP1 dysregulation and maybe the cell is trying to force DRP1 migration to the mitochondria.

Results

The mechanism of CaN-DRP1-induced mitochondrial fission is illustrated in Figure 11C. The activity of CaN is mainly regulated by cytosolic Ca^{2+} levels and one of its main targets is the GTPase DRP1, which is dephosphorylated and thereby activated to induce mitochondrial fragmentation (Cereghetti et al., 2008). To address the question if inhibition of CaN might have an effect on the mitochondrial shape in our cells, we decided to inhibit CaN with the pharmacological inhibitor tacrolimus (FK506) and to observe the change of mitochondrial morphology over time in the KD cells with their respective control cell line (Figure 11D) (Dumont, 2012; Kawamura and Su, 1995). The cells were treated with 10 nM FK506 for 30 min, 1 h and 2 h. Figure 11D shows the percentages of fragmented, intermediate, or tubular mitochondria in GDAP1 KD and control cells. Surprisingly, the percentages dropped down from 37 to 31 % cells with tubular mitochondria for the KD cells, compared to the control, which declined to 17 %. Thus, the mitochondrial shape changed dose-dependently, but it did not vary between the two cell lines. We concluded that there are distinct mechanisms other than CaN dysregulation implicated in the observed distorted mitochondrial shape.

6.1.5. Proteomic analysis of isolated mitochondria and MAMs

Accumulation and arrangement of specialized proteins in the MAMs is crucial for the optimized Ca^{2+} exchange and lipid transfer between mitochondria and the ER (Lee and Min, 2018). A proteomic approach of isolated mitochondria and MAMs served to investigate if GDAP1 KD alters the composition and protein levels in these fractions. A colleague in our laboratory isolated mitochondria and MAMs as described in Figure 12A from Ctrl and GDAP1 KD cells in order to determine any kind of alteration of the proteome upon GDAP1 silencing. The purity of the fractions was successfully confirmed via western blotting by colleagues and I will here shed light on the analysis and describe the findings of mass spectrometric analyses of these fractions. The fractions of crude mitochondria contained the organelle components that were further processed to obtain purified mitochondria and MAMs for liquid chromatography-mass spectrometry (LC-MS) (Figure 12A). The KD of GDAP1 was confirmed and furthermore, its presence in MAMs was also verified here. VDAC1-3 as an important mitochondrial Ca^{2+} import channel was enriched to a high extent in all three fractions, but without any obvious differences between Ctrl and KD. In contrast to the IB analyses, MFF and DRP1 did not show any regulation, similar to MFN1 and MFN2. DRP1 was not detected in the MAM fractions and hence not included in the graph (Figure 12D).

Results

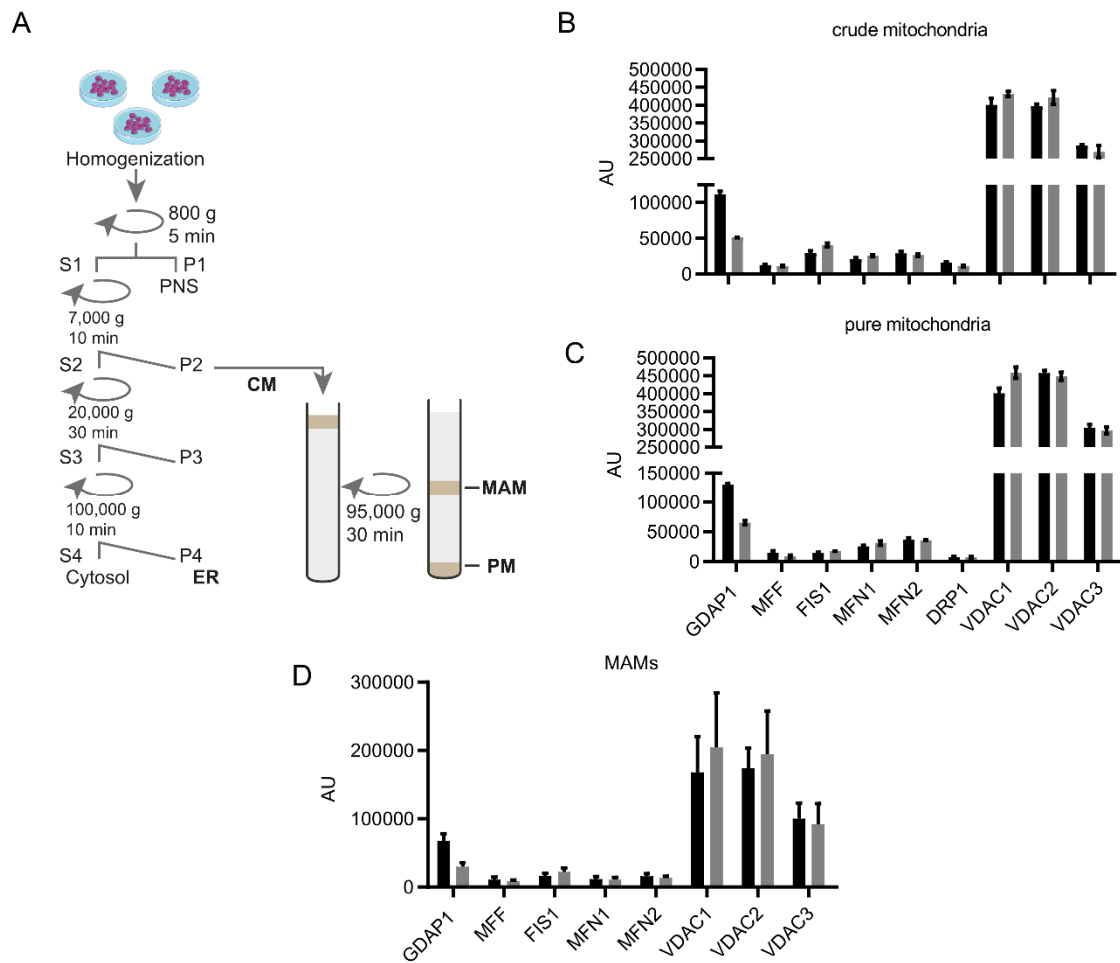


Figure 12 Expression pattern of proteins involved in mitochondrial dynamics

A) Schematic illustration of the enrichment of analyzed cellular fractions. CM – crude mitochondria; PM – pure mitochondria; MAM – Mitochondria-associated membrane. Abundance in [AU] of proteins implicated in mitochondrial dynamics after liquid chromatography-mass spectrometry analysis of the cellular fractions B) crude mitochondria C) pure mitochondria or D) MAMs. Data are displayed as bar graphs with SEM and were from three independent experiments. Statistical significance was calculated with the nonparametric t-test in combination with Bonferoni correction. * $p < 0.05$.

Furthermore, various proteins controlling metabolic processes were detected and showed an altered expression level in the KD cells in crude or pure mitochondria. Since such metabolic proteins were poorly enriched in the MAM fraction, I only concentrated on the crude and pure mitochondrial fractions (Figure 13). There were neither differences for the hexokinases (HK1/2) nor for the lactate dehydrogenase A (LDHA), which preferentially converts pyruvate to lactate. LDHB in contrast, which has a higher affinity for lactate, converting it to pyruvate and NAD^+ to NADH (Urbańska and Orzechowski, 2019), showed a tendency towards a lower expression. The imported pyruvate is converted to acetyl-CoA via the pyruvate dehydrogenase complex (PDC), which is composed of three subunits. The PDH E1 and E3 (DLD, Dihydrolipoyl-Dehydrogenase) subunits were not clearly regulated in the KD cells. The citrate synthase (CISY) was also detected, which converts acetyl-CoA to citrate to either enter the TCA cycle

Results

or to be shuttled out of the mitochondrion to be further used for fatty acid synthesis. It is slightly increased in the GDAP1 KD cells, though not statistically significant yet in both crude and pure mitochondrial fractions. 2-oxoglutarate dehydrogenase (ODO1) generates succinyl-CoA from α -ketoglutarate and the KD cells appeared to have elevated levels here, as well. The conversion of glutamate to α -ketoglutarate is processed by the glutamate dehydrogenase (GDH), which is also increased in the KD cells. Taken together, the findings of this proteomic approach revealed that GDAP1 KD cells have a higher demand for citrate for either fatty acid production or mitochondrial ATP production via oxidative phosphorylation. This could be a compensatory response to an impaired mitochondrial ATP production. The elevated GDH levels could be in line with this – to consume glutamine and glutamate more efficiently to supply the TCA cycle with α -ketoglutarate.

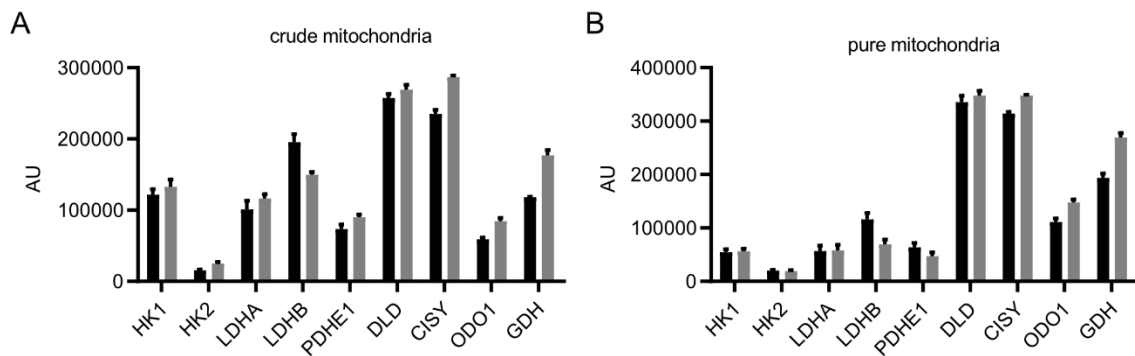


Figure 13 Expression levels of metabolic proteins implicated in TCA cycle, glycolysis and glutaminolysis are altered in GDAP1 KD cells

Mass spectrometric analyses of crude (A) and pure (B) mitochondrial fractions revealed a dysregulation of proteins regulating glucose, pyruvate, or glutamine metabolism. Data were from three independent experiments and displayed as bar graphs with SEM. Statistical significance was calculated with the nonparametric t-test in combination with Bonferroni correction. * $p < 0.05$.

6.1.6. Increased glutaminolysis but reduced fatty acid synthesis upon GDAP1 KD

According to the analysis of the proteomic approach, we began investigating the metabolic pattern and mitochondrial ATP production in GDAP1 KD cells compared to the control.

The majority of ATP is produced via oxidative phosphorylation, driven by the mitochondrial membrane potential (Bender and Martinou, 2016; Capaldi et al., 1994; Jonckheere et al., 2012). The mitochondrial membrane potential ($\Delta\psi_m$) was measured with the fluorescent dye tetramethylrhodamine (TMRM) in non-quenching mode (Perry et al., 2011). Its accumulation in the mitochondrial matrix is dependent on the membrane potential – the higher it is, the higher fluorescence intensity can be detected. Compared to the Ctrl cells, the KD cells had a significantly higher mitochondrial membrane potential (Figure 14A). Previous data generated

Results

in our group showed that cells lacking GDAP1 have a higher oxygen consumption. We therefore measured changes in membrane potential upon addition of oligomycin (Omy), an inhibitor of the ATP synthase, which leads to an increase of the membrane potential (Joshi and Bakowska, 2011; Ruas et al., 2016). To verify the TMRM signal, the cells were treated with the uncoupler FCCP and a rapid decline of the signal was observed (Figure 14B) (Joshi and Bakowska, 2011). There was no difference, neither in the maximum signal upon Omy addition nor in the slope of the signal increase between both cell lines. Blue native polyacrylamide gel electrophoresis (PAGE) of isolated mitochondria was performed to examine the complex formation of the electron transport system complexes (Figure 14C). Via blue native PAGE, proteins in their native structure can be separated based on protein size and hydrophobicity (Schägger and von Jagow, 1991). Digitonin was chosen as a mild detergent to dissolve mitochondrial membrane proteins without affecting the intermolecular bindings between the proteins. The IB membranes were stained for subunits of each complex I-IV as well as ATP5, the ATP synthase subunit 5. Alterations in complex size, supercomplex formation or a complete absence of a complex can indicate an inefficient complex arrangement impairing the mitochondrial respiratory function (Jha et al., 2016; Konovalova, 2019). However, there were no differences in the complex formation of the electron transport system complexes. Another parameter of mitochondrial function is ATP generation as a direct mitochondrial product resulting primarily from oxidative phosphorylation. Thus, we measured the ATP levels with the luminescent BTeam sensor via transient transfection of the cell lines (Yoshida et al., 2016). It integrates an ATP-binding unit, a yellow fluorescent protein (YFP), as well as an ATP-independent luciferase (nLuc) (Yoshida, Kakizuka, & Imamura, 2016). Upon ATP binding and in presence of nLuc substrate, bioluminescence resonance energy transfer (BRET) takes place, which leads to a change in emission spectra for nLuc and YFP. The biosensor carries either no targeting sequence or a mitochondrial targeting sequence for quantifying cytoplasmic and intramitochondrial ATP levels, respectively and the data were expressed as BRET ratio, YFP/nLuc luminescence ratio. While cytosolic ATP levels were constant between Ctrl and KD cells, mitochondrial ATP was significantly reduced in KD cells (Figure 14D). Hence, we measured ATP production over time after treating the cells with the glucose antimetabolite 2-Deoxyglucose (2-DG) as a substitute for glucose (Yetkin-Arik et al., 2019). This allowed us to evaluate the non-mitochondrial ATP production since the 2-DG inhibits glycolysis by irreversibly binding hexokinase (Zhong et al., 2009). As illustrated in Figure 14E, there is a

Results

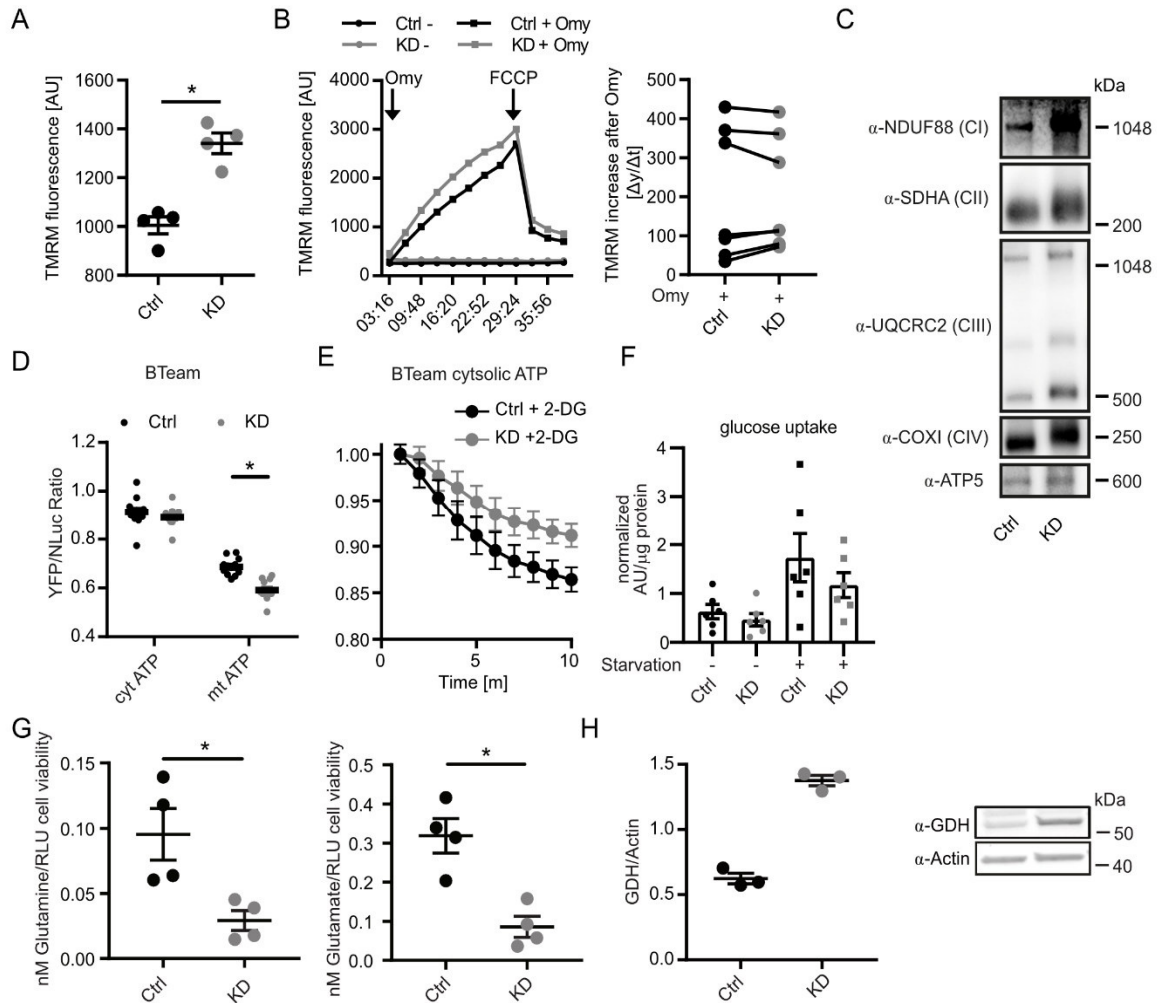


Figure 14 Increased glutaminolysis upon GDAP1 KD

A) SH-SY5Y cells were stained with TMRM, an indicator for mitochondrial membrane potential and nuclei were counterstained with Höchst. Image acquisition was performed with the high content microscope by Perkin Elmer™. Steady-state mitochondrial membrane potential ($\Delta\psi_m$) was significantly increased in GDAP1 KD cells, $n=4$ (in triplicates each) B) Example curve of both cell lines showing the increase of $\Delta\psi_m$ after Omy addition in a concentration of $2 \mu\text{g}/\mu\text{l}$ and decrease after addition of the uncoupler FCCCP ($1 \mu\text{M}$). The slope of the $\Delta\psi_m$ increase was not different between Ctrl and GDAP1 KD cells. The $\Delta\psi_m$ of untreated cells did not change over time, $n=6$. C) Blue native PAGE of isolated mitochondria for analysis of the integrity of respiratory system complexes, which did not show any differences between the cell lines. C) Cells were transfected with the BRET-BTeam plasmid. Upon ATP binding, the YFP/NLuc luminescence ratio increases and gives evidence for the respective ATP levels, both cytosolic and mitochondrial. Here, GDAP1 KD cells revealed lower mitochondrial ATP levels, $n=12$. E) Cytosolic ATP production after 2-DG addition ($25 \mu\text{M}$) as a glucose analog to inhibit glycolysis. Less cytosolic ATP reduction in KD cells indicated higher mitochondrial ATP generation in KD cells, $n=6$. F) Glucose uptake was measured after incubation of the fluorescent glucose analog 2-NBDG. Starved cells were incubated with PBS for 20 min prior to the addition of 2-NBDG. The glucose uptake did not vary significantly between the Ctrl and GDAP1 KD cells, $n=6$ (in triplicate each) G) Glutamine and Glutamate levels were determined by a luminescence-based assay and revealed a significant reduction of both glutamine and glutamate levels in GDAP1 KD cells after normalization of the signal to the cell number calculated with a viability assay (each experiment was done in triplicates) H) IB quantification of GDH expression levels normalized to actin indicated elevated GDH levels in GDAP1 KD cells, $n=3$. Data are displayed as scatter dot plots with SEM, XY graph (B) with SEM (E) and statistical significance was calculated using the nonparametric Mann-Whitney test (B,G-H), two-way ANOVA with Sidak's multiple comparisons test (D) or the two-way ANOVA with Tukey's multiple comparisons test (F), $*p<0.05$.

Results

clear reduction of cytosolic ATP production over time in the Ctrl cells, but surprisingly less in the KD cells – indicating that these cells either have a higher glycolytic capacity or rely less on glycolysis. The observation of presumably more ATP production besides glycolysis made me investigate the glucose uptake of these cell lines with the fluorescent glucose analog 2-NBDG (Figure 14F) (Zou et al., 2005). Under basal culture conditions, the glucose uptake itself showed a tendency towards reduced glucose uptake in GDAP1 KD cells, though not statistically significant. Expectedly, with prior nutrient starvation with PBS for 20 minutes before the addition of the fluorescent glucose analog 2-NBDG, there was an increased glucose uptake observed in both cell lines, though the values had a high heterogeneity in both.

Glutamine can substitute glucose in supplying α -ketoglutarate to the TCA cycle (Figure 2). The glutamate dehydrogenase (GDH) catalyzes the production of α -ketoglutarate from glutamate, after glutaminase-driven conversion of glutamine (Vacanti et al., 2014). Therefore, I quantified both glutamine and glutamate concentrations, as well as the expression levels of GDH. Glutamine and glutamate were both measured with a luminescent Luciferase-based assay performed after cell lysis. The values were normalized to the luminescence signal of a cell viability assay that was performed beforehand to diminish any variations caused by different cell numbers. In our cells, both glutamine and glutamate concentrations were reduced significantly in the KD cells, confirming the hypothesis of compensated glutamine uptake to fuel mitochondrial energy production via OXPHOS. In line with these findings, we observed significantly higher GDH expression levels in the KD cells compared to control cells. Hence, the glutaminolysis pathway seems to be upregulated to compensate the lack of pyruvate entering the TCA and to meet the cell's energy demand.

Citrate, which does not enter the TCA, is shuttled out of the mitochondria into the cytosol, where it can further contribute to fatty acid production, as illustrated in Figure 2 (Menendez and Lupu, 2007). If less pyruvate enters the mitochondrial matrix or if less pyruvate is converted to acetyl-CoA, there may also be an impairment of fatty acid production. Alternatively, a shift towards β -oxidation of fatty acids could favor the production of acetyl-CoA, entering the TCA cycle (Watmough et al., 1989). Interestingly, Rambold et al. observed a pronounced β -oxidation of fatty acids in elongated mitochondria rather than in fragmented (Rambold et al., 2015). Therefore, I now focused on the synthesis of fatty acids and the transition of such to the mitochondria upon starvation.

I performed live cell imaging of Bodipy™ 558/568 C₁₂ stained cells – a fluorescent fatty acid for visualizing cytosolic spots of lipids. Besides basal conditions, the cells were also starved of nutrients by substituting normal growth medium with HBSS medium for indicated time intervals before imaging. Starvation can induce catabolic pathways and β -oxidation of fatty acids in order to produce ATP due to the lack of glucose or glutamine as primary energy supply

Results

(Rambold et al., 2015). This effect should increase with time of starvation, which was verified in the experiment (Figure 15A). Analysis of the spot size of each cell did not reveal any difference, but the number of spots per cell was significantly decreased in the KD cells (Figure 15B-C). There was a significant increase in signal upon 24 hours of starvation for both parameters, but not after 6 hours. These changes were similar in both cell lines. Also, the translocation of the fatty acids to the mitochondria and the cytoplasmic Bodipy™ intensity were elevated after 24 of hours of starvation, but not impaired in the KD cells in comparison to the control (Figure 15D-E).

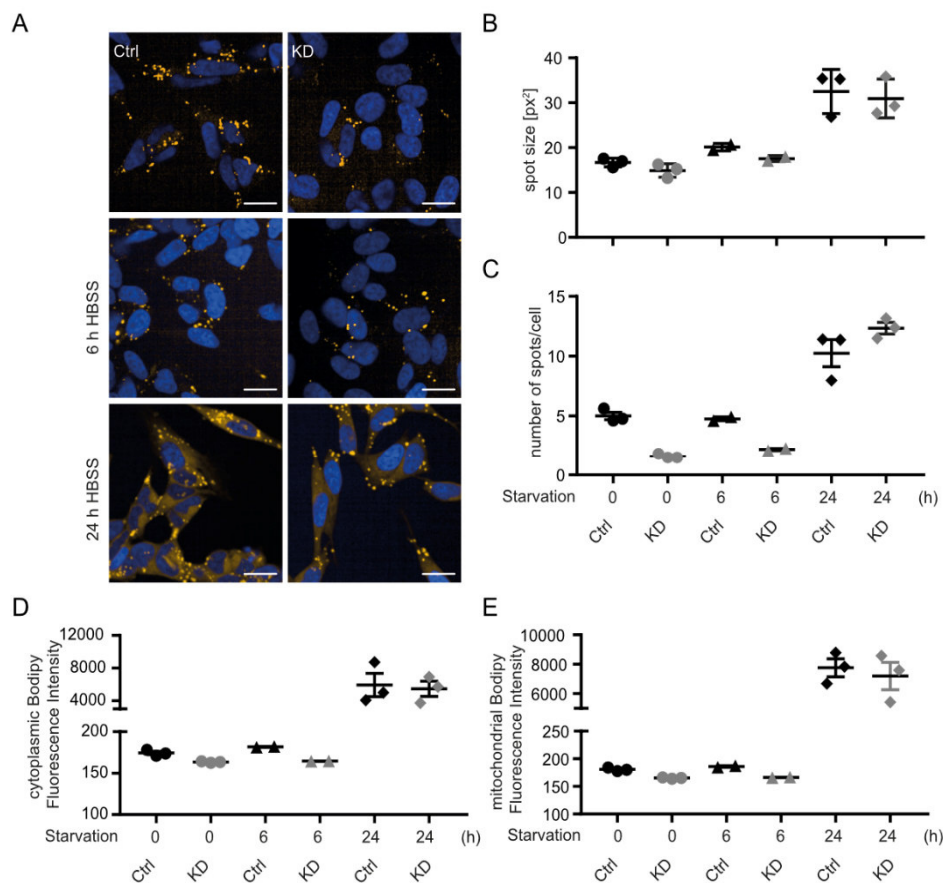


Figure 15 Reduced fatty acid synthesis upon GDAP1 KD

SH-SY5Y cells were stained with Bodipy™ and Mito Tracker™ Green FM and live cell imaging was performed with the Opera Phenix™ high content microscope. Nuclei were counterstained with Hoechst and starvation with HBSS was performed as indicated. A) Representative images of respective cell lines and conditions, scale bar refers to 20 μ m B) Spot size analysis of lipid droplets neither showed a difference between the cell lines under basal conditions nor under starvation. C) The number of Bodipy™-positive spots was significantly reduced in GDAP1 KD cells D) Bodipy™ intensity in the cytosol or in D) mitochondria did not vary between the cell lines. Data were from >10000 cells in total and were analyzed in 3 or 2 (6 h starvation) independent experiments. Data are displayed as scatter dot plots with SEM and statistical significance was calculated using one-way ANOVA. Each data point corresponds to the mean of the replicates in one experiment, * $p < 0.05$.

Altogether, a loss of GDAP1 expression resulted in a dysregulation of mitochondrial ATP generation. KD cells exposed a decreased glycolytic capacity and a strengthened glutaminolysis, which eventually leads to lower mitochondrial ATP levels. Fatty acid synthesis

Results

is also reduced significantly, but there is presumably no difference in β -oxidation of fatty acids in steady-state or upon starvation.

6.1.7. GDAP1 silencing leads to reduced pyruvate conversion by an inactive PDH

The AMP-activated protein kinase (AMPK) is a central regulator of the cell metabolism to adjust main cellular processes such as autophagy and energy production (Garcia and Shaw, 2017). Thus, in response to any kind of energy stress and an altered AMP:ATP ratio, its activity has a dramatic influence on the inhibition of anabolic cellular processes to initiate catabolic reactions that help to restore the energy levels of the cell (Garcia and Shaw, 2017). AMPK activation has also been proven to have a triggering effect on MFF upon phosphorylation, initiating mitochondrial fission (Toyama et al., 2016). This process of mitochondrial degradation goes along with PGC1 α activation, promoting mitochondrial biogenesis, most likely to improve mitochondrial ATP production (Jäger et al., 2007). Interestingly, Lassiter et al. observed a downregulation of GDAP1 upon AMPK activation (Lassiter et al., 2018). Paired with the decreased fatty acid synthesis and less mitochondrial ATP supply of the cell, and with the reported connection between AMPK activity and GDAP1 translation (Lassiter et al., 2018), we suggested that the AMPK activity may be altered compared to the Ctrl cells. Since these core processes are impaired in our cells, we sought to evaluate the activity of AMPK by addressing I) AMPK activation levels or II) if AMPK inhibition reverses the metabolic outcome in GDAP1 KD cells. Unfortunately, we could not approach the former question by western blotting for phosphorylated AMPK, the active form of this kinase, because we did not find a reliably working antibody. Thus, we decided to inhibit the calcium/calmodulin-dependent kinase kinase 2 (CAMKK β), which – activated by Ca²⁺ – phosphorylates the α -subunit of AMPK (Figure 16A) (Mairet-Coello et al., 2013; Woods et al., 2005). As a reliable readout, we chose to monitor the mitochondrial shape with increasing concentrations of STO609 (500 nM-20 μ M), a compound specifically inhibiting the CAMKK β , one hour before live cell image acquisition (Jin et al., 2009). Indeed, inhibiting AMPK activation with 0.5 μ M did not affect the mitochondrial shape, either in the GDAP1 KD or the control (Figure 16B). Increasing the concentration to 1 μ M showed a shift towards less fission activity and more elongated mitochondria. This effect was more pronounced with increasing STO609-concentrations. Though the mitochondrial shape was affected in a dose-dependent manner, the changes were equal in KD versus control – showing both an increase of around 20 % more cells with tubular mitochondria after 10 μ M STO609. Treating the cells with 20 μ M STO609 possibly had a toxic effect on the cells, since the mitochondrial shape reached a maximum of tubularity for both cell lines (Figure 16B). Judging from these experiments and mitochondrial shape as readout, we did not observe an evident

Results

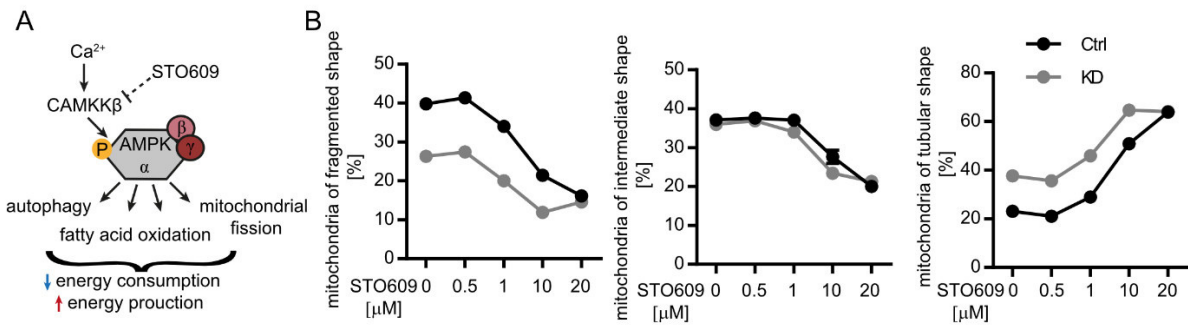


Figure 16 Inhibition of the AMPK signaling pathway does not reverse GDAP1-induced mitochondrial modifications

AMPK is a central regulator of ATP production and consumption. A) Schematic illustration of AMPK function and inhibition with STO609. Ca^{2+} -induced activation of CAMKK β leads to phosphorylation of the α -subunit of AMPK. Upon AMPK activation, pathways starting the ATP production are being triggered, whereas intracellular processes of high energy consumption are arrested. This leads to increased autophagy, fatty acid oxidation or mitochondrial fission. STO609 inhibits the CAMKK β . B) High content microscopy of live cells yielding mitochondrial classification of SH-SY5Y by staining with MitoTracker™ Green FM; nuclei were counterstained with H \ddot{o} chst; $n > 20000$ cells per condition in three independent experiments; data are displayed as XY line with SEM and statistical significance was calculated using two-way ANOVA with Sidak's multiple comparisons test, $*p < 0.05$.

response of GDAP1 KD cells compared to the control cell line.

We then assumed that the metabolic shift towards increased glutamine consumption in GDAP1 KD cells is caused by an altered activity of the Ca^{2+} -inducible pyruvate dehydrogenase (PDH) which converts pyruvate into acetyl-CoA (Figure 17A) (Tovar-Mendez et al., 2003). A reduced pyruvate conversion at this point would also explain the reduced fatty acid levels. The PDH consists of three subunits, PDH E1, E2 and E3, whereof E1 has three phosphorylation sites (Figure 17A) (Tovar-Mendez et al., 2003). The PDH phosphatase subunit 1 (PDP1) dephosphorylates and activates the PDC enzyme in a Ca^{2+} -dependent manner (Roche et al., 2001). To quantify the phosphorylation status of the PDH in our cells, I established Phostag™ blots. It includes protein separation via SDS-PAGE with immobilized Phostag™ acrylamide molecules, which bind phosphorylated proteins; this results in slower migration of the specific protein (Kinoshita et al., 2006). Hence, a separation of phosphorylated and non-phosphorylated protein is achieved. Indeed, the PDH E1 subunit resulted in slower gel migration and revealed an increased phosphorylation state, while its endogenous levels were not altered in normal SDS-PAGE IB (Figure 17B). An increased phosphorylation of PDH E1 subunit serine 293 (S293) was also confirmed using phospho-PDH (S293) antibody (Figure 17C). PDH E3 in contrast, was increased in GDAP1 KD cells compared to the Ctrl (Figure 17D). A decreased activity of the PDH leads to an inefficient conversion of pyruvate into acetyl-CoA, which either inhibits the pyruvate entry into the mitochondria or strengthens the gluconeogenesis under ATP consumption to remove accumulated mitochondrial pyruvate (Bender and Martinou, 2016). This might be an explanation for the deficiency in mitochondrial ATP production and the tremendous shift towards glutaminolysis.

Results

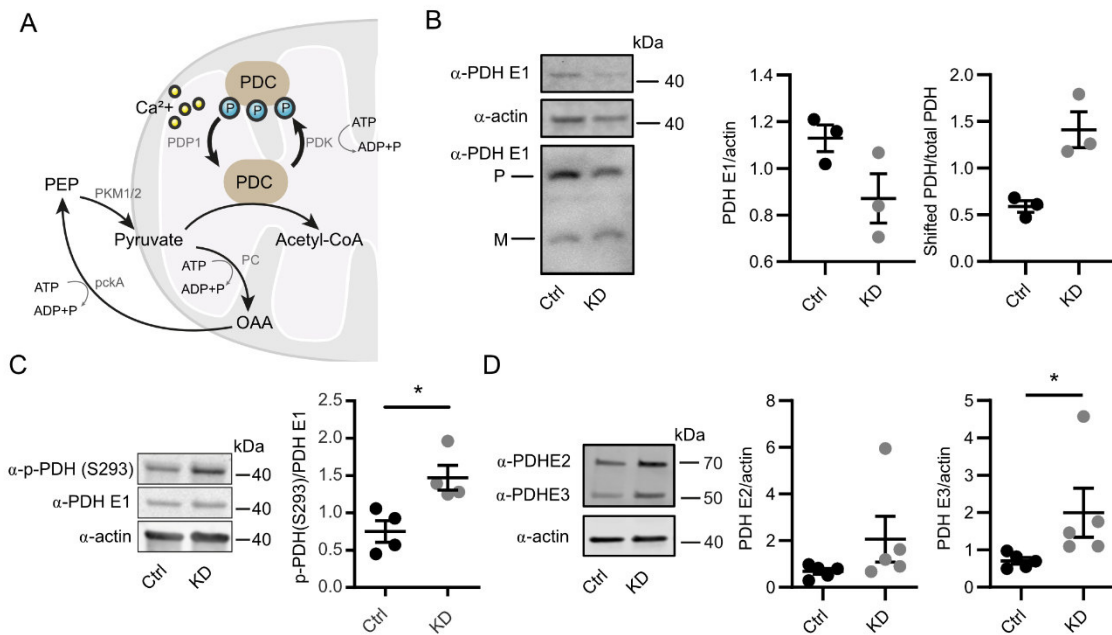


Figure 17 Abundance and activity of the Pyruvate dehydrogenase

A) Schematic illustration of the pyruvate conversion to acetyl-CoA or OAA. Pyruvate can be converted to acetyl-CoA by the active unphosphorylated pyruvate dehydrogenase (PDH). PDH can be phosphorylated by the catalytic activity of the PDH kinase (PDK) under ATP consumption. The PDH phosphatase subunit 1 (PDP1) in turn can dephosphorylate the serine residues upon activation by Ca^{2+} . Acetyl-CoA can now be converted to citrate, which either enters the TCA cycle or shuttled out of the mitochondrion to be converted to Acetyl-CoA and fatty acids. MPC, mitochondrial pyruvate carrier; PDC, pyruvate dehydrogenase complex; PDK1, pyruvate dehydrogenase kinase 1. B) Phostag™ blot against PDH E1 α ; reducing immunoblots served to determine the endogenous levels of PDH E1 α subunit and actin served as loading control. Shifted bands in the Phostag™ blot indicate phosphorylated (P) PDH E1 α , M – unphosphorylated PDH E1 α monomer. C) Immunoblots of Ctrl and KD cell lysates to determine phosphorylation of PDH E1 α subunit. Actin served as loading control and p-PDH (S293) band intensities were normalized to total PDH E1 protein levels. D) Immunoblots of Ctrl and KD cell lysates to determine endogenous levels of PDH E2 and E3 subunit, actin served as loading control. Data are displayed as scatter dot plot with SEM and statistical significance was calculated using nonparametric Mann Whitney test, * $p < 0.05$.

The dysregulations in energy metabolism caused by a reduced expression of the GDAP1 protein are illustrated in Figure 18. A reduced CCH-mediated Ca^{2+} extrusion from the ER into the cytosol through the IP3R was observed, together with elevated MCU protein levels, but no change in mt[Ca^{2+}] upon CCH stimulation. Still, steady-state mt[Ca^{2+}] could be impaired, partly due to the increased distance of MERCS (Figure 9), and hence leading to a deficiency in Ca^{2+} import into the mitochondria, increased phosphorylation and inhibition of the PDC, accompanied by a reduced pyruvate conversion to acetyl-CoA. Additionally, attenuated fatty acid production, most probably due to a concomitant citrate reduction went along with a compensatory increase of glutaminolysis in these cells compared to control cells. Despite the increased glutamate transport into the mitochondria, mitochondrial ATP levels were still affected.

Results

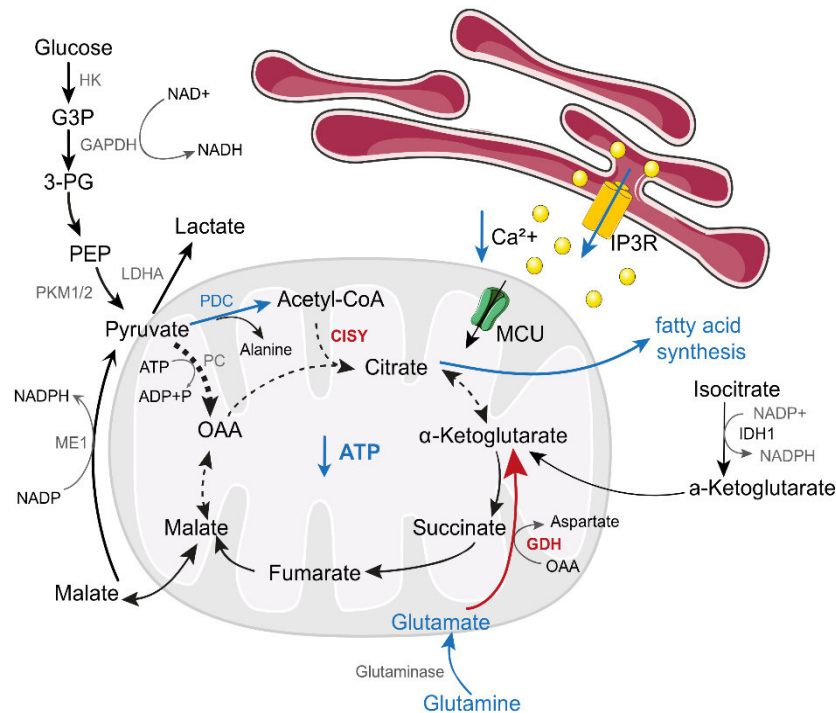


Figure 18 Schematic illustration of the TCA cycle and dysregulations upon reduction of GDAP1 expression

Glycolysis produces pyruvate, which is transported into the mitochondria by the mitochondrial pyruvate carrier to enter the TCA cycle after decarboxylation and oxidation into Acetyl-CoA. This reaction is catalyzed by the PDH that is activated in a Ca^{2+} -dependent manner. We observed fewer MERCS and reduced proximity with less IP3R-related Ca^{2+} release in GDAP1 KD cells, as well as increased PDC inhibition. Proteomic data revealed slightly increased levels for the citrate synthase (CYSY). Bodipy™ experiments showed reduced fatty acid synthesis; increased glutaminolysis was observed; glutamine and glutamate contents are both reduced, while the glutamate dehydrogenase (GDH) level is strongly elevated, as well as reduced mitochondrial ATP levels in GDAP1 KD cells. Arrows are color-coded if regulated in our GDAP1 KD model – red for increased levels or activity, blue for a reduction. Dotted arrows indicate presumably reduced or elevated processes.

6.1.8. Mitochondrial shape in patient-derived neuronal progenitor cells shift towards increased fusion activity

We were now interested if these alterations were also pathogenic in CMT4A patients and performed experiments with differentiated iPSCs derived from CMT patients' fibroblasts. It remains unclear what leads to the pathogenic phenotype of Charcot-Marie-Tooth disease caused by GDAP1 mutations. In our cell lines with abnormal expression of GDAP1 we showed that these cells have more elongated mitochondria, less MERCS and a defect in the mitochondrial energy production including a shift towards glycolysis and glutaminolysis. To see if these effects can be transferred to processes in affected neurons of patients, we switched to neuronal progenitor cells (NPCs) derived from patients' fibroblasts and differentiated from iPSCs (Figure 19A) (Noack et al., 2012). Patient #1 has two heterozygous point-mutations L239F and R273G in the C-terminal GST domain, while patient #2 possesses a homozygous mutation in the donor site of the intron 4, which leads to exon 4 skipping and eventually to a

Results

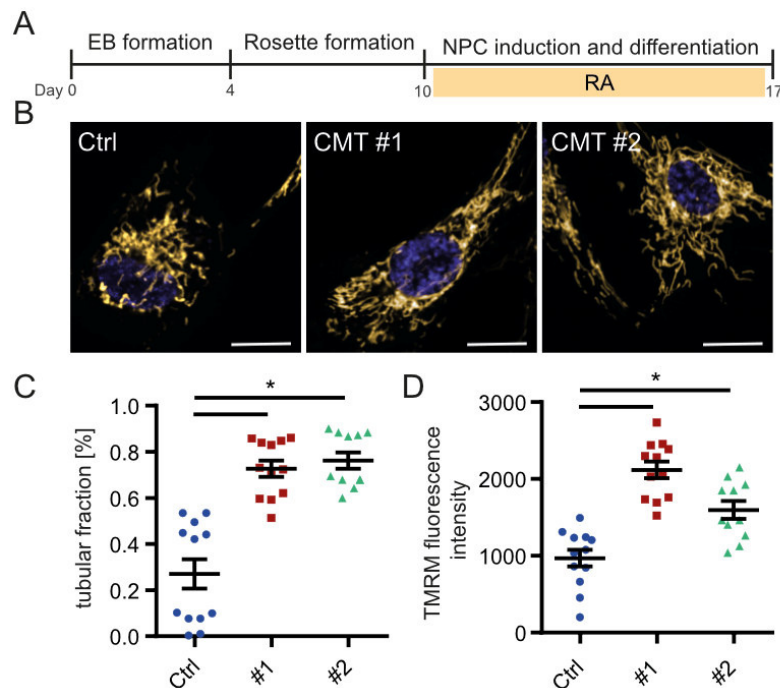


Figure 19 More elongated mitochondria in patient-derived neuronal progenitor cells

NPCs were stained with TMRM, MitoTracker™ Green FM and Höchst for live cell imaging with the Opera Phenix™ high content microscope A) Schematic illustration of the differentiation timeline of iPSCs to NPCs. B) Representative images of NPC Ctrl and patient-derived cells showing mitochondrial staining with TMRM. C) Analysis of mitochondrial shape indicated a higher percentage of cells with elongated mitochondria with GDAP1 disease-related mutation. D) Mitochondrial membrane potential is elevated in patient-derived NPCs; C and D) n=12, 5-8 replicates were done per experiment with a range of 92 to 1235 cells per well; Data are displayed as scatter dot plots with SEM and statistical significance was calculated using the one-way ANOVA with Dunn's (C) or Tukey's (D) multiple comparisons test, *p<0.05.

truncated protein lacking the C-terminal GST, HD, and transmembrane domain of GDAP1 (Noack et al., 2012). As already performed for the SH-SY5Y cells, the NPCs were stained with TMRM and MitoTracker™ Green FM to study the mitochondrial morphology and membrane potential. Figure 19B shows representative images for each cell line.

The quantification of mitochondrial shape showed a clear shift towards tubular mitochondria in both patient-derived cells (Figure 19C). Additionally, the mitochondrial membrane potential was elevated in both mutant NPCs, though more pronounced in patient #1 (Figure 19D). Thus, mitochondrial shape in patient-derived neuronal cells was similarly shifted towards more elongated mitochondria as previously observed in the GDAP1 KD cell line compared to the respective controls expressing endogenous WT GDAP1. Equal observations accounted for the mitochondrial membrane potential, which was also elevated in both patient-derived cells and GDAP1 KD cells.

Results

6.1.9. Transmission electron microscopy reveals increased number of MERCS in patient-derived NPCs

Transmission electron microscopy was done with these cells to further investigate mitochondrial shape. Mitochondria were analyzed individually for their area, perimeter as well as the Feret's diameter, which defines the longest diameter inside the object of interest (Walton, 1948). In contrast to the live cell imaging results, the patient-derived cells rather had smaller mitochondria regarding mitochondrial area and perimeter (Figure 20A-D). The Feret's diameter also showed a significant reduction.

Additionally, we examined the mitochondria-ER contact sites in these cells. Figure 21A shows representative magnifications especially illustrating the MERCS. Quantifying the number of MERCS revealed an increase in the number of contact sites per mitochondrion in patient #1

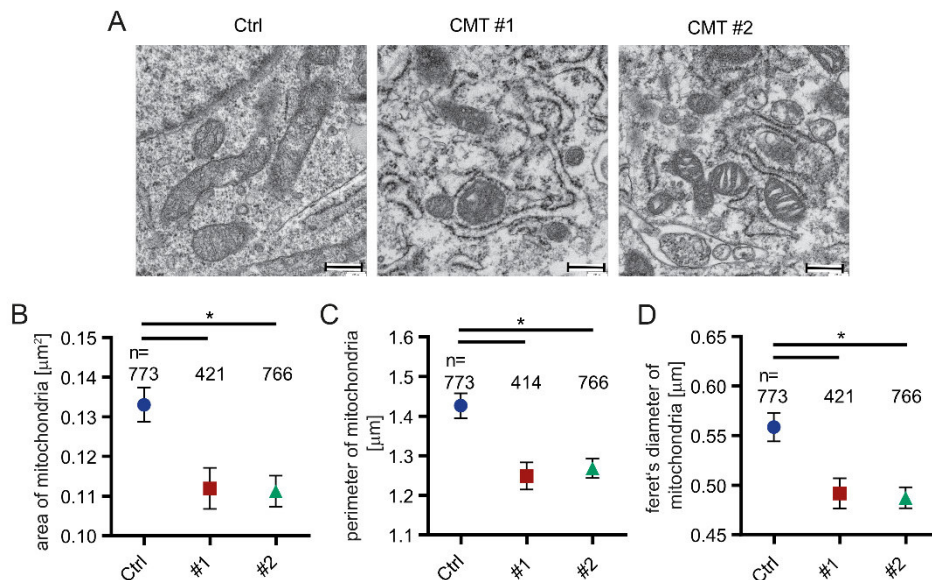


Figure 20 TEM reveals reduced mitochondrial size in patient-derived NPCs

A) Representative TEM images of each cell line, scale bar refers to 400 nm. Each mitochondrion of every acquired cell was analyzed for B) mitochondrial area, C) perimeter of mitochondria D) Feret's diameter of mitochondria. Analyzed parameters revealed shortened mitochondria in patient-derived NPCs; data are displayed as mean with SEM and statistical significance was calculated using one-way ANOVA with Dunn's multiple comparisons test, * $p < 0.05$.

and #2, as illustrated in Figure 21B. Patient-derived cells possessed more mitochondria with one or more ER-contacts compared to the control. Also, the length of these contacts was slightly enhanced (Figure 21C).

One important finding in the GDAP1 KD (see 6.1.2) was that the distance between the two organelles was increased, which possibly impairs further Ca^{2+} -derived processes inside the mitochondria. This led us to measure this parameter in the patient-derived cells and interestingly, the patient #1-derived cells did not show differences here, whereas the cells derived from patient #2 exhibited greater distance between the two organelles. Hence, in contrast to the stable cell lines, cells derived from patient #1 rather revealed intensified contact

Results

of mitochondria with the ER – in respect to both the length and width of contact sites, whereas the width is elevated in patient #2, expressing the truncated GDAP1 protein.

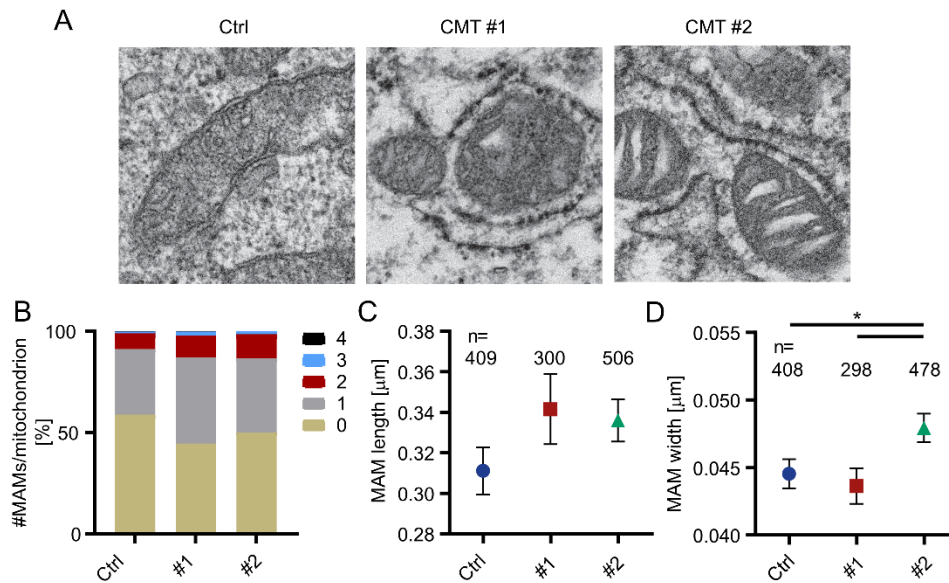


Figure 21 TEM reveals an increased number of MERCS in patient-derived NPCs but reduced integrity

A) Representative magnifications of TEM images of NPC lines. B) The number of MERCS per mitochondrion did not show any variations between the cell strains. C) The length of the contact sites was not significantly different. D) The distance between the ER and mitochondria was significantly enhanced in patient #2-derived NPCs. Data are displayed as bar graphs (B) or means (C-D) with SEM and statistical significance was calculated using one-way ANOVA and Dunn's multiple comparisons test, *p < 0.05.

6.1.10. Patient-derived small molecule neuronal progenitor cells (smNPCs) reveal diminished intracellular glutamine concentrations

Thanks to a cooperation with the group of [REDACTED] we were able to perform experiments with small molecule neuronal progenitor cells (smNPCs) and eventually, specifically differentiated motoneurons (MN) (Reinhardt et al., 2013). The major advantage of smNPCs is the stability and more straightforward cultivation with improved reproducibility and without manual cell selection (Reinhardt et al., 2013). Initially, the human iPSCs were differentiated to embryoid bodies and further to NPCs (Figure 22A). Immunoblotting of the three iPSC strains confirmed the GDAP1 expression for the Ctrl cells, as well as the patient #1 cells, carrying the point mutation in the GST region, which however shows weaker GDAP1 expression levels; actin levels remained unaffected (Figure 22B). In contrast, patient #2 cells carrying the mutation which induces the expression of a truncated GDAP1 protein did not reveal any protein band for GDAP1. The GDAP1 antibody recognizes the amino acids 59-118 of the human GDAP1 protein and hence, should bind to the truncated GDAP1 in this patient.

Results

Apparently, the truncated protein is unstable or rapidly degraded and thus not detectable by western blotting. The actin band is as strong as for the other two cell lines.

Repeating high content microscopy for fatty acid quantification in the smNPCs did not reveal any differences in the number of spots normalized to the mitochondrial area. Due to the massive morphological difference of neuronal progenitor cells compared to SH-SY5Y cells regarding neurite growth, it was not practicable to analyze the number of Bodipy-positive spots per cell. We decided to generate more reliable values by normalization to the mitochondrial area. However, normalization to the summarized area of the nuclei that were counterstained with Höchst gave the same results.

Intracellular glutamine concentration measured with the above described luciferase assay did not vary greatly between the cells, though there might be a tendency towards a reduction of glutamine levels in both patients. The amount of glutamate in contrast was significantly

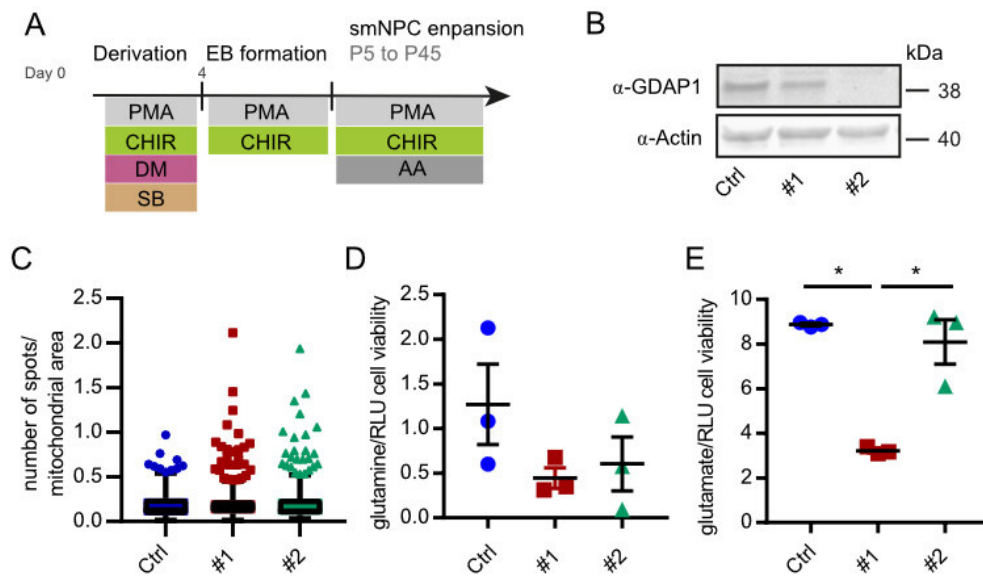


Figure 22 Patient-derived small molecule NPCs (smNPCs) reveal diminished intracellular glutamine concentrations

A) Differentiation protocol to obtain smNPCs from induced pluripotent stem cells (iPSCs) with indicated small molecules and additives B) Immunoblot of total cell lysates to verify the GDAP1 protein expression. Actin was additionally incubated as loading control. C) Bodipy live cell imaging was performed to quantify the amount of lipid droplets but did not show any difference between the cell lines, $n > 20000$ cells from 3 independent differentiations. D) Intracellular glutamine determination showed a weak reduction in both patient-derived cells, $n = 3$ (in triplicates each). E) Intracellular glutamate concentration only showed a reduction in patient #1-derived NPCs, $n = 3$ (in triplicates each). Data are displayed as Tukey's box and whiskers plots (C) or scatter dot plots with SEM (D,E) and statistical significance was calculated using two-way ANOVA with Tukey's multiple comparisons test, $*p < 0.05$.

reduced in patient #1 cells, but not in patient #2. Thus, only one patient harboring the point mutation showed similar alterations of glutamine and glutamate values as the KD cells, but there was no change in fatty acids in both patient-derived cells compared to the healthy donor control.

6.1.11. CMT patient-derived motoneurons share similarities with the KD cells in MCU and DRP1 expression levels

Though patient-derived NPCs and smNPCs cells are a more representative model than immortalized cell lines, NPCs are still different in their function, and cellular characteristics compared to differentiated neurons, specifically motoneurons (MN). The methodological possibilities and expertise provided by [REDACTED] group to specifically differentiate these smNPCs to motoneurons (Figure 23A) enabled us to further investigate these parameters in patient-derived motoneurons (Reinhardt et al., 2013). To begin with, I verified the GDAP1 expression in the motoneurons. Immunoblotting of total cell lysates of the differentiated MN clearly revealed a similar pattern as already seen in Figure 22B for the smNPCs – specific protein bands for GDAP1 in control and patient #1, but not in patient #2 with the truncated protein – actin served as loading control and was equally present in all samples (Figure 23B). Additionally, the GDAP1 expression level in patient #1 cells appeared to be lower again compared to the Ctrl. To verify the neuronal identity of the cells, immunocytochemistry was performed with the dendritic marker microtubule-associated protein 2 (MAP2). The antibody Smi32 binds to neurofilaments of motor neurons and was taken to identify the maturation of NPCs to motoneurons (Figure 23C) (Reinhardt et al., 2013). Indeed, the stained MN were positive for all tested markers, whereas human embryonic kidney cells (HEK) cells taken as non-neuronal negative control did not show any specific antibody staining. In order to reproduce the findings concerning the mitochondrial morphology as well as the regulation of the Ca²⁺- related proteins MCU and CaN we observed in the SH-SY5Y cells, we continued with western blotting proteins from total cell lysates of the MN (Figure 23D-F).

Both patient-derived cells showed slightly higher levels of MCU. Calcineurin, in contrast, did not show any variations between the samples. Quantification of the mitochondrial fission factor DRP1 showed a slight tendency towards downregulation in MN of patient #1 compared to the control. Altogether, MCU but also DRP1 levels showed a tendency of altered protein levels in the patient-derived and differentiated MN as seen in the GDAP1 KD cells, though they were not significant yet and require a larger set of samples and values.

Results

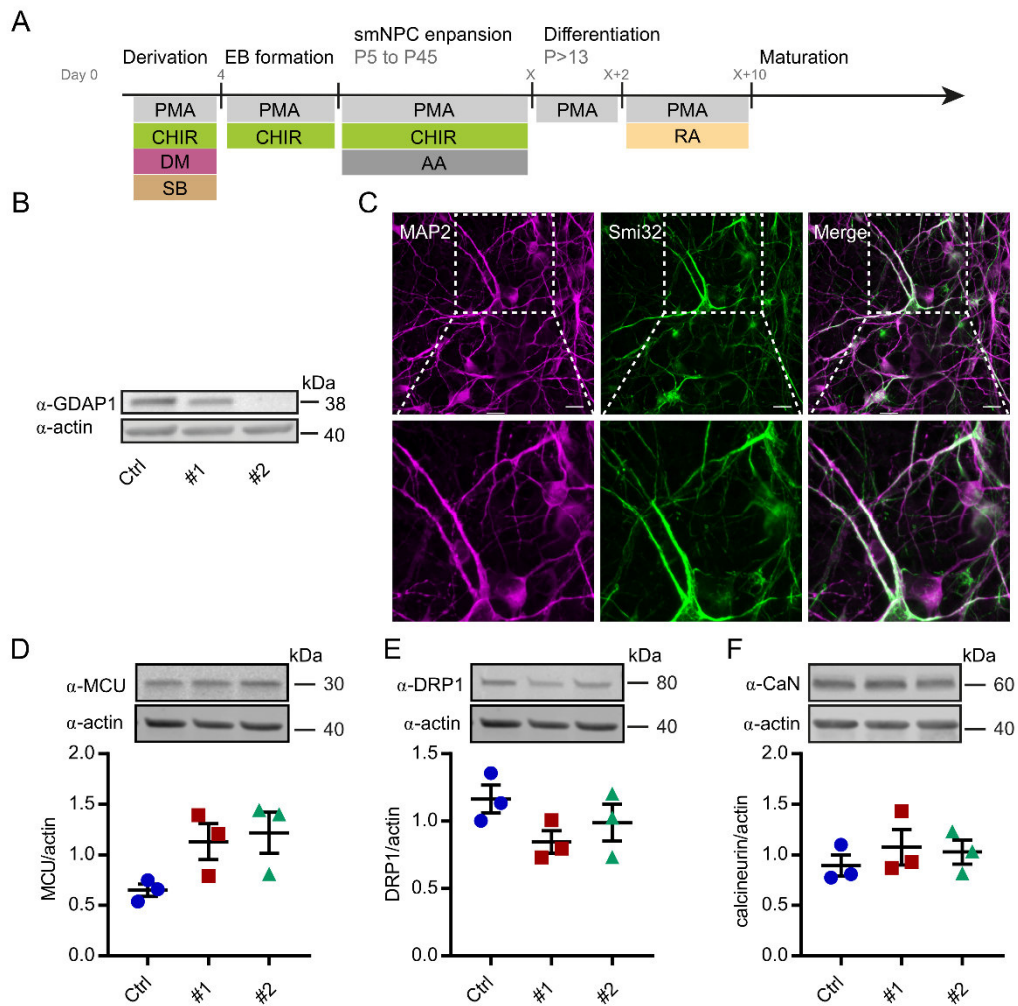


Figure 23 CMT patient-derived motoneurons share similarities with the KD cells in MCU and DRP1 expression

A) Differentiation protocol to obtain motoneurons (MN) from induced pluripotent stem cells (iPSCs) B) Immunoblot of total cell lysates to verify the GDAP1 protein expression in differentiated motoneurons derived from CMT4A patients and control; actin served as loading control. C) Confirmatory immunocytochemistry of motoneurons with the dendrite marker MAP2 and motoneuronal neurofilament Smi32. D) MCU levels showed tendencies towards increased levels in patient-derived cells compared to the Ctrl. E) DRP1 levels appeared to be slightly reduced in patient #1. F) No variations in CaN levels between the cell lines. Data are displayed as scatter dot plots with SEM and statistical significance was calculated using the one-way ANOVA and Dunn's multiple comparisons test, * $p < 0.05$.

6.1.12. CMT-derived motoneurons exhibit increased glutaminolysis and reduced fatty acids

To evaluate changes in the glutamine metabolism, the levels of glutamine and glutamate were quantified in the MN. The assay revealed a significant decline of both glutamine (Figure 24 A) and glutamate (Figure 24 B) in MN derived from both patients studied compared to the control, whereas the glutamate reduction was even more pronounced in patient #2-derived cells. In line with this, I compared the levels of glutamate dehydrogenase between the cells via

Results

immunoblotting. Normalized to actin, GDH protein levels showed an upregulation in both patients, though not yet significant for patient #2 (Figure 24C). In contrast to the GDAP1 KD cells, LDHA did not show any dysregulation (Figure 24D). I proceeded with the MitoTracker™ and Bodipy™ staining of mitochondria and intracellular lipids in these cells, respectively, and quantified the appearance of both. This exposed a significant increase in the mitochondrial area and the number of Bodipy™-positive spots normalized to the mitochondrial area were reduced in both patient-derived MN, more pronouncedly in patient #2. Interestingly, these results indicating an increased glutaminolysis are fully in line with the outcome in the GDAP1 KD cell lines (see 6.1.6). Thus, together with the stronger glutaminolysis and the reduced lipid droplets, both patient-derived MN showed the same trends as GDAP1 KD cells in comparison to the respective controls.

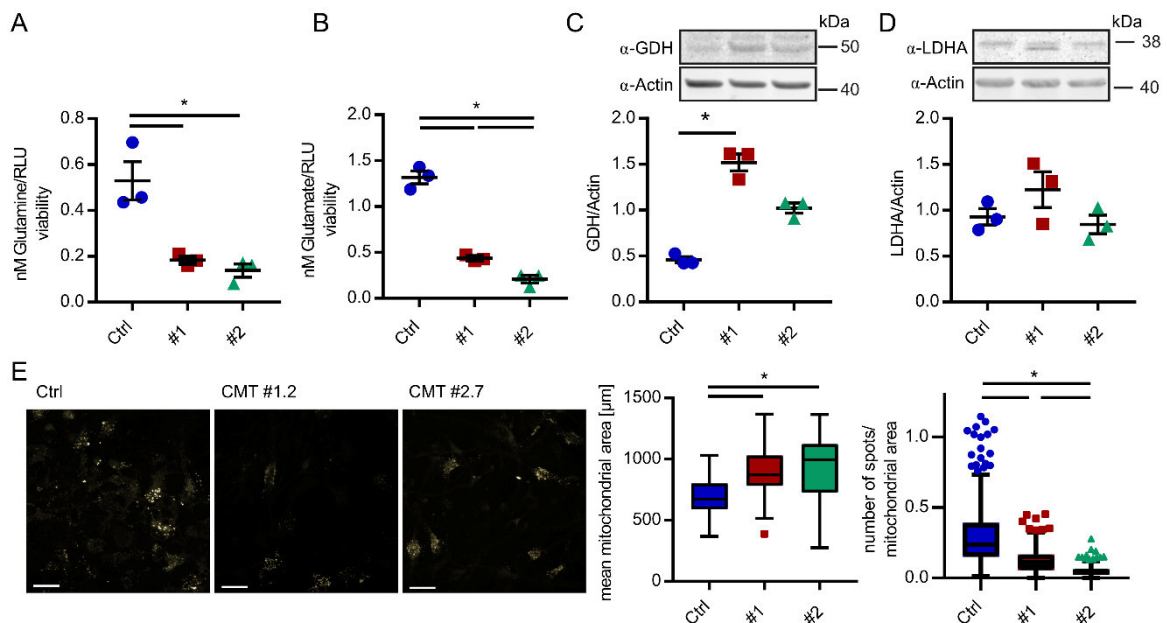


Figure 24 CMT-derived motoneurons reveal increased glutaminolysis and reduced fatty acid synthesis

Measurement of intracellular A) glutamine and B) glutamate showed significantly attenuated levels in both patient-derived MN compared to the Ctrl, n=3 (in triplicates each). C) GDH levels were elevated in patient-derived MN after normalization to actin, n=3. D) Immunoblot analysis did not reflect any difference in expression levels between the cell lines, n=3. E) Bodipy staining and quantification of Bodipy-positive spots and mitochondrial area; n>40000 cells from 3 independent differentiations; data are displayed as scatter dot plots with SEM (A-D) or Tukey's box and whiskers plots and statistical significance was calculated using two-way ANOVA with Tukey's multiple comparisons test (A,B) or one-way ANOVA with Dunn's multiple comparisons test, *p<0.05.

To evaluate if this can also be pinned down to an inhibition of the PDH activity, we continued with the Phostag™ blot against PDH E1 subunit, as well as endogenous levels for the E2 and E3 subunits, which were altered in the KD cells. Similarly, there was a tendency for the CMT4A MN towards reduced PDH E1 levels, especially in patient #2 but no effect on the phosphorylation unfortunately. In contrast, E3 levels seemed to be increased to some extent.

Results

In summary, the results from my experiments with SH-SY5Y cell lines with a GDAP1 KD, but also with patient-derived and differentiated motoneurons, indicated that an impairment of GDAP1 function leads to major alterations in neuron metabolism and ATP generation. The pyruvate metabolism of the mitochondria appeared to be especially affected – whether this is due to a less active PDC or whether the pyruvate import into the matrix is already affected still remains unclear. But both cell culture models appeared to force the cellular metabolism into increased glutaminolysis and a less effective mitochondrial ATP supply.

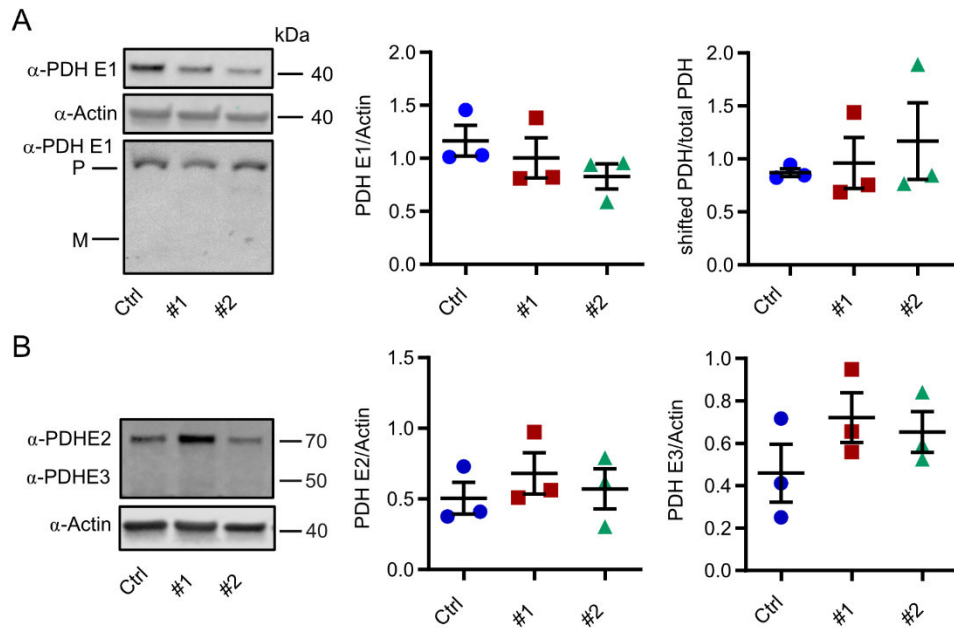


Figure 25 Abundance and activity of the PDH in CMT-derived motoneurons

A) Phostag™ blot against PDH E1 α ; reducing immunoblots served to determine the endogenous levels of PDH E1 α subunit. Actin served as loading control. Shifted bands in the Phostag blot indicate phosphorylated (P) PDH, M – unphosphorylated PDH monomer. B) Immunoblots and analysis of Ctrl and KD cell lysates to determine endogenous levels of PDH E2 and E3 subunit. Actin served as loading control. Data are displayed as scatter dot plot with SEM and statistical significance was calculated using the nonparametric Mann Whitney test, * $p < 0.05$.

To further unravel the mechanism by which GDAP1 function regulates the mitochondrial shape and affects the mitochondrial ATP production, I investigated the redox-related impact of GDAP1, since the exact function of GDAP1 and its GST domain is not yet studied in detail and redox signaling pathways are highly regulatory – especially for the so-called redox-triangle composed of the ER, peroxisomes and mitochondria.

Results

6.2. The influence of GDAP1 expression on the intracellular redox state and on redox modification of proteins

6.2.1. Mitochondrial phenotype can be reproduced with cells overexpressing WT and mutant GDAP1

The protein GDAP1 shares sequence similarities to GSTs, out of which the N-terminal part (GST-N) supposedly exhibits an enzymatic function (Huber et al., 2016). To investigate redox-related effects of GDAP1 expression, I included additional four cell lines overexpressing empty vector (EV), GDAP1 WT (WT) and either of the two point mutations R310Q, a CMT-disease related mutation, and S34A, a loss of function mutation in the N-terminal GST domain (Crimella et al., 2010; Huber et al., 2016; Niemann et al., 2009; Noack et al., 2012). To begin with, I investigated if these cells show changes like the ones in GDAP1 KD cells and patient-derived cells in regard to mitochondrial shape and ATP production.

An immunoblot of total cell lysates stained against GDAP1 and actin served to confirm the expression (Figure 26A). Due to the HA-tag fused to the GDAP1 protein, the specific GDAP1 bands were slightly higher than the endogenous GDAP1 protein.

CMT2K patient-derived fibroblasts with a dominant inherited GDAP1 mutation have been shown to have a less efficient CI activity (Cassereau et al., 2009). To evaluate the correct complex formation of the electron transport system complexes in these cells, we also performed a blue native PAGE of isolated mitochondria, looking for any alteration of the complex arrangement in the respiratory system. Similar to the KD cells, there was no detectable difference in the blue native PAGE for the electron transport system proteins (Figure 26B).

Regarding the mitochondrial morphology in these cells, the analysis of mitochondrial shape in the cell lines confirmed the literature findings – GDAP1 WT overexpression induced a significant increase in fragmented mitochondria and a concomitant decrease in tubular mitochondria. Both the recessive disease-associated mutation and loss-of-function mutation induced the opposite outcome with increasingly tubular mitochondria and a loss of fission activity in these cells (Figure 26C) (Azzedine et al., 2003; Niemann et al., 2005, 2009; Wagner et al., 2009).

To measure the cytosolic and mitochondrial ATP levels, we performed the same BRET assay as for the KD cells in Figure 26D. Remarkably, overexpression of WT GDAP1 showed a reduction in cytosolic ATP. This effect was diminished in the mutant cells. The mitochondrial ATP was slightly reduced in WT overexpressing cells and thus has a similar effect as the KD of this protein. This effect was reversed and significantly increased for the R310Q mutant

Results

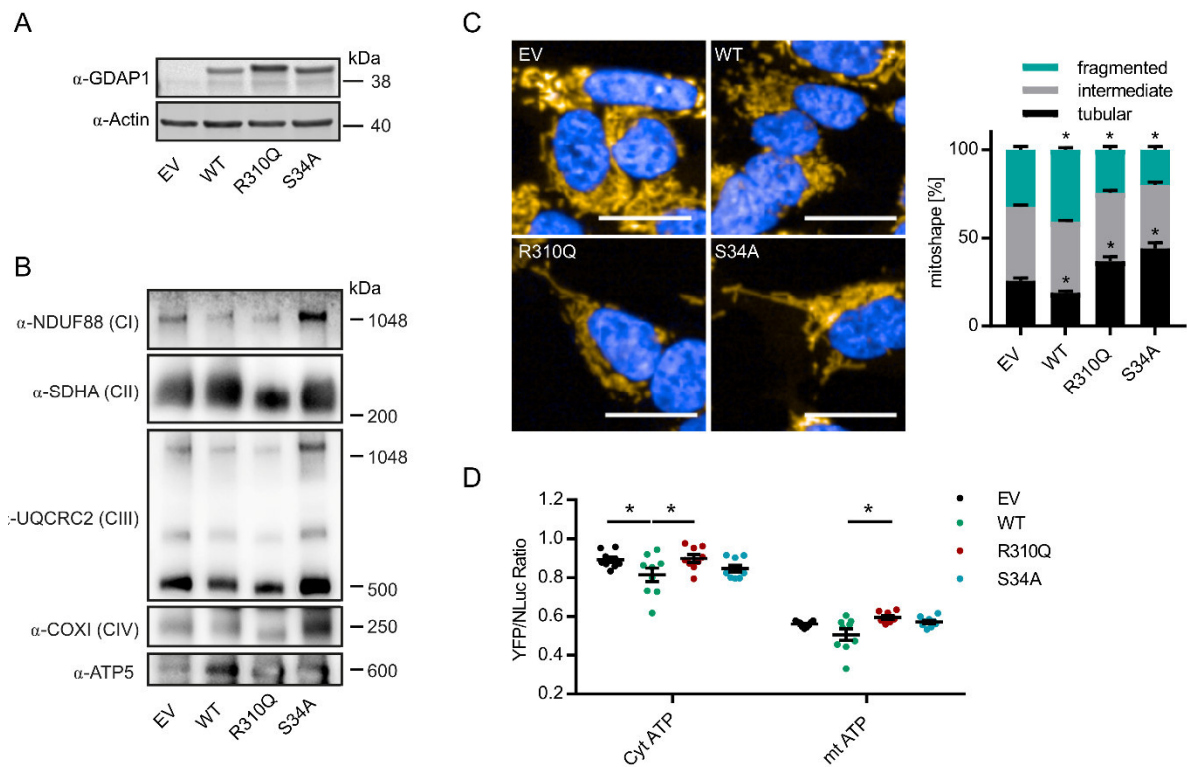


Figure 26 The mitochondrial shape is changed in cells overexpressing WT and mutant GDAP1

SH-SY5Y cell lines stably overexpressing either empty vector (EV), WT GDAP1 (WT), GDAP1-R310Q (R310Q) or GDAP1-S34A (S34A) were used for these experiments. A) Immunoblot of total cell lysates against GDAP1 and actin as loading control to confirm GDAP1 protein expression. B) Blue native PAGE of isolated mitochondria for analysis of the integrity of respiratory chain complexes, which did not show any differences between the cell lines. C) Live cell imaging of both cell lines was performed via high content microscopy after mitochondrial staining with MitoTracker™ Green FM, nuclei were counterstained with Höchst. Scale bar equals 20 μ m. Automated mitochondrial shape analysis and classification was performed with Perkin Elmer harmony software and revealed increased fission activity in GDAP1 WT overexpressing cells, but more fused mitochondria in mutant GDAP1 expressing cells; $n > 17000$ cells per cell line in 3 independent experiments (in triplicates each). D) Cells were transfected with the BRET-BTEAM sensor plasmid for evaluation of cytosolic and mitochondrial ATP levels. WT expressing cells showed a reduction in cyt[ATP] compared to EV control, whereas mitochondrial ATP levels do not vary significantly between EV and WT, but are elevated in R310Q expressing cells; $n = 3$, experiments were performed in triplicates. Data are displayed as bar graphs with SEM (C) scatter dot plots with SEM (D) and statistical significance was calculated using the two-way ANOVA with Tukey's multiple comparisons test (C,D), $*p < 0.05$.

compared to GDAP1 WT.

Immunoblotting of total cell lysates from these cells was performed to investigate if the observations of mitochondrial shape can also be traced back to dysregulations of mitochondrial fusion or fission proteins. Though there was no difference for DRP1 expression levels in the WT overexpressing cells, I detected a significant elevation of DRP1 levels in the R310Q cells, including an equal tendency for the S34A mutant cells (Figure 27A). Regarding the expression levels of MFF there was an upregulation in the S34A expressing cells (Figure 27B). This upregulation of both DRP1 and MFF in the mutant cells with predominantly tubular mitochondria may be a compensatory effect to counteract this outcome.

Results

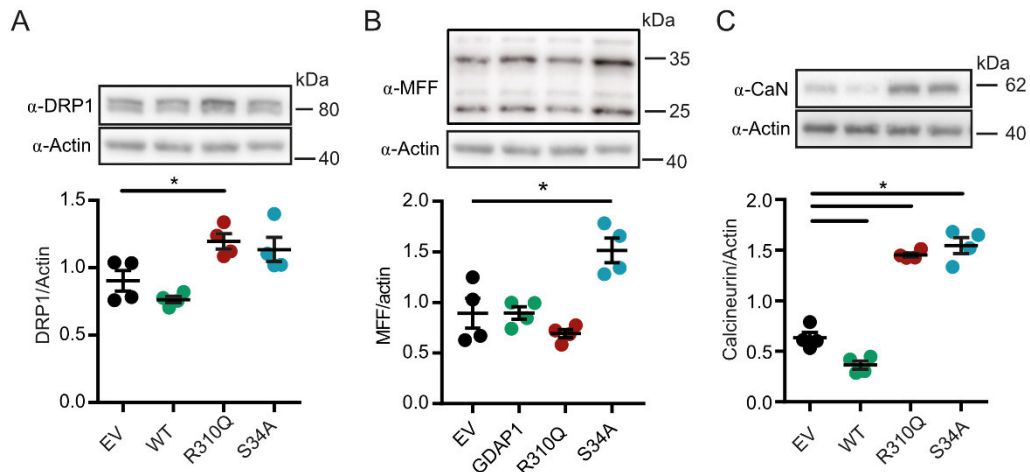


Figure 27 Altered expression levels of mitochondrial fission proteins in cells overexpressing WT and mutant cells

Immunoblots from whole cell lysates of EV, GDAP1-WT, R310Q and S34A were analyzed for A) DRP1 B) MFF and C) calcineurin (CaN) levels, showing upregulation in both mutant GDAP1-overexpressing cells of DRP1 and CaN, MFF was only elevated in S34A mutants. WT-overexpressing cells have reduced CaN levels. Actin was taken as loading control and for normalization. Data are displayed as scatter dot plots with SEM and statistical significance against the EV control was calculated using the one-way ANOVA test with Sidak's multiple comparisons test, * $p < 0.05$.

The quantification of the phosphatase calcineurin revealed reduced protein levels in the WT-expressing cells compared to EV, whereas both mutant-expressing cells revealed significantly higher levels of CaN (Figure 27C).

In general, the mitochondrial shape of the four introduced cell lines confirmed previous findings, as an overexpression of GDAP1 induced mitochondrial fission, whereas both mutations led to increased fusion of mitochondria. Furthermore, I observed that cytosolic, but not mitochondrial ATP levels were affected in WT-overexpressing cells. Both GDAP1 mutations resulted in an elevation of DRP1 and CaN levels. In contrast to the CaN levels in KD cells, the WT overexpressing cells showed the opposite outcome compared to the respective controls.

6.2.2. Neither inhibition of CaN nor AMPK signaling can reverse the mitochondrial shape in overexpressing cell lines

As in the case of KD cells, I investigated the effect of the calcineurin inhibitor (FK506) on mitochondrial structure. CaN levels were elevated in response to the expression of both GDAP1 mutations but decreased by GDAP1 WT expression. To rule out an altered CaN activity in these cells, which could affect the DRP1-induced fission activity, we treated the cells with the CaN inhibitor FK506 (Dumont, 2012; Kawamura and Su, 1995). In contrast to the KD

Results

cells, we observed an elongation of the mitochondria in response to FK506 addition. Initially, EV and WT increased slightly in mitochondrial fragmentation, but after 30 min incubation all four cell lines equally showed a shift towards increased fusion activity or rather an inhibition of mitochondrial fission. Thus, all four cell lines react with an equal change of mitochondrial morphology and there is no specific effect due to an altered GDAP1 expression, though the

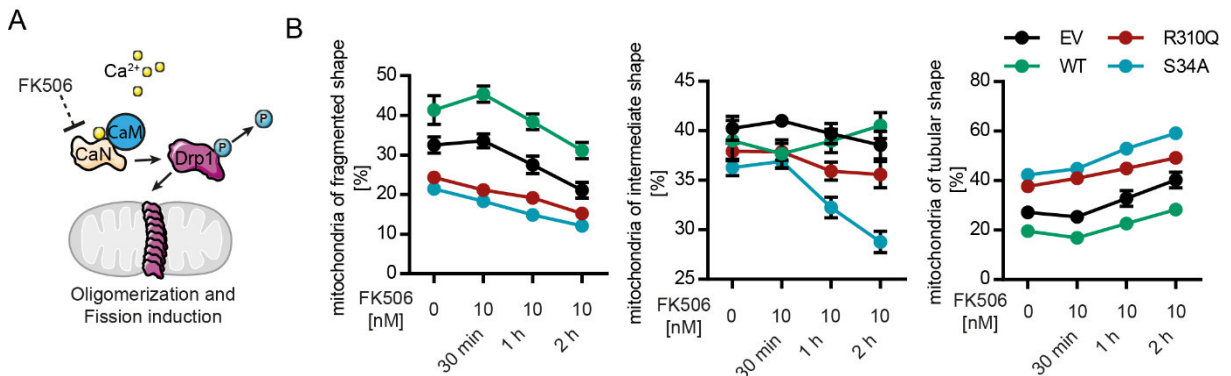


Figure 28 Inhibition of CaN does not reverse the mitochondrial shape in GDAP1 overexpressing cells

A) Schematic illustration of CaN inhibition; CaM and Ca^{2+} -induced activation of CaN induces DRP1 S637 dephosphorylation, initiating the migration of DRP1 to its specific outer mitochondrial membrane receptors, where it forms oligomers, allowing fission of this mitochondrion. FK506 binds its intracellular immunophilin receptor FK506-binding protein of 12 kDa (FKB12) and interacts with CaN, which is in turn unable to bind its substrates. CaN – Calcineurin, CaM – Calmodulin B) High content microscopy of live cells yielding mitochondrial classification of SH-SY5Y by staining with MitoTracker™ Green FM; nuclei were counterstained with Höchst; experiments were performed in duplicates, $n > 7900$ cells per condition in 3 independent experiments. Data are displayed as XY line with SEM and statistical significance was calculated using two-way ANOVA with Sidak's multiple comparisons test, $*p < 0.05$.

rapid decline of the mitochondria classified as an intermediate shape in GDAP1-S34A expressing cells is very striking. This could be a cell line-specific effect induced by the loss of function protein GDAP1-S34A.

Nevertheless, there were no overall effects in regard to mitochondrial shape, leading to the conclusion that though CaN protein levels vary greatly upon expression of GDAP1 WT, R310Q and S34A mutations, CaN inhibition does not reverse the phenotype induced by expression of GDAP1.

Similar experiments were performed for AMPK inhibition to evaluate if this signaling pathway is altered in any of these overexpressing cell lines and sensitive for AMPK inhibition. The same observations were made for the overexpressing cell lines compared to the KD cells in 0 – an equal change of modification of the mitochondrial shape throughout the cell lines and a saturation after $20 \mu\text{M}$ of the CAMKK β inhibitor STO609 (Figure 29B). The WT overexpressing cell lines reveal more fragmented mitochondria under basal conditions, but the decline with increasing concentrations of the CAMKK β inhibitor is equal to the EV or R310Q and S34A mutant. Thus, we assume that AMPK activation is not significantly altered in cells with a

Results

dysregulation of GDAP1 or an inefficient mutant form of GDAP1 protein.

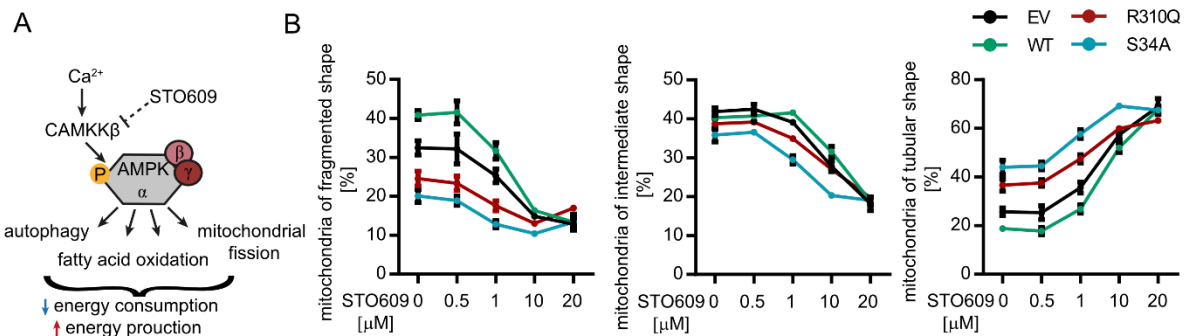


Figure 29 Inhibition of the AMPK signaling pathway in GDAP1 overexpressing cell lines does not show any alteration of mitochondrial shape

A) Schematic illustration of AMPK function and inhibition with STO609. Ca²⁺-induced activation of CAMKKβ leads to phosphorylation of the α-subunit of AMPK. Upon AMPK activation, pathways initiating the ATP production are triggered, whereas intracellular processes of high energy consumption are arrested. This leads to increased autophagy, fatty acid oxidation or mitochondrial fission. STO609 inhibits the CAMKKβ. B) High content microscopy of live cells yielding mitochondrial classification of SH-SY5Y by staining with MitoTracker™ Green FM; nuclei were counterstained with Höchst; experiments were performed in triplicates, n>2400 cells per condition in three independent experiments; data are displayed as XY line with SEM and statistical significance was calculated using two-way ANOVA with Sidak's multiple comparisons test, *p<0.05.

Altogether, the previous results indicate that GDAP1 KD and overexpression have opposite effects on the mitochondrial shape – knockdown leads to elongated mitochondria, whereas its overexpression induces mitochondrial fission. Also, the mitochondria in cells expressing the disease-associated point mutation of R310Q as well as the GST loss-of-function mutation S34A revealed an increased fusion activity. An equal pattern can be observed regarding the expression levels of CaN – the KD cells as well as the mutant GDAP1 expressing cells show higher CaN levels, whereas the WT GDAP1 shows the opposite. But its inhibition with FK506 does not have a distinguishing effect on mitochondrial shape between the cell lines and to its respective control. Equally, inhibition of AMPK signaling did not result in a specifically altered process in these cells.

In parallel to the experiments concentrating on cell metabolism, I asked the question to what extent the presumed GST-function of GDAP1 affects the cells' redox state, since the intracellular redox state is an important parameter and signaling pathway for various cytosolic and especially mitochondrial processes. We then focused our investigation more on GDAP1's GST function and looked for potential interaction partners. An approach to address possible interaction partners may help to explain how GDAP1 function regulates mitochondrial shape, ER-contact sites and ATP production.

Results

6.2.3. Glutathione levels in SH-SY5Y cell lines

The above-mentioned analyses of mitochondrial and MAM fractions (6.1.3) were also evaluated regarding redox-regulating proteins. Concentrating on peroxiredoxins (PRDX), glutathioneperoxidases (GPX) and the zeta class GST (GSTZ1) indicated several differences between Ctrl and KD. PRDX and GPX are the main drivers of intracellular H₂O₂ detoxification while the reduction of H₂O₂ via GPX is dependent on the antioxidant GSH as a cofactor (Cox et al., 2010; Lubos et al., 2011). The GSTZ1 enzyme was included because it shares structural similarities in the GST-N domain with GDAP1 (Shield et al., 2006). Crude mitochondria showed an increase in the expression of PRDX4, which is mainly located in the ER lumen (Figure 30A) (Tavender et al., 2008). This increase was even more pronounced in the MAM fraction, together with a reduction of the cytosolic PRDX1 and PRDX2 (Figure 30C). In contrast, pure mitochondria showed a tendency towards increased PRDX5 levels, but this needs to be investigated further. Interestingly, the GSTZ1, which is suggested structurally similar to the N-terminal GST domain in GDAP1, seemed to be elevated upon GDAP1 depletion (Shield et al., 2006).

Published data show that GDAP1 expression increases the intracellular GSH concentration (Del Amo et al., 2015; Noack et al., 2012). I performed GSH and protein glutathionylation (PrSSG) quantification to examine if the basal glutathione levels were altered in these cells, which could give a first hint towards a change in ROS scavenging upon GDAP1 KD and the ability of GDAP1 as a GST. This was done for both the KD cells and the overexpressing cell lines with their respective controls with an enzymatic recycling assay (Rahman et al., 2007). After GSSG reduction to GSH by the addition of glutathione reductase and NADPH to the reaction, reduced glutathione reacts with 5,5'-Dithiobis-(2-Nitrobenzoic Acid) (DTNB), resulting in GSSG and 5-thio-2-nitrobenzoic acid (TNB) (Rahman et al., 2007). The formation of TNB leads to a shift in the absorption maximum to 412 nm which can be monitored over time. Hence, the glutathione concentration can be deduced from the slope of the reaction – the faster the absorption increases, the higher the GSH levels. During sample preparation, the proteins are precipitated and can be further processed to specifically reduce the protein thiols. This reaction results in free GSH in the supernatant, which can be quantified again revealing the amount of protein glutathionylation (Rahman et al., 2007). Surprisingly, the GSH measurement did not reflect previous results our group generated. Upon reduced expression of GDAP1 in the KD cells there was no difference in total GSH levels, which includes both the reduced and oxidized glutathione levels (Figure 30A). While there was no difference in the GSH content in the KD and Ctrl cell lines (Figure 30B), there was indeed a slight reduction in protein glutathionylation in the KD cells (Figure 30C).

Results

Identical experiments were also performed in the overexpressing cell lines. Again, the total GSH content of WT overexpressing cells was not in line with previous data. The levels were rather reduced in WT cells compared to EV. On the other hand, the S34A mutant expressing

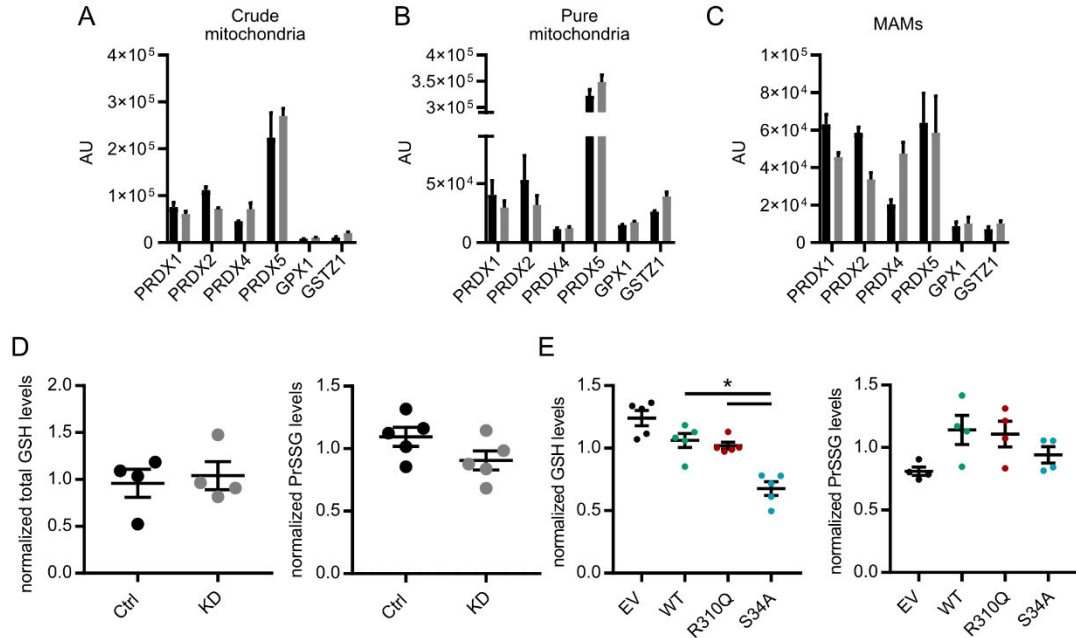


Figure 30 Glutathione levels in SH-SY5Y cell lines

Mass spectrometry analyses of mitochondrial and MERCS fractions revealed a change in redox homeostasis. The abundance of redox regulating enzymes peroxiredoxins (PRDX), glutathione redoxin in A) crude mitochondria B) pure mitochondria C) MERCS. Data were from 3 independent experiments and Bonferroni corrected. D-E) Glutathione levels were evaluated via DTNB reduction to TNB, whose formation can be monitored at an absorption maximum of 412 nm. The reaction was acquired over time with a Tecan™ plate reader and GSH levels were calculated from the slope of the absorption curve's increase. D) Total GSH content and protein glutathionylation (PrSSG) of proteins in Ctrl and GDAP1 KD cells, n=4 (in duplicates each) E) Total GSH and PrSSG content in GDAP1 overexpressing cell lines, n= 4,5 (in duplicates each). Data are displayed as scatter dot plots with SEM and statistical significance was calculated using nonparametric Mann-Whitney test (A-C) or one-way AOVA with Tukey's multiple comparisons test (D-F), *p<0.05.

cells showed a decline of 50% in GSH content compared to EV (Figure 30E). Interestingly, the PrSSG levels in WT and R310Q cells compared to EV were slightly but not statistically significantly increased. The S34A mutant expressing cells revealed a PrSSG level comparable to EV control, which could reflect the loss-of-function in this mutant.

These results indicate that alteration of GDAP1 expression leads to a variation in the protein level of redox-regulating enzymes. Hence, I observed a difference in cytosolic PRDX1 and PRDX2 expression levels, as well as an increase in PRDX4. Additionally, there were differences in protein modification and cellular GSH levels in both GDAP1 KD cells and cells expressing the loss-of-function mutation S34A.

Results

6.2.4. GAPDH glutathionylation is not affected upon reduced GDAP1 expression

One protein that is very accessible for glutathionylation and complex formation is the glyceraldehyde 3-phosphate dehydrogenase (GAPDH), a central protein regulating glycolysis (Barinova et al., 2017; Bedhomme et al., 2012; Ercolani et al., 1988; Kulbe et al., 1975; Zaffagnini et al., 2019). GAPDH is a 37 kDa enzyme taking part in glycolysis, where it catalyzes the reaction from G3P to 3-PG (Ercolani et al., 1988; Kulbe et al., 1975). Besides its function in glycolysis, it is also involved in a broad spectrum of cellular processes such as DNA repair, membrane fusion, Ca^{2+} homeostasis or cell death (reviewed in Tristan et al., 2011). During these processes, GAPDH undergoes either subcellular organelle translocation, oligomerization or posttranslational modification such as nitrosylation or glutathionylation (Tristan et al., 2011). Due to this central function of GAPDH in glycolysis and various mitochondrial and redox-related processes, I did some experimental approaches on a potential regulatory role of GAPDH in our cells. I quantified GAPDH protein levels in total cell lysates, which did not show any variation after normalization to actin (Figure 31A). It was reported that GAPDH may influence the activity of the IP3R via interaction upon glutathionylation of GAPDH (Patterson et al., 2005). Since the KD cells revealed less Ca^{2+} release upon IP3R stimulation, I was interested whether a GAPDH-mediated alteration of IP3R activity was an explanation. A co-immunoprecipitation was not successful, and therefore, I isolated the ER from these cells and performed IB. The cytosolic supernatant after mitochondrial pelleting was taken for ultracentrifugation and purification of the ER. The immunoblot in Figure 31B shows protein bands for the ER protein Sec62, GAPDH and the mitochondrial protein COXIV. All proteins were present in the whole cell lysate (CL), similar to the crude mitochondrial fraction (CM). Due to the close contacts between mitochondria and the ER, there were still ER proteins detectable in the mitochondrial fractions. Successful purification of ER proteins on the other hand was verified by the enrichment of Sec62 and the absence of COXIV. GAPDH bands were also present and intensities were quantified. Normalized to the Sec62 protein level, I saw a significant reduction of GAPDH localization in ER fractions (Figure 31B). To further follow up on this, I performed non-reducing immunoblots (data not shown), since the assumed interaction between GAPDH and IP3R happens via disulfide bridges. However, I could not confirm an interaction between GAPDH and IP3R neither by non-reducing, nor by blue native page, but it still seems to be a promising approach for further experiments.

I additionally wanted to clarify if the translocation of GAPDH to the mitochondria was somehow altered in our cells. GAPDH localization and interaction with VDAC at the outer mitochondrial membrane has been discussed to be an indicator for mitophagy induction (Tarze et al., 2007; Tristan et al., 2011). In this line, GAPDH migrates to the mitochondria, forms oligomers and induces mitochondrial degradation. Mitophagy can also be induced by a disturbed intracellular

Results

redox state, including a depletion of GSH. The addition of the GST substrate ethacrynic acid (EA) binds GSH and results in intracellular GSH reduction, which in turn can lead to oxidative stress conditions and eventually to enhanced mitophagy (Deffieu et al., 2009). Hence, I analyzed the mitochondrial localization of GAPDH in GDAP1 KD versus Ctrl cells and addressed the question if mitochondria are more prone to mitophagy in KD cells in steady-state, but also under redox stress conditions after the addition of EA. The analysis was performed by western blotting of the isolated mitochondria and staining against GAPDH and COXIV to normalize the GAPDH amount to the mitochondrial quantity (Figure 31C). Under basal conditions, there was no difference in GAPDH localization in the mitochondrial fraction. Interestingly, upon EA treatment, more GAPDH was detected at the mitochondrial surface in the Ctrl cells, whereas this effect was abolished in GDAP1 KD cells. The tetramer formation of GAPDH at the mitochondria showed high heterogeneity. Additionally, I analyzed GAPDH glutathionylation via a streptavidin-biotin based pulldown assay. In order to do this, cell-permeable biotinylated glutathione was added to isolated mitochondria from both cell lines additionally to H₂O₂ when indicated as a positive assay control, as H₂O₂ has been shown to induce GAPDH glutathionylation (Cyrne et al., 2010). After 30 min incubation at 37°C, I purified the glutathionylated proteins by adding streptavidin beads. SDS-PAGE was performed with the eluted proteins and quantified by protein band intensity. The expected effect of GAPDH glutathionylation in response to H₂O₂ failed to appear in the Ctrl but was slightly increased in the KD cells. However, there was no obvious difference in GAPDH PrSSG under basal conditions.

In total, GDAP1 KD results in less localization of the glycolytic enzyme GAPDH at the ER, presumably regulating IP3R-derived Ca²⁺ release from the ER. However, we did not detect any differences in GAPDH localization at the mitochondria as an indication for a mechanism involved in mitophagy induction. Interestingly, GAPDH abundance at the mitochondria was significantly reduced in KD cells compared to Ctrl upon EA treatment, which depletes intracellular GSH levels. So far, an increased susceptibility to apoptosis has been observed in dmGDAP1 and rmGDAP1 mutations (Niemann et al., 2009), but these results would rather indicate a reduced susceptibility of GDAP1 KD cells in a mechanism of mitophagy induced by redox stimuli. GAPDH glutathionylation in particular was not altered in our cell lines.

Results

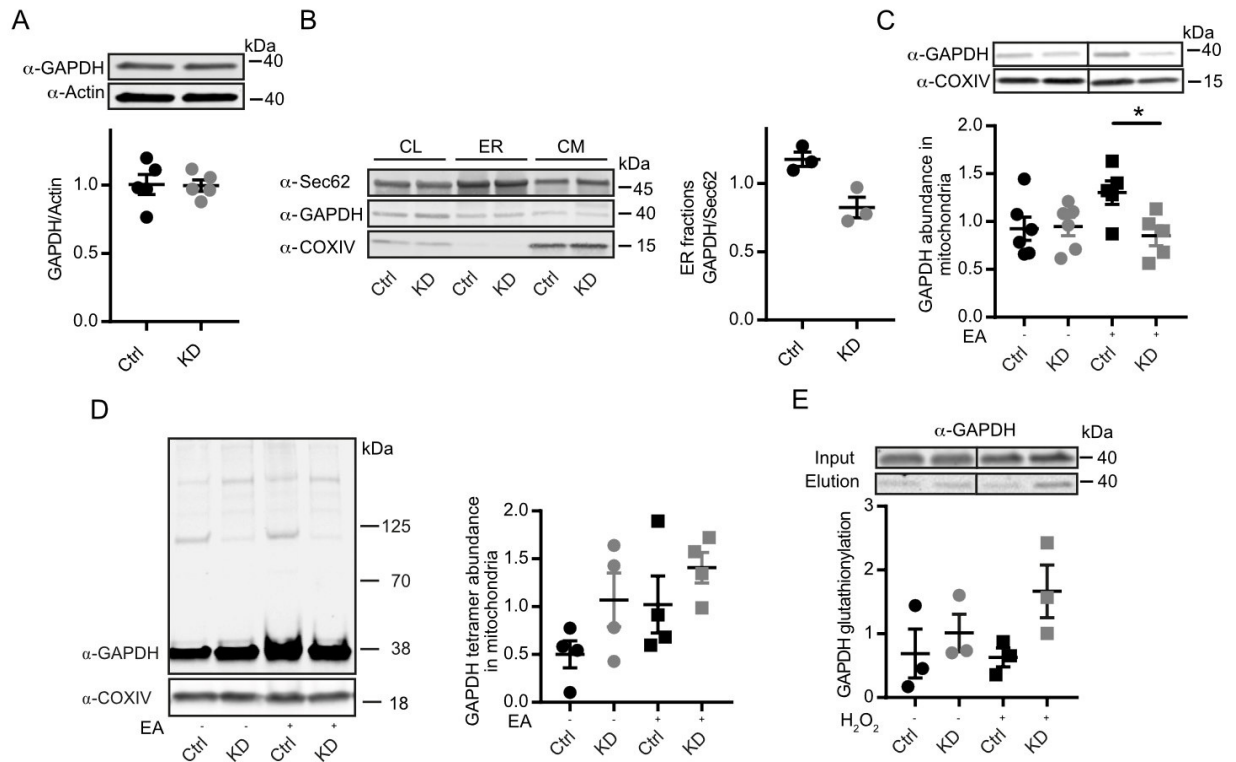


Figure 31 Altered GAPDH migration in GDAP1 KD cells

SH-SY5Y Ctrl and GDAP1 KD cells were used for these experiments. A) Whole-cell lysates were analyzed for their total GAPDH levels normalized to actin as loading control. B) Analysis of GAPDH abundance at the ER after fractionation of crude mitochondria (CM) and ER, normalized to whole-cell GAPDH levels (CL). C) Analysis of GAPDH abundance at the mitochondria normalized to COXIV. D) GAPDH abundance as a tetramer in non-reducing gels. E) Abundance of glutathionylated GAPDH in Ctrl vs KD cells via BioGEE pulldown. Eluted GAPDH band intensities were normalized to the respective input controls. Data are displayed as scatter dot plots with SEM and statistical significance was calculated using Mann-Whitney test (A,B) or unpaired t-test (C), * $p < 0.05$.

6.2.5. Posttranslational modification of Mitofusin 2 is dependent on GDAP1 expression

There are outstanding connections between the mitochondrial proteins GDAP1 and Mitofusin 2 (MFN2). Mutations of both proteins can lead to CMT disease, type CMT4A or CMT2A respectively, but are clinically indistinguishable (Cassereau et al., 2009; Feely et al., 2011). Moreover, both proteins have opposite effects on the mitochondrial shape and MFN2 thiol modification has confirmed influences on mitochondrial respiration and hyperfusion (Shutt et al., 2012; Thaher et al., 2017). While MFN2 can counteract the GDAP1-induced fission, it fails to tether adjacent mitochondria in the presence of dmGDAP1 (Niemann et al., 2005, 2009). I pursued several approaches to investigate if GDAP1 has an impact on the thiol modification of MFN2. I began with a so-called biotin-switch assay, which is based on the irreversible masking of free protein thiols with NEM (Figure 32A) (Kehr et al., 2011). Subsequently, a reducing agent can be added, such as DTT, which nonspecifically removes all reversible PTMs. In a second step, a biotinylated thiol-reactive reagent was added to bind the free thiols,

Results

which were previously binding -SG, -SO, -NO etc. These labeled proteins were now purified with magnetic streptavidin beads and eluted proteins were subjected to SDS-PAGE to perform western blotting. The membranes were stained against MFN2 and band intensities were measured. Interestingly, under basal conditions, significantly less MFN2 was eluted from GDAP1 KD cells, revealing that MFN2 is less modified in these cells compared to the Ctrl cells. After treatment with EA, the difference between the cell lines was diminished. Thus, we next questioned what kind of PTM is altered for MFN2. To address this question, I incubated the lysates with glutaredoxin1 (GRX1) instead of DTT to specifically reduce the glutathionylated cysteines (Figure 32B). Analyzing the protein bands, I saw an increase of glutathionylated MFN2 and GAPDH in KD cells compared to the Ctrl.

I performed the biotin switch assay with the overexpressing cell lines and additional EA treatment (Figure 32C-D). Quantifying the assay revealed less MFN2 modification in R310Q mutant-expressing cells and a significant increase in the S34A mutant cells. The EA treatment did not show any effect. MFN2 glutathionylation, in contrast, was reduced in WT, but not in the S34A-expressing cell lines compared to EV control. GAPDH glutathionylation revealed a similar pattern – less in WT overexpressing cells and slightly more in the loss-of-function mutation.

Combining these results, we saw an effect of GDAP1 expression on the cysteine modification of MFN2 and GAPDH. While GDAP1 KD reduces MFN2 modification but led to increased glutathionylation of MFN2, overexpression led to the opposite effect. Cells expressing GDAP1 with the S34A point mutation seemed to exhibit the opposite effect, indicating that the GST-domain of GDAP1 has an effect on protein thiol modification.

Unfortunately, due to experimental limitations, we were not able to reproduce these experiments. Hence, I changed the method and used polyethyleneglycol (PEG) which binds free thiols and induces a slower migration in SDS PAGE (Kozlowski and Milton Harris, 2001). I performed this acetylation gel shift assay with isolated mitochondria of the Ctrl cell line and additionally treated the mitochondria with 100 μ M H₂O₂ when indicated. The immunoblots of these experiments are shown in Figure 32E. Previous reduction with TCEP served as a positive control to induce a maximum shift depending on the number of accessible cysteines. The shift assay for MFN2 showed no difference between the maximum shift and steady-state, which means that none of the accessible cysteines in MFN2 were modified and labeled with PEG. GAPDH protein bands shifted compared to the unlabeled sample. Under steady-state conditions, without TCEP addition, bands of different sizes were detected, indicating a cysteine modification of GAPDH. Equal experiments were now performed with mitochondria isolated from the KD cells to evaluate if the difference in MFN2 modification could be reproduced (Figure 32F). This assay unfortunately did not confirm the observed cysteine modification in

Results

MFN2, as there was no difference of gel shift detectable neither in the Ctrl nor in the KD cells. Hence, contradictory results were gained regarding MFN2 and GAPDH posttranslational modification, and glutathionylation in particular. Reduced expression of GDAP1 also reduced the amount of PTMs but could be increasing the glutathionylation of MFN2 and GAPDH in particular, whereas its overexpression rather decreased MFN2 and GAPDH glutathionylation.

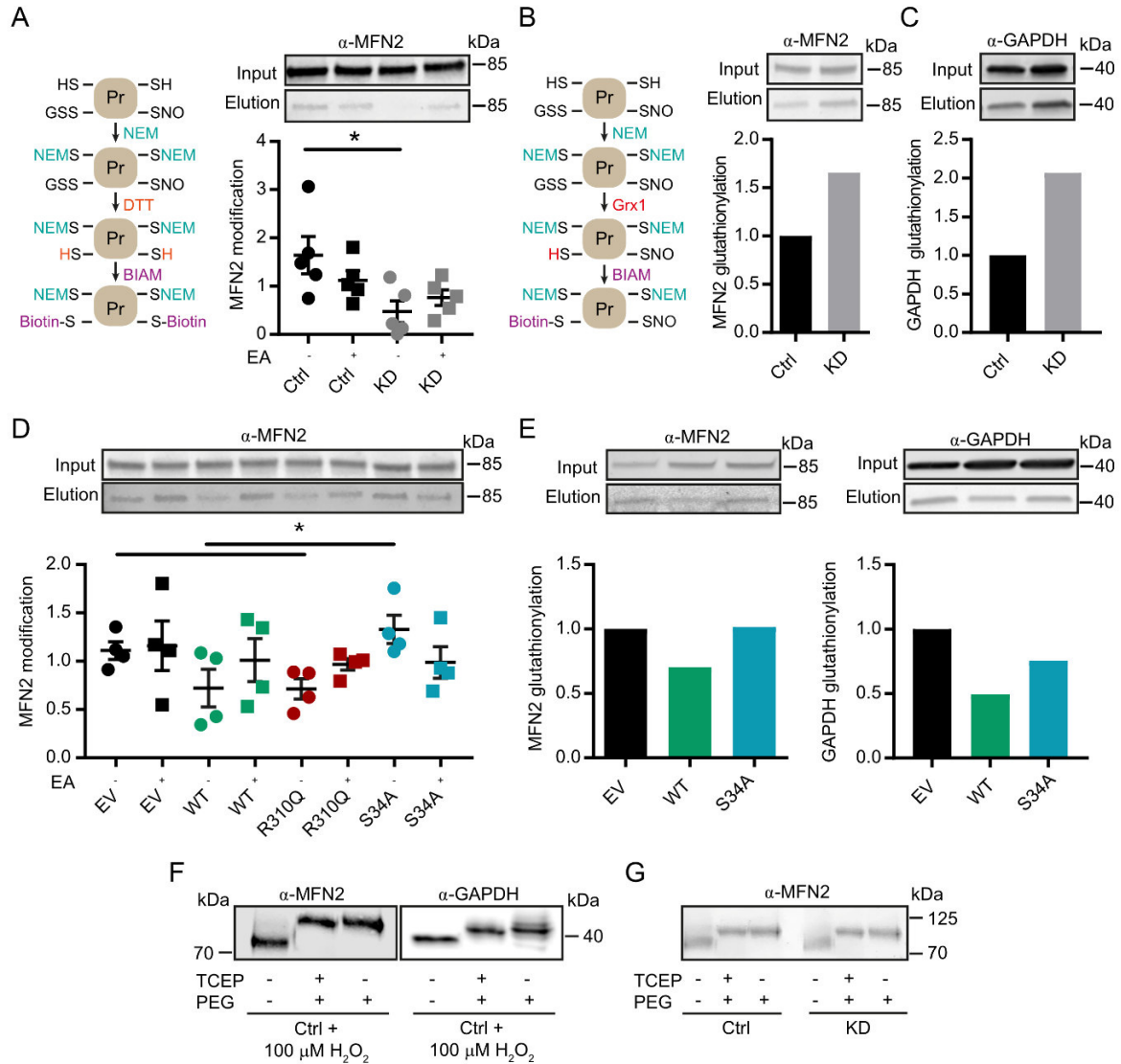


Figure 32 Posttranslational modification is dependent on GDAP1 expression

SH-SY5Y Ctrl and GDAP1 KD cells, as well as EV, WT, GDAP1-R310Q and GDAP1-S34A overexpressing cells were used for these experiments. A) Schematic illustration of the biotin-switch assay protocol for the reduction of all reversible PTMs with DTT; immunoblot and quantification of MFN2 and GAPDH modification, n=5 B) Schematic illustration of the biotin-switch assay protocol for the reduction of glutathionylated thiols with Grx1; immunoblot and quantification of glutathionylated MFN2 and GAPDH, n=1. C) Immunoblot and quantification of modified MFN2 in overexpressing cell lines after biotin-switch assay, n=4. D) Immunoblot and quantification of glutathionylated MFN2 and GAPDH in overexpressing cell lines after biotin-switch assay, n=1. E) Immunoblot of PEGylation shift assay of isolated mitochondria stained against MFN2 and GAPDH after H₂O₂ treatment. F) Immunoblot of PEGylation shift assay of isolated mitochondria comparing the thiol modification of MFN2 between Ctrl and KD cells. Data are displayed as scatter dot plots with SEM and statistical significance was calculated using Mann-Whitney test (A) or unpaired t-test (C), *p<0.05.

Results

It remains to be elucidated if this effect is a direct reaction of the GST domain with the thiols or rather an indirect effect on the intracellular redox state due to an altered GDAP1 expression.

6.3. Proteomic analysis of GDAP1 interaction partners in dependence of the redox state

A proteomic approach to identify interaction partners of GDAP1 consisted of the transduction of primary murine neurons overexpressing the *E. coli* biotin ligase BirA with adeno-associated viruses (AAVs) encoding the sequences for either HA-tagged GDAP1 (further referred to as GDAP1) or Avi-HA tagged GDAP1 (further referred to as Avi-GDAP1). BirA can covalently transfer biotin to the lysine residue in the Avi-tag sequence (Cull and Schatz, 2000; Schatz, 1993). Hence, Avi-GDAP1 was co-immunoprecipitated with magnetic streptavidin-beads and GDAP1 served as a non-biotinylated control. Immunoblotting together with neurons transduced with a virus encoding an empty vector-mCherry sequence only (EV) confirmed the biotinylation and GDAP1 expression in Avi-GDAP1 transduced neurons, while HA-GDAP1 overexpressing neurons only showed a positive band for elevated GDAP1 levels (Figure 33A). Isolated biotinylated proteins were analyzed and quantified via LC-MS. For the analysis, I chose the proteins which were tested as statistically significant for increased protein enrichment by comparing GDAP1 vs. Avi-GDAP1 and thus excluding the background signal. The Panther (Protein Analysis Through Evolutionary Relationships) classification system allows to classify data sets of proteins according to their molecular function, biological process or signaling pathway. Hence, Figure 33B (designed via <http://www.pantherdb.org>) gives an overview of these enriched proteins' function in different biological processes. More than 20 % of the enriched proteins were involved in metabolic processes, while another 15, 11 or 8 % of proteins were involved in cellular component organization, cellular response to stimulus or signal transduction, respectively. Such an overrepresentation of metabolic proteins would be in line with previous findings that link GDAP1 dysfunction to an impact on mt[Ca²⁺] levels, pyruvate metabolism and glycolysis. To further unravel these numerous results, I concentrated on proteins and highlighted those which play a role during glucose metabolism, cytoskeleton organization, glutathione metabolic processes, Ca²⁺ signaling or oxidative stress via String database (Figure 33C, designed via www.string-db.org). Besides others, Ca²⁺ signaling-derived proteins were detected, such as the calcium/calmodulin-dependent protein kinase, a serine threonine kinase that is activated by calmodulin upon Ca²⁺ binding. The CAMK2A and CAMK2B (subunit α/β) are both known to be involved in synaptic plasticity, neurotransmitter

Results

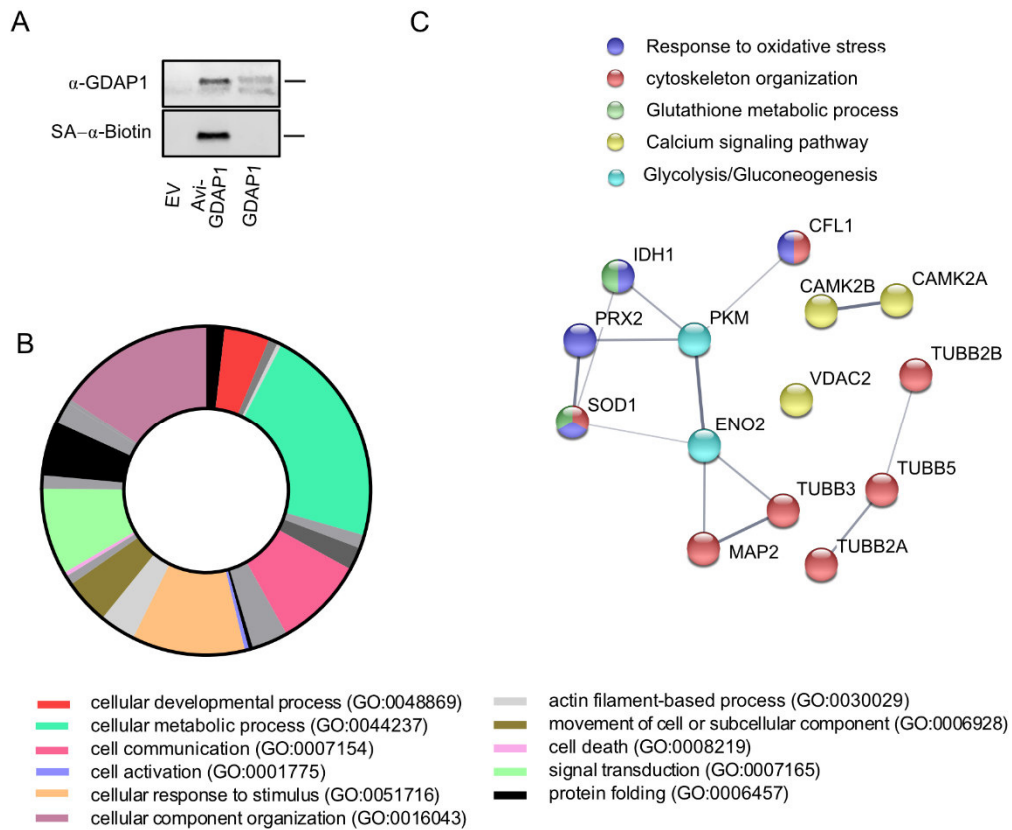


Figure 33 Proteomic screen for GDAP1 interaction partner

A) Immunoblot of cell lysates prior to the pulldown of biotinylated GDAP1 stained against GDAP1 and Biotin with fluorescently labeled streptavidin (SA) shows an overlap of biotinylation and GDAP1 protein. BirA pulldown was performed from neurons isolated from E16 embryos and cultured separately. B) Assignment of the identified proteins which were found as interaction partners for GDAP1 according to their biological function. A large proportion of the proteins regulate metabolic processes or cellular component organization. C) Network of proteins that were identified in the screen for GDAP1 interaction partners. CAMK2A/2B – calcium/calmodulin-dependent protein kinase 2A/2B; CFL1 – cofilin1; ENO2 – gamma-enolase 2; IDH1 – isocitrate dehydrogenase 1; MAP2 – microtubule-associated protein 2; PKM – pyruvate kinase M1/2; PRDX2 – peroxiredoxin 2; SOD1 – superoxide dismutase 1; VDAC1 – voltage-dependent anion channel 1; TUBB2A/2B/3/5 – tubulin β -2A/2B/3/5. The thickness of the connecting lines indicates the confidence of protein-protein associations. Data were from three independent experiments, which were measured in quadruplicates each. Only statistically significant proteins are shown, which were determined by t-test with Bonferroni correction; * $p < 0.05$.

release, synapse formation and sarcoplasmic reticulum (SR) Ca^{2+} transport (Borgesius et al., 2011; Küry et al., 2017; Narayanan and Xu, 1997; Tao et al., 2013). Purified proteins connected to glucose and pyruvate were the pyruvate kinase (PKM), as well as the isocitrate dehydrogenase 1 (IDH1), and the gamma-enolase 2 (ENO2). The presence of several tubulins appearing in this screen was very evident. Tubulins are crucial components of the cytoskeleton and control besides others mitotic spindle formation and cell growth and development, but can also serve as scaffold for mitochondrial transport (Bittermann et al., 2019; Compagnucci et al., 2016). The tubulins tubulin β -2A (TUBB2A), TUBB2B, TUBB3 and TUBB5 in particular are highly enriched in neurons (Cai et al., 2020) and interestingly, an interaction between GDAP1 and TUBB has been reported before in a yeast-two-hybrid experiment by Estela et al. (Estela

Results

et al., 2011). Cofilin1 is a cytosolic actin-binding factor, which induces the depolymerization of actin filaments in mitochondrial proximity and hence reduces DRP1 recruitment to the

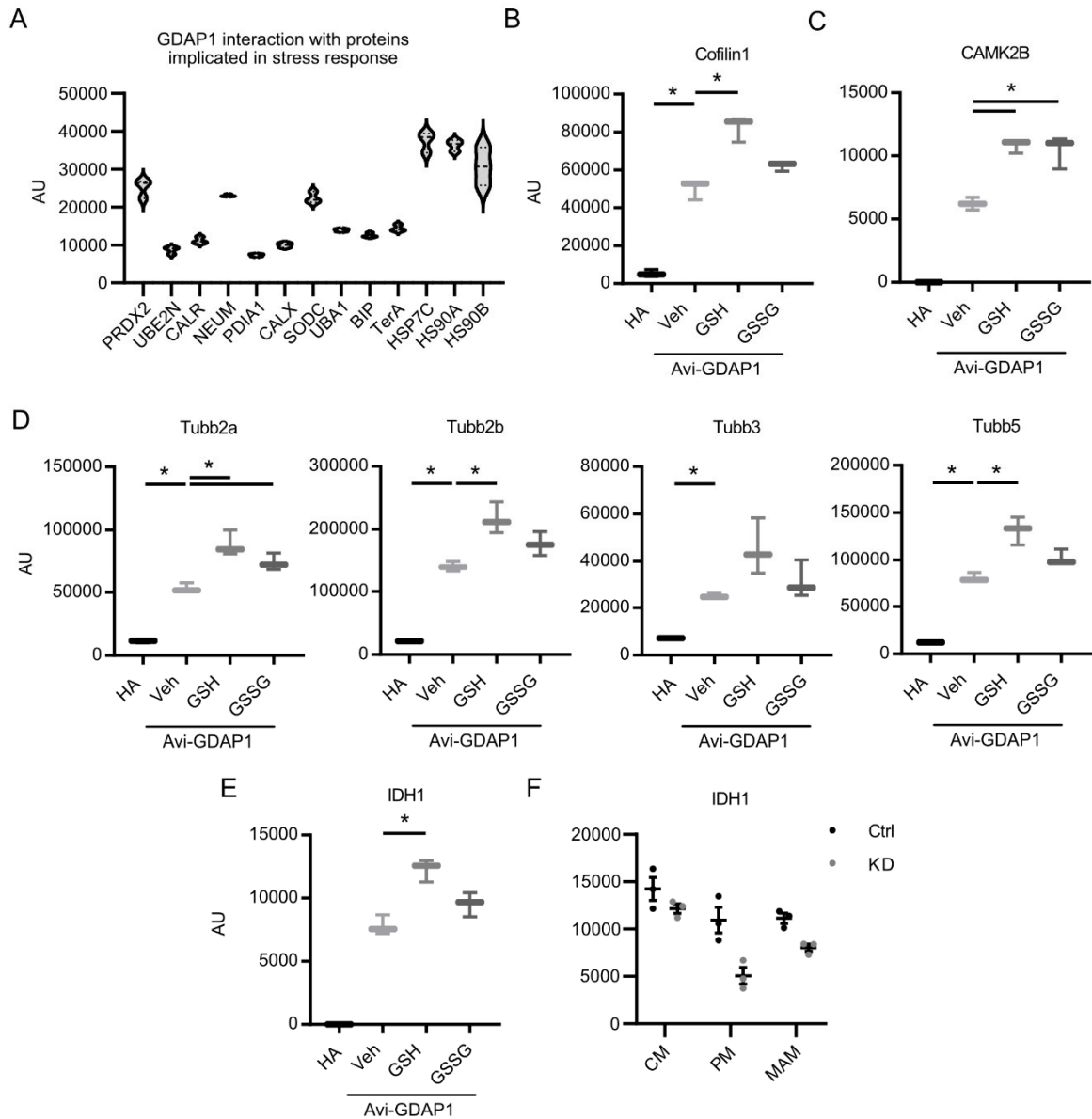


Figure 34 GDAP1 interaction partners in dependence of the redox state

A) Selected proteins that were identified in the pulldown screen as possible GDAP1 interaction partners and which play a role in cellular stress response. PRDX2, NEUM, SOD and heat shock proteins were amongst the more abundant proteins in this group. B-D) Co-purified proteins under basal conditions or upon GSH or GSSG addition prior to protein pulldown. B) Increased Cfl1 (cofilin1) levels upon GSH, but not GSSG addition C) Increased CAMK2b (calcium/calmodulin-dependent protein kinase IIb) levels after GSH and GSSG addition. D) Altered TUBB interaction with GDAP1 in dependence of the redox state. E) Increased IDH1 (isocitrate dehydrogenase 1) levels upon GSH, but not GSSG addition F) IDH1 abundance in mitochondrial or MERCs fractions of Ctrl and GDAP1 KD cells shows tendencies towards reduced IDH1 levels of mitochondria and MERCs in KD cells. Data are displayed as violin plots (A), Tukey's box and whiskers plots (B-E) and scatter dot plot and statistical significance was calculated with the nonparametric t-test in combination with Bonferroni correction; * $p < 0.05$.

mitochondria for fission induction (Bernstein and Bamberg, 2010; Li et al., 2015). Li et al. could show that cofilin1 migrates to the mitochondria simultaneously with regulation of DRP1 activity, and hence, affects the mitochondrial shape (Li et al., 2018).

Results

The probable interaction of GDAP1 with cofilin1, TUBB and IDH1 together with the ROS scavengers SOD1 and PRDX2 are further addressed in Figure 34. It shows the subset of proteins that were identified in the screen as possible interaction partners in the classification of protein subsets via Panther and which were in the group of proteins involved in cellular stress response. PRDX2 and SOD1 are amongst the more abundant proteins together with heat-shock proteins involved in stress-response and protein folding, and with neuromodulin (NEUM), which is a neuronal protein substrate for protein kinase C and which interacts with calmodulin in a Ca^{2+} -dependent manner, but is also involved in the development of synaptic plasticity (Kumar et al., 2013).

Additionally, prior to the SA-Biotin, I treated the cell lysates with either GSH or GSSG and compared the data set of pulled proteins to the untreated condition. Interestingly, GSH addition elevated GDAP1 interaction with cofilin1, but not the presence of GSSG (Figure 34B). CAMK2B levels were increased with both GSH and GSSG. Among the β -tubulins TUBB2B and TUBB5 also indicated an elevated interaction with GDAP1 in the presence of additional GSH instead of GSSG (Figure 34D). Increased levels of TUBB2A were detected in the pulldown both after GSH and GSSG addition. GSH addition also elevated the interaction of GDAP1 with the beforementioned IDH1 (Figure 34E) and there was no increase under GSSG addition. IDH1 catalyzes the conversion of isocitrate to α -ketoglutarate, which in turn can be taken up by the mitochondria to enter the TCA cycle (Raineri and Mellor, 2018). Analyzing the IDH1 levels in the mitochondrial and MAM fractions revealed a tendency towards reduced IDH1 at the mitochondria and the MAM fraction in GDAP1 KD cells (Figure 34F). Unfortunately, cofilin1 and CAMK2B peptides were not detected in the proteomic screen of the mitochondrial and MAM fractions, but in order to study if the altered MAM appearance and DRP1 recruitment are a consequence of altered cofilin1 regulation in GDAP1 KD cells, we did further studies on this protein and went back to the GDAP1 KD cell lines.

Quantification of the total protein levels of cofilin1 in whole cell lysates via IB did not show any variation in protein abundance between Ctrl and GDAP1 KD cells (Figure 35A). Phosphorylation of cofilin1 at serine 3 (S3) inhibits its actin depolymerization activity, leading to increased actin polymers encircling the mitochondria and to DRP1 recruitment to the OMM, eventually inducing mitochondrial fission (Siudeja et al., 2012). Quantification of p-cofilin1 via immunoblotting also did not reveal any differences between the cell lines (Figure 35A). To evaluate the mitochondrial proximity, I performed immunocytochemistry against cofilin1 and GRP75 as an OMM-protein, which was acquired with a confocal microscope (Figure 35B). The Imaris software and surface-surface contact XTensions allowing surface contact evaluation were used for further analysis and quantification. The software was first used to create 3D surfaces of mitochondria and cofilin1 spots, whose area were measured. Conforming to our

Results

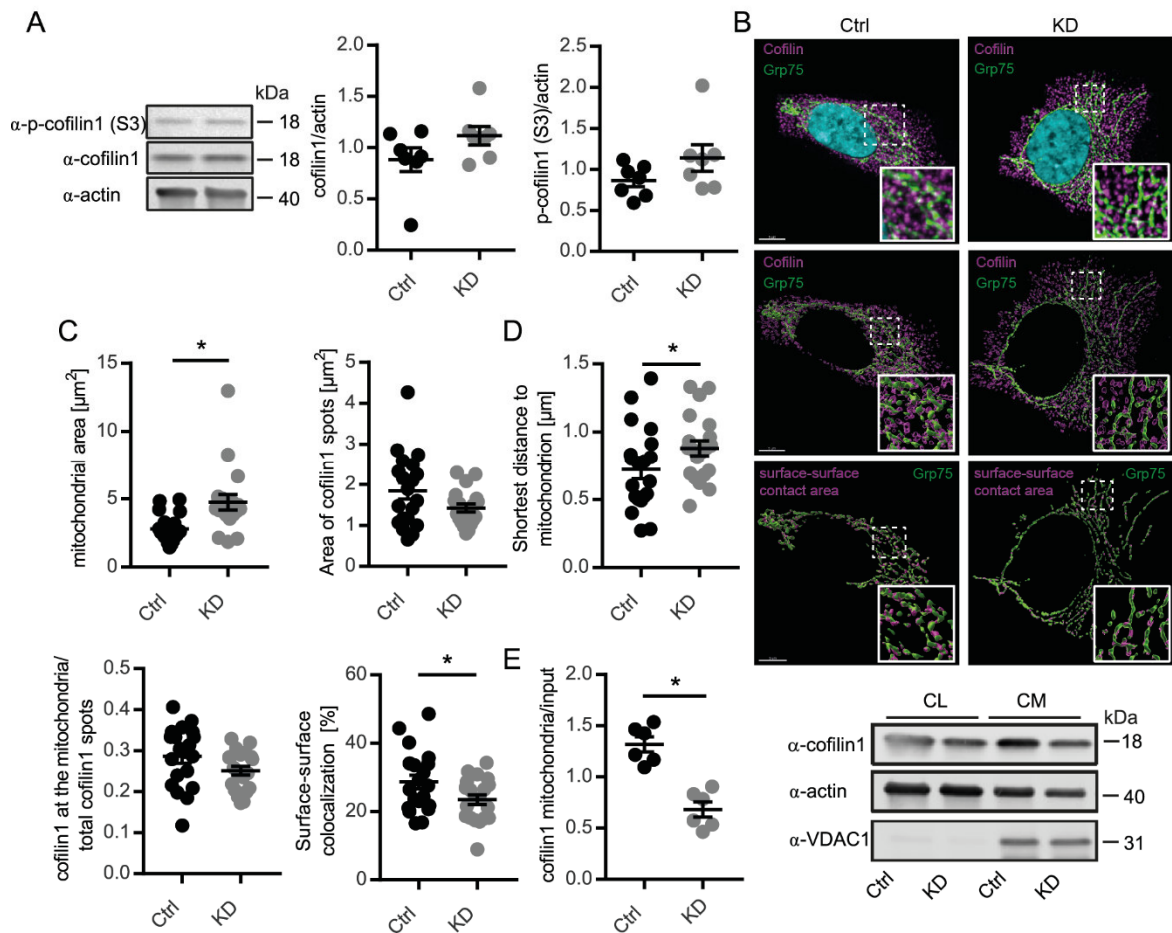


Figure 35 No alteration in cofilin1 protein levels but reduced cofilin1-mitochondria contacts in GDAP1 KD cells

Immunoblot of whole cell lysates and quantification of cofilin1 and p-cofilin1 (S3) protein levels. Actin served as loading control. B) Immunostaining of Ctrl and GDAP1 KD cells for Cofilin1 (magenta) and GRP75 (green) as mitochondrial protein. Image acquisition was done with the inverse confocal fluorescence microscope Leica TCS SP8. Nuclei were counterstained with 4',6-diamidino-2-phenylindole (DAPI). Conversion of the structures into surfaces using Imaris software (row 2) allowed evaluation of the contact area (row 3, red). Scale bar equals 5 μ m; n=20 cells per cell line. C) Quantification of mitochondrial area and cofilin1 spot size illustrated in (B) using Imaris software. D) Analysis of the distance between cofilin1 spots to the closest mitochondrion revealed an increased distance in GDAP1 KD cells. Imaris surface surface contact XTension was used to determine the proportion of the mitochondrial surface area in contact with cofilin1, which revealed a significant reduction. E) Analysis of cofilin1 abundance at the mitochondria after fractionation of crude mitochondria (CM) normalized to whole-cell cofilin1 levels (CL). Data are represented as scatter dot plot with SEM and statistical significance was calculated using nonparametric Mann Whitney test, * $p < 0.05$.

previous results indicating more elongated mitochondria, mitochondrial area was increased in GDAP1 KD cells, while there was no difference detected for the area of cofilin1 spots (Figure 35C). Interestingly, assessing the shortest distance between cofilin1 spots to mitochondria revealed a difference between the cell lines and was significantly increased in KD cells compared to the control (Figure 35D). Hence, I further analyzed the mitochondrial proximity of cofilin1. Though the number of cofilin1 spots colocalizing with mitochondria did not vary between Ctrl and KD, there was a significant reduction of the mitochondrial area colocalizing with cofilin1 (Figure 35D). To confirm these results in a second approach, we isolated

Results

mitochondria and quantified the amount of cofilin1 in the mitochondrial fraction normalized to the whole cell lysate, which also revealed significantly less cofilin1 protein in the mitochondrial fraction. Though GDAP1 expression did not impair the protein levels of cofilin1 and its phosphorylation state, it appears to be important for the mitochondrial proximity. Regarding the role of cofilin1 in respect to DRP1 recruitment to the OMM and mitochondrial shape, these results point towards an inhibition of cofilin1 via interaction with GDAP1. Cells with a reduced expression of GDAP1 and increased levels of active cofilin1 protein hence showed reduced DRP1 recruitment and more elongated mitochondria (Figure 36). Furthermore, the observation of increased width of MERCS in GDAP1 KD cells, greatly fits this idea and explains the upregulation of MCU to counterbalance impaired Ca^{2+} transition into the mitochondria, leading to the metabolic phenotype of increased PDH inhibition and a shift towards enhanced glutaminolysis in these cells (Figure 36).

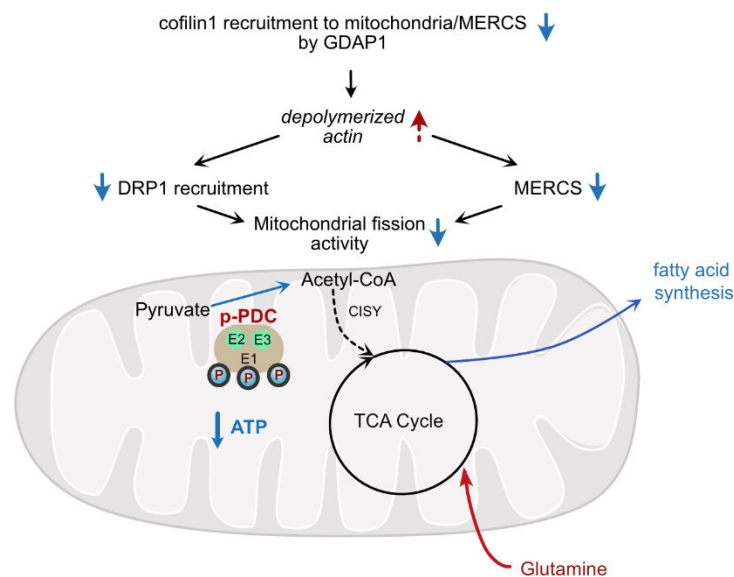


Figure 36 Regulation of mitochondrial dynamics via cofilin1 and DRP1 recruitment to the OMM and alterations in metabolism of GDAP1 KD cells

A reduced GDAP1-mediated recruitment of cofilin1 to the outer mitochondrial membrane (OMM) was observed in GDAP1 KD cells. Postulating an increased activity of the actin-binding protein cofilin1 leads to an hypothesized increase of actin depolymerization, which contributes to the observed reduced mitochondria-ER contact sites (MERCS), leading to diminished DRP1 recruitment to the OMM and more elongated mitochondria. Moreover, elevated levels of the inactive p-PDC cause the metabolic shift of GDAP1 KD cells towards increased glutaminolysis instead of glycolysis. However, mitochondrial ATP production was less efficient in GDAP1 KD cells and ATP levels were lowered. Arrows are color-coded if regulated in our GDAP1 KD model – red for increased levels or activity, blue for a reduction. Dotted arrows and italic letters indicate presumably reduced or elevated processes.

7. Discussion

In this work, I investigated the mitochondrial phenotype and metabolic changes of cell lines with a perturbation of GDAP1. Besides the changes in mitochondrial dynamics, I observed that both GDAP1 KD and CMT4A patient-derived cells reveal a strong metabolic phenotype with a blocked pyruvate conversion and a concomitant stronger glutaminolysis.

7.1. More elongated mitochondria in GDAP1 KD cells

Mitochondrial dynamics imply the ongoing processes of fusion and fission, rapidly responding to several signaling events. Hence, mitochondrial fusion can be a process that spares mitochondria from mitophagy, while mitochondrial fission enables the transport of mitochondria along the axons, but mitochondrial fragmentation can also facilitate mitophagy and the disposal of damaged mitochondria (Mao and Klionsky, 2013; Palikaras et al., 2018). Both GDAP1 and MFN2 can affect the mitochondrial shape to a great extent – if overexpressed, GDAP1 leads to increased fission while MFN2 leads to elevated fusion activity of the mitochondria. Niemann et al. already postulated that GDAP1 may not be an active mitochondrial fission factor by showing that GDAP1 is not able to induce fragmentation in the absence of Fis1 or the GTPase DRP1 in N1E-115 cells (Niemann et al., 2009). This was observed in cells expressing rmGDAP1 and dmGDAP1 mutants. In this work, I also saw a concomitant decrease in DRP1 levels and reduced DRP1-induced mitochondrial fission activity and hence, increased elongated mitochondrial shape in GDAP1 KD cells, together with reduced MFF protein levels. CMT patient-derived cells may reveal equal tendencies but more replicates are required for confirmation. From these findings, we can conclude and support the hypothesis that GDAP1 does not actively induce mitochondrial fission, but rather influences and regulates the activity of DRP1.

As described previously, there are several mechanisms and (de-)phosphorylation processes of DRP1 that control and regulate its activity. A further disease-associated finding is that NO- and A β -induced nitrosylation of DRP1 Cys644 occurs, activating the GTPase function of this protein and hence leading to mitochondrial fragmentation. This was shown in cell culture models and post-mortem Alzheimer's patients' brains (Cho et al., 2009a). In contrast, a later study could not confirm these results and did not see an effect of DRP1 nitrosylation on its activity. The researchers rather observed a NO-stress induced phosphorylation of Ser616, which initiated DRP1 oligomerization and mitochondrial fragmentation (Bossy et al., 2010). Lee and Kim recently introduced the cytoplasmic and ER chaperone protein disulfide isomerase (PDI) as an important regulator of nitrosylation and phosphorylation of DRP1. They propose that PDI acts as a NO-donor to DRP1, which induces its activity and mitochondrial fission. Hence, a PDI-KD leads to decreased levels of DRP1 nitrosylation and phosphorylation and to

more elongated mitochondria, though the precise mechanism of how nitrosylation favors the phosphorylation still remains largely unclear (Lee and Kim, 2018). These studies show that there is a redox-regulated mitochondrial fission and fusion activity and DRP1 may be an important protein involved in these processes, most probably by redox-modification of the DRP1 C644.

The cytosolic phosphatase calcineurin (CaN) showed altered expression levels in our cell lines – decreased in WT overexpressing cells but increased in KD and R310Q or S34A overexpressing cells. CaN not only controls the dephosphorylation of various enzymes or the NFAT translocation to the nucleus upon stress stimuli, but also seems to be regulated by superoxide (O_2^-) and nitric oxide (NO) (Namgaladze et al., 2002). Its redox-sensitive Fe^{2+} Zn^{2+} active center can be oxidized by O_2^- and NO – while O_2^- apparently inhibits the CaN activity, NO and SOD rather antagonize this function, both in a calcium/calmodulin-dependent manner (Namgaladze et al., 2002). CaN also regulates the Ca^{2+} -release of the ryanodine receptor (RyR), a second crucial ER-resident Ca^{2+} channel besides the IP3R (Bandyopadhyay et al., 2000). Via the FKBP12.6 protein, CaN mediates RyR activity in a Ca^{2+} -dependent manner upon caffeine addition – Ca^{2+} -release is elevated in cardiac muscle cells when CaN is inhibited, because the RyR remains in a hyperphosphorylated state (Bandyopadhyay et al., 2000; Shin et al., 2002). However, we did not detect an effect of NFAT translocation due to the altered CaN expression but we saw I) altered DRP1 migration to the mitochondria and II) increased $cyt[Ca^{2+}]$ levels. We ruled out an altered calcineurin activity in our cells as an active regulator of DRP1 activity, though its protein levels are elevated in the GDAP1 KD and S34A/R310Q mutant overexpressing cells.

7.2. Impaired Ca^{2+} signaling and reduced MERCS in GDAP1 KD cells

Pla-Martín et al. generated the GDAP1 KD cell line and provided us with the cells to further study the mechanism of GDAP1 (Pla-Martín et al., 2013). For the first time they showed that GDAP1 is indeed enriched in the MAMs and that the KD reduces these contact sites, though they did not see a morphological effect on the mitochondria in KD cells. This work not only revealed a shift of the mitochondrial shape towards more elongated mitochondria, but also an alteration of the MERCS, MAM composition and Ca^{2+} derived signaling. The most important finding about the MERCS' characteristics was that the proximity between mitochondria and ER was significantly increased. How mitochondrial shape and Ca^{2+} homeostasis are connected still needs further investigation but Kowaltowski et al. recently provided some evidence that there are mechanistical links (Kowaltowski et al., 2019). Apparently, the capacity for mitochondrial Ca^{2+} uptake varies upon mitochondrial morphology and membrane potential

Discussion

(Kowaltowski et al., 2019). An inhibition of mitochondrial fission results in increased mitochondrial Ca^{2+} uptake, while more fused mitochondria appear to have diminished mitochondrial Ca^{2+} levels at steady-state (Kowaltowski et al., 2019). To favor the local Ca^{2+} buffering and subsequent ATP supply, the motility of mitochondria is arrested upon oscillations of ER- Ca^{2+} release by the IP3R or the ryanodine receptor (RyR) (Yi et al., 2004).

It is widely accepted that the structure and proximity of MERCS are modulating the mitochondrial function and fate. They shape the Ca^{2+} homeostasis of the mitochondria and strongly influence their survival and susceptibility to mitophagy or even cell death (Bernard-Marissal et al., 2018; Hayashi et al., 2009; Rowland and Voeltz, 2012). These mechanisms have been found to be disturbed by either protein mutation or loss and other pathogenic phenotypes in neurodegenerative diseases, such as Parkinson's disease or CMT (Basso et al., 2018; Bernard-Marissal et al., 2018; de Brito and Scorrano, 2009). As mentioned previously, besides its vital role in mitochondrial fusion induction, it is still under debate to what extent MFN2 regulates the MERCS formation. Recent studies propose that MFN2 tethering between ER and mitochondrial MFN2 takes place to avoid a toxic proximity of the organelles, preventing Ca^{2+} overload in the mitochondrial matrix, which might lead to mPTP opening and hence, increased mitophagy and cell death (Cosson et al., 2012; Filadi et al., 2015). CMT2A patient-derived fibroblasts carrying the R94Q mutation in MFN2 reveal a loss of MERCS, accompanied by Ca^{2+} handling defects and ER stress (Bernard-Marissal et al., 2019). Recent studies from Larrea et al. with different CMT2A patient-derived fibroblasts with mutations in MFN2 confirmed these findings of disturbed contact sites with increased distances between the organelles and a pronounced phenotype which correlates with disease-progression (Larrea et al., 2019). In MEF cells expressing MFN2 carrying the R94Q mutation we did not observe differences in mitochondrial respiration, but an affected mitochondrial shape towards less fusion activity, which was even more pronounced after low H_2O_2 concentration (Wolf et al., 2019). Furthermore, these cells revealed a metabolic shift towards increased cellular and mitochondrial uptake of glucose and pyruvate, respectively, but a supposedly dysfunctional mitochondrial quality control and degradation mechanism (Wolf et al., 2019).

Interestingly, MERCS have been proven to be implicated in the mechanism of mitochondrial fission, as stated by Friedmann et al. (Friedman et al., 2011). Together with actin polymers that are formed, the ER shapes tubular structures that encircle the mitochondria and hence marks the site of constriction, even prior to DRP1 translocation.

The ER-anchored protein inverted formin 2 (INF2), which once mutated can also lead to CMT disease (Boyer et al., 2011), is strongly linked to this mechanism. Its Ca^{2+} -dependent activation goes along with enhanced mitochondria-ER contact sites and INF2 appears to regulate mitochondrial dynamics by inducing actin polymerization at these sites (Shao et al., 2015).

Discussion

This is followed by a recruitment of DRP1 and an initiation of mitochondrial fragmentation (Chakrabarti et al., 2018; Korobova et al., 2013). Chakrabarti et al. also proposed that this INF2-induced actin polymerization is crucial for mitochondrial Ca^{2+} uptake in response to stimulated ER Ca^{2+} release (Chakrabarti et al., 2018). The subsequent Ca^{2+} increase in the matrix via MCU apparently induces inner mitochondrial membrane constriction and fusion induction (Chakrabarti et al., 2018; Cho et al., 2017; Ji et al., 2015). Cofilin1, a member of the ADF/cofilin family – which is composed of muscle-cofilin, non-muscle cofilin and the actin depolymerizing factor (ADF) – potentially interferes with these sites of actin polymerization by ER-anchored INF2 that is required for fission induction via DRP1 recruitment (Rehklau et al., 2017). Phosphorylation of serine 3 in cofilin1 inhibits its actin-binding ability and was even observed to correlate to the neurodegenerative disease pantothenate kinase-associated neurodegeneration (PKAN) which leads to diminished levels of CoA, the acetyl-CoA precursor (Siudeja et al., 2012). In this context, an inactivation of cofilin1 was observed with a reduction of CoA levels (Siudeja et al., 2012). Interestingly, dephosphorylation of cofilin1 is mediated by CaN-induced activation of the protein phosphatase slingshot-1L in a Ca^{2+} -dependent manner (Descazeaud et al., 2012; Zhao et al., 2012). This process is counteracted by CAMK2, which phosphorylates slingshot-1L (Zhao et al., 2012). In this work, we also identified the two CAMK2 subunits, CAMK2A and CAMK2B as a potential interaction partner of GDAP1. The non-muscle cofilin actively depolymerizes actin filaments, thereby preventing DRP1-induced fission. During oxidative stress, the four cysteines 39, 80, 139 and 147 of cofilin1 appear to be oxidized to intramolecular disulfides, which largely affect its actin-binding ability (Gellert et al., 2015; Hoffmann et al., 2019). In response to the oxidant taurine chloramine, Luo et al. observed oxidation of the methionine 115 in cofilin1, which also prevents its actin depolymerization activity and rather induces mitochondrial translocation of cofilin1, followed by cytochrome c release and swelling of the mitochondria (Luo et al., 2014). These findings also give cofilin1 a decisive role in the induction of oxidant-mediated apoptosis (Klamt et al., 2009; Luo et al., 2014). An impact of cofilin1 expression and mitochondrial shape was determined by Rehklau et al., who observed increased DRP1 migration towards the mitochondrial outer membrane and elevated fission activity in cofilin1 knockout (KO) MEF cells, but no change in mitochondrial function (Rehklau et al., 2017). Cofilin1 KO MEF cells revealed increased fission activity, concomitant with increased Ser616 phosphorylation and Ser637 dephosphorylation of DRP1. Restoring the cofilin1 expression with an actin-binding deficient mutant of cofilin1 does not rescue the mitochondrial shape (Rehklau et al., 2017). Moreover, cofilin1 also undergoes glutathionylation, first identified in a screen for glutathionylated proteins in T-lymphocytes upon treatment with the thiol-oxidizing reagent diamide (Fratelli et al., 2002). This PTM seems to have an inhibiting effect on its actin-binding activity and hence leads to INF2-induced DRP1

Discussion

transmigration and mitochondrial fragmentation (Fratelli et al., 2002; Kruyer et al., 2019). These indications that cofilin1 is redox-sensitive and activated upon oxidative stress, together with the fact that cofilin1 was found in our screen for GDAP1 interaction partners, raise the question if an interaction somehow regulates DRP1-induced. Despite the downregulation of DRP1 protein levels and migration to the mitochondria, I also observed significantly elevated DRP1 levels in cells overexpressing rmGDAP1 R310Q and loss-of-function mutation S34A – though mitochondria appear hyperfused in these cells. Furthermore, GDAP1 interaction with cofilin1 was even more pronounced in the presence of GSH, but not GSSG. Hence, assuming a regulation of GDAP1 to cofilin1 via its GST and substrate-binding domain, an interaction could lead to cofilin1 glutathionylation, inactivation of actin depolymerization, DRP1 migration to the mitochondria and eventually result in fragmented mitochondria. The weaker interaction of ER and mitochondria in GDAP1 KD cells is also be in line with this hypothesis. Indeed, we showed that there is a reduced proximity and colocalization area of cofilin1 with the mitochondria in the KD cells compared to the control. In these experiments, we co-stained cofilin1 with the OMM protein GRP75, which is particularly enriched in MAMs (Honrath et al., 2017; Szabadkai et al., 2006). Thus, the reduced colocalization of cofilin1 directly refers to the reduced abundance of cofilin at these contact sites. A mechanism of such kind would be a great help to explain our findings and to unravel one of the processes through which GDAP1 acts on mitochondrial dynamics (Figure 37). A comparison of actin filament dynamics in our cell culture models is a follow-up approach of high interest. These cofilin1-regulating functions could be abolished by GDAP1 mutation. The observation made by Niemann et al. regarding GDAP1's inability in inducing mitochondrial fission in the absence of DRP1 and Fis1 (Niemann et al., 2009), also greatly fit this idea. Furthermore, we confirmed an interaction of GDAP1 with β -tubulins, which has been reported by Estela et al, who also proposed that this interaction is mediated by the α 4- α 5 loop in the GDAP1 sequence (Estela et al., 2011).

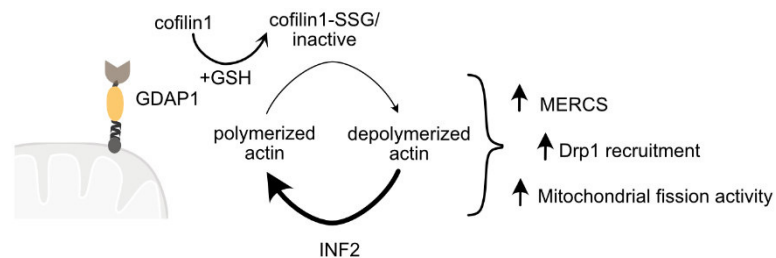


Figure 37 Hypothesized mechanism of GDAP1 and cofilin interaction on mitochondrial shape

A redox-dependent interaction of GDAP1 and cofilin1 could lead to glutathionylation (-SSG) and inhibition of cofilin1's actin depolymerization activity. Hence, the INF-driven polymerization of actin filaments is enhanced, favoring the MERCS appearance, DRP1 recruitment to the OMM and eventually, mitochondrial fission activity.

7.3. Impaired IP3-mediated Ca^{2+} release from the ER

Patterson et al. described a mechanism that involves the interaction between GAPDH and the IP3R. The IP3R releases Ca^{2+} to the cytosol upon IP3- and NADH binding, while one by-product of GAPDH activity is the generation of NADH (Kaplin et al., 1996; Patterson et al., 2005). Thus, Patterson et al. showed that upon disulfide bridge formation between GAPDH and the IP3R and NADH delivery, the IP3R-driven Ca^{2+} release from the ER to the cytosol is activated. This may be due to the cysteines C992 and C995 in the IP3R and C150 in GAPDH. We indeed saw that upon IP3R stimulation with CCH, the IP3R is less active in our model of GDAP1 KD cells, leading to augmented cyt[Ca^{2+}] levels and dynamics of the Ca^{2+} released from the ER (Figure 9F), but similar levels of the IP3R protein itself compared to the control cells. Additionally, ER fractionations of GDAP1 KD cells exhibited less GAPDH located at the ER, all indicating that this may be a promising approach to understand the phenotype caused by a disturbed GDAP1 expression.

CCH stimulates the production of IP3, which can in turn bind and stimulate the IP3R for channel opening and Ca^{2+} release from the ER lumen into the cytosol (Van Acker et al., 2002; White and McGeown, 2002). IP3 is hydrolyzed from phosphatidylinositol 4,5-bisphosphate (PIP_2) by the enzyme phospholipase C. Thus, besides caffeine or ATP, CCH is often used for stimulating Ca^{2+} release from the ER to measure the Ca^{2+} uptake of the mitochondria. It can serve to characterize and quantify the MERCS' abundance in cells or tissues. Yet unpublished data generated in our group showed a reduced mitochondrial Ca^{2+} load in GDAP1 KD cells, but I did not observe a difference in the CCH-driven mitochondrial Ca^{2+} uptake. Importantly, I could reproducibly show GDAP1 location at the MAMs and that the proximity between ER and mitochondria was elevated by GDAP1 silencing. However, the overregulation of the mitochondrial Ca^{2+} import channel MCU may indicate an impaired Ca^{2+} transition into the mitochondrial matrix.

In the study by Xu et al. on Ca^{2+} levels together with apoptosis in podocytes, the research group performed co-immunoprecipitation experiments and confirmed the importance of the proteins enriched in the MAMs which regulate the Ca^{2+} exchange (Xu et al., 2018). Complex formation of the IP3R together with VDAC1 and Grp75 route the Ca^{2+} influx from the ER to the mitochondrial intermembrane space and further into the mitochondrial matrix by MCU (Xu et al., 2018). GRP75 thereby functions as a stabilizing and bridging protein between VDAC1 and the IP3R (Xu et al., 2018). In the absence of either one of these proteins, the mitochondrial inward flux of Ca^{2+} upon the addition of apoptosis-inducing reagents adriamycin (ADR) or angiotensin II (Ang II) – usually leading to mt[Ca^{2+}] overload – is reduced (Xu et al., 2018). In our GDAP1 KD cells, there was no difference in protein levels of neither the IP3R, nor of VDAC1 or Grp75. Only the MCU shows an upregulation in the KD cells, which points towards

Discussion

an insufficient Ca^{2+} transport into the mitochondrial matrix. The observed reduced mitochondrial ATP production in our GDAP1 KD cells could also trigger an increased Ca^{2+} import into the mitochondrial matrix, because Ca^{2+} is known to stimulate several matrix dehydrogenases, resulting in increased metabolic turnover in the TCA cycle and hence, in elevated ATP generation (reviewed in Denton, 2009). Favaro et al. studied mice with a depletion of DRP1 expression in skeletal muscle and observed a concomitant decline in muscle fibers and protein synthesis including increased catabolism but less autophagy and mitophagy (Favaro et al., 2019). Mitochondrial shape in DRP1 KO skeletal muscle fibers was elongated compared to the control mice. While the ETS complex formation was not altered, the mitochondrial respiration was reduced in these mice. Besides indications of ER stress, Favaro et al. detected that high-frequency stimulation of 60 Hz induced an increased Ca^{2+} influx into the mitochondrial matrix in DRP1 KO tissue and a lower $\text{cyt}[\text{Ca}^{2+}]$ peak. But Ca^{2+} release upon caffeine or thapsigargin was also reduced in DRP1 deficient muscle tissue (Favaro et al., 2019). Furthermore, DRP1 KO induces a reduction in microRNA-1 (miR1), which is a known regulator of MCU translation and protein expression (Zaglia et al., 2017). Hence, reduction in miR1 leads to an increase in MCU upon DRP1 KO, while steady-state $\text{mt}[\text{Ca}^{2+}]$ was unchanged (Favaro et al., 2019). This MCU upregulation rather led to an overload of mitochondria, which revealed a swollen and unhealthy appearance in ultrastructural images of muscle tissue (Favaro et al., 2019). Unless miR1 is muscle-specific, it would be interesting if there is an equivalent regulatory pathway in neuronal cells that might be affected in our cells as well (Zaglia et al., 2017).

Looking at the Ca^{2+} released from the ER upon CCH stimulation, it is evident that not only the amount of Ca^{2+} release but also the kinetics were lowered in our KD cells. These findings can also be connected to the redox-sensitivity and redox-dependent activity of the IP3R (Joseph et al., 2018) or an impaired IP3 production in response to CCH. Interaction of type 1 IP3R (IP3R1) and the ER chaperone ERp44 under reducing conditions is known and favors IP3R inhibition (Joseph et al., 2019). The IP3R1 harbors 5 cysteines located in the ER lumen, while 55 cysteines are cytosolic and it is still largely unclear how oxidation and other PTMs in IP3Rs affect the function; however, Joseph et al. compared WT IP3R1 response to the oxidant compound thimerosal, which usually potentiates the CCH-induced Ca^{2+} release. Interestingly, IP3R1 constructs deficient of the first 12 N-terminal cysteines lack this response (Joseph et al., 2018, 2019). Besides others, the overexpression of the glutathione peroxidase 8 (GPX8) has recently been shown to affect the IP3R activity (Yoboue et al., 2017). In that study, the IP3R was stimulated with histamine and the authors discovered an attenuated Ca^{2+} release from the ER to both the cytosol and the mitochondria. They also observed that GPX8 might be important for $\text{ER}[\text{Ca}^{2+}]$ refilling through SERCA interaction (Yoboue et al., 2017). Before

combining these studies with the GDAP1 protein, it is valuable to mention that an impaired SOCE-driven Ca^{2+} entry and $\text{ER}[\text{Ca}^{2+}]$ was identified in SH-SY5Y cells with silenced GDAP1 expression and GDAP1 KO mice together with an impaired mitochondrial distribution at the subplasmalemmal membrane (Barneo-Muñoz et al., 2015; González-Sánchez et al., 2017; Pla-Martín et al., 2013). The finding of an equal dysregulation of mitochondrial distribution and SOCE activation in HeLa cells overexpressing either DRP1 or Fis1 emphasizes the impact of mitochondrial dynamics and motility on cellular Ca^{2+} homeostasis and may even provide a mechanistic connection between GDAP1 and the mitochondrial fission proteins DRP1 and Fis1 (Frieden et al., 2005). One presumable mechanism through which GDAP1 acts on SOCE activity may be an interaction of the ER-protein junctophilin, which mediates the interaction between STIM1 and Orai1 channels at the plasma membrane (Pla-Martín et al., 2015). Interestingly, the assembly and dynamics of actin filaments and the cytoskeleton are also highly regulated by intracellular Ca^{2+} kinetics, in particular the SOCE (Galán et al., 2011; Martín-Romero et al., 2017). Thus, depolymerization of actin filaments was reported to result in an increase of SOCE (Galán et al., 2011).

7.4. Metabolic defects upon aberrant GDAP1 expression

An important Ca^{2+} -dependent process in the mitochondrial matrix is the conversion of pyruvate to acetyl-CoA by pyruvate dehydrogenase, which is a crucial link between glycolysis and the TCA cycle. Especially neurons highly depend on oxidative phosphorylation for energy production rather than on glycolysis, which highlights the importance of a well-functioning TCA cycle (Szelechowski et al., 2018). The PDH consists of an α and β subunit (E1) and forms the pyruvate dehydrogenase complex (PDC) together with dihydrolipoyl transacetylase (E2/DLAT) and dihydrolipoyl dehydrogenase (E3/DLD) (Lander et al., 2018). The PDC is activated via dephosphorylation by the pyruvate dehydrogenase phosphatase, which in turn is activated by Ca^{2+} . In its inactive state, the PDC is phosphorylated at three serine residues, S293, S300, and S232, all of them located in the α 1 subunit of the PDH E1 (Korotchkina and Patel, 2001; Linn et al., 1969). Thus, less $\text{mt}[\text{Ca}^{2+}]$ can lead to less active PDC and diminished levels of acetyl-CoA.

Upstream of the PDH, regulating the pyruvate conversion, is the mitochondrial pyruvate carrier (MPC), which is located at the inner mitochondrial membrane and imports pyruvate into the mitochondrial matrix. Several mutations in the *MPC* gene are known to date with consequences ranging from early death to peripheral neuropathies or visual impairments which were recently described by Oonthonpan et al. (Oonthonpan et al., 2019). The described mutations can amongst others lead to either impaired ability of MPC1 complex formation with

MPC2 or to an inactive MPC complex (Oonthonpan et al., 2019). The dysfunction of either of the subtypes also results in the loss of the other and cannot be compensated or recovered at this point, thus leading to a loss of mitochondrial pyruvate uptake (Bricker et al., 2012; Herzig et al., 2012; Schell et al., 2014). In some cases of a disrupted MPC function, increased glutaminolysis, ketogenesis or β -oxidation of fatty acids can be observed in a compensatory manner, mainly dependent on the cell type or tissue specification (Gray et al., 2015; Vacanti et al., 2014; Yang et al., 2014).

GDAP1 KD cells, compared to the control cell line, revealed an increase in the phosphorylated PDH E1 α subunit, indicating a decreased PDH activity and pyruvate conversion. Though it is known that glutamine stimulation can induce PDH phosphorylation and inhibition (Haussinger et al., 1982), the results from this work rather implicate that glutaminolysis is strengthened as a result of impaired cytosolic and mitochondrial Ca^{2+} signaling, inefficient pyruvate conversion to acetyl-CoA and hence, citrate entry into the TCA in GDAP1 KD cells.

We also ruled out hyperactivated glycolysis due to the increased decline of cytosolic ATP upon 2-DG addition. This has only been shown before in skeletal muscle cells (Lassiter et al., 2018). Rather, the cells rely less on glucose than on glutamine. Our GDAP1 KD cell lines revealed increased phosphorylation of PDH, and both *in vitro* models including patient-derived motoneurons showed less fatty acid synthesis as well as dramatically reduced glutamine and glutamate levels, together with elevated GDH levels. A possible ATP-consuming process which is more active in GDAP1 KD cells could be gluconeogenesis. The pyruvate carboxylase is activated by an accumulation of pyruvate in the mitochondrial matrix and the conversion of pyruvate to OAA happens under ATP consumption (Bender and Martinou, 2016). The mitochondrial ATP levels in GDAP1 KD cells are significantly reduced, which could be a result of the inhibited PDH and increased gluconeogenesis.

Recently, Szelechowski et al. studied primary motoneurons of an Amyotrophic Lateral Sclerosis (ALS) mouse model carrying a point mutation in the SOD1 protein, for their metabolic characteristics. They observed reduced respiration and ATP generation in both fibroblasts and motoneurons of SOD1G93A mice – an overall defect of the oxidative phosphorylation (Szelechowski et al., 2018). Additionally, they observed that these motoneurons rely not only on glycolysis for energy production, but also more on fatty acid oxidation in comparison to fibroblasts to feed the energy metabolism and to improve cell survival (Szelechowski et al., 2018). The induction of β -oxidation was also seen in terms of nutrient stress and autophagy induction, where lipid droplets (LDs) were observed in close proximity to mitochondria. This proximity allowed a transition of fatty acids into the mitochondria, enabling β -oxidation of fatty acids and further processing into acetyl-CoA, which enters the TCA cycle to finally boost the oxidative phosphorylation and ATP production (Rambold et al., 2015). This process was more

efficient in fused and elongated mitochondria, whereas increased fragmented mitochondria rather revealed an uneven fatty acid uptake and hence an increase in number and size of the LDs and reduced energy production via oxidative phosphorylation (Rambold et al., 2015). Inspired by these findings, we also performed this experiment, including HBSS starvation for several time periods and quantified I) the amount and size of lipid droplets and II) the translocation of fatty acids into the mitochondria under basal and starved conditions. We did see a reduction in the number of LDs in GDAP1 KD cells only under basal conditions. Starvation induced both the increase of LD number and the fatty acid transfer into mitochondria in both cell lines. However, we did not see an altered lipid transfer into the mitochondria in KD cells neither under basal nor under stressed conditions, which excludes an altered activity of β -oxidation of fatty acids. Given the observed interaction of GDAP1 with several proteins involved in metabolism such as IDH1 and PKM (Figure 33), the question arises whether GDAP1 has a regulatory function on these proteins.

AMPK is a central regulator of cellular processes controlling ATP generation and ATP consumption and its activation via CAMKK β is mediated by elevated Ca^{2+} levels (Woods et al., 2005). Also, mitochondrial fragmentation is induced upon AMPK activation, and GDAP1 is downregulated (Lassiter et al., 2018). In this work, unfortunately, I could not establish IB against phosphorylated AMPK, but I inhibited AMPK activation via CAMKK β and chose mitochondrial shape as a GDAP1-specific readout. However, no alteration was noticeable neither in GDAP1 KD nor overexpression compared to respective controls (Figure 16, Figure 29).

It is apparent that alterations in mitochondrial shape induced by a GDAP1 KD are tightly linked to Ca^{2+} homeostasis and metabolism, eventually affecting ATP production.

7.5. Altered protein glutathionylation in GDAP1 KD cells

Initially, GDAP1 was structurally compared to zeta class 1 (GSTZ1), omega class 1 (GSTO1) and theta class 1 (GSTT1) GST due to its sequence identity of 29-32% of the GST-N domain (Shield et al., 2006). A sequence identity of 29 % was declared for the presumed GST-C domain with another GST-like protein, the chloride intracellular ion channel 5 (CLIC-5) (Shield et al., 2006). CLIC proteins are anion channels with a broad range of distribution and function (Khamici et al., 2015; Littler et al., 2010). They can exist as both soluble and membrane-bound proteins, where they adopt an ion channel function (Littler et al., 2010). Though the functions need to be distinguished depending on their localization, the active center cysteine can regulate its channel function of CLIC1 in a redox-sensitive manner (Singh and Ashley, 2006). However, no enzymatic GST activity has been proven so far, and CLIC proteins have a GRX-

like activity, appear to dimerize upon oxidizing conditions and can inhibit the ER-Ca²⁺ channel ryanodine receptor (Khamici et al., 2015; Littler et al., 2010; Rao et al., 2017).

Still, it is controversially discussed if GDAP1 has a GST-like enzymatic function and how it leads to the pathogenesis of CMT4A patients. Huber et al. proposed the model of an amphipathic pattern of the HD domain, which regulates the GST activity of the protein (Huber et al., 2016). Depending on the mode of inheritance of GDAP1 mutation, GDAP1 would adapt the active or the inactive conformation. Hence, dominant mutations in GDAP1 (dmGDAP1) leads to a hyperactive GST function, whereas recessive mutations (rmGDAP1) shifts the protein into an inactive GST and hyperfused mitochondrial network (Huber et al., 2016). Googins et al. in contrast did not confirm a GSH-binding ability of GDAP1 but verified a substrate-binding ability towards EA and involvement of both, the α 4- α 5 loop and HD domain in substrate-binding and protein stability (Googins et al., 2020). Immunoblotting the lysates of our CMT4A patient-derived cells revealed no GDAP1 protein band for patient #2, whose mutations lead to exon 4 skipping and a loss of GST-C, HD and the TMD domains (Figure 22B, Figure 23B). An increased protein instability due to the loss of the HD domain may thus lead to protein degradation and an inability to detect GDAP1 on the protein level.

Oxidative decarboxylation of isocitrate and NADP⁺ to α -ketoglutarate and NADPH is catalyzed by IDH1, which is mainly located in the cytosol and peroxisomes and has also been identified as a possible interaction partner of GDAP1 in this work. NADPH is a cofactor for GSH biosynthesis and maintains the levels of thioredoxins and peroxiredoxins (Kaminska et al., 2019; Shi et al., 2014). Additionally, glutathione reductase (GR) is NADPH-dependent, resulting in the reduction of oxidized glutathione (GSSG) to GSH. Hence, the activity of IDH1 usually goes along with an increase of reduced glutathione to inactivate ROS (Shi et al., 2014). Mutations of IDH1 can lead to glioblastoma multiforme and result in GSH depletion and elevation of ROS (Parsons et al., 2008; Shi et al., 2014). Moreover, an elevation of ROS results in increased levels and activity of both mitochondrial and cytoplasmic IDH and α -ketoglutarate, which in turn act as ROS scavengers in the TCA cycle (Mailloux et al., 2007). We saw an interaction of GDAP1 with IDH1, which was enhanced upon GSH addition, but not GSSG, and a tendency towards decreased levels of IDH1 in mitochondrial and MAM fractions. Various studies already showed an increase in GSH levels upon both overexpression and KD of GDAP1 (Del Amo et al., 2015; Noack et al., 2012), which unfortunately could not be reproduced here, but decreased PrSSG levels observed in this work in GDAP1 KD would be in line with these findings. Increased PrSSG levels can be an indication of oxidative stress and protect the proteins from harmful irreversible thiol oxidation (Gallogly and Mieyal, 2007). An open question would be if GDAP1 has a regulatory role on IDH1 in the presence of elevated GSH concentrations.

Discussion

In the proteomic analysis of isolated mitochondria and MAMs, altered expression levels of several peroxiredoxins were observed (PRDX1, PRDX2, PRDX4) – less PRDX1 and 2, but increased PRDX4 in the KD cells. H₂O₂ levels in the ER increase during protein folding and intramolecular disulfide formation via oxidoreductases, which are mainly oxidized in the ER lumen by PRDX4, GPRX7/8, as well as PDI and reduced glutathione (Zhang et al., 2019). The pathways that counterbalance the oxidized environment in the ER lumen in detail are still largely unclear (Bulleid and Van Lith, 2014). However, as mentioned previously, there are indications that the IP3R1 forms intramolecular disulfide bridges upon oxidation, thus mediating Ca²⁺ release similarly to protein glutathionylation, whereas reducing conditions rather lead to an inhibition of the IP3R activity (Hempel and Trebak, 2017; Lock et al., 2012). Though the cytosolic PRDXs are lowered, it remains to be examined if their activity is also altered. The activity of PRDX occurs at the expense of NADH and their main function involves the reduction of H₂O₂ via oxidation of GSH, leading to GSSG formation or protein glutathionylation (Nelson & Parsonage, 2011). Hence, reduced cytosolic PRDX activity indicates either reduced H₂O₂ levels and augmented protein glutathionylation in GDAP1 KD cells or an inability of the PRDXs to scavenge intracellular H₂O₂. A compensatory activity of GPXs to convert H₂O₂ may also be a plausible explanation, but the reduced PrSSG levels would point towards the former option, along with a reducing environment in these cells.

MFN2 is a redox-sensitive protein that oligomerizes upon increase of GSSG, the core intracellular stress indicator (Shutt et al., 2012). This oligomerization is driven by its C684 and induces mitochondrial hyperfusion, a cellular stress response that enhances mitochondrial ATP production (Shutt et al., 2012). In a separate project, we compared the mitochondrial function of MEF cells expressing either MFN2 WT or C684A point mutation and measured the cellular respiration in response to GSH treatment or after induction of mild oxidative stress by H₂O₂ addition in low concentrations (Thaher et al., 2017). The depletion of MFN2 already revealed a concomitant reduction of mitochondrial respiration and coenzyme Q production (Bach et al., 2003; Mourier et al., 2015). How these conclusions are connected to the MFN2 function remains unclear. However, we observed that C684A mutation induced a reduction of the electron transport capacity in response to GSH, but not to GSSG, while oxidative eustress increased the respiration compared to the control, indicating that this thiol-switch makes the mitochondria and MFN2 itself more susceptible to alterations in the intracellular redox state (Thaher et al., 2017). In this work, I investigated the possibility of a regulatory function of GDAP1 on MFN2 in a redox-mediated manner. I observed a significant reduction of MFN2 PTM in GDAP1 KD and R310Q expressing cells compared to the respective controls, while more MFN2 proteins were modified in the S34A loss-of-function GDAP1 expressing cells. The level of total protein glutathionylation was slightly reduced. In particular, the MFN2

glutathionylation increased in GDAP1 KD cells, similar to the S34A loss-of-function GDAP1 expressing cells. GDAP1 WT, in contrast, reduced the GSH-conjugation to MFN2. This experiment needs further replicates, but it may point towards a GDAP1-regulated MFN2 posttranslational modification. However, MFN2 was not detected in our screen for GDAP1 interaction partners and the observed PTM may be occurring via secondary factors. Such mechanisms could be regulated by an altered redox state in the cells, nitrosative or oxidative stress responses, which need to be investigated further.

Less is known about GDAP1 expression and mitophagy, though it is already proven that *rmGDAP1* and *dmGDAP1* mutations increase ROS and susceptibility to apoptotic stimuli, but not GDAP1 KD (Niemann et al., 2009). Treatment of cells with the GST substrate ethacrynic acid (EA) can lead to GSH depletion. This intracellular GSH reduction results in an imbalance of the GSH:GSSG ratio, increased oxidative stress and can eventually trigger mitophagy (Deffieu et al., 2009). We quantified GAPDH migration to the mitochondria in response to EA treatment. As a redox-sensitive and regulated protein, GAPDH can interact with VDAC1 at the OMM and induce mitochondrial degradation; we were addressing the question whether GAPDH is not only a target for protein glutathionylation in GDAP1 KD cells but also if its function regarding redox-procured mitophagy is altered (Tarze et al., 2007; Tristan et al., 2011). Surprisingly, we noticed less GAPDH at the mitochondria upon EA treatment in GDAP1 KD cells. Maybe these cells are more resistant to EA due to their increase in GSH levels and reveal diminished susceptibility to this stimulus.

7.6. Metabolic alterations are reproducible in CMT4A patient-derived motoneurons

Many of the characteristics of our KD cells were also observed in CMT4A patient-derived cells with mutations in GDAP1, albeit stronger in patient #2 than patient #1. Patient #1 has two heterozygous point-mutations L239F and R273G in the C-terminal GST domain, while patient #2 possesses a homozygous mutation in the donor site of the intron 4, which leads to exon 4 skipping and eventually to a truncated protein lacking the C-terminal GST, HD, and transmembrane domain of GDAP1 (Noack et al., 2012). Attributable to the truncated GDAP1 protein, no GDAP1 bands appear in IB analyses, most probably due to a protein instability and concomitant degradation of this protein. However, both patients reflect the findings we gathered from GDAP1 KD cells, especially in regard to metabolic processes and mitochondrial shape, where we observed an increased mitochondrial area.

TEM analysis of NPC cells rather revealed opposite findings – increased number of MERCS per mitochondrion. A live cell imaging approach in the NPCs or even motoneurons may diminish any artifacts of the fixatives to confirm these results. In GDAP1 KD mice, Niemann et al. observed a compensatory overexpression of the paralogue GDAP1L1, which is restricted to brain and testes (www.proteinatlas.org). In contrast to GDAP1, it resides in the cytosol under basal conditions but translocates to mitochondria upon increased levels of oxidized glutathione, where it is also able to induce mitochondrial fission (Niemann et al., 2014). I also tried to examine if our motoneurons showed such a compensatory effect in GDAP1L1 expression, especially in patient #2, but could not detect any protein expression here. Likely, the differentiated motoneurons rather resemble spinal MN, which originate in the spinal cord and belong to the PNS and thus do not express GDAP1L1, unlike CNS alpha MN, which derive from the cerebral cortex (Stifani, 2014).

Furthermore, it would be of great interest to investigate if the CMT4A patient-derived cells reveal loss of MERCS-proximity and DRP1-induced fission activity of mitochondria and hence reduced mitochondrial ATP production. Motoneurons in particular strongly depend on high energy production via oxidative phosphorylation to provide for mitochondrial transport all along the cells' compartments, especially to supply the axons and synapses with energy (Perez-Siles et al., 2016). An insufficient ATP production can lead to detrimental consequences. Interestingly, expression levels of the MCU had similar tendencies towards increased levels, presumably to yield a more efficient mitochondrial Ca^{2+} influx and to sustain ATP production.

Detailed metabolomic screens are currently performed to further unravel both the glucose and glutamine uptake and processing in these cells. However, the results presented in this work regarding the metabolic shift of GDAP1 KD cells was reproducible in the patient-derived motoneurons. We detected an elevated glutaminolysis in patient-derived cells, possibly pointing towards a dysregulation in the mitochondrial pyruvate entry or conversion. Fatty acid synthesis was not changed in the NPCs, but significantly reduced in both patient-derived motoneuron cultures, which is why we concluded that loss of GDAP1 expression also leads to a defect in fatty acid synthesis. We did not detect any differences between Ctrl and GDAP1 KD cells in starved conditions and starving the patient-derived neurons of supplemental nutrients such as N2 or B27 was lethal for the cells. Hence, we only performed Bodipy™ staining in patient-derived smNPCs and MN under basal conditions.

We therefore propose a model which indicates that cells with a loss-of-function GDAP1 mutation turn out to have a defective pyruvate metabolism, whereupon the cells try to compensate for this defect with increased glutaminolysis.

8. Literature

- Van Acker, K., Nadif Kasri, N., De Smet, P., Parys, J.B., De Smedt, H., Missiaen, L., and Callewaert, G. (2002). IP₃-mediated Ca²⁺ signals in human neuroblastoma SH-SY5Y cells with exogenous overexpression of type 3 IP₃ receptor. *Cell Calcium* 32, 71–81.
- Allocati, N., Masulli, M., Di Ilio, C., and Federici, L. (2018). Glutathione transferases: Substrates, inhibitors and pro-drugs in cancer and neurodegenerative diseases. *Oncogenesis* 7, 1–15.
- Altmann, R. (1894). *Die Elementarorganismen und ihre Beziehungen zu den Zellen*.
- Amiott, E.A., Lott, P., Soto, J., Kang, P.B., McCaffery, J.M., DiMauro, S., Abel, E.D., Flanigan, K.M., Lawson, V.H., and Shaw, J.M. (2008). Mitochondrial fusion and function in Charcot-Marie-Tooth type 2A patient fibroblasts with mitofusin 2 mutations. *Exp. Neurol.* 211, 115–127.
- Del Amo, V.L., Seco-Cervera, M., García-Giménez, J.L., Whitworth, A.J., Pallardó, F. V., and Galindo, M.I. (2015). Mitochondrial defects and neuromuscular degeneration caused by altered expression of *Drosophila* Gdap1: Implications for the Charcot-Marie-Tooth neuropathy. *Hum. Mol. Genet.* 24, 21–36.
- Anghelescu, C., Francou, B., Cardas, R., Guiochon-Mantel, A., Aubourg, P., Servais, L., and Gidaro, T. (2017). Targeted exomes reveal simultaneous MFN2 and GDAP1 mutations in a severe Charcot-Marie-Tooth disease type 2 phenotype. *Eur. J. Neurol.* 24, e15–e16.
- Appenzeller-Herzog, C. (2011). Glutathione- and non-glutathione-based oxidant control in the endoplasmic reticulum. *J. Cell Sci.* 124, 847–855.
- Arnold, W.D., Isfort, M., Roggenbuck, J., and Hoyle, J.C. (2015). The genetics of Charcot-Marie-Tooth disease: current trends and future implications for diagnosis and management. *Appl. Clin. Genet.* 8, 235.
- Awasthi, S., Srivastava, S.K., Ahmad, F., Ahmad, H., and Ansari, G.A. (1993). Interactions of glutathione S-transferase-pi with ethacrynic acid and its glutathione conjugate. *Biochim. Biophys. Acta* 1164, 173–178.
- Azzedine, H., Ruberg, M., Ente, D., Gilardeau, C., Périé, S., Wechsler, B., Brice, A., LeGuern, E., and Dubourg, O. (2003). Variability of disease progression in a family with autosomal recessive CMT associated with a S194X and new R310Q mutation in the GDAP1 gene. *Neuromuscul. Disord.* 13, 341–346.

- Bach, D., Pich, S., Soriano, F.X., Vega, N., Baumgartner, B., Oriola, J., Daugaard, J.R., Lloberas, J., Camps, M., Zierath, J.R., et al. (2003). Mitofusin-2 determines mitochondrial network architecture and mitochondrial metabolism: A novel regulatory mechanism altered in obesity. *J. Biol. Chem.* *278*, 17190–17197.
- Bak, D.W., and Weerapana, E. (2015). Cysteine-mediated redox signalling in the mitochondria. *Mol. Biosyst.* *11*, 678–697.
- Banchs, I., Casasnovas, C., Albertí, A., De Jorge, L., Povedano, M., Montero, J., Martínez-Matos, J.A., and Volpini, V. (2009). Diagnosis of Charcot-Marie-Tooth disease. *J. Biomed. Biotechnol.* *2009*, 985415.
- Bandyopadhyay, A., Shin, D.W., Ahn, J.O., and Kim, D.H. (2000). Calcineurin regulates ryanodine receptor/Ca(2+)-release channels in rat heart. *Biochem. J.* *352 Pt 1*, 61–70.
- Barinova, K. V., Serebryakova, M. V., Muronetz, V.I., and Schmalhausen, E. V. (2017). S-glutathionylation of glyceraldehyde-3-phosphate dehydrogenase induces formation of C150-C154 intrasubunit disulfide bond in the active site of the enzyme. *Biochim. Biophys. Acta - Gen. Subj.* *1861*, 3167–3177.
- Barneo-Muñoz, M., Juárez, P., Civera-Tregón, A., Yndriago, L., Pla-Martin, D., Zenker, J., Cuevas-Martín, C., Estela, A., Sánchez-Aragó, M., Forteza-Vila, J., et al. (2015). Lack of GDAP1 Induces Neuronal Calcium and Mitochondrial Defects in a Knockout Mouse Model of Charcot-Marie-Tooth Neuropathy. *PLoS Genet.* *11*.
- Basso, V., Marchesan, E., Peggion, C., Chakraborty, J., von Stockum, S., Giacomello, M., Ottolini, D., Debattisti, V., Caicci, F., Tasca, E., et al. (2018). Regulation of ER-mitochondria contacts by Parkin via Mfn2. *Pharmacol. Res.* *138*, 43–56.
- Bedhomme, M., Adamo, M., Marchand, C.H., Couturier, J., Rouhier, N., Lemaire, S.D., Zaffagnini, M., and Trost, P. (2012). Glutathionylation of cytosolic glyceraldehyde-3-phosphate dehydrogenase from the model plant *Arabidopsis thaliana* is reversed by both glutaredoxins and thioredoxins in vitro. *Biochem. J.* *445*, 337–347.
- Bender, T., and Martinou, J.C. (2016). The mitochondrial pyruvate carrier in health and disease: To carry or not to carry? *Biochim. Biophys. Acta - Mol. Cell Res.* *1863*, 2436–2442.
- Bernard-Marissal, N., Chrast, R., and Schneider, B.L. (2018). Endoplasmic reticulum and mitochondria in diseases of motor and sensory neurons: A broken relationship? *Cell Death Dis.* *9*, 1–16.
- Bernard-Marissal, N., Van Hameren, G., Juneja, M., Pellegrino, C., Louhivuori, L., Bartesaghi,

- L., Rochat, C., El Mansour, O., Médard, J.J., Croisier, M., et al. (2019). Altered interplay between endoplasmic reticulum and mitochondria in Charcot-Marie-Tooth type 2A neuropathy. *Proc. Natl. Acad. Sci. U. S. A.* *116*, 2328–2337.
- Bernstein, B.W., and Bamburg, J.R. (2010). ADF/Cofilin: A functional node in cell biology. *Trends Cell Biol.* *20*, 187–195.
- Berthet, A., Margolis, E.B., Zhang, J., Hsieh, I., Zhang, J., Hnasko, T.S., Ahmad, J., Edwards, R.H., Sesaki, H., Huang, E.J., et al. (2014). Loss of mitochondrial fission depletes axonal mitochondria in midbrain dopamine neurons. *J. Neurosci.* *34*, 14304–14317.
- Biedler, J.L., Roffler-Tarlov, S., Schachner, M., and Freedman, L.S. (1978). Multiple Neurotransmitter Synthesis by Human Neuroblastoma Cell Lines and Clones. *Cancer Res.* *38*.
- Bittermann, E., Abdelhamed, Z., Liegel, R.P., Menke, C., Timms, A., Beier, D.R., and Stottmann, R.W. (2019). Differential requirements of tubulin genes in mammalian forebrain development. *PLoS Genet.* *15*.
- Bonora, M., Giorgi, C., Bononi, A., Marchi, S., Patergnani, S., Rimessi, A., Rizzuto, R., and Pinton, P. (2013). Subcellular calcium measurements in mammalian cells using jellyfish photoprotein aequorin-based probes. *Nat. Protoc.* *8*, 2105–2118.
- Borgesius, N.Z., van Woerden, G.M., Buitendijk, G.H.S., Keijzer, N., Jaarsma, D., Hoogenraad, C.C., and Elgersma, Y. (2011). β CaMKII plays a nonenzymatic role in hippocampal synaptic plasticity and learning by targeting α CaMKII to synapses. *J. Neurosci.* *31*, 10141–10148.
- Bossy, B., Petrilli, A., Klingmayr, E., Chen, J., Lütz-Meindl, U., Knott, A.B., Masliah, E., Schwarzenbacher, R., and Bossy-Wetzler, E. (2010). S-nitrosylation of DRP1 does not affect enzymatic activity and is not specific to Alzheimer’s disease. *J. Alzheimer’s Dis.* *20*, S513.
- Bouschet, T., and Henley, J.M. (2005). Calcium as an extracellular signalling molecule: Perspectives on the Calcium Sensing Receptor in the brain. *Comptes Rendus - Biol.* *328*, 691–700.
- Boyer, O., Nevo, F., Plaisier, E., Funalot, B., Gribouval, O., Benoit, G., Cong, E.H., Arrondel, C., Tête, M.-J., Montjean, R., et al. (2011). *INF2* Mutations in Charcot–Marie–Tooth Disease with Glomerulopathy. *N. Engl. J. Med.* *365*, 2377–2388.
- Bricker, D.K., Taylor, E.B., Schell, J.C., Orsak, T., Boutron, A., Chen, Y.C., Cox, J.E., Cardon, C.M., Van Vranken, J.G., Dephoure, N., et al. (2012). A mitochondrial pyruvate carrier

- required for pyruvate uptake in yeast, *Drosophila*, and humans. *Science* (80-.). 336, 96–100.
- Brini, M., Marsault, R., Bastianutto, C., Alvarez, J., Pozzan, T., and Rizzuto, R. (1995). Transfected aequorin in the measurement of cytosolic Ca²⁺ concentration ([Ca²⁺]_c). A critical evaluation. *J. Biol. Chem.* 270, 9896–9903.
- de Brito, O.M., and Scorrano, L. (2009). Mitofusin-2 regulates mitochondrial and endoplasmic reticulum morphology and tethering: the role of Ras. *Mitochondrion* 9, 222–226.
- Bulleid, N.J., and Van Lith, M. (2014). Redox regulation in the endoplasmic reticulum. In *Biochemical Society Transactions*, (Portland Press Ltd), pp. 905–908.
- Bygrave, F.L., and Benedetti, A. (1996). What is the concentration of calcium ions in the endoplasmic reticulum? *Cell Calcium* 19, 547–551.
- Cai, S., Li, J., Wu, Y., and Jiang, Y. (2020). De novo mutations of TUBB2A cause infantile-onset epilepsy and developmental delay. *J. Hum. Genet.* 65, 601–608.
- Camões, F., Bonekamp, N.A., Delille, H.K., and Schrader, M. (2009). Organelle dynamics and dysfunction: A closer link between peroxisomes and mitochondria. In *Journal of Inherited Metabolic Disease*, pp. 163–180.
- Capaldi, R.A., Aggeler, R., Turina, P., and Wilkens, S. (1994). Coupling between catalytic sites and the proton channel in F1F0-type ATPases. *Trends Biochem. Sci.* 19, 284–289.
- Capps, G.J., Samuels, D.C., and Chinnery, P.F. (2003). A model of the nuclear control of mitochondrial DNA replication. *J. Theor. Biol.* 221, 565–583.
- Cassereau, J., Chevrollier, A., Gueguen, N., Malinge, M.C., Letournel, F., Nicolas, G., Richard, L., Ferre, M., Verny, C., Dubas, F., et al. (2009). Mitochondrial complex I deficiency in GDAP1-related autosomal dominant Charcot-Marie-Tooth disease (CMT2K). *Neurogenetics* 10, 145–150.
- Cassereau, J., Chevrollier, A., Gueguen, N., Desquiret, V., Verny, C., Nicolas, G., Dubas, F., Amati-Bonneau, P., Reynier, P., Bonneau, D., et al. (2011a). Mitochondrial dysfunction and pathophysiology of Charcot-Marie-Tooth disease involving GDAP1 mutations. *Exp. Neurol.* 227, 31–41.
- Cassereau, J., Casasnovas, C., Gueguen, N., Malinge, M.C., Guillet, V., Reynier, P., Bonneau, D., Amati-Bonneau, P., Banchs, I., Volpini, V., et al. (2011b). Simultaneous MFN2 and GDAP1 mutations cause major mitochondrial defects in a patient with CMT. *Neurology* 76, 1524–1526.

- Cassereau, J., Chevrollier, A., Codron, P., Goizet, C., Gueguen, N., Verny, C., Reynier, P., Bonneau, D., Lenaers, G., and Procaccio, V. (2020). Oxidative stress contributes differentially to the pathophysiology of Charcot-Marie-Tooth disease type 2K. *Exp. Neurol.* *323*.
- Cereghetti, G.M., Stangherlin, A., Martins De Brito, O., Chang, C.R., Blackstone, C., Bernardi, P., and Scorrano, L. (2008). Dephosphorylation by calcineurin regulates translocation of Drp1 to mitochondria. *Proc. Natl. Acad. Sci. U. S. A.* *105*, 15803–15808.
- Chakrabarti, R., Ji, W.K., Stan, R. V., Sanz, J. de J., Ryan, T.A., and Higgs, H.N. (2018). INF2-mediated actin polymerization at the ER stimulates mitochondrial calcium uptake, inner membrane constriction, and division. *J. Cell Biol.* *217*, 251–268.
- Chan, D.C. (2006). Mitochondria: Dynamic Organelles in Disease, Aging, and Development. *Cell* *125*, 1241–1252.
- Chan, D.C. (2012). Fusion and Fission: Interlinked Processes Critical for Mitochondrial Health. *Annu. Rev. Genet.* *46*, 265–287.
- Chang, C.R., and Blackstone, C. (2007). Cyclic AMP-dependent protein kinase phosphorylation of Drp1 regulates its GTPase activity and mitochondrial morphology. *J. Biol. Chem.* *282*, 21583–21587.
- Chen, Y., and Dorn, G.W. (2013). PINK1-phosphorylated mitofusin 2 is a parkin receptor for culling damaged mitochondria. *Science (80-)*. *340*, 471–475.
- Chen, H., Detmer, S.A., Ewald, A.J., Griffin, E.E., Fraser, S.E., and Chan, D.C. (2003). Mitofusins Mfn1 and Mfn2 coordinately regulate mitochondrial fusion and are essential for embryonic development. *J. Cell Biol.* *160*, 189–200.
- Cho, B., Cho, H.M., Jo, Y., Kim, H.D., Song, M., Moon, C., Kim, H., Kim, K., Sesaki, H., Rhyu, I.J., et al. (2017). Constriction of the mitochondrial inner compartment is a priming event for mitochondrial division. *Nat. Commun.* *8*, 1–17.
- Cho, D.H., Nakamura, T., Fang, J., Cieplak, P., Godzik, A., Gu, Z., and Lipton, S.A. (2009a). β -Amyloid-related mitochondrial fission and neuronal injury. *Science (80-)*. *324*, 102–105.
- Cho, D.H., Nakamura, T., Fang, J., Cieplak, P., Godzik, A., Gu, Z., and Lipton, S.A. (2009b). β -Amyloid-related mitochondrial fission and neuronal injury. *Science (80-)*. *324*, 102–105.
- Clementi, E., Brown, G.C., Feelisch, M., and Moncada, S. (1998). Persistent inhibition of cell respiration by nitric oxide: Crucial role of S-nitrosylation of mitochondrial complex I and protective action of glutathione. *Proc. Natl. Acad. Sci. U. S. A.* *95*, 7631–7636.

Literature

- Compagnucci, C., Piemonte, F., Sferra, A., Piermarini, E., and Bertini, E. (2016). The cytoskeletal arrangements necessary to neurogenesis. *Oncotarget* 7, 19414–19429.
- Compan, V., Pierredon, S., Vanderperre, B., Krznar, P., Marchiq, I., Zamboni, N., Pouyssegur, J., and Martinou, J.C. (2015). Monitoring Mitochondrial Pyruvate Carrier Activity in Real Time Using a BRET-Based Biosensor: Investigation of the Warburg Effect. *Mol. Cell* 59, 491–501.
- Cosson, P., Marchetti, A., Ravazzola, M., and Orci, L. (2012). Mitofusin-2 independent juxtaposition of endoplasmic reticulum and mitochondria: an ultrastructural study. *PLoS One* 7, e46293.
- Cowdry, E. V (1953). Historical background of research on mitochondria. *J. Histochem. Cytochem.* 1, 183–187.
- Cox, A.G., Winterbourn, C.C., and Hampton, M.B. (2010). Mitochondrial peroxiredoxin involvement in antioxidant defence and redox signalling. *Biochem. J.* 425, 313–325.
- Crimella, C., Tonelli, A., Airoldi, G., Baschiroto, C., D'Angelo, M.G., Bonato, S., Losito, L., Trabacca, A., Bresolin, N., and Bassi, M.T. (2010). The GST domain of GDAP1 is a frequent target of mutations in the dominant form of axonal Charcot Marie Tooth type 2K. *J. Med. Genet.* 47, 712–716.
- Csordás, G., Várnai, P., Golenár, T., Roy, S., Purkins, G., Schneider, T.G., Balla, T., and Hajnóczky, G. (2010). Imaging Interorganelle Contacts and Local Calcium Dynamics at the ER-Mitochondrial Interface. *Mol. Cell* 39, 121–132.
- Cuesta, A., Pedrola, L., Sevilla, T., García-Planells, J., Chumillas, M.J., Mayordomo, F., LeGuern, E., Marín, I., Vílchez, J.J., and Palau, F. (2002). The gene encoding ganglioside-induced differentiation-associated protein 1 is mutated in axonal Charcot-Marie-Tooth type 4A disease. *Nat. Genet.* 30, 22–25.
- Cull, M.G., and Schatz, P.J. (2000). Biotinylation of proteins in vivo and in vitro using small peptide tags. *Methods Enzymol.* 326, 430–440.
- Cuozzo, J.W., and Kaiser, C.A. (1999). Competition between glutathione and protein thiols for disulphide-bond formation. *Nat. Cell Biol.* 1, 130–135.
- Cyrne, L., Antunes, F., Sousa-Lopes, A., Diaz-Bérrio, J., and Marinho, H.S. (2010). Glyceraldehyde-3-phosphate dehydrogenase is largely unresponsive to low regulatory levels of hydrogen peroxide in *Saccharomyces cerevisiae*. *BMC Biochem.* 11, 49.
- D'Autréaux, B., and Toledano, M.B. (2007). ROS as signalling molecules: Mechanisms that

- generate specificity in ROS homeostasis. *Nat. Rev. Mol. Cell Biol.* **8**, 813–824.
- Davies, K.M., Strauss, M., Daum, B., Kief, J.H., Osiewacz, H.D., Rycovska, A., Zickermann, V., and Kühlbrandt, W. (2011). Macromolecular organization of ATP synthase and complex I in whole mitochondria. *Proc. Natl. Acad. Sci. U. S. A.* **108**, 14121–14126.
- Deffieu, M., Bhatia-Kiššová, I., Salin, B., Galinier, A., Manon, S., and Camougrand, N. (2009). Glutathione participates in the regulation of mitophagy in yeast. *J. Biol. Chem.* **284**, 14828–14837.
- Denton, R.M. (2009). Regulation of mitochondrial dehydrogenases by calcium ions. *Biochim. Biophys. Acta - Bioenerg.* **1787**, 1309–1316.
- Deponte, M. (2013). Glutathione catalysis and the reaction mechanisms of glutathione-dependent enzymes. *Biochim. Biophys. Acta - Gen. Subj.* **1830**, 3217–3266.
- Descazeaud, V., Mestre, E., Marquet, P., and Essig, M. (2012). Calcineurin regulation of cytoskeleton organization: A new paradigm to analyse the effects of calcineurin inhibitors on the kidney. *J. Cell. Mol. Med.* **16**, 218–227.
- Distler, U., Kuharev, J., Navarro, P., Levin, Y., Schild, H., and Tenzer, S. (2014). Drift time-specific collision energies enable deep-coverage data-independent acquisition proteomics. *Nat. Methods* **11**, 167–170.
- Distler, U., Kuharev, J., Navarro, P., and Tenzer, S. (2016). Label-free quantification in ion mobility-enhanced data-independent acquisition proteomics. *Nat. Protoc.* **11**, 795–812.
- Docampo, R., and Moreno, S.N.J. (2017). Biochemistry of *Trypanosoma cruzi*. In *American Trypanosomiasis Chagas Disease: One Hundred Years of Research: Second Edition*, (Elsevier Inc.), pp. 371–400.
- Drew, R., and Miners, J.O. (1984). The effects of buthionine sulphoximine (BSO) on glutathione depletion and xenobiotic biotransformation. *Biochem. Pharmacol.* **33**, 2989–2994.
- Driegen, S., Ferreira, R., Van Zon, A., Strouboulis, J., Jaegle, M., Grosveld, F., Philipsen, S., and Meijer, D. (2005). A generic tool for biotinylation of tagged proteins in transgenic mice. *Transgenic Res.* **14**, 477–482.
- Dumont, F. (2012). FK506, An Immunosuppressant Targeting Calcineurin Function. *Curr. Med. Chem.* **7**, 731–748.
- Eiberg, H., Kjer, B., Kjer, P., and Rosenberg, T. (1994). Dominant optic atrophy (OPA1)

Literature

- mapped to chromosome 3q region. I. Linkage analysis. *Hum. Mol. Genet.* **3**, 977–980.
- Eijkenboom, I., Vanoevelen, J.M., Hoeijmakers, J.G.J., Wijnen, I., Gerards, M., Faber, C.G., and Smeets, H.J.M. (2019). A zebrafish model to study small-fiber neuropathy reveals a potential role for GDAP1. *Mitochondrion* **47**, 273–281.
- Ercolani, L., Florence, B., Denaro, M., and Alexander, M. (1988). Isolation and complete sequence of a functional human glyceraldehyde-3-phosphate dehydrogenase gene. *J. Biol. Chem.* **263**, 15335–15341.
- Ernster, L., and Schatz, G. (1981). Mitochondria: A historical review. *J. Cell Biol.* **91**, 227s–255s.
- Estela, A., Pla-Martín, D., Sánchez-Piris, M., Sesaki, H., and Palau, F. (2011). Charcot-Marie-Tooth-related gene GDAP1 complements cell cycle delay at G2/M phase in *Saccharomyces cerevisiae* fis1 gene-defective cells. *J. Biol. Chem.* **286**, 36777–36786.
- Favaro, G., Romanello, V., Varanita, T., Andrea Desbats, M., Morbidoni, V., Tezze, C., Albiero, M., Canato, M., Gherardi, G., De Stefani, D., et al. (2019). DRP1-mediated mitochondrial shape controls calcium homeostasis and muscle mass. *Nat. Commun.* **10**, 1–17.
- Feely, S.M.E., Laura, M., Siskind, C.E., Sottile, S., Davis, M., Gibbons, V.S., Reilly, M.M., and Shy, M.E. (2011). MFN2 mutations cause severe phenotypes in most patients with CMT2A. *Neurology* **76**, 1690–1696.
- Fernandez-Lizarbe, S., Civera-Tregón, A., Cantarero, L., Herrer, I., Juarez, P., Hoenicka, J., and Palau, F. (2019). Neuroinflammation in the pathogenesis of axonal Charcot-Marie-Tooth disease caused by lack of GDAP1. *Exp. Neurol.* **320**, 113004.
- Fernie, A.R., Carrari, F., and Sweetlove, L.J. (2004). Respiratory metabolism: Glycolysis, the TCA cycle and mitochondrial electron transport. *Curr. Opin. Plant Biol.* **7**, 254–261.
- Feske, S., Rao, A., and Hogan, P.G. (2007). The Ca²⁺-calcineurin-NFAT signalling pathway. *New Compr. Biochem.* **41**, 365–401.
- Filadi, R., Greotti, E., Turacchio, G., Luini, A., Pozzan, T., and Pizzo, P. (2015). Mitofusin 2 ablation increases endoplasmic reticulum-mitochondria coupling. *Proc. Natl. Acad. Sci. U. S. A.* **112**, E2174–E2181.
- Finkel, T., and Holbrook, N.J. (2000). Oxidants, oxidative stress and the biology of ageing. *Nature* **408**, 239–247.
- Fratelli, M., Demol, H., Puype, M., Casagrande, S., Eberini, I., Salmona, M., Bonetto, V.,

Literature

- Mengozi, M., Duffieux, F., Miclet, E., et al. (2002). Identification by redox proteomics of glutathionylated proteins in oxidatively stressed human T lymphocytes. *Proc. Natl. Acad. Sci. U. S. A.* *99*, 3505–3510.
- Frieden, M., Arnaudeau, S., Castelbou, C., and Demaurex, N. (2005). Subplasmalemmal mitochondria modulate the activity of plasma membrane Ca²⁺-ATPases. *J. Biol. Chem.* *280*, 43198–43208.
- Friedman, J.R., Lackner, L.L., West, M., DiBenedetto, J.R., Nunnari, J., and Voeltz, G.K. (2011). ER tubules mark sites of mitochondrial division. *Science* (80-). *334*, 358–362.
- Fucci, L., Oliver, C.N., Coon, M.J., and Stadtman, E.R. (1983). Inactivation of key metabolic enzymes by mixed function oxidation reactions: possible implication in protein turnover and ageing. *Proc. Natl. Acad. Sci. U. S. A.* *80*, 1521–1525.
- Fukumitsu, K., Hatsukano, T., Yoshimura, A., Heuser, J., Fujishima, K., and Kengaku, M. (2016). Mitochondrial fission protein Drp1 regulates mitochondrial transport and dendritic arborization in cerebellar Purkinje cells. *Mol. Cell. Neurosci.* *71*, 56–65.
- Galán, C., Dionisio, N., Smani, T., Salido, G.M., and Rosado, J.A. (2011). The cytoskeleton plays a modulatory role in the association between STIM1 and the Ca²⁺ channel subunits Orai1 and TRPC1. *Biochem. Pharmacol.* *82*, 400–410.
- Gallogly, M.M., and Mieyal, J.J. (2007). Mechanisms of reversible protein glutathionylation in redox signaling and oxidative stress. *Curr. Opin. Pharmacol.* *7*, 381–391.
- Gandre-Babbe, S., and Van Der Bliek, A.M. (2008). The novel tail-anchored membrane protein Mff controls mitochondrial and peroxisomal fission in mammalian cells. *Mol. Biol. Cell* *19*, 2402–2412.
- Garcia, D., and Shaw, R.J. (2017). AMPK: Mechanisms of Cellular Energy Sensing and Restoration of Metabolic Balance. *Mol. Cell* *66*, 789–800.
- Gellert, M., Hanschmann, E.M., Lepka, K., Berndt, C., and Lillig, C.H. (2015). Redox regulation of cytoskeletal dynamics during differentiation and de-differentiation. *Biochim. Biophys. Acta - Gen. Subj.* *1850*, 1575–1587.
- Giacomello, M., and Pellegrini, L. (2016). The coming of age of the mitochondria-ER contact: A matter of thickness. *Cell Death Differ.* *23*, 1417–1427.
- González-Sánchez, P., Pla-Martín, D., Martínez-Valero, P., Rueda, C.B., Calpena, E., Del Arco, A., Palau, F., and Satrústegui, J. (2017). CMT-linked loss-of-function mutations in GDAP1 impair store-operated Ca²⁺ entry-stimulated respiration. *Sci. Rep.* *7*.

Literature

- Googins, M.R., Woghiren-Afegbua, A.O., Calderon, M., St. Croix, C.M., Kiselyov, K.I., and VanDemark, A.P. (2020). Structural and functional divergence of GDAP1 from the glutathione S-transferase superfamily. *FASEB J.* *34*, 7192–7207.
- Gray, L.R., Sultana, M.R., Rauckhorst, A.J., Oonthonpan, L., Tompkins, S.C., Sharma, A., Fu, X., Miao, R., Pawa, A.D., Brown, K.S., et al. (2015). Hepatic mitochondrial pyruvate carrier 1 is required for efficient regulation of gluconeogenesis and whole-body glucose homeostasis. *Cell Metab.* *22*, 669–681.
- Groeger, G., Quiney, C., and Cotter, T.G. (2009). Hydrogen peroxide as a cell-survival signaling molecule. *Antioxidants Redox Signal.* *11*, 2655–2671.
- Guillet, V., Gueguen, N., Cartoni, R., Chevrollier, A., Desquiret, V., Angebault, C., Amati-Bonneau, P., Procaccio, V., Bonneau, D., Martinou, J.-C., et al. (2011). Bioenergetic defect associated with mK ATP channel opening in a mouse model carrying a mitofusin 2 mutation . *FASEB J.* *25*, 1618–1627.
- Gurda, G.T., St John, T., and Williams, J.A. (2018). The Calcineurin-NFAT Pathway and Regulation of Pancreatic Function.
- Halestrap, A.P. (2009). What is the mitochondrial permeability transition pore? *J. Mol. Cell. Cardiol.* *46*, 821–831.
- Han, D., Antunes, F., Canali, R., Rettori, D., and Cadenas, E. (2003). Voltage-dependent anion channels control the release of the superoxide anion from mitochondria to cytosol. *J. Biol. Chem.* *278*, 5557–5563.
- Haussinger, D., Gerok, W., and Sies, H. (1982). Inhibition of Pyruvate Dehydrogenase during the Metabolism of Glutamine and Proline in Hemoglobin-Free Perfused Rat Liver. *Eur. J. Biochem.* *126*, 69–76.
- Hayashi, T., Rizzuto, R., Hajnoczky, G., and Su, T.P. (2009). MAM: more than just a housekeeper. *Trends Cell Biol.* *19*, 81–88.
- He, Y., and Casaccia-Bonnel, P. (2008). The Yin and Yang of YY1 in the nervous system. *J. Neurochem.* *106*, 1493–1502.
- Hempel, N., and Trebak, M. (2017). Crosstalk between calcium and reactive oxygen species signaling in cancer. *Cell Calcium* *63*, 70–96.
- Herzig, S., Raemy, E., Montessuit, S., Veuthey, J.L., Zamboni, N., Westermann, B., Kunji, E.R.S., and Martinou, J.C. (2012). Identification and functional expression of the mitochondrial pyruvate carrier. *Science* (80-.). *336*, 93–96.

- Hoffmann, L., Rust, M.B., and Culmsee, C. (2019). Actin(g) on mitochondria—a role for cofilin1 in neuronal cell death pathways. *Biol. Chem.* *400*, 1089–1097.
- Honrath, B., Metz, I., Bendridi, N., Rieusset, J., Culmsee, C., and Dolga, A.M. (2017). Glucose-regulated protein 75 determines ER–mitochondrial coupling and sensitivity to oxidative stress in neuronal cells. *Cell Death Discov.* *3*, 1–13.
- Huber, N., Guimaraes, S., Schrader, M., Suter, U., and Niemann, A. (2013). Charcot-Marie-Tooth disease-associated mutants of GDAP1 dissociate its roles in peroxisomal and mitochondrial fission. *EMBO Rep.* *14*, 545–552.
- Huber, N., Bieniossek, C., Wagner, K.M., Elsässer, H.-P., Suter, U., Berger, I., and Niemann, A. (2016). Glutathione-conjugating and membrane-remodeling activity of GDAP1 relies on amphipathic C-terminal domain.
- Ishihara, N., Fujita, Y., Oka, T., and Mihara, K. (2006). Regulation of mitochondrial morphology through proteolytic cleavage of OPA1. *EMBO J.* *25*, 2966–2977.
- Jäger, S., Handschin, C., St-Pierre, J., and Spiegelman, B.M. (2007). AMP-activated protein kinase (AMPK) action in skeletal muscle via direct phosphorylation of PGC-1 α . *Proc. Natl. Acad. Sci. U. S. A.* *104*, 12017–12022.
- Jha, P., Wang, X., and Auwerx, J. (2016). Analysis of Mitochondrial Respiratory Chain Supercomplexes Using Blue Native Polyacrylamide Gel Electrophoresis (BN-PAGE). *Curr. Protoc. Mouse Biol.* *6*, 1–14.
- Ji, W.K., Hatch, A.L., Merrill, R.A., Strack, S., and Higgs, H.N. (2015). Actin filaments target the oligomeric maturation of the dynamin GTPase Drp1 to mitochondrial fission sites. *Elife* *4*.
- Jin, B.Y., Sartoretto, J.L., Gladyshev, V.N., and Michel, T. (2009). Endothelial nitric oxide synthase negatively regulates hydrogen peroxide-stimulated AMP-activated protein kinase in endothelial cells. *Proc. Natl. Acad. Sci. U. S. A.* *106*, 17343–17348.
- Jonckheere, A.I., Smeitink, J.A.M., and Rodenburg, R.J.T. (2012). Mitochondrial ATP synthase: Architecture, function and pathology. *J. Inherit. Metab. Dis.* *35*, 211–225.
- Joseph, S.K., Young, M.P., Alzayady, K., Yule, D.I., Ali, M., Booth, D.M., and Hajnóczky, G. (2018). Redox regulation of type-I inositol trisphosphate receptors in intact mammalian cells. *J. Biol. Chem.* *293*, 17464–17476.
- Joseph, S.K., Booth, D.M., Young, M.P., and Hajnóczky, G. (2019). Redox regulation of ER and mitochondrial Ca²⁺ signaling in cell survival and death. *Cell Calcium* *79*, 89–97.

- Joshi, D.C., and Bakowska, J.C. (2011). Determination of mitochondrial membrane potential and reactive oxygen species in live rat cortical neurons. *J. Vis. Exp.*
- Kabzińska, D., Kotruchow, K., Cegielska, J., Hausmanowa-Petrusewicz, I., and Kochański, A. (2014). A severe recessive and a mild dominant form of Charcot-Marie-Tooth disease associated with a newly identified Glu222Lys GDAP1 gene mutation. *Acta Biochim. Pol.* *61*, 739–744.
- Kaminska, B., Czapski, B., Guzik, R., Król, S.K., and Gielniewski, B. (2019). Consequences of IDH1/2 mutations in gliomas and an assessment of inhibitors targeting mutated IDH proteins. *Molecules* *24*, 968.
- Kaplin, A.I., Snyder, S.H., and Linden, D.J. (1996). Reduced nicotinamide adenine dinucleotide-selective stimulation of inositol 1,4,5-trisphosphate receptors mediates hypoxic mobilization of calcium. *J. Neurosci.* *16*, 2002–2011.
- Kashatus, J.A., Nascimento, A., Myers, L.J., Sher, A., Byrne, F.L., Hoehn, K.L., Counter, C.M., and Kashatus, D.F. (2015). Erk2 phosphorylation of Drp1 promotes mitochondrial fission and MAPK-driven tumor growth. *Mol. Cell* *57*, 537–551.
- Kawamura, A., and Su, M.S.S. (1995). Interaction of FKBP12-FK506 with calcineurin A at the B subunit-binding domain. *J. Biol. Chem.* *270*, 15463–15466.
- Kazamel, M., and Boes, C.J. (2015). Charcot Marie Tooth disease (CMT): historical perspectives and evolution. *J. Neurol.* *262*, 801–805.
- Kehr, S., Jortzik, E., Delahunty, C., Yates, J.R., Rahlfs, S., and Becker, K. (2011). Protein S-glutathionylation in malaria parasites. *Antioxidants Redox Signal.* *15*, 2855–2865.
- Ketterer, B., Coles, B., and Meyer, D.J. (1983). The role of glutathione in detoxication. *Environ. Health Perspect.* *49*, 59–69.
- Khamici, H. Al, Brown, L.J., Hossain, K.R., Hudson, A.L., Sinclair-Burton, A.A., Ng, J.P.M., Daniel, E.L., Hare, J.E., Cornell, B.A., Curmi, P.M.G., et al. (2015). Members of the chloride intracellular ion channel protein family demonstrate glutaredoxin-like enzymatic activity. *PLoS One* *10*.
- Kim, B., Takeuchi, A., Koga, O., Hikida, M., and Matsuoka, S. (2012). Pivotal role of mitochondrial Na⁺-Ca²⁺ exchange in antigen receptor mediated Ca²⁺ signalling in DT40 and A20 B lymphocytes. *J. Physiol.* *590*, 459–474.
- Kinoshita, E., Kinoshita-Kikuta, E., Takiyama, K., and Koike, T. (2006). Phosphate-binding tag, a new tool to visualize phosphorylated proteins. *Mol. Cell. Proteomics* *5*, 749–757.

Literature

- Klamt, F., Zdanov, S., Levine, R.L., Parisera, A., Zhang, Y., Zhang, B., Yu, L.R., Veenstra, T.D., and Shacter, E. (2009). Oxidant-induced apoptosis is mediated by oxidation of the actin-regulatory protein cofilin. *Nat. Cell Biol.* *11*, 1241–1246.
- Koch, G.L.E. (1990). The endoplasmic reticulum and calcium storage. *BioEssays* *12*, 527–531.
- Konovalova, S. (2019). Analysis of Mitochondrial Respiratory Chain Complexes in Cultured Human Cells using Blue Native Polyacrylamide Gel Electrophoresis and Immunoblotting. *J. Vis. Exp* 59269.
- Korobova, F., Ramabhadran, V., and Higgs, H.N. (2013). An actin-dependent step in mitochondrial fission mediated by the ER-associated formin INF2. *Science* (80-.). *339*, 464–467.
- Korotchkina, L.G., and Patel, M.S. (2001). Site Specificity of Four Pyruvate Dehydrogenase Kinase Isoenzymes toward the Three Phosphorylation Sites of Human Pyruvate Dehydrogenase. *J. Biol. Chem.* *276*, 37223–37229.
- Kostera-Pruszczyk, A., Kosinska, J., Pollak, A., Stawinski, P., Walczak, A., Wasilewska, K., Potulska-Chromik, A., Szczudlik, P., Kaminska, A., and Ploski, R. (2014). Exome sequencing reveals mutations in MFN2 and GDAP1 in severe Charcot-Marie-Tooth disease. *J. Peripher. Nerv. Syst.* *19*, 242–245.
- Kowaltowski, A.J., Menezes-Filho, S.L., Assali, E.A., Gonçalves, I.G., Cabral-Costa, J.V., Abreu, P., Miller, N., Nolasco, P., Laurindo, F.R.M., Bruni-Cardoso, A., et al. (2019). Mitochondrial morphology regulates organellar Ca²⁺ uptake and changes cellular Ca²⁺ homeostasis. *FASEB J.* *33*, 13176–13188.
- Kozlowski, A., and Milton Harris, J. (2001). Improvements in protein PEGylation: Pegylated interferons for treatment of hepatitis C. *J. Control. Release* *72*, 217–224.
- Kruyer, A., Ball, L.E., Townsend, D.M., Kalivas, P.W., and Uys, J.D. (2019). Post-translational S-glutathionylation of cofilin increases actin cycling during cocaine seeking. *PLoS One* *14*.
- Kühlbrandt, W. (2015). Structure and function of mitochondrial membrane protein complexes. *BMC Biol.* *13*, 89.
- Kulbe, K.D., Jackson, K.W., and Tang, J. (1975). Structural evidence for a liver-specific glyceraldehyde-3-phosphate dehydrogenase. *Biochem. Biophys. Res. Commun.* *67*, 35–42.
- Kumar, V., Chichili, V.P.R., Zhong, L., Tang, X., Velazquez-Campoy, A., Sheu, F.S.,

- Seetharaman, J., Gerges, N.Z., and Sivaraman, J. (2013). Structural basis for the interaction of unstructured neuron specific substrates neuromodulin and neurogranin with calmodulin. *Sci. Rep.* *3*, 1–9.
- Küry, S., van Woerden, G.M., Besnard, T., Proietti Onori, M., Latypova, X., Towne, M.C., Cho, M.T., Prescott, T.E., Ploeg, M.A., Sanders, S., et al. (2017). De Novo Mutations in Protein Kinase Genes CAMK2A and CAMK2B Cause Intellectual Disability. *Am. J. Hum. Genet.* *101*, 768–788.
- Lam, A.K.M., and Galione, A. (2013). The endoplasmic reticulum and junctional membrane communication during calcium signaling. *Biochim. Biophys. Acta - Mol. Cell Res.* *1833*, 2542–2559.
- Lander, N., Chiurillo, M.A., Bertolini, M.S., Storey, M., Vercesi, A.E., and Docampo, R. (2018). Calcium-sensitive pyruvate dehydrogenase phosphatase is required for energy metabolism, growth, differentiation, and infectivity of *Trypanosoma cruzi*. *J. Biol. Chem.* *293*, 17402–17417.
- Landstrom, A.P., Beavers, D.L., and Wehrens, X.H.T. (2014). The junctophilin family of proteins: From bench to bedside. *Trends Mol. Med.* *20*, 353–362.
- Larrea, D., Pera, M., Gonnelli, A., Quintana-Cabrera, R., Akman, H.O., Guardia-Laguarta, C., Velasco, K.R., Area-Gomez, E., Dal Bello, F., De Stefani, D., et al. (2019). MFN2 mutations in charcot-marie-Tooth disease alter mitochondria-Associated er membrane function but do not impair bioenergetics. *Hum. Mol. Genet.* *28*, 1782–1800.
- Lassiter, D.G., Sjögren, R.J.O., Gabriel, B.M., Krook, A., and Zierath, J.R. (2018). AMPK activation negatively regulates GDAP1, which influences metabolic processes and circadian gene expression in skeletal muscle. *Mol. Metab.* *16*, 12–23.
- Lee, D. shin, and Kim, J.E. (2018). PDI-mediated S-nitrosylation of DRP1 facilitates DRP1-S616 phosphorylation and mitochondrial fission in CA1 neurons. *Cell Death Dis.* *9*, 1–13.
- Lee, S., and Min, K.T. (2018). The interface between ER and mitochondria: Molecular compositions and functions. *Mol. Cells* *41*, 1000–1007.
- Lee, M., Park, C.H., Chung, H.K., Kim, H.J., Choi, Y., Yoo, J.H., Yoon, Y.C., Hong, Y. Bin, Chung, K.W., Choi, B.O., et al. (2017). Cerebral white matter abnormalities in patients with charcot-marie-tooth disease. *Ann. Neurol.* *81*, 147–151.
- Lescuyer, P., Martinez, P., and Lunardi, J. (2002). YY1 and Sp1 activate transcription of the human NDUFS8 gene encoding the mitochondrial complex I TYKY subunit. *Biochim.*

- Biophys. Acta - Gene Struct. Expr. 1574, 164–174.
- Lewerenz, J., Hewett, S.J., Huang, Y., Lambros, M., Gout, P.W., Kalivas, P.W., Massie, A., Smolders, I., Methner, A., Pergande, M., et al. (2013). The cystine/glutamate antiporter system x(c)(-) in health and disease: from molecular mechanisms to novel therapeutic opportunities. *Antioxid. Redox Signal.* 18, 522–555.
- Lewis, T.L., Kwon, S.K., Lee, A., Shaw, R., and Polleux, F. (2018). MFF-dependent mitochondrial fission regulates presynaptic release and axon branching by limiting axonal mitochondria size. *Nat. Commun.* 9.
- Li, G., Zhou, J., Budhreja, A., Hu, X., Chen, Y., Cheng, Q., Liu, L., Zhou, T., Li, P., Liu, E., et al. (2015). Mitochondrial translocation and interaction of cofilin and Drp1 are required for erucin-induced mitochondrial fission and apoptosis. *Oncotarget* 6, 1834–1849.
- Li, G.B., Zhang, H.W., Fu, R.Q., Hu, X.Y., Liu, L., Li, Y.N., Liu, Y.X., Liu, X., Hu, J.J., Deng, Q., et al. (2018). Mitochondrial fission and mitophagy depend on cofilin-mediated actin depolymerization activity at the mitochondrial fission site. *Oncogene* 37, 1485–1502.
- Li, H., Ding, X., Lopez, J.R., Takeshima, H., Ma, J., Allen, P.D., and Eltit, J.M. (2010). Impaired Orai1-mediated resting Ca²⁺ entry reduces the cytosolic [Ca²⁺] and sarcoplasmic reticulum Ca²⁺ loading in quiescent junctophilin 1 knock-out myotubes. *J. Biol. Chem.* 285, 39171–39179.
- Li, Y.J., Cao, Y.L., Feng, J.X., Qi, Y., Meng, S., Yang, J.F., Zhong, Y.T., Kang, S., Chen, X., Lan, L., et al. (2019). Structural insights of human mitofusin-2 into mitochondrial fusion and CMT2A onset. *Nat. Commun.* 10.
- Lin, Y.S., Hung, S.C., Wei, Y.H., and Tarng, D.C. (2009). GST M1 polymorphism associates with DNA oxidative damage and mortality among hemodialysis patients. *J. Am. Soc. Nephrol.* 20, 405–415.
- Linn, T.C., Pettit, F.H., and Reed, L.J. (1969). Alpha-keto acid dehydrogenase complexes. X. Regulation of the activity of the pyruvate dehydrogenase complex from beef kidney mitochondria by phosphorylation and dephosphorylation. *Proc. Natl. Acad. Sci. U. S. A.* 62, 234–241.
- Littler, D.R., Harrop, S.J., Goodchild, S.C., Phang, J.M., Mynott, A. V., Jiang, L., Valenzuela, S.M., Mazzanti, M., Brown, L.J., Breit, S.N., et al. (2010). The enigma of the CLIC proteins: Ion channels, redox proteins, enzymes, scaffolding proteins? *FEBS Lett.* 584, 2093–2101.
- Liu, H., Nakagawa, T., Kanematsu, T., Uchida, T., and Tsuji, S. (1999). Isolation of 10

- differentially expressed cDNAs in differentiated Neuro2a cells induced through controlled expression of the GD3 synthase gene. *J. Neurochem.* 72, 1781–1790.
- Liu, S., He, L., and Yao, K. (2018). The Antioxidative Function of Alpha-Ketoglutarate and Its Applications. *Biomed Res. Int.* 2018.
- Liu, Z., Zhou, T., Ziegler, A.C., Dimitrion, P., and Zuo, L. (2017). Oxidative Stress in Neurodegenerative Diseases: From Molecular Mechanisms to Clinical Applications. *Oxid. Med. Cell. Longev.* 2017.
- Lock, J.T., Sinkins, W.G., and Schilling, W.P. (2012). Protein S -glutathionylation enhances Ca²⁺-induced Ca²⁺ release via the IP₃ receptor in cultured aortic endothelial cells. *J. Physiol.* 590, 3431–3447.
- López del Amo, V., Palomino-Schätzlein, M., Seco-Cervera, M., García-Giménez, J.L., Pallardó, F.V., Pineda-Lucena, A., and Galindo, M.I. (2017). A *Drosophila* model of GDAP1 function reveals the involvement of insulin signalling in the mitochondria-dependent neuromuscular degeneration. *Biochim. Biophys. Acta - Mol. Basis Dis.* 1863, 801–809.
- Lubos, E., Loscalzo, J., and Handy, D.E. (2011). Glutathione peroxidase-1 in health and disease: From molecular mechanisms to therapeutic opportunities. *Antioxidants Redox Signal.* 15, 1957–1997.
- Luo, S., Uehara, H., and Shacter, E. (2014). Taurine chloramine-induced inactivation of cofilin protein through methionine oxidation. *Free Radic. Biol. Med.* 75, 84–94.
- Mai, P.-T., Le, D.-T., Nguyen, T.-T., Gia, H.-L. Le, Le, T.-H.N., Le, M., and Do, D.-M. (2019). Novel GDAP1 Mutation in a Vietnamese Family with Charcot-Marie-Tooth Disease. *Biomed Res. Int.* 2019.
- Mailloux, R.J., Bériault, R., Lemire, J., Singh, R., Chénier, D.R., Hamel, R.D., and Appanna, V.D. (2007). The Tricarboxylic Acid Cycle, an Ancient Metabolic Network with a Novel Twist. *PLoS One* 2, e690.
- Mairet-Coello, G., Courchet, J., Pieraut, S., Courchet, V., Maximov, A., and Polleux, F. (2013). The CAMKK2-AMPK Kinase Pathway Mediates the Synaptotoxic Effects of A β Oligomers through Tau Phosphorylation. *Neuron* 78, 94–108.
- Malka, F., Guillery, O., Cifuentes-Diaz, C., Guillou, E., Belenguer, P., Lombés, A., and Rojo, M. (2005). Separate fusion of outer and inner mitochondrial membranes. *EMBO Rep.* 6, 853–859.
- Mangialasche, F., Polidori, M.C., Monastero, R., Ercolani, S., Camarda, C., Cecchetti, R., and

Literature

- Mecocci, P. (2009). Biomarkers of oxidative and nitrosative damage in Alzheimer's disease and mild cognitive impairment. *Ageing Res. Rev.* **8**, 285–305.
- Mao, K., and Klionsky, D.J. (2013). Mitochondrial fission facilitates mitophagy in *Saccharomyces cerevisiae*. *Autophagy* **9**, 1900–1901.
- Marco, A., Cuesta, A., Pedrola, L., Palau, F., and Marín, I. (2004). Evolutionary and structural analyses of GDAP1, involved in Charcot-Marie-Tooth disease, characterize a novel class of glutathione transferase-related genes. *Mol. Biol. Evol.* **21**, 176–187.
- Martin-Romero, F.J., Lopez-Guerrero, A.M., Pascual-Caro, C., and Pozo-Guisado, E. (2017). The Interplay between Cytoskeleton and Calcium Dynamics. In *Cytoskeleton - Structure, Dynamics, Function and Disease*, (InTech), p.
- Martin, A.M., Maradei, S.J., and Velasco, H.M. (2015). Charcot Marie Tooth disease (CMT4A) due to GDAP1 mutation: report of a Colombian family. *Colomb. Medica (Cali, Colomb.* **46**, 194–198.
- Marx, U., Schenk, F., Behrens, J., Meyr, U., Wanek, P., Zang, W., Schmitt, R., Brüstle, O., Zenke, M., and Klocke, F. (2013). Automatic production of induced pluripotent stem cells. In *Procedia CIRP*, (Elsevier B.V.), pp. 2–6.
- Meeusen, S., McCaffery, J.M., and Nunnari, J. (2004). Mitochondrial fusion intermediates revealed in vitro. *Science (80-.)*. **305**, 1747–1752.
- Mekahli, D., Bultynck, G., Parys, J.B., de Smedt, H., and Missiaen, L. (2011). Endoplasmic-reticulum calcium depletion and disease. *Cold Spring Harb. Perspect. Biol.* **3**, 1–30.
- Menendez, J.A., and Lupu, R. (2007). Fatty acid synthase and the lipogenic phenotype in cancer pathogenesis. *Nat. Rev. Cancer* **7**, 763–777.
- Mishra, J., Jhun, B.S., Hurst, S., O-Uchi, J., Csordás, G., and Sheu, S.S. (2017). The mitochondrial Ca²⁺ uniporter: Structure, function, and pharmacology. In *Handbook of Experimental Pharmacology*, (Springer New York LLC), p. 129.
- Mishra, P., Carelli, V., Manfredi, G., and Chan, D.C. (2014). Proteolytic cleavage of Opa1 stimulates mitochondrial inner membrane fusion and couples fusion to oxidative phosphorylation. *Cell Metab.* **19**, 630–641.
- Molkentin, J.D. (2004). Calcineurin-NFAT signaling regulates the cardiac hypertrophic response in coordination with the MAPKs. *Cardiovasc. Res.* **63**, 467–475.
- Mourier, A., Motori, E., Brandt, T., Lagouge, M., Atanassov, I., Galinier, A., Rappl, G.,

Literature

- Brodesser, S., Hultenby, K., Dieterich, C., et al. (2015). Mitofusin 2 is required to maintain mitochondrial coenzyme Q levels. *J. Cell Biol.* *208*, 429–442.
- Murphy, M.P. (2009). How mitochondria produce reactive oxygen species. *Biochem. J.* *417*, 1–13.
- Naghdi, S., Waldeck-Weiermair, M., Fertschai, I., Poteser, M., Graier, W.F., and Malli, R. (2010). Mitochondrial Ca²⁺ uptake and not mitochondrial motility is required for STIM1-Orai1-dependent store-operated Ca²⁺ entry. *J. Cell Sci.* *123*, 2553–2564.
- Namgaladze, D., Hofer, H.W., and Ullrich, V. (2002). Redox control of calcineurin by targeting the binuclear Fe²⁺-Zn²⁺ center at the enzyme active site. *J. Biol. Chem.* *277*, 5962–5969.
- Naon, D., Zaninello, M., Giacomello, M., Varanita, T., Grespi, F., Lakshminarayanan, S., Serafini, A., Semenzato, M., Herkenne, S., Hernández-Alvarez, M.I., et al. (2016). Critical reappraisal confirms that Mitofusin 2 is an endoplasmic reticulum-mitochondria tether. *Proc. Natl. Acad. Sci. U. S. A.* *113*, 11249–11254.
- Narayanan, N., and Xu, A. (1997). Phosphorylation and regulation of the Ca²⁺-pumping ATPase in cardiac sarcoplasmic reticulum by calcium/calmodulin-dependent protein kinase. *Basic Res. Cardiol.* *92*, 25–35.
- Nicholson, G., and Myers, S. (2006). Intermediate forms of charcot-marie-tooth neuropathy: A review. *NeuroMolecular Med.* *8*, 123–130.
- Niemann, A., Ruegg, M., La Padula, V., Schenone, A., and Suter, U. (2005). Ganglioside-induced differentiation associated protein 1 is a regulator of the mitochondrial network: new implications for Charcot-Marie-Tooth disease. *J. Cell Biol.* *170*, 1067–1078.
- Niemann, A., Berger, P., and Suter, U. (2006). Pathomechanisms of mutant proteins in Charcot-Marie-Tooth disease. *Neuromolecular Med.* *8*, 217–242.
- Niemann, A., Wagner, K.M., Ruegg, M., and Suter, U. (2009). GDAP1 mutations differ in their effects on mitochondrial dynamics and apoptosis depending on the mode of inheritance. *Neurobiol. Dis.* *36*, 509–520.
- Niemann, A., Huber, N., Wagner, K.M., Somandin, C., Horn, M., Lebrun-Julien, F., Angst, B., Pereira, J.A., Halfter, H., Welzl, H., et al. (2014). The Gdap1 knockout mouse mechanistically links redox control to Charcot-Marie-tooth disease. *Brain* *137*, 668–682.
- Nisoli, E., Clementi, E., Paolucci, C., Cozzi, V., Tonello, C., Sciorati, C., Bracale, R., Valerio, A., Francolini, M., Moncada, S., et al. (2003). Mitochondrial biogenesis in mammals: The role of endogenous nitric oxide. *Science* (80-.). *299*, 896–899.

Literature

- Noack, R., Frede, S., Albrecht, P., Henke, N., Pfeiffer, A., Knoll, K., Dehmel, T., Meyer Zu Hörste, G., Stettner, M., Kieseier, B.C., et al. (2012). Charcot-Marie-Tooth disease CMT4A: GDAP1 increases cellular glutathione and the mitochondrial membrane potential. *Hum. Mol. Genet.* *21*, 150–162.
- Ono, T., Isobe, K., Nakada, K., and Hayashi, J.I. (2001). Human cells are protected from mitochondrial dysfunction by complementation of DNA products in fused mitochondria. *Nat. Genet.* *28*, 272–275.
- Oonthonpan, L., Rauckhorst, A.J., Gray, L.R., Boutron, A.C., and Taylor, E.B. (2019). Two human patient mitochondrial pyruvate carrier mutations reveal distinct molecular mechanisms of dysfunction.
- Otera, H., Wang, C., Cleland, M.M., Setoguchi, K., Yokota, S., Youle, R.J., and Mihara, K. (2010). Mff is an essential factor for mitochondrial recruitment of Drp1 during mitochondrial fission in mammalian cells. *J. Cell Biol.* *191*, 1141–1158.
- Ottolini, D., Cali, T., and Brini, M. (2014). Methods to measure intracellular Ca²⁺ fluxes with organelle-targeted aequorin-based probes. In *Methods in Enzymology*, (Academic Press Inc.), pp. 21–45.
- Ouvrier, R.A., McLeod, J.G., Morgan, G.J., Wise, G.A., and Conchin, T.E. (1981). Hereditary motor and sensory neuropathy of neuronal type with onset in early childhood. *J. Neurol. Sci.* *51*, 181–197.
- Owens, H., Gamble, G.D., Bjornholdt, M.C., Boyce, N.K., and Keung, L. (2007). Imported from <https://ghr.nlm.nih.gov/condition/parkinson-disease>. *Cornea* *26*, 312–318.
- Palade, G.E. (1953). An electron microscope study of the mitochondrial structure. *J. Histochem. Cytochem.* *1*, 188–211.
- Palikaras, K., Lionaki, E., and Tavernarakis, N. (2018). Mechanisms of mitophagy in cellular homeostasis, physiology and pathology. *Nat. Cell Biol.* *20*, 1013–1022.
- Papa, S., Francavilla, A., Paradies, G., and Meduri, B. (1971). The transport of pyruvate in rat liver mitochondria. *FEBS Lett.* *12*, 285–288.
- Papp, S., Dziak, E., Michalak, M., and Opas, M. (2003). Is all of the endoplasmic reticulum created equal? The effects of the heterogeneous distribution of endoplasmic reticulum Ca²⁺-handling proteins. *J. Cell Biol.* *160*, 475–479.
- Parsons, D.W., Jones, S., Zhang, X., Lin, J.C.H., Leary, R.J., Angenendt, P., Mankoo, P., Carter, H., Siu, I.M., Gallia, G.L., et al. (2008). An integrated genomic analysis of human

- glioblastoma multiforme. *Science* (80-.). 321, 1807–1812.
- Patterson, R.L., Van Rossum, D.B., Kaplin, A.I., Barrow, R.K., and Snyder, S.H. (2005). Inositol 1,4,5-trisphosphate receptor/GAPDH complex augments Ca²⁺ release via locally derived NADH. *Proc. Natl. Acad. Sci. U. S. A.* 102, 1357–1359.
- Pedrola, L., Espert, A., Wu, X., Claramunt, R., Shy, M.E., and Palau, F. (2005). GDAP1, the protein causing Charcot-Marie-Tooth disease type 4A, is expressed in neurons and is associated with mitochondria. *Hum. Mol. Genet.* 14, 1087–1094.
- Pedrola, L., Espert, A., Valdés-Sánchez, T., Sánchez-Piris, M., Sirkowski, E.E., Scherer, S.S., Fariñas, I., and Palau, F. (2008). Cell expression of GDAP1 in the nervous system and pathogenesis of Charcot-Marie-Tooth type 4A disease. *J. Cell. Mol. Med.* 12, 679–689.
- Perez-Siles, G., Ly, C., Grant, A., Drew, A.P., Yiu, E.M., Ryan, M.M., Chuang, D.T., Tso, S.C., Nicholson, G.A., and Kennerson, M.L. (2016). Pathogenic mechanisms underlying X-linked Charcot-Marie-Tooth neuropathy (CMTX6) in patients with a pyruvate dehydrogenase kinase 3 mutation. *Neurobiol. Dis.*
- Perry, S.W., Norman, J.P., Barbieri, J., Brown, E.B., and Gelbard, H.A. (2011). Mitochondrial membrane potential probes and the proton gradient: A practical usage guide. *Biotechniques* 50, 98–115.
- Pla-Martín, D., Rueda, C.B., Estela, A., Sánchez-Piris, M., González-Sánchez, P., Traba, J., de la Fuente, S., Scorrano, L., Renau-Piqueras, J., Alvarez, J., et al. (2013). Silencing of the Charcot-Marie-Tooth disease-associated gene GDAP1 induces abnormal mitochondrial distribution and affects Ca²⁺ homeostasis by reducing store-operated Ca²⁺ entry. *Neurobiol. Dis.* 55, 140–151.
- Pla-Martín, D., Calpena, E., Lupo, V., Márquez, C., Rivas, E., Sivera, R., Sevilla, T., Palau, F., and Espinó, C. (2015). Junctophilin-1 is a modifier gene of GDAP1-related Charcot-Marie-Tooth disease. *Hum. Mol. Genet.* 24, 213–229.
- Putney, J.W., and Tomita, T. (2012). Phospholipase C signaling and calcium influx. *Adv. Biol. Regul.* 52, 152–164.
- Pyakurel, A., Savoia, C., Hess, D., and Scorrano, L. (2015). Extracellular Regulated Kinase Phosphorylates Mitofusin 1 to Control Mitochondrial Morphology and Apoptosis. *Mol. Cell* 58, 244–254.
- Rahman, I., Kode, A., and Biswas, S.K. (2007). Assay for quantitative determination of glutathione and glutathione disulfide levels using enzymatic recycling method. *Nat. Protoc.*

- 1, 3159–3165.
- Raineri, S., and Mellor, J. (2018). IDH1: Linking Metabolism and Epigenetics. *Front. Genet.* 9.
- Rambold, A.S., Cohen, S., and Lippincott-Schwartz, J. (2015). Fatty acid trafficking in starved cells: Regulation by lipid droplet lipolysis, autophagy, and mitochondrial fusion dynamics. *Dev. Cell* 32, 678–692.
- Rao, S.G., Ponnalagu, D., Sukur, S., Singh, H., Sanghvi, S., Mei, Y., Jin, D.J., and Singh, H. (2017). Identification and Characterization of a Bacterial Homolog of Chloride Intracellular Channel (CLIC) Protein. *Sci. Rep.* 7.
- Ratajewski, M., and Pulaski, L. (2009). YY1-dependent transcriptional regulation of the human GDAP1 gene. *Genomics* 94, 407–413.
- Rehklau, K., Hoffmann, L., Gurniak, C.B., Ott, M., Witke, W., Scorrano, L., Culmsee, C., and Rust, M.B. (2017). Cofilin1-dependent actin dynamics control DRP1-mediated mitochondrial fission. *Cell Death Dis.* 8, e3063.
- Reinhardt, P., Glatza, M., Hemmer, K., Tsytsyura, Y., Thiel, C.S., Höing, S., Moritz, S., Parga, J.A., Wagner, L., Bruder, J.M., et al. (2013). Derivation and Expansion Using Only Small Molecules of Human Neural Progenitors for Neurodegenerative Disease Modeling. *PLoS One* 8, e59252.
- Rizzuto, R., De Stefani, D., Raffaello, A., and Mammucari, C. (2012). Mitochondria as sensors and regulators of calcium signalling. *Nat. Rev. Mol. Cell Biol.* 13, 566–578.
- Robert, S.M., Ogunrinu-Babarinde, T., Holt, K.T., and Sontheimer, H. (2014). Role of glutamate transporters in redox homeostasis of the brain. *Neurochem. Int.* 73, 181–191.
- Roche, T.E., Baker, J.C., Yan, X., Hiromasa, Y., Gong, X., Peng, T., Dong, J., Turkan, A., and Kasten, S.A. (2001). Distinct regulatory properties of pyruvate dehydrogenase kinase and phosphatase isoforms. *Prog. Nucleic Acid Res. Mol. Biol.* 70, 33–75.
- Rowland, A.A., and Voeltz, G.K. (2012). Endoplasmic reticulum-mitochondria contacts: Function of the junction. *Nat. Rev. Mol. Cell Biol.* 13, 607–615.
- Ruas, J.S., Siqueira-Santos, E.S., Amigo, I., Rodrigues-Silva, E., Kowaltowski, A.J., and Castilho, R.F. (2016). Underestimation of the maximal capacity of the mitochondrial electron transport system in oligomycin-treated cells. *PLoS One* 11.
- Rutter, J., Winge, D.R., and Schiffman, J.D. (2010). Succinate dehydrogenase - Assembly, regulation and role in human disease. *Mitochondrion* 10, 393–401.

- Salin, K., Auer, S.K., Rey, B., Selman, C., and Metcalfe, N.B. (2015). Variation in the link between oxygen consumption and ATP production, and its relevance for animal performance. *Proc. R. Soc. B Biol. Sci.* 282.
- Saraste, M. (1999). Oxidative phosphorylation at the fin de siecle. *Science* (80-). 283, 1488–1493.
- Schägger, H., and von Jagow, G. (1991). Blue native electrophoresis for isolation of membrane protein complexes in enzymatically active form. *Anal. Biochem.* 199, 223–231.
- Schatz, P.J. (1993). Use of peptide libraries to map the substrate specificity of a peptide-modifying enzyme: A 13 residue consensus peptide specifies biotinylation in *Escherichia coli*. *Bio/Technology* 11, 1138–1143.
- Schell, J.C., Olson, K.A., Jiang, L., Hawkins, A.J., VanVranken, J.G., Xie, J., Egnatchik, R.A., Earl, E.G., DeBerardinis, R.J., and Rutter, J. (2014). A role for the mitochondrial pyruvate carrier as a repressor of the warburg effect and colon cancer cell growth. *Mol. Cell* 56, 400–413.
- Schlesinger, P.H., Gross, A., Yin, X.M., Yamamoto, K., Saito, M., Waksman, G., and Korsmeyer, S.J. (1997). Comparison of the ion channel characteristics of proapoptotic BAX and antiapoptotic BCL-2. *Proc. Natl. Acad. Sci. U. S. A.* 94, 11357–11362.
- Shao, X., Li, Q., Mogilner, A., Bershadsky, A.D., and Shivashankar, G. V. (2015). Mechanical stimulation induces formin-dependent assembly of a perinuclear actin rim. *Proc. Natl. Acad. Sci. U. S. A.* 112, E2595–E2601.
- Sheehan, D., Meade, G., Foley, V.M., and Dowd, C.A. (2001). Structure, function and evolution of glutathione transferases: implications for classification of non-mammalian members of an ancient enzyme superfamily.
- Shi, J., Zuo, H., Ni, L., Xia, L., Zhao, L., Gong, M., Nie, D., Gong, P., Cui, D., Shi, W., et al. (2014). An IDH1 mutation inhibits growth of glioma cells via GSH depletion and ROS generation. *Neurol. Sci.* 35, 839–845.
- Shield, A.J., Murray, T.P., and Board, P.G. (2006). Functional characterisation of ganglioside-induced differentiation-associated protein 1 as a glutathione transferase. *Biochem. Biophys. Res. Commun.* 347, 859–866.
- Shin, D.W., Pan, Z., Bandyopadhyay, A., Bhat, M.B., Kim, D.H., and Ma, J. (2002). Ca²⁺-dependent interaction between FKBP12 and calcineurin regulates activity of the Ca²⁺ release channel in skeletal muscle. *Biophys. J.* 83, 2539–2549.

Literature

- Shutt, T., Geoffrion, M., Milne, R., and McBride, H.M. (2012). The intracellular redox state is a core determinant of mitochondrial fusion. *EMBO Rep.* *13*, 909–915.
- Sielaff, M., Kuharev, J., Bohn, T., Hahlbrock, J., Bopp, T., Tenzer, S., and Distler, U. (2017). Evaluation of FASP, SP3, and iST Protocols for Proteomic Sample Preparation in the Low Microgram Range. *J. Proteome Res.* *16*, 4060–4072.
- Sies, H., Berndt, C., and Jones, D.P. (2017). Oxidative Stress: Annual Review of Biochemistry. *Annu. Rev. Biochem.* *86*, 715–748.
- De Simoni, S., Linard, D., Hermans, E., Knoop, B., and Goemaere, J. (2013). Mitochondrial peroxiredoxin-5 as potential modulator of mitochondria-ER crosstalk in MPP⁺-induced cell death. *J. Neurochem.* *125*, 473–485.
- Singh, H., and Ashley, R.H. (2006). Redox regulation of CLIC1 by cysteine residues associated with the putative channel pore. *Biophys. J.* *90*, 1628–1638.
- Siudeja, K., Grzeschik, N.A., Rana, A., de Jong, J., and Sibon, O.C.M. (2012). Cofilin/Twinstar phosphorylation levels increase in response to impaired coenzyme A metabolism. *PLoS One* *7*.
- Skre, H. (1974). Genetic and clinical aspects of Charcot-Marie-Tooth's disease. *Clin. Genet.* *6*, 98–118.
- Smirnova, E., Griparic, L., Shurland, D.L., and Van der Bliek, A.M. (2001). Dynamin-related protein Drp1 is required for mitochondrial division in mammalian cells. *Mol. Biol. Cell* *12*, 2245–2256.
- Song, Z., Chen, H., Fiket, M., Alexander, C., and Chan, D.C. (2007). OPA1 processing controls mitochondrial fusion and is regulated by mRNA splicing, membrane potential, and Yme1L. *J. Cell Biol.* *178*, 749–755.
- Sultana, R., Poon, H.F., Cai, J., Pierce, W.M., Merchant, M., Klein, J.B., Markesbery, W.R., and Butterfield, D.A. (2006). Identification of nitrated proteins in Alzheimer's disease brain using a redox proteomics approach. *Neurobiol. Dis.* *22*, 76–87.
- Szabadkai, G., Bianchi, K., Várnai, P., De Stefani, D., Wieckowski, M.R., Cavagna, D., Nagy, A.I., Balla, T., and Rizzuto, R. (2006). Chaperone-mediated coupling of endoplasmic reticulum and mitochondrial Ca²⁺ channels. *J. Cell Biol.* *175*, 901–911.
- Szelechwski, M., Amoedo, N., Obre, E., Léger, C., Allard, L., Bonneu, M., Claverol, S., Lacombe, D., Oliet, S., Chevallier, S., et al. (2018). Metabolic Reprogramming in Amyotrophic Lateral Sclerosis. *Sci. Rep.* *8*, 1–14.

- Szymczak, A.L., and Vignali, D.A.A. (2005). Development of 2A peptide-based strategies in the design of multicistronic vectors. *Expert Opin. Biol. Ther.* *5*, 627–638.
- Takehima, H., Komazaki, S., Nishi, M., Iino, M., and Kangawa, K. (2000). Junctophilins: A novel family of junctional membrane complex proteins. *6*, 11–22.
- Tao, L., Xie, Q., Ding, Y.H., Li, S.T., Peng, S., Zhang, Y.P., Tan, D., Yuan, Z., and Dong, M.Q. (2013). CAMKII and calcineurin regulate the lifespan of *Caenorhabditis elegans* through the FOXO transcription factor DAF-16. *Elife* *2013*.
- Tarze, A., Deniaud, A., Le Bras, M., Maillier, E., Molle, D., Larochette, N., Zamzami, N., Jan, G., Kroemer, G., and Brenner, C. (2007). GAPDH, a novel regulator of the pro-apoptotic mitochondrial membrane permeabilization. *Oncogene* *26*, 2606–2620.
- Tavender, T.J., Sheppard, A.M., and Bulleid, N.J. (2008). Peroxiredoxin IV is an endoplasmic reticulum-localized enzyme forming oligomeric complexes in human cells. *Biochem. J.* *411*, 191–199.
- Thafer, O., Wolf, C., Dey, P.N., Pouya, A., Wüllner, V., Tenzer, S., and Methner, A. (2017). The thiol switch C684 in Mitofusin-2 mediates redox-induced alterations of mitochondrial shape and respiration. *Neurochem. Int.* *117*, 167–173.
- Timmerman, V., Clowes, V.E., and Reid, E. (2013). Overlapping molecular pathological themes link Charcot-Marie-Tooth neuropathies and hereditary spastic paraplegias. *Exp. Neurol.* *246*, 14–25.
- Tomar, D., Dong, Z., Shanmughapriya, S., Koch, D.A., Thomas, T., Hoffman, N.E., Timbalia, S.A., Goldman, S.J., Breves, S.L., Corbally, D.P., et al. (2016). MCUR1 Is a Scaffold Factor for the MCU Complex Function and Promotes Mitochondrial Bioenergetics. *Cell Rep.* *15*, 1673–1685.
- Tovar-Mendez, A., Miernyk, J.A., and Randall, D.D. (2003). Regulation of pyruvate dehydrogenase complex activity in plant cells. *Eur. J. Biochem.* *270*, 1043–1049.
- Toyama, E.Q., Herzig, S., Courchet, J., Lewis, T.L., Losón, O.C., Hellberg, K., Young, N.P., Chen, H., Polleux, F., Chan, D.C., et al. (2016). Metabolism: AMP-activated protein kinase mediates mitochondrial fission in response to energy stress. *Science* (80-.). *351*, 275–281.
- Tristan, C., Shahani, N., Sedlak, T.W., and Sawa, A. (2011). The diverse functions of GAPDH: Views from different subcellular compartments. *Cell. Signal.* *23*, 317–323.
- Turkan, I. (2018). ROS and RNS: Key signalling molecules in plants. *J. Exp. Bot.* *69*, 3313–3315.

- Turrens, J.F. (1997). Superoxide production by the mitochondrial respiratory chain. *Biosci. Rep.* 17, 3–8.
- Turrens, J.F. (2003). Mitochondrial formation of reactive oxygen species. *J. Physiol.* 552, 335–344.
- Twig, G., and Shirihai, O.S. (2011). The interplay between mitochondrial dynamics and mitophagy. *Antioxidants Redox Signal.* 14, 1939–1951.
- Urbańska, K., and Orzechowski, A. (2019). Unappreciated role of LDHA and LDHB to control apoptosis and autophagy in tumor cells. *Int. J. Mol. Sci.* 20.
- Uttara, B., Singh, A. V, Zamboni, P., and Mahajan, R.T. (2009). Oxidative stress and neurodegenerative diseases: a review of upstream and downstream antioxidant therapeutic options. *Curr. Neuropharmacol.* 7, 65–74.
- Vacanti, N.M., Divakaruni, A.S., Green, C.R., Parker, S.J., Henry, R.R., Ciaraldi, T.P., Murphy, A.N., and Metallo, C.M. (2014). Regulation of substrate utilization by the mitochondrial pyruvate carrier. *Mol. Cell* 56, 425–435.
- Verhoeven, K., Claeys, K.G., Züchner, S., Schröder, J.M., Weis, J., Ceuterick, C., Jordanova, A., Nelis, E., De Vriendt, E., Van Hul, M., et al. (2006). MFN2 mutation distribution and genotype/phenotype correlation in Charcot-Marie-Tooth type 2. *Brain* 129, 2093–2102.
- Wagner, K.M., Rüegg, M., Niemann, A., and Suter, U. (2009). Targeting and function of the mitochondrial fission factor GDAP1 are dependent on its tail-anchor. *PLoS One* 4, e5160.
- Wallace, D.C. (2005). A Mitochondrial Paradigm of Metabolic and Degenerative Diseases, Aging, and Cancer: A Dawn for Evolutionary Medicine. *Annu. Rev. Genet.* 39, 359–407.
- Walton, W.H. (1948). Feret's statistical diameter as a measure of particle size [2]. *Nature* 162, 329–330.
- Wanders, R.J.A., and Waterham, H.R. (2006). Biochemistry of Mammalian Peroxisomes Revisited. *Annu. Rev. Biochem.* 75, 295–332.
- Watmough, N.J., Turnbull, D.M., Sherratt, H.S.A., and Bartlett, K. (1989). Measurement of the acyl-CoA intermediates of β -oxidation by h.p.l.c. with on-line radiochemical and photodiode-array detection. Application to the study of [U- 14 C]hexadecanoate oxidation by intact rat liver mitochondria. *Biochem. J.* 262, 261–269.
- Whitaker, M. (2004). Calcium imaging. *Methods Cell Biol.* 2004, 443–468.
- White, C., and McGeown, J.G. (2002). Carbachol triggers RyR-dependent Ca^{2+} release via

- activation of IP3 receptors in isolated rat gastric myocytes. *J. Physiol.* *542*, 725–733.
- Wolf, C., Zimmermann, R., Thaher, O., Bueno, D., Wüllner, V., Schäfer, M.K.E., Albrecht, P., and Methner, A. (2019). The Charcot–Marie Tooth Disease Mutation R94Q in MFN2 Decreases ATP Production but Increases Mitochondrial Respiration under Conditions of Mild Oxidative Stress. *Cells* *8*, 1289.
- Wolf, C., Amo, V.L. del, Arndt, S., Bueno, D., Tenzer, S., Hanschmann, E.-M., Berndt, C., and Methner, A. (2020). Redox Modifications of Proteins of the Mitochondrial Fusion and Fission Machinery. *Cells* *9*.
- Woods, A., Dickerson, K., Heath, R., Hong, S.P., Momcilovic, M., Johnstone, S.R., Carlson, M., and Carling, D. (2005). Ca²⁺/calmodulin-dependent protein kinase kinase- β acts upstream of AMP-activated protein kinase in mammalian cells. *Cell Metab.* *2*, 21–33.
- Wüllner, U., Seyfried, J., Groscurth, P., Beinroth, S., Winter, S., Gleichmann, M., Heneka, M., Löschmann, P.-A., Schulz, J.B., Weller, M., et al. (1999). Glutathione depletion and neuronal cell death: the role of reactive oxygen intermediates and mitochondrial function. *Brain Res.* *826*, 53–62.
- Xu, H., Guan, N., Ren, Y.L., Wei, Q.J., Tao, Y.H., Yang, G.S., Liu, X.Y., Bu, D.F., Zhang, Y., and Zhu, S.N. (2018). IP3R-Grp75-VDAC1-MCU calcium regulation axis antagonists protect podocytes from apoptosis and decrease proteinuria in an Adriamycin nephropathy rat model. *BMC Nephrol.* *19*.
- Yang, C., Ko, B., Hensley, C.T., Jiang, L., Wasti, A.T., Kim, J., Sudderth, J., Calvaruso, M.A., Lumata, L., Mitsche, M., et al. (2014). Glutamine oxidation maintains the TCA cycle and cell survival during impaired mitochondrial pyruvate transport. *Mol. Cell* *56*, 414–424.
- Yang, M., Camara, A.K.S., Wakim, B.T., Zhou, Y., Gadicherla, A.K., Kwok, W.-M., and Stowe, D.F. (2012). Tyrosine nitration of voltage-dependent anion channels in cardiac ischemia-reperfusion: reduction by peroxynitrite scavenging. *Biochim. Biophys. Acta - Bioenerg.* *1817*, 2049–2059.
- Yetkin-Arik, B., Vogels, I.M.C., Nowak-Sliwinska, P., Weiss, A., Houtkooper, R.H., Van Noorden, C.J.F., Klaassen, I., and Schlingemann, R.O. (2019). The role of glycolysis and mitochondrial respiration in the formation and functioning of endothelial tip cells during angiogenesis. *Sci. Rep.* *9*, 1–14.
- Yi, M., Weaver, D., and Hajnóczky, G. (2004). Control of mitochondrial motility and distribution by the calcium signal: A homeostatic circuit. *J. Cell Biol.* *167*, 661–672.

Literature

- Yoboue, E.D., Rimessi, A., Anelli, T., Pinton, P., and Sitia, R. (2017). Regulation of Calcium Fluxes by GPX8, a Type-II Transmembrane Peroxidase Enriched at the Mitochondria-Associated Endoplasmic Reticulum Membrane. *Antioxid. Redox Signal.* 27, 583–595.
- Yoboue, E.D., Sitia, R., and Simmen, T. (2018). Redox crosstalk at endoplasmic reticulum (ER) membrane contact sites (MCS) uses toxic waste to deliver messages. *Cell Death Dis.* 9.
- Yoon, Y., Pitts, K.R., and McNiven, M.A. (2001). Mammalian dynamin-like protein DLP1 tubulates membranes. *Mol. Biol. Cell* 12, 2894–2905.
- Yoon, Y., Krueger, E.W., Oswald, B.J., and McNiven, M.A. (2003). The Mitochondrial Protein hFis1 Regulates Mitochondrial Fission in Mammalian Cells through an Interaction with the Dynamin-Like Protein DLP1. *Mol. Cell. Biol.* 23, 5409–5420.
- Yoshida, T., Kakizuka, A., and Imamura, H. (2016). BTeam, a Novel BRET-based Biosensor for the Accurate Quantification of ATP Concentration within Living Cells. *Sci. Rep.* 6, 1–9.
- Zaffagnini, M., Marchand, C.H., Malferrar, M., Murail, S., Bonacchi, S., Genovese, D., Montalti, M., Venturoli, G., G., F., Baaden, M., et al. (2019). Glutathionylation primes soluble GAPDH for late collapse into insoluble aggregates. *Proc. Natl. Acad. Sci.* 116, 26057–26065.
- Zaglia, T., Ceriotti, P., Campo, A., Borile, G., Armani, A., Carullo, P., Prando, V., Coppini, R., Vida, V., Stølen, T.O., et al. (2017). Content of mitochondrial calcium uniporter (MCU) in cardiomyocytes is regulated by microRNA-1 in physiologic and pathologic hypertrophy. *Proc. Natl. Acad. Sci. U. S. A.* 114, E9006–E9015.
- Zhang, Z., Zhang, L., Zhou, L., Lei, Y., Zhang, Y., and Huang, C. (2019). Redox signaling and unfolded protein response coordinate cell fate decisions under ER stress. *Redox Biol.* 25, 101047.
- Zhao, J.W., Gao, Z.L., Ji, Q.Y., Wang, H., Zhang, H.Y., Yang, Y.D., Xing, F.J., Meng, L.J., and Wang, Y. (2012). Regulation of cofilin activity by CaMKII and calcineurin. *Am. J. Med. Sci.* 344, 462–472.
- Zhong, D., Xiong, L., Liu, T., Liu, X., Liu, X., Chen, J., Sun, S.Y., Khuri, F.R., Zong, Y., Zhou, Q., et al. (2009). The glycolytic inhibitor 2-deoxyglucose activates multiple prosurvival pathways through IGF1R. *J. Biol. Chem.* 284, 23225–23233.
- Zou, C., Wang, Y., and Shen, Z. (2005). 2-NBDG as a fluorescent indicator for direct glucose uptake measurement. *J. Biochem. Biophys. Methods* 64, 207–215.
- Züchner, S., Mersiyanova, I. V., Muglia, M., Bissar-Tadmouri, N., Rochelle, J., Dadali, E.L.,

Literature

Zappia, M., Nelis, E., Patitucci, A., Senderek, J., et al. (2004). Mutations in the mitochondrial GTPase mitofusin 2 cause Charcot-Marie-Tooth neuropathy type 2A. *Nat. Genet.* 36, 449–451.

9. Appendix

Abbreviations

°C	Degree Celsius	BIAM	N-(Biotinoyl)-N-(Iodoacetyl) Ethylenediamide
µm	micrometer		
2-DG	1-Deoxyglucose	BioGEE	Biotinylated glutathione ethyl ester
2-NBDG	2-(N-(7-Nitrobenz-2-oxa-1,3-diazol-4-yl)Amino)-2-Deoxyglucose	BRET	Bioluminescence resonance energy transfer
A		C	
A	Alanine	C	Cysteine
aa	aminoacid	Ca ²⁺	Calcium
AA	Ascorbic acid	CaM	Calmodulin
ADP	Adenosine-diphosphate	CAMKKβ	Calcium/calmodulin-dependent kinase kinase 2
ADR	Adriamycin	CaN	Calcineurin
Aeq	Aequorine	CCH	Carbachol
AMP	Adenosine-monophosphate	CFP	Cyan fluorescent protein
AMPK	AMP-activated proteinkinase	CISY	Citrate synthetase
Ang II	Angiotensin II	CM	Crude mitochondria
ANOVA	Analysis of variance	CMT	Charcot-Marie Tooth disease
ATP	Adenosine-triphosphate	COXI	Cyclooxygenase I
ATP5	ATP synthase subunit 5	COXIV	Mitochondrial cytochrome c oxidase IV
AU	Arbitrary Units		
B		Ctrl	Control
BDNF	Brain-derived neurotrophic factor	Cyt	Cytosolic

Appendix

D		FDR	False discovery rate
dbcAMP	Dibutyryl cAMP	FKB12	FK506-binding protein of 12 kDa
DIA	Data-independent acquisition	FKBP	FK506 binding protein
DLAT	Dihydrolipoyl transacetylase	FRB	FKBP–rapamycin binding domain
DLD	Dihydrolipoyl dehydrogenase	FRET	Fluorescence Resonance Energy Transfer
DM	Dorsomorphin		
DMSO	Dimethyl-sulfoxide	G	
DRP1	Dynammin-related protein 1	G	Glycine
DTNB	5,5'-dithiobis-(2-nitrobenzoic acid)	GAPDH	Glyceraldehyde 3-phosphate dehydrogenase
DTT	Dithiothreitol	GDAP1	Ganglioside Differentiation associated protein
E		GDH	Glutamate dehydrogenase
E	Glutamic acid	GDNF	Glial cell-derived neurotrophic factor
EA	Ethacrynic acid		
EB	Embryonic bodies	GPX	Glutathione peroxidase
EDTA	Ethylenediaminetetraacetic	GRP75	Glucose-regulated protein 75
EMRT	Exact mass retention time	GRX1	Glutaredoxin
ER	Endoplasmic reticulum	GSH	Reduced glutathione
EtOH	Ethanol	GSR	Glutathione reductase
ETS	Electron transport system	GSSG	Glutathione disulfide
EV	Empty vector	GST	Glutathion transferase
Ex/em	Excitation/emission	GTP	Guanidine-triphosphate
F		GED	GTPase effector domain
F	Phenylalanine		
FCS	Fetal bovine/calf serum		

Appendix

H		Map2	Microtubule-associated protein 2
H	Histidine		
HD	Heptad-repeat domain	MAPEG	membrane-associated proteins involved in eicosanoid and glutathione
HEK	Human embryonic kidney		
HK	Hexokinase	MCU	Mitochondrial calcium uniporter
I			
ICC	Immunocytochemistry	ME	Malic enzyme
IDH	Isocitrate dehydrogenase	MEF	Mouse embryonic fibroblasts
IMM	Inner mitochondrial membrane	MERCs	Mitochondria-ER-contact sites
IMS	Ion-mobility separation		
INF2	Inverted Formin 2	MFF	Mitochondrial fission factor
IP3	Inositol-1,4,5-tris-phosphate	MFN	Mitofusin
IP3R	Inositol-1,4,5-tris-phosphate receptor	MN	Motoneuron
		MPC	Mitochondrial pyruvate carrier
K			
K	Lysine	Mt	Mitochondrial
KD	Knockdown	N	
kDa	Kilodalton	NADPH	Nicotinamide adenine dinucleotide phosphate
L		NEAA	Non-essential amino acids
L	Leucine	NEM	N-Ethylmaleimide
LC-MS	Liquid chromatography-mass spectrometry	NFAT	Nuclear factor of activated T cells
LDHA	Lactate dehydrogenase A	Nm	Nanometer
M		NPC	Neuronal progenitor cell
MAM	Mitochondria-associated membrane		

Appendix

O			PRDX	Peroxiredoxin
OAA	Oxaloacetate		PrSSG	Protein glutathionylation
OMM	Outer mitochondrial membrane		PTM	Posttranslational modification
Omy	Oligomycine		PVDF	Polyvinylidene difluoride
OPA1	Optic Atrophy 1		Q	
P			Q	Glutamine
P	Proline		qPCR	Quantitative real-time polymerase chain reaction
P/S	Penicillin/streptomycin		R	
PBS	phosphate buffered saline		R	Arginine
PC	Pyruvate carboxylase		RA	Retinoic acid
PDC	Pyruvate dehydrogenase complex		Rapa	Rapamycin
PDH	Pyruvate dehydrogenase		RIPA	Radioimmunoprecipitation assay
PDK	Pyruvate dehydrogenase kinase		RLU	Relative luminescence unit
PDL	Poly-D-Lysine		RNS	Reactive nitrogen species
PDP1	Pyruvate dehydrogenase phosphatase subunit 1		ROI	Region of interest
PEG ₂₄	MM(PEG) ₂₄ Methyl-PEG-Maleimide reagent		ROS	Reactive oxygen species
PEP			Rpm	Revolutions per minute
PFA	Paraformaldehyde		RT	Room temperature
PIP ₂	Phosphatidylinositol 4,5-bisphosphate		RyR	Ryanodine receptor
PM	Pure mitochondria		S	
PMA	Phorbol 12-myristate 13-acetate		S	Serine
			SA	Streptavidin
			SDS	Sodium dodecyl sulfate

Appendix

SDS PAGE	Sodium dodecyl sulfate polyacrylamide gel electrophoresis	TEM	Transmission electron microscopy
		TMD	Transmembrane domain
SEM	Standard error of the mean	TMRM	Tetramethylrhodamine
smNPC	Small molecule induced neuronal progenitor cell	V	
		v/v	Volume/volume
SOD	Superoxide dismutase	VDAC	Voltage-dependent anion channel
SSA	Salicylic acid		
Stim1	Stromal interaction molecule 1	W	
		W	Tryptophan
T		w/v	Weight/volume
T	Threonine	WT	Wildtype
T2A	Thosea asigna virus 2A peptide	Y	
		Y	Tyrosine
TCEP	Tris(2-carboxyethyl) phosphine	YFP	Yellow fluorescent protein

Appendix

Acknowledgements

Appendix

Belikan, P., Buehler, U., Birkenstock, J., **Wolf, C.**, Zipp, F., & Siffrin, V. (2014). Chemokine receptor CCR7 on CD4+ T cells plays a crucial role in the induction of experimental autoimmune encephalomyelitis. *Journal of Neuroimmunology*, 275(1–2), 196.